

Investigating Acoustic Emission in Selective Laser Melting

Cardiff University

Stephen Ball

**A thesis submitted in fulfilment for the degree
Doctor of Philosophy**

September 2021

Abstract

As additive manufacturing continues to develop as a manufacturing technique, companies such as Renishaw plc are increasingly looking for ways to make it a more cost-effective and practical alternative to traditional methods. A major part of this is the use of in-process condition monitoring techniques, such as acoustic emission, to allow the suitability of AM parts for loading to be assessed without expensive post-processing methods. Acoustic emission will allow not only the detection but also the location of defects as they occur throughout the build volume.

This project was undertaken with the aim of assessing the use of acoustic emission within the Renishaw AM500. This work was split into three main sections; assessing how AE signals propagate through a build plate assembly, assessing how to accurately locate AE sources and whether it is then possible to classify defects based on collected AE signals. Studies were carried out using a 3D scanning laser vibrometer to assess how signals propagate through various parts of the build plate assembly. Work was also carried out to assess the accuracy of using the Time of Arrival and delta-T methods to locate sources, with studies done to improve the implementation of each. Finally, work was done to assess the viability of using machine learning methods to classify signals in such a complex geometry.

The results of these propagation studies led to a design change to the heater plate within the AM500 to simplify propagation paths to give more reliable location results. Studies into using the delta-T location method showed that differences in plate thickness led to negligible differences in delta-T training maps meaning that a single map can be used throughout the lifetime of a build plate. Further results showed that in a homogeneous material such as an AM build plate, data from as few as four training points are needed to produce a reliable delta-T training set. Finally, results of characterisation studies showed that not only will the complex geometry of the system make distinguishing signals difficult, but differences between parts being built will make developing a standard set of training data exceedingly difficult.

Acknowledgements

I would first like to thank Professor Rhys Pullin, Dr Matthew Pearson, Dr Mark Eaton and Dr Davide Crivelli for all of their guidance and encouragement throughout the course of this project. They gave me the self-belief to see this project through to the end. I would also like to thank Dr John McCrory and Frederick Purcell for all the assistance they provided in experimental work.

I am also grateful to Damon Northeast and Jonathan Mansell at Renishaw plc, whose practical assistance and input was vital to the completion of this project.

I would like to thank the Engineering & Physical Sciences Research Council and Renishaw plc for providing the funding which made all of this possible.

I would like to thank my fiancé Hannah for all the emotional support she has provided over the last 4 years, without out which I doubtless would have quit years ago. And thank you to my parents for giving me the belief that I could achieve everything I set my mind do. I am also grateful to my cat Dolly for making every day a little brighter.

Finally, I'd like to thank the Covid-19 Virus for making the last 18 months far more difficult than they ever needed to be.

Glossary of Terms

AE- Acoustic emission. The phenomena by which elastic waves are generated by a sudden release of strain energy in a material

AM- Additive Manufacturing. A manufacturing process where material is gradually deposited or undergoes a change to form a part

PBF- Powder Bed Fusion. A group of additive manufacturing methods where powders are fused to form a part

SLM- Selective Laser Melting. A form of additive manufacturing where powders are fully melted and fused to form a part in a layer-by-layer process

SLS- Selective Laser Sintering. A form of additive manufacturing where powders are partially melted and fused to form a part in a layer-by-layer process

Rayleigh-Lamb Waves- A family of waves which are formed when a bulk wave becomes constricted by one or two surfaces. These are made up of symmetric and anti-symmetric modes

Dispersion- The phenomenon by which the different frequency components of a signal travel at different velocities

Group Velocity- The velocity at which a wave packet of multiple frequencies travels through a material

Phase Velocity- The velocity at which a single frequency component travels through a material. In non-dispersive media this is equal to the group velocity

Wavenumber- The number of wavelengths or cycles per unit distance

TOA- Time of Arrival. A method of locating source locations by using the time difference between sensors and the known wave velocity in that material

Delta-T- A method of locating source locations where a training map is collected across the area of interest and sources are located on those maps

AIC- Akaike Information Criterion. A method of measuring the variance in a signal which can be used to ascertain the true beginning of a signal emerging from noise

PCA- Principal Component Analysis. A method of measuring the variance of a data set and reducing it to a smaller set of components that are more easily interpreted

Wavelet Transform- A method of determining the frequency content of a signal which is more appropriate for highly transient multi-frequency signals such as AE than Fourier transform

Piezoelectric- The phenomenon where mechanical signals are transformed to electrical signals or vice versa, by means of a highly sensitive piezoelectric crystal

Nomenclature

c_p	Longitudinal velocity in a plate, also known as the pressure or P-wave velocity (ms^{-1})
c_s	Transverse velocity in a plate, also known as the shear or S-wave velocity (ms^{-1})
c_l	Longitudinal velocity in a rod, also known as the bar velocity (ms^{-1})
λ, μ	Lamé Constants, functions of Young's Modulus, Poisson's ratio and density
ρ	Material density (kgm^{-3})
E	Young's Modulus (Pa)
ν	Poisson's ratio
k	Wavenumber (m^{-1})
c_{ph}	Phase Velocity, the velocity of a particle in a wave
c_g	Group velocity, the velocity of a wave packet
ω	Angular velocity (rads^{-1})
l	Length of a waveguide (m)
R	Radius of a location hyperbola (m)
Δt	Time difference between a signal reaching two sensors (s)
D	Distance between 2 sensors (m)
θ	Angle between sensor and possible signal source ($^\circ$)

Contents

1. Introduction	1
1.1. Background	1
1.2. Challenges.....	4
1.3. Objectives	5
1.4. Novelty Statement	5
1.5. Thesis Structure	6
1.6 Contribution to Knowledge	7
2. Theory and Literature Review	8
2.1. Introduction.....	8
2.2. Additive Manufacturing	8
2.3. Condition Monitoring.....	12
2.4. Acoustic Emission	15
2.4.1. Mechanisms of Acoustic Emission	15
2.4.2. Breakdown of an Acoustic Emission Signal	16
2.4.3. Applications of Acoustic Emission.....	18
2.4.4. Additive Manufacturing with Acoustic Emission	19
2.5. Propagation of Sound through Solids	20
2.5.1. Bulk Waves	20
2.5.2. Rayleigh-Lamb Waves	21
2.4.3. Dispersion of Signals	23
2.5.4. Attenuation of Signals	27
2.5.5. Waves in Waveguides	28
2.6. Location of Signals	29
2.6.1. Time of Arrival Location Method	29
2.6.2. Delta-T Location Method.....	30
2.5.3. Other Signal Location Methods	32
2.6.4. Akaike Information Criterion	33
2.7. Characterisation of Signals.....	34
2.7.1. Feature Extraction Techniques	34
2.7.2. Machine Learning.....	36
3. Experimental Techniques.....	38
3.1. Introduction.....	38
3.2. Platform.....	38
3.3. AE System.....	42

3.4. Sensors	43
3.5. Signal Generation	45
3.6. Couplant	47
3.7. Vibrometry	47
3.8. Software	49
4. Propagation	50
4.1. Introduction	50
4.2. Propagation through Heater Plate	51
4.2.1. Experimental Techniques	51
4.2.2. Results	52
4.2.3. Discussion	54
4.3. Propagation through Build Plate	55
4.3.1. Experimental Procedure	55
4.3.2. Results	58
4.3.3. Discussion	72
4.4. Propagation through Waveguides	73
4.4.1. Experimental Procedure	73
4.4.2. Results	74
4.4.3. Discussion	81
4.5. Conclusions	81
5. Location	84
5.1. Introduction	84
5.2. Effect of Poor Plate Fixing	85
5.2.1. Experimental Procedures	85
5.2.2. Results	87
5.2.3. Discussion	102
5.3. Effect of Plate Thickness	103
5.3.1. Experimental Procedures	103
5.3.2. Results	106
5.3.3. Discussion	121
5.4. Optimising Delta-T Collection	122
5.4.1. Experimental Procedures	122
5.4.2. Results	124
5.4.3. Discussion	134
5.5. Locating In-Process Signals	134
5.5.1. Experimental Procedures	134

5.5.2. Results	135
5.4.3. Discussion	138
5.6. Conclusion	138
6. Characterisation	140
6.1. Introduction.....	140
6.2. Effect of Waveguide Geometry on Signals.....	141
6.2.1. Experimental Procedure.....	141
6.2.2. Results	144
6.2.3. Discussion	156
6.3. Effect of Plate Thickness on Signals	157
6.3.1. Experimental Procedure.....	157
6.3.2. Results	157
6.3.3. Discussion	170
6.4. Separating In-Process Signals	171
6.4.1. Experimental Procedure.....	171
6.4.2. Results	171
6.4.3. Discussion	180
6.5. Conclusion	180
7. Conclusion and Future Work.....	182
7.1. Conclusion	182
7.2. Future Work	187

1. Introduction

1.1. Background

With additive manufacturing entering the mainstream, companies such as Renishaw plc are looking for ways to make the creation of production parts more realistic. Additive manufactured parts are far more likely to have defects such as cracks and low porosity areas than traditionally manufactured parts due to the immaturity of the process compared to conventional manufacturing and a lack of established standards (Everton, et al., 2016). This means that parts require extensive post-processing monitoring to ensure finished components are safe to use and are more suited to unloaded than loaded applications. The great strength of additive manufacturing, however, is that it allows greater optimisation of designs with features that would not be possible with conventional machining. Examples of uses include small parts such as seatbelt buckles on aeroplanes where optimised design means a significant weight saving across the whole aeroplane (Technavio, 2018). Another example includes the GE LEAP engine, where additive manufacturing allowed the design of a new fuel nozzle 25% lighter and five times stronger than previous iterations (Metal AM, 2021). Additive manufacturing can also be used to produce parts with complex internal geometries that cannot be produced by conventional machining, such as the cooling channels shown in Figure 1. Renishaw plc funded this project to develop an acoustic emission (AE) system for the Renishaw AM500, capable of detecting and locating defects in-situ and, if possible, classify defects based upon the AE signal. This gives an impression of the quality of the part without extensive post-processing and allows the process to be stopped as soon as

a major defect is detected. This in turn reduces manufacturing times for unusable parts and reduces costly material wastage.

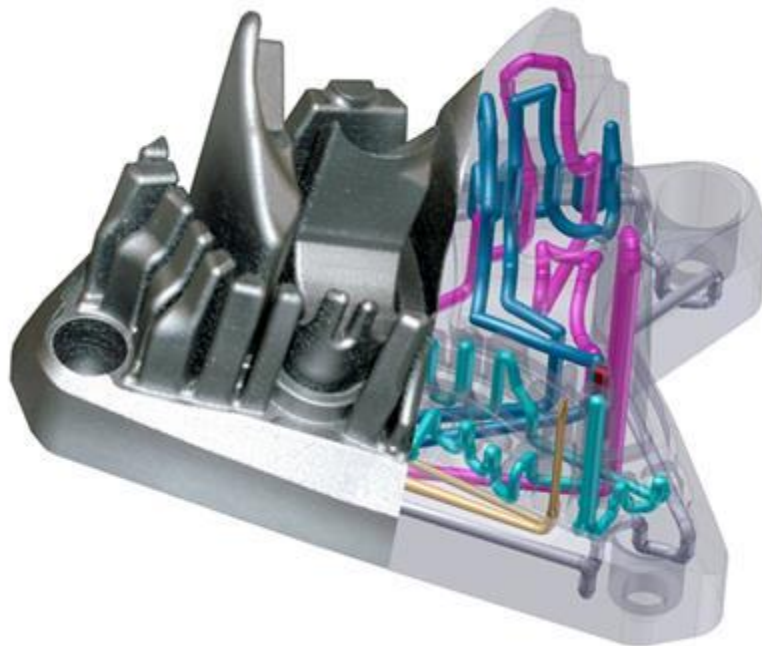


Figure 1. An example of how additive manufacturing can be used to introduce more complex elements, such as cooling channels, into a design (Renishaw plc, 2021)

In recent years, additive manufacturing has developed from a niche method of rapid prototyping to a fully-fledged manufacturing method. Additive manufacturing is a catch-all term used to describe various technologies such as selective laser sintering (SLS), fused-deposition modelling (FDM), stereolithography (SLA) and direct metal deposition (DMD). This is in contrast to more traditional subtractive manufacturing methods such as milling, turning or drilling.

Selective laser sintering was first patented by the University of Texas in the 1980s, while the first metal system was patented by DTM Corp in 1996 (Gibson, et al., 2015), though this system sintered a polymer part before infiltrating with copper. Over time, this progressed to metallic powders with a thermoplastic binder coating and then to fully weldable metallic powders. This led to the selective laser melting (SLM) technology used in the Renishaw AM500.

To be used in a load-bearing capacity, it is important that a part be free from cracks or voids as these can lead to stress concentrations and thus failures. In traditionally manufactured parts this is not an expected issue due to the methods and decades of research. This is not the case with SLS manufactured parts, which will often contain voids and cracks caused by the build-up of thermal stresses during manufacture. Because of this, an SLS manufactured part needs to be inspected to ensure it can suitably bear the required load.

To check the quality of a SLS manufactured part, it is common to use a CT scan or X-ray to identify voids. This is an expensive and time-consuming process to perform for every part, so a process that can verify the quality of the part as it is manufactured is highly desirable. This also can provide a way of identifying and locating errors as they occur during manufacture so that the specific build can be stopped so as not to waste powder and energy.

There are many avenues that have been explored in relation to in-process monitoring in additive manufacturing. These include ultrasonic monitoring, optical monitoring, thermal monitoring and X-ray monitoring.

Increasingly acoustic methods are being explored for in process monitoring. This includes audible acoustics with microphones placed above the print area and ultrasonic applications. Single sensor AE monitoring has been carried out, but at the outset of this study there was no system that used an array of sensors to identify the location of defects.

The advantage that AE has over the previously mentioned techniques is the ability to identify sub-surface cracks. Most other techniques scan the surface of each layer being printed and do not account for defects occurring within the bulk material due

to accumulated stresses. It is also less affected by other process noises such as laser and pump noise which would impact on an audible acoustic system. AE is caused by an elastic stress wave from deformation within a material which is then detected by piezoelectric sensors on the surface of the material. AE can be caused by internal friction, cracking or porosity.

Renishaw plc wanted to investigate the use of AE within the build process with the aim of identifying and locating defects as they occur during a build process.

1.2. Challenges

There are several challenges associated with implementing an AE system with the Renishaw AM500. AE is generally used in large-scale applications such as bridges and thin-walled vessels. However, in this case, the task is to implement an AE system in the limited space of the AM500 build area.

The first challenge is the geometry of the print area within the Renishaw AM500. The geometry and nature of the build chamber mean that any AE sensors have to be mounted away from where signals are generated, giving rise to complex propagation paths. Additionally, the proximity of heating elements presents a further challenge to sensor positioning.

A further challenge is presented by the non-static nature of the build area. After every build the build plate is removed and the printed parts are cut from the plate, with the top layer of the build plate being skimmed to present a fresh surface for the next build. This means that the fastenings and plate thickness will change for every single build, leading to a different geometry for each build. Finally, each new

built part is different, in terms of component geometry material and build location within the machine.

1.3. Objectives

The primary aim of this project was to identify and locate defects as they occur within a Renishaw AM500 using AE. This will ultimately allow parts to be produced without expensive post-processing procedures and reduce waste. To achieve this aim will require a detailed understanding of how AE waves propagate through the entire structure from source to sensor and a method to characterise acoustic signatures from the differing mechanisms that occur during the process. Therefore, the specific objectives of this project were:

- To develop an understanding of how signals propagate through the build plate assembly;
- To develop location strategies within the build area and assess the most effective method;
- To assess the feasibility of characterising signals originating from the build area of the AM500.

1.4. Novelty Statement

This thesis is primarily focussed on implementing and optimising an AE system within a SLM additive manufacturing machine, the Renishaw AM500. The novelty of this project is as follows:

- Implemented a full four sensor AE array within a SLM machine which can be used to accurately locate defects;

- Used a 3D laser vibrometer to analyse AE signals that travel through an SLM build plate, directly leading to design changes within the AM500;
- Carried out studies into how build plate thickness effects AE signal propagation and location.

1.5. Thesis Structure

The thesis is structured around seven chapters, beginning with this introductory chapter. The remaining six are as follows:

Chapter 2: Theory and Literature Review- This chapter summarises the literature surrounding additive manufacturing and AE to identify the current state of the art and explains the theoretical concepts behind the work presented in future chapters. This includes sections on additive manufacturing and AE, as well as sections for each results chapter.

Chapter 3: Experimental Techniques- This chapter summarises the equipment and experimental techniques used over the course of the thesis. This includes descriptions of the Renishaw AM500, AE equipment, software and other equipment used such as the laser vibrometer.

Chapter 4: Propagation- This chapter summarises the work completed investigating how signals travel from the source location above the build plate to the sensors. This is broken down into how signals propagate through the heater plate, through the build plate and through the waveguides.

Chapter 5: Location- This chapter summarises the work completed on locating signals in the build plate under various conditions. This is split into sections

concerning the effects of poor plate fixing and plate thickness changes, as well as a section on locating in-process signals. Finally, there is a section on how to optimise data collection for the delta-T method, a novel approach to source location within an additive manufacturing setting.

Chapter 6: Characterisation- This chapter summarises the work completed to investigate the feasibility of characterising signals collected in the Renishaw AM500. This is separated into sections on how signals are affected by waveguide geometry and plate thickness and on how to identify the source of a signal.

Chapter 7: Conclusion and Future Work- This chapter summarises the conclusions of the thesis and suggests work that could be undertaken to build upon the conclusions drawn.

1.6 Contribution to Knowledge

Conferences Attended

Ball, S.; Pullin, R.; Crivelli, D.; McCrory, J.; Northeast, D.; Mansell, J. "Detection and Location of Cracking in Additive Layer Manufacturing Processes Using Acoustic Emission". *60th Meeting of the Acoustic Emission Working Group*, (2018)

Ball, S.; Pullin, R.; Crivelli, D.; McCrory, J.; Northeast, D.; Mansell, J. "Location of Cracks Occurring in an Additive Manufacturing Process by Acoustic Emission". *BSSM 13th Conference*, (2018)

2. Theory and Literature Review

2.1. Introduction

Before covering the experimental work carried out in this project, it is necessary to establish the theoretical concepts upon which that work was based. In this chapter the theoretical concepts used throughout this project are detailed, and relevant literature is reviewed. This begins by detailing the origins and development of additive manufacturing, before focussing more closely on the SLM process used by the Renishaw AM500. The use of condition monitoring techniques within additive manufacturing was then reviewed, covering the advantages and disadvantages of each technique. This was followed by a review of the use of specifically AE within additive manufacturing to establish the novelty of the use of an AE system within AM in this project.

There are then further sections of literature review to reflect each subsequent testing chapter, namely signal propagation, source location and characterisation. The propagation section covers the theory of Rayleigh-Lamb waves through solids, and other phenomena such as dispersion. The source location section details the various methods of locating AE signals, mainly focusing on the time of arrival and delta-T methods. Finally, the characterisation section details how features can be calculated from a signal alongside methods of supervised and unsupervised learning that use these features to characterise the signals are explored.

2.2. Additive Manufacturing

Additive manufacturing first emerged in the 1980s (Srivatsen, 2016) as a method of rapid prototyping and later developed as a fully-fledged manufacturing method.

Numerous additive manufacturing techniques have been developed in the intervening years, which Gibson (2021) grouped in the following categories:

- Vat Photopolymerization (VPP): liquid photopolymer in a vat is fused by selective delivery of energy to cure specific parts of the cross-section
- Material Extrusion (MEX): material is deposited by being extruded through a nozzle, which follows a pattern that produces a part cross-section
- Material Jetting (MJT): material is selectively deposited as droplets to build up a part following a cross-section pattern
- Binder Jetting (BJT): a liquid binding agent is deposited onto a powder bed to form part cross-sections
- Sheet Lamination (SHL): sheets of material are bonded to form a part
- Directed Energy Deposition (DED): wire or powder material is deposited and energy is simultaneously provided to form the part
- Powder Bed Fusion (PBF): utilises a powder-filled container that is selectively fused using a scanning laser or electron beam

Each of these have their own uses and advantages and disadvantages. Production of metallic parts is primarily by PBF or DED methods, with the Renishaw AM500 utilising a PBF method. The Renishaw AM500 utilises the SLM method, which is a type of powder bed fusion and is closely associated with Selective Laser Sintering (SLS) which was patented at the University of Texas. The defining features of a powder bed fusion process are a heat source to encourage the fusing of particles, a method of controlling said fusion and a mechanism of adding further powder for each layer. A simple diagram illustrating the powder bed fusion method is shown in Figure 2.

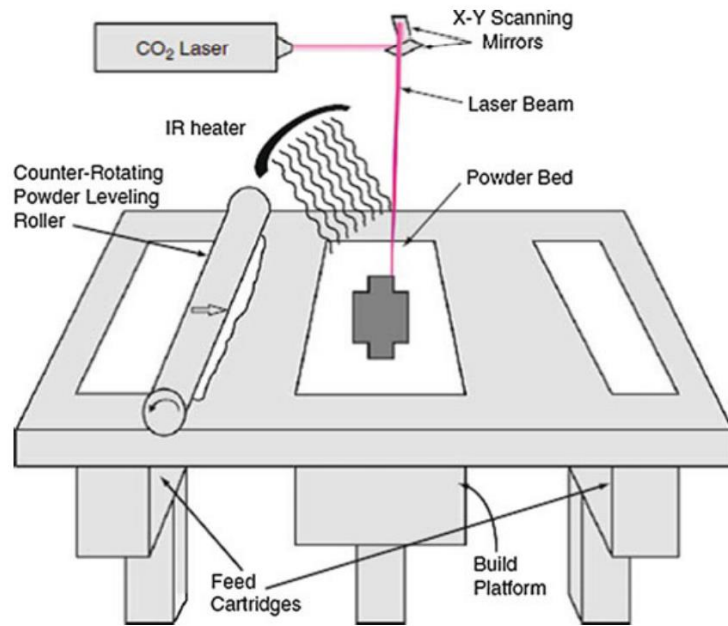


Figure 2. Interior setup of a SLS or SLM machine (Gibson, 2021)

SLS was originally developed for producing wax or polymer prototypes, but over time this was extended to ceramics and weldable metals. Initially, metal powders would be coated or mixed with a polymer binder and infiltrated by another metal afterwards to produce a dense part, as developed by DTM Corp in 1996 (Gibson, et al., 2015). Later, a broader range of particle sizes were used to remove the need for post-process infiltration, and methods of full melting, as in SLM, were developed which removed the need for binders and produced denser parts.

To reduce warping and minimise the laser energy required, powder in the bed is maintained at just below melting temperature, normally using a heater fixed below the bed. This helps to maintain a consistent temperature gradient throughout the build and reduces thermal stresses. The chamber maintains a non-oxygenated atmosphere around the build, typically nitrogen or, in the Renishaw AM500, argon (Renishaw plc, 2021), to prevent oxidation of the powder during welding. Between

each layer, extra powder will be deposited and spread by a roller or wiper to create uniform a layer of up to 0.1mm thick.

A metal SLM machine is made up of a high-power laser, typically 200-400W (Buchbinder, et al., 2011) depending on the powder used and the powder bed. Initially, the powder bed is empty with its base (the build plate) level with the wiper and the bottom of the build area. A layer of powder is then deposited in the build area and spread over the build plate as a uniform layer by the wiper. The first layer is welded to the build plate, which aids in preventing the part from warping. The high-power laser then activates and follows a pattern set out by slicing software. The laser will follow a scanning strategy, which involves following the outline of the part cross-section then following a hatching pattern to fill out the centre. Examples of hatching patterns are shown in Figure 3. This will affect the density of the part and the hatching angle can be altered between layers to improve intra-layer bonding and improve part strength (Parry, et al., 2016).

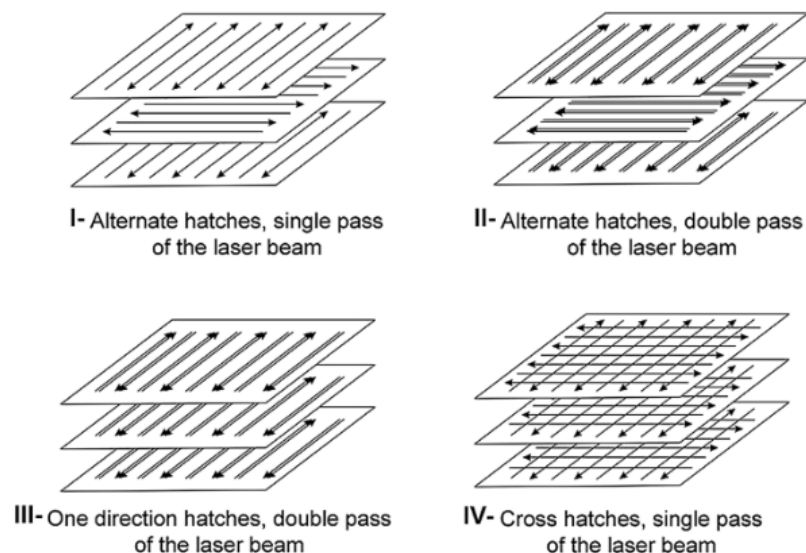


Figure 3. Examples of different hatching strategies (Yu, et al., 2019)

This fuses the powder together in a micro-welding process, either by fully or partly melting the powder. An SLS process only partially melts the powder, resulting in a more porous part than an SLM process, though this requires a lower amount of laser energy (Gibson, 2021).

There are multiple defect mechanisms at work within the AM process. As layers of material are built up, the loading stresses on the build plate and lower layers increase due to increased material mass, which can lead to bending of the plate and lower layers (Srivatsen, 2016). This leads to cracks forming that can be hard to identify with conventional monitoring methods. The other main defect mechanism in SLS is thermal stresses. These are caused by the temperature gradient that forms throughout the part, from the laser to the build plate. This can be offset by heating the build plate to 100-200°C to reduce the temperature gradient (Gibson, 2021). However, thermal stresses are still an issue near where the laser is active, as powder will be repeatedly heated and reheated.

Defects such as voids will also be formed by turbulence in the melt pool about the laser, or by incompletely melted powder. These voids can go on to form cracks when the part is loaded.

2.3. Condition Monitoring

To confirm the strength of an AM part currently there are a number of post-processing techniques that are commonly used to check for porosity and defects. The industrial standard for investigating porosity and internal defects is X-ray tomography (Bidare, et al., 2017). However, this is an expensive and time consuming process and not practical for large numbers of parts.

In-processing monitoring normally involves monitoring process parameters or process signatures. Process parameters are aspects of the process that can easily be adjusted through the machine software such as laser energy, laser scanning velocity, hatch distance, powder layer thickness and scanning strategy. Process signatures arise during the part manufacture and typically include melt pool properties such as depth shape and temperature, or other characteristics linked to the heating, melting and solidifying of the powder (Mani, et al., 2017).

There have been many studies which have investigated how process parameters affect the quality of the final part. For Example, Yadroitsev, et al., (2007) found that a build with a low scanning speed will be more likely to be distorted whilst a high scanning speed will lead to a 'balling' of the melted powder, exhibited in Figure 4.

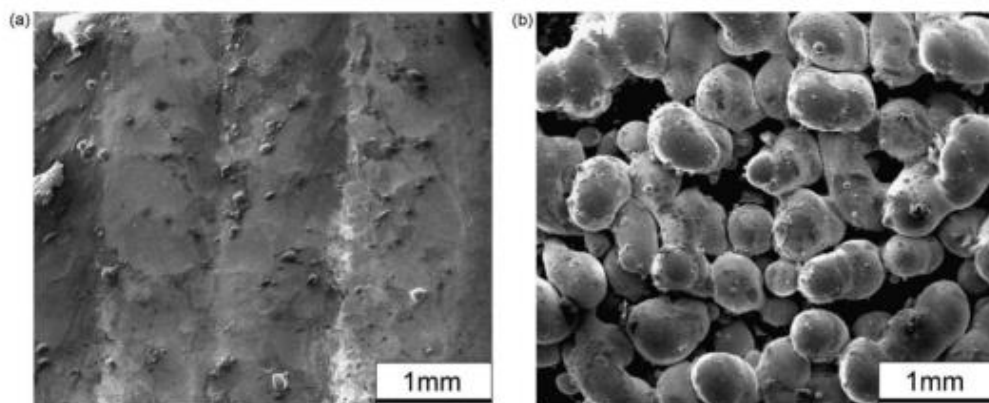


Figure 4. An example of a consistent surface (left) and a surface that has undergone balling (right) (Hanzl, et al., 2015)

Mercelis & Kruth (2006) described how residual stresses would develop in a part due to large thermal gradients around the laser spot and how this can be reduced by heating the build plate, as well as how residual stresses are greater perpendicular to the laser scan direction. Craeghs, et al. (2012) developed a 2-pronged monitoring system; an inspection of the powder deposition and a real-time monitoring of the

melt pool shape and infrared (IR) signature. This involved a charge-couple device (CCD) camera monitoring the entire surface and a photo-detector for looking at more detailed melt pool signatures. Defects could then be identified by mapping the infrared signature of the melt pool for each layer. Unfortunately, to build a detailed temperature of the part the emissivity of the material must be known through powder, melted and solidified forms. For example, it has been noted that un-melted powder will glow more brightly than solidified material despite being at a likely lower temperature (Rodriguez, et al., 2015). In addition, material thrown up by the laser can coat lenses or windows and make it much more difficult to monitor the print bed. A vision system was designed by D'Angelo, et al. (2014) which would measure the distortion of each layer and adjust to compensate. Schwerdtfeger, et al. (2012) used a thermal imaging system on an electron beam melting (EBM) system to record IR images for each layer of a build. Metallographic images were then taken and a comparison made for a selection of layers. A correlation was seen between the IR images and metallographic images, though the IR images were limited by a low resolution. Methods have also been developed using surface acoustic waves to detect surface and sub-surface defects (Clark, et al., 2011), optical coherence tomography (Guan, et al., 2015) and X-ray imaging (Bidare, et al., 2017).

Another avenue of in-process conditioning monitoring is the use of AE, which would allow defects to be detected throughout the volume of the build, without the need to pause the build to collect defect data.

2.4. Acoustic Emission

AE has a long history, with observations in tin as far back as the eighth century, with scientific observation dating back to 1933 (Miller, et al., 2005). AE research advanced with the development of piezoelectric sensors and advances in computing power, with some of the most notable work being done by Josef Kaiser in the 1950s. His work related AE to stress-strain curves in metals, and revealed the mechanisms by which AE was generated, as well as giving his name to the Kaiser effect. This states that if a force is removed after the beginning of AE release, AE will continue after the load is reapplied and the previous peak is exceeded. The use of AE outside laboratories began in the 1970s with applications in pipes and pressure vessels and concrete structures such as bridges (Boving, 1989).

2.4.1. Mechanisms of Acoustic Emission

AE signals are transient elastic waves generated by a sudden release of strain energy in a material caused by an external force. Typical sources of AE activity are impact, friction, cavitation and turbulence (Holroyd, 2000). Impact is when the monitored material is subjected to a momentary surface displacement releasing energy into the bulk of the material. Friction is caused either by external friction, or by rubbing between two sides of an internal crack. Cavitation is caused by the formation or collapse of internal micro-cavities of the material. Finally, turbulence is more often found in fluid-borne AE and is caused by the development and collapse of vortices. Figure 5 shows the path that an AE signal takes before being processed by the recording software. In the AM500, the signal passes through the printed material between the source and the plate. This signal then propagates across the build plate,

into the corners of the plate where the waveguides are positioned. These signals then pass down the waveguide to the piezoelectric sensor, where it is converted into an electrical signal. The signal is altered by the frequency response of the sensor, which may amplify certain frequencies. It then travels through a cable to a preamplifier which has its own frequency response and serves to amplify the signal to be interpreted by the AE system. Each of the fused material, build plate and waveguide will also have a frequency response that will have an impact on the detected signal. This process is exhibited in Figure 5.

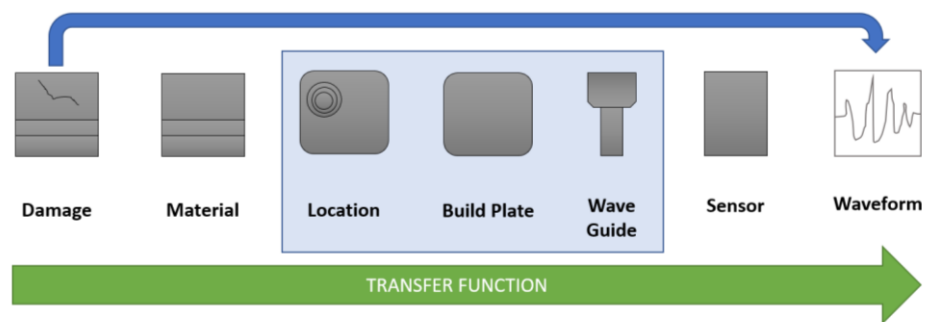


Figure 5. The transfer function of a signal from the initial source to the recording software

2.4.2. Breakdown of an Acoustic Emission Signal

AE signals are commonly defined by a number of features, many of which are defined by the user threshold set before recording (Figure 6). This threshold will prevent insignificant low amplitude signals and AE recording is only activated when it is crossed, with a pre-trigger time to capture the actual signal onset. These features include (Physical Acoustics Corporation, 2007):

Duration- Length of the signal (in microseconds) between the first and last threshold crossing points

Amplitude- Maximum magnitude of the signal. This is expressed in dB using Equation 1

$$dB = 20 \log(V_{max}/1\mu\text{volt}) - (\text{Preamplifier Gain})$$

(Eq. 1)

Counts- Total number of times the signal crosses over the threshold in the signal duration.

Counts to Peak- Total number of times the signal crosses over the threshold before the peak amplitude.

Rise Time- usually measured in microseconds, is the time from the first threshold crossing to the signal peak.

Decay Time- usually measured in microseconds, is the time taken for the signal to decay from the peak amplitude to the final threshold crossing point.

Absolute Energy- usually measured in aJ, is a measure of the energy released by the AE event, derived from the integral of the squared voltage divided by the reference resistance.

Average Frequency- usually measured in kHz, is determined by the counts divided by duration

Reverberation Frequency- usually measured in kHz, is the average frequency from the waveform peak to the final threshold crossing

Initiation Frequency- usually measured in kHz, is the average frequency from the first threshold crossing to the waveform peak

An AE signal will contain a broad range of ultrasonic frequencies from 20kHz to 1MHz.

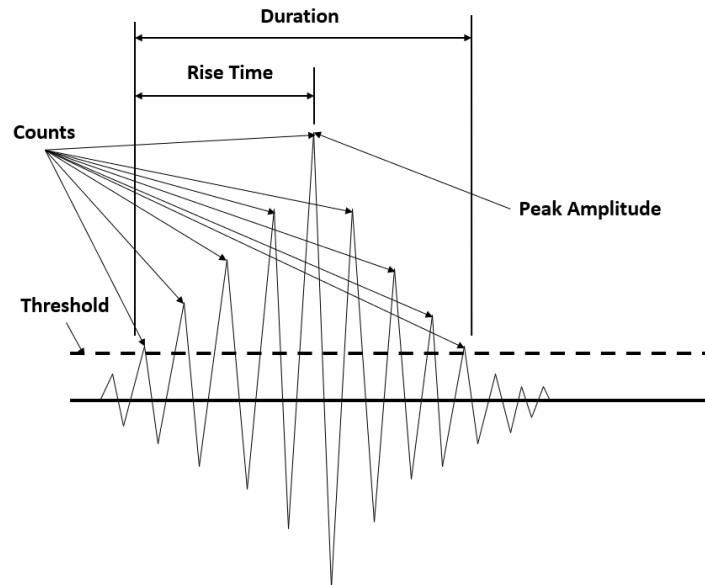


Figure 6. Breakdown of an AE signal

2.4.3. Applications of Acoustic Emission

AE is a passive monitoring method and can be used in tool wear monitoring due to the frequency range of AE being much higher than that of machine noise. In tool wear applications AE signals can be broken down into continuous and transient signals, where continuous signals can be used to assess the sharpness of the tool and transient signals can be used to recognise tool breakage (Li, 2002).

There are several challenges associated with the use of AE. Background noise can be a major issue, especially in a process monitoring situation. It is important to gain a full understanding of the acoustic signature of different types of defects from different densities of material. For example, emissions from the bulk material may be more relevant to the quality of the build than emissions originating from the lower porosity support material. AE propagation is a major challenge, as the waveform can be altered in a way that makes characterisation and location more difficult.

2.4.4. Additive Manufacturing with Acoustic Emission

The use of AE in conjunction with additive manufacturing is still in its relative infancy. Koester, et al. (2018) used AE to identify process issues in direct metal deposition (DMD). However, this was mainly focused on identifying issues with powder deposition and laser power and focused on a very different geometry to those seen in SLS. Gaja & Liou (2017) similarly used AE in a direct metal deposition setting and found they could differentiate between pores and cracks based upon energy, decay time and amplitude. Plotnikov, et al. (2019) recognised the difficulty in interpreting AE signals from AM due to layer build up and hatching variations and attempted to pair AE with an infrared camera to increase the data available for interpretation. Specifically, the infrared was used to determine the surface temperature across the surface of the build volume. (Shevchik, et al., 2018) used a fibre Bragg grating sensor to distinguish void and crack formation using a convolutional neural network. Wasmer, et al. (2019) similarly made use of a fibre Bragg grating to identify AE, but found that it was difficult to correctly classify the signals recorded, with further optimisation needed. Kouprinoff & Luwes (2017) used a microphone to record airborne AE and found the waveform changed depending on layer depth and layer thickness.

2.5. Propagation of Sound through Solids

2.5.1. Bulk Waves

In a material there are two types of waves that will develop and propagate, longitudinal waves and transverse waves. In the case of longitudinal waves, particle motion is parallel to wave propagation, whilst with transverse waves particles will move perpendicular to the propagation direction (Figure 7).

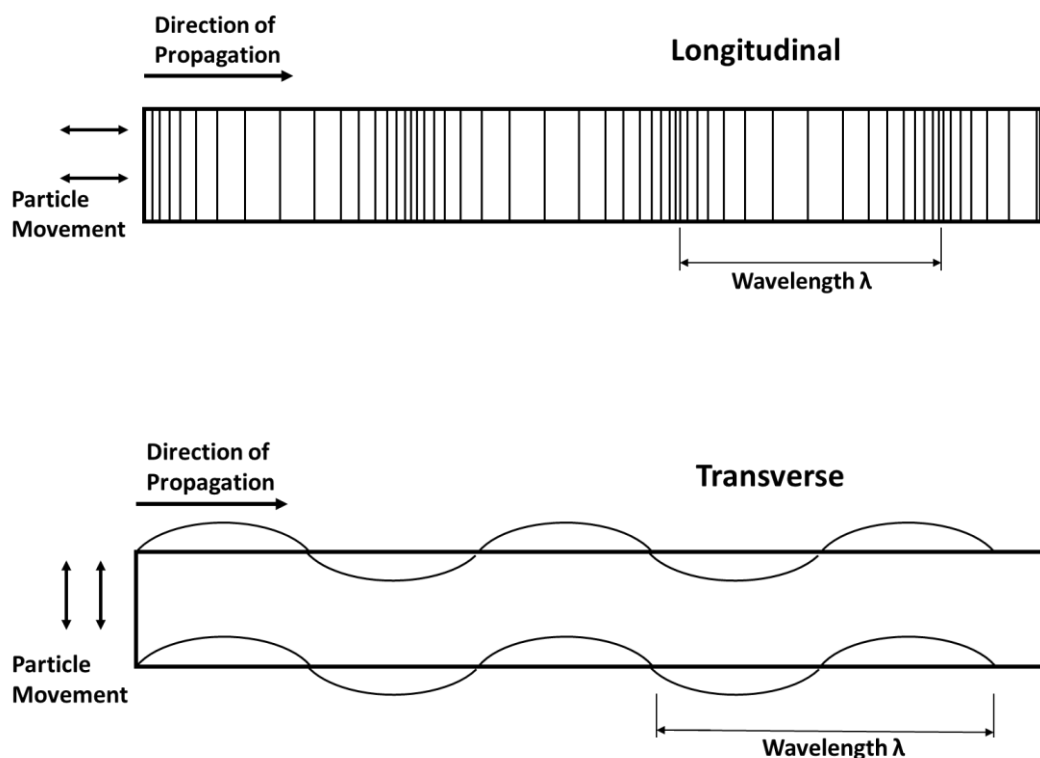


Figure 7. Longitudinal wave (top) and transverse wave (bottom)

This movement is driven by compressive and rotational forces which can be modelled using the Navier-Stokes equations. From these equations the equations below are derived for the longitudinal velocity (or P-Wave) and the transverse velocity (or S-Wave). These are shown in Equation 2 and Equation 3. This also shows that the longitudinal wave will always travel much faster than the transverse wave.

$$c_p = \sqrt{\frac{\lambda + 2\mu}{\rho}}$$

(Eq. 2)

$$c_s = \sqrt{\frac{\mu}{\rho}}$$

(Eq. 3)

Where μ and λ are the Lamé Constants, which are functions of the Young's modulus, E , and the Poisson's ratio, ν , and ρ is the material density. The Lamé Constants are shown in Equation 4 and Equation 5.

$$\lambda = \frac{E\nu}{(1 + \nu)(1 - 2\nu)}$$

(Eq. 4)

$$\mu = \frac{E}{2(1 + \nu)}$$

(Eq. 5)

2.5.2. Rayleigh-Lamb Waves

When a wave becomes bound by a single surface, the longitudinal and transverse waves interact to form Rayleigh surface waves, shown in Figure 8. If a second surface is then added to fully bound the signal in a plate, the longitudinal and transverse waves interact to form Lamb waves.

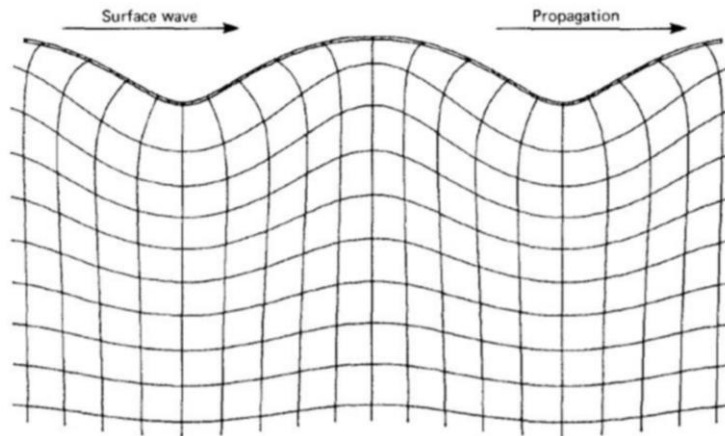


Figure 8. Signals interacting at a surface to form Rayleigh waves, demonstrating a combination of longitudinal and transverse waves (Rindorf, 1981)

Lamb waves are made up of two modes, the symmetric S_0 mode and the antisymmetric A_0 mode, also known as extensional and flexural modes. The difference between these is demonstrated in Figure 9. These also exist as higher modes A_1 , A_2 , S_1 , S_2 and so on which can develop as the thickness or length of the plate increase.

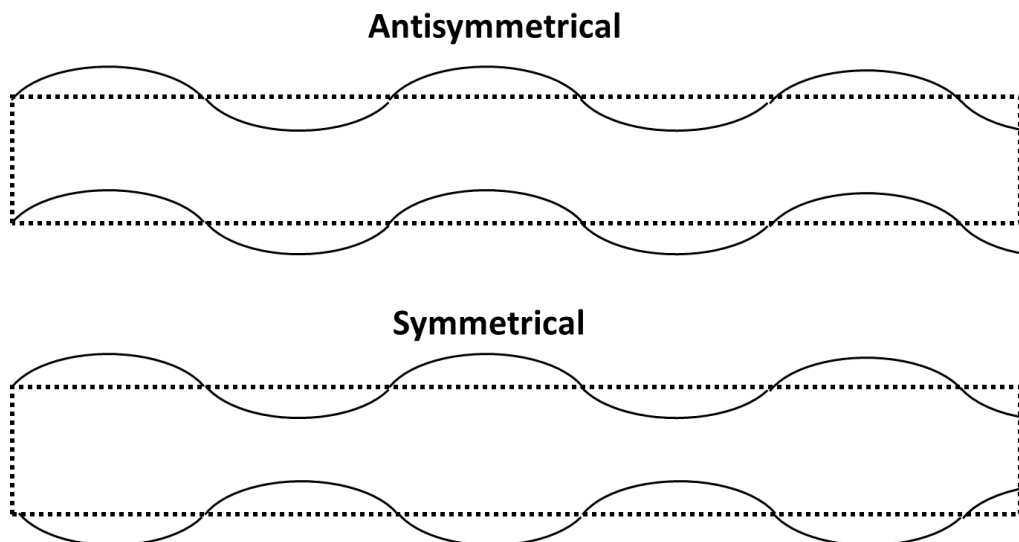


Figure 9. Demonstration of the forms of antisymmetric (top) and symmetric (bottom) wave modes

2.4.3. Dispersion of Signals

AE signals contain a broad range of frequencies, which in a dispersive solid each travel at a unique velocity. As a result of this, frequencies originating at a single instantaneous source will spread out as it travels away. This results in a wave packet travelling at a different velocity to a particle in the wave, as shown in Figure 10. The blue dot represents the group velocity, and the red dot represents the phase velocity travelling along the dotted line. In a non-dispersive medium, the group and phase velocities are equal, resulting in the relative positions of a wave packet and a particle on that wave remaining equal, as shown in Figure 11.

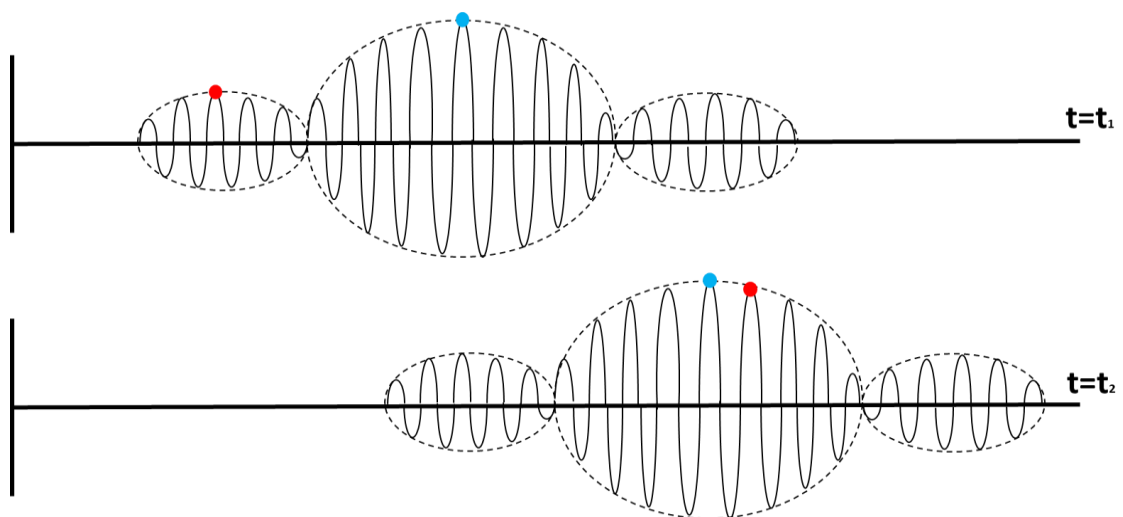


Figure 10. A wave packet travelling through dispersive media with a phase velocity greater than the group velocity, with the phase velocity represented by the red dot and group velocity by the blue dot

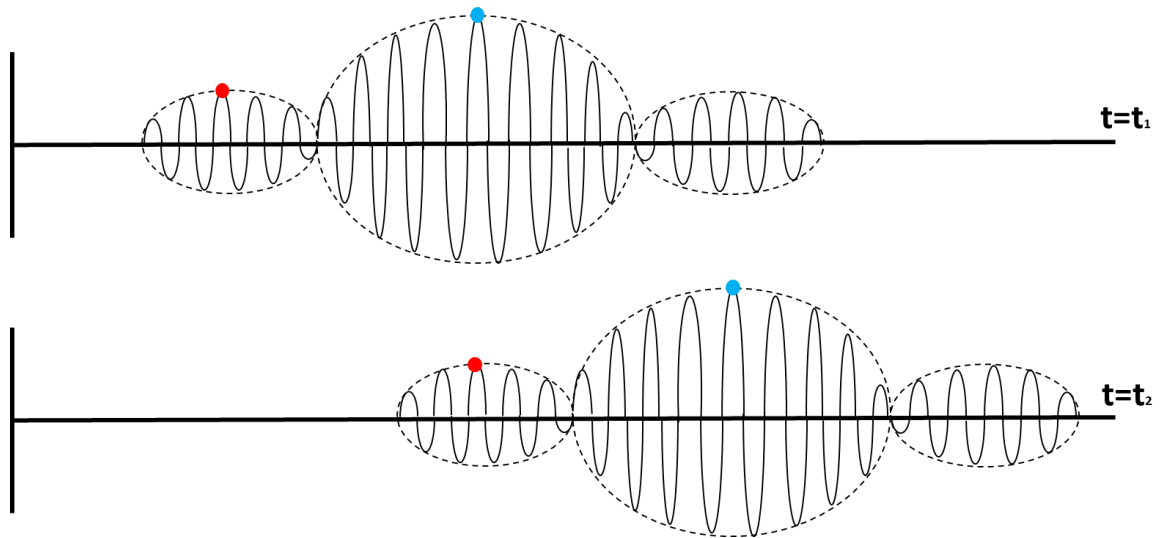


Figure 11. A wave packet travelling through non-dispersive media with equal group and phase velocities, with the phase velocity represented by the red dot and group velocity by the blue dot

The Rayleigh-Lamb equations shown below (Equations 6 and 7) can be used numerically to calculate the wavenumber at each frequency for the symmetric and antisymmetric modes.

$$\frac{\tan(qd)}{\tan(pd)} = \frac{4k^2pq}{(q^2 - k^2)^2} \quad (\text{Eq. 6})$$

$$\frac{\tan(qd)}{\tan(pd)} = \frac{(q^2 - k^2)^2}{4k^2pq} \quad (\text{Eq. 7})$$

where d is the half thickness of the plate and k is the wavenumber. p and q are shown below in Equations 8 and 9, where ω is the angular frequency, c_t is the angular velocity and c_l is the transverse velocity.

$$p^2 = k^2 - \frac{\omega^2}{c_l^2} \quad (\text{Eq. 8})$$

$$q^2 = k^2 - \frac{\omega^2}{c_t^2}$$

(Eq. 9)

From these equations the wavenumber k (Equation 10) is derived, which can then be used to derive the phase velocity c_{ph} and the group velocity c_g .

$$c_{ph} = \frac{\omega}{k}$$

(Eq. 10)

$$c_g = \frac{d\omega}{dk}$$

(Eq. 11)

Dispersion curves are then plotted with wavenumber, phase velocity or group velocity against frequency or frequency-thickness. Examples of these are shown in Figure 12, Figure 13 and Figure 14.

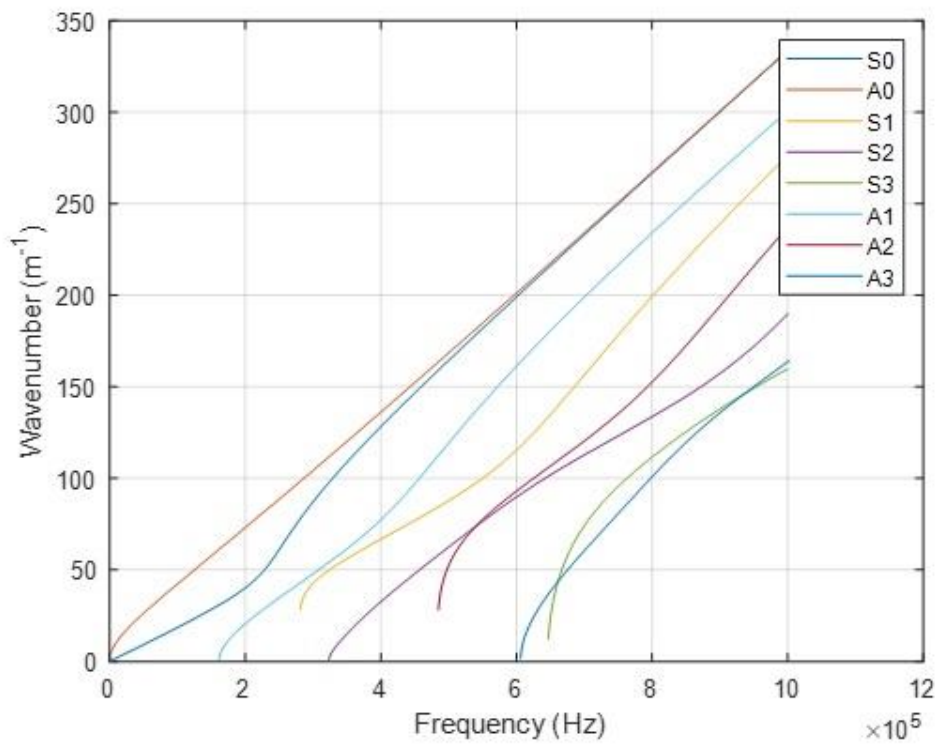


Figure 12. Dispersion of Wavenumber in a 10mm Titanium Plate

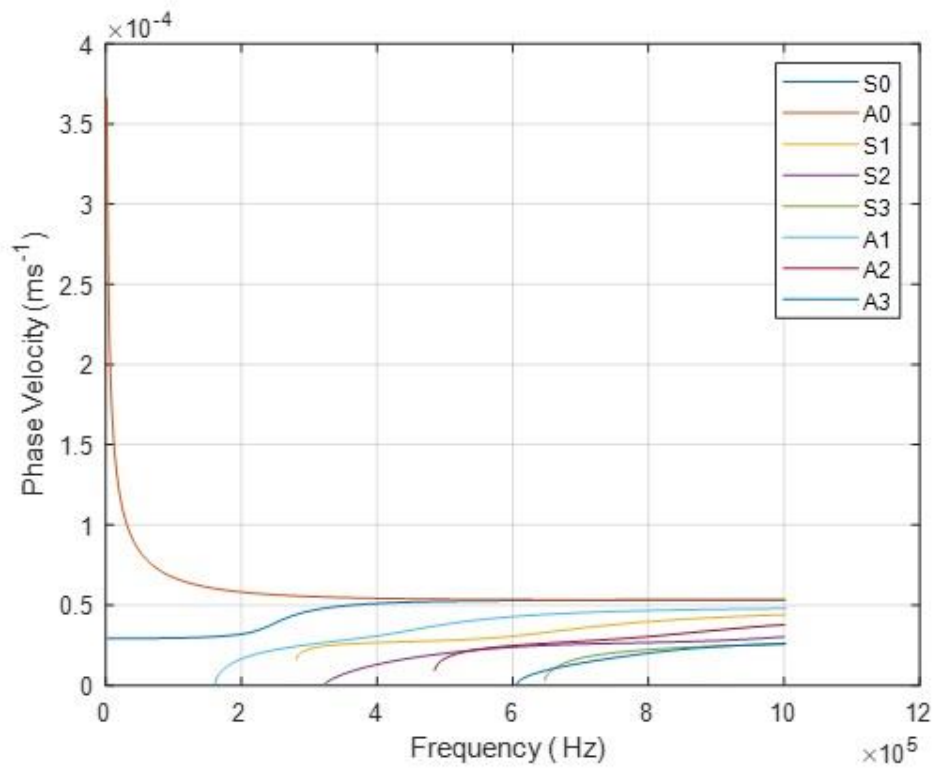


Figure 13. Dispersion of Phase Velocity in a 10mm Titanium Plate

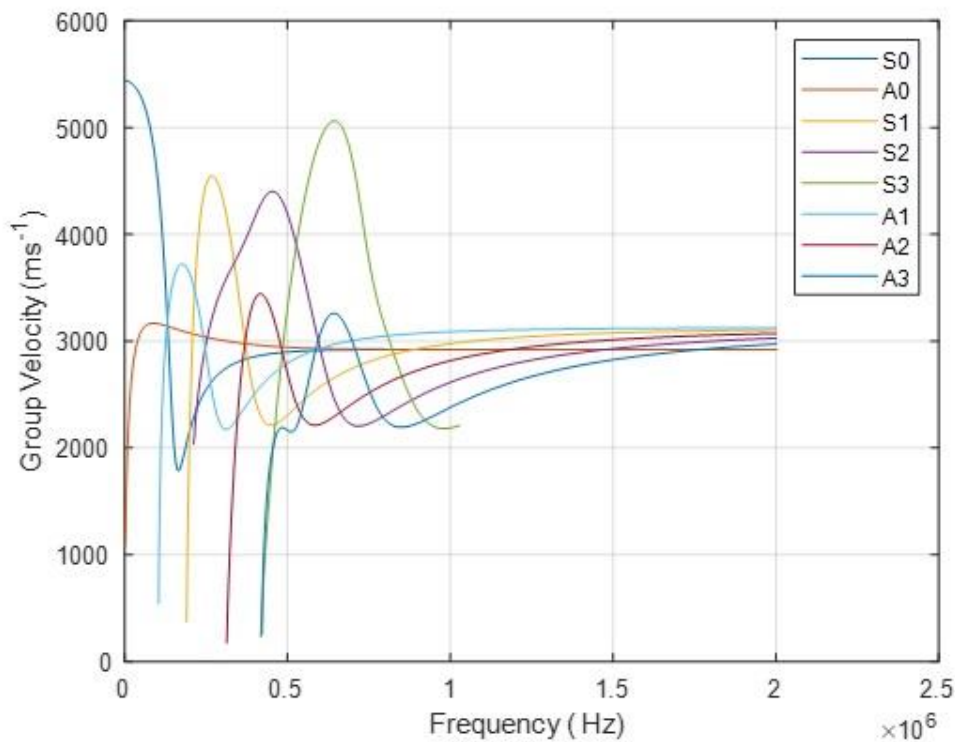


Figure 14. Dispersion of Group Velocity in a 10mm Titanium Plate

2.5.4. Attenuation of Signals

Attenuation is the mechanism by which the energy of a wave travelling is gradually diminished as it propagates further away from the source. These mechanisms are geometric spreading, absorption, dissipation and dispersion (Pollock, 1986). Geometric spreading occurs when a signal travels further from the source, the energy of the wave is spread over an increasing wave front. Absorption is when the kinetic energy of the signal is lost as it is converted to heat, which has a greater effect on higher frequencies. Dissipation is when a signal comes across a boundary or discontinuity in the material and is partially reflected away and partially transmitted into the adjacent media. Dispersion is as previously described as the wave energy spreads out as a result of different frequencies moving at different velocities resulting in longer wave packet and a lower peak amplitude.

2.5.5. Waves in Waveguides

The propagation of signals through a cylindrical rod such as a waveguide can be modelled by the Pochhammer-Chree Equations in much the same way that Rayleigh-Lamb equations govern propagation through a plate. The longitudinal wave motion is mathematically similar to wave motion on a taut string (Graff, 1991), and due to the constrained nature of the system will undergo amplitude doubling when it encounters a boundary. Rods are susceptible to harmonic motion, with the natural frequencies being given by Equation 12.

$$f_n = \frac{nc_l}{2l} \quad (n = 0,1,2 \dots)$$

(Eq. 12)

where c_l is the longitudinal velocity and l is the length of the rod.

In addition to longitudinal modes, there are two other modes that can develop in circular rods, torsional and flexural. Torsional waves will only arise in specific twisting conditions, and flexural waves will begin to arise at higher frequencies. The longitudinal and flexural waves are dispersive at higher frequencies, with higher modes arising as the frequency-diameter product increases. The fundamental longitudinal wave is referred to as L(0,1), with further modes referred to as L(0,2), L(0,3) and so on. Flexural waves are referred to as F(1,1), F(1,2) and so on. Dispersion in a rod can be induced by the so-called 'horn effect', where a gradual expansion in the diameter can force dispersion (Graff, 1991).

Ono & Cho (2016) studied the characteristics of waveguides using a 1 microsecond displacement pulse. Studies into copper and steel rods found that a 6mm diameter is a good compromise between attenuation and signal broadening. Studies additionally have found that the longitudinal resonant frequency to be dominant in

the 18-177mm length range. Hamstad (2006) performed studies on dispersion in waveguides with diameters of 1.6 to 12.7mm and lengths from 59 to 913mm. It was found that above 6.4mm diameters higher rod-wave modes developed and that a longer rod with a diameter below 6mm was best for retaining signal fidelity.

2.6. Location of Signals

2.6.1. Time of Arrival Location Method

The most common and commercially used methods of locating sources in a simple structure is the Time of Arrival method (TOA). TOA relies upon using the distance between each of the sensors, and the expected speed of sound through that material. By calculating the radii of hyperbolae between each sensor pair, the crossing points between the hyperbolae can then be used to estimate a source location. The equation used to calculate the radii of each hyperbola is shown in Equation 14 (Holroyd, 2000). This equation is derived from the cosine rule, with the geometry shown in Figure 15.

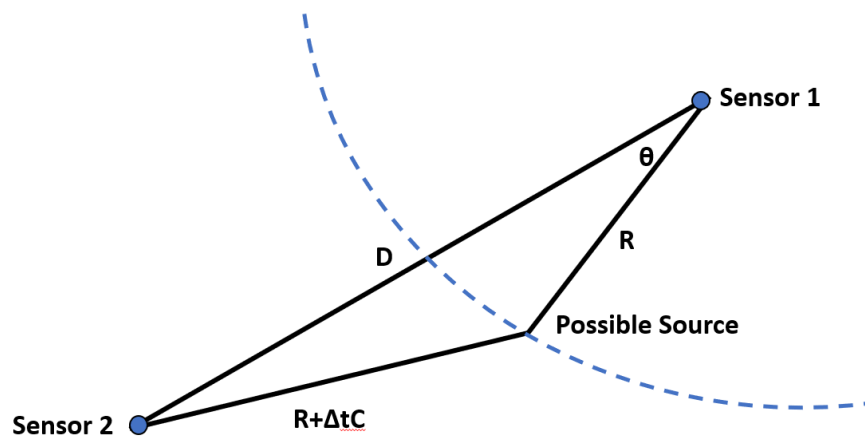


Figure 15. Calculating the location using TOA

$$(R + \Delta tC)^2 = D^2 + R^2 - 2DR \cos \theta$$

(Eq. 13)

$$R = \frac{1}{2} \frac{D^2 - \Delta t^2 C^2}{\Delta t C + D \cos \theta}$$

(Eq. 14)

In this equation, R is the radius of the hyperbolae, D is the distance between 2 sensors, Δt is the time difference between 2 sensors and C_{AE} is the speed of sound through the material. θ is the angle between the source and the sensor and will vary along the length of the hyperbolae. At least one further sensor is then needed so that multiple hyperbolae can be plotted, and the crossing points found (Holroyd, 2000). Computationally, the area of interest is divided into a fine grid with a binary system recording whether or not a hyperbola enters each grid square for each sensor pair. Summing each grid then provides a grid containing values from zero up to the number of sensor pairs. The grid squares with the highest values indicate the most crossing points and can then be averaged to give a location value.

The time of arrival method is very effective for locating signals in simple plate-like structures, however it is less suitable in cases where the material is non-homogeneous or is a more complex assembly of multiple parts. This is because it considers the material to have an equal wave velocity in all directions.

2.6.2. Delta-T Location Method

A more modern technique is the delta-T method, in which artificial AE data is generated across the area of interest to acquire time of arrival data between each sensor pair (Baxter et al, 2006). This method accounts for geometry features such as curves, holes and variable thicknesses. The process for delta-T is as follows:

Determine Area of Interest- In order to make the process of collecting data as efficient as possible, a relatively small area should be selected to collect signals in

Construct grid- With the sensors positioned around the area of interest, a grid should then be constructed, with a higher resolution providing higher accuracy but requiring more data collection

Obtain Time of Arrival Data- Use Hsu-Neilsen events to collect time of arrival data at each sensor. Multiple events should be generated at each grid node, typically five to ten to ensure repeatability

Calculate delta-T maps- For each event a delta-T value can be calculated and averaged for each node point. This then creates a map for each sensor pair. For example, four sensors produces six maps.

Compare to actual data- When actual test data is collected, contours are drawn across each map. The crossing points of these contours can then be used estimate a source location.

Baxter et al (2006) found that using delta-T produced an average source location error of 1.77%, which compares favourably with an average source location error of 4.81% when using the TOA method. The delta-T technique was further developed to further improve location accuracy and ensure its suitability with more complex geometries. Pearson, et al. (2017) implemented improved onset-picking of a signal using AIC (described in Section 2.5.4.), which provides a less subjective value than the first crossing of a user defined threshold. Further work was carried out by Eaton, et al. (2012) to verify the effectiveness of this technique in non-homogeneous materials such as carbon-fibre composites. Al-Jumaili, et al. (2016) automated the process of selecting events to create delta-T grids. This was done by automatically removing sources which had triggered less than the full number of signals and used an unsupervised clustering algorithm to remove uncorrelated data. Experimental

work gave an optimum cluster size of 8mm, though it is noted that this may not be the same for every use-case. Hensman, et al. (2010) adopted a Gaussian process to model the relationship between the delta-T values and source locations, and used this to produce accurate delta-T maps using a single source instead of the average of multiple sources at each point.

2.5.3. Other Signal Location Methods

There are further location methods that were not considered suitable for this project. The single sensor modal analysis location (SSMAL) method relies on the dispersion of Lamb waves to provide a location using the S_0 and A_0 wave velocities. This would not be suitable in this project due to the more complex geometry of the build plate assembly.

Another method is the Zone Location Technique (Miller, et al., 2005). This method assumes equal source amplitudes and that the sensors are well matched. It works by identifying which sensors recorded the highest amplitude and locating within a zone around that sensor. However, this method requires that the difference in attenuation exhibited is high enough to give an accurate location and is thus more suitable when locating AE signals across a large area.

The Signal Amplitude Measurement Technique works in much the same way as the Time of Arrival Technique, but uses differences in amplitude instead of time. This method however relies on an absence of ambient noise to accurately locate signals.

2.6.4. Akaike Information Criterion

When calculating the time of arrival from a signal accuracy is essential, as a small error can relate to a much larger location error due to the high velocity of the waves. The simplest way of doing this is to find where the signal first crosses the threshold, however there may be a long 'ramping up' period before the signal crosses the threshold or high background noise requires a higher threshold.

In order to overcome this, the Akaike Information Criterion (AIC) can be used (Pearson, et al., 2017). The AIC is a measure of variance in a signal, and can be calculated at each point of a signal using the equation below (Akaike, 1998).

$$AIC = i \log \sigma_i^2 + j \log \sigma_j^2$$

(Eq. 15)

Where i and j are the number of points before and after the point of interest respectively and σ_i^2 and σ_j^2 are the variance of the signal before and after the point of interest.

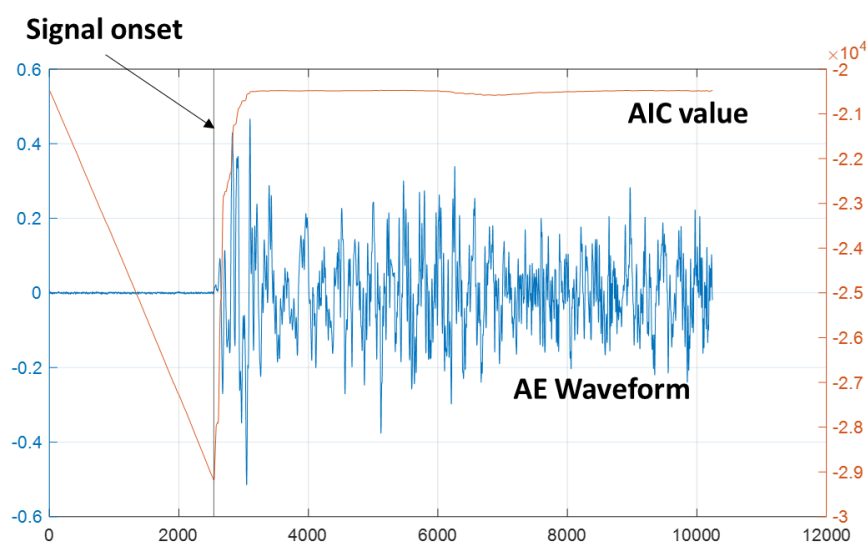


Figure 16. AIC plotted alongside a sample AE waveform

The AIC value will fall gradually until the desired signal is detected, as there will be little variation in the noise leading to this. When the signal begins, the variation after this point compared to before will begin to rise. Therefore, the minimum value of the AIC will generally mark the 'true' beginning of the signal.

2.7. Characterisation of Signals

2.7.1. Feature Extraction Techniques

Many methods have been tried to characterise AE signals. Attempts have been made to use traditional AE features (amplitude, rise time, counts, etc.) to classify signal, however these are insufficient due to many of those features being geometry dependent or dependent on each other (de Oliveira & Marques, 2008). For this reason, more features need to be derived from various mathematical methods. These can include skewness, kurtosis, taking features from a section of the signal (Samanta, 2003), or conducting a transform such as a wavelet transform (Downs, et al., 2003).

Before these features can be used to classify the signal, it needs to be ensured that features are as independent as possible. For example, the AE features amplitude and counts are normally linked as a waveform with a higher peak will cross the threshold more times than a lower amplitude signal. This can be achieved by calculating correlation coefficients between every pair of features. This value will range from zero for uncorrelated to one for fully correlated data. Removal of data with a correlation of greater than 0.9 should be sufficient (Vishal, 2018).

A large number of variables can be further reduced by use of principal component analysis (PCA) (Jolliffe, 2002). This involves first normalising the features, by subtracting the mean and dividing by standard variation for each variable. This gives

each variable a mean of zero and a standard deviation of 1. A covariance matrix is then constructed with this data and eigenvalues are extracted. These eigenvalues describe the variance of the data, and from these the percentage variance attributed to each variable is found. This is commonly presented in a Scree plot to aid with selecting principal components, an example is shown in Figure 17. Once the desired principal components have been selected, they are matrix multiplied by the normalised dataset to give data that can be used by learning algorithms to identify groupings. Eaton, et al. (2010) used PCA to automatically differentiate between AE source types, which was successfully achieved against a high level of background noise.

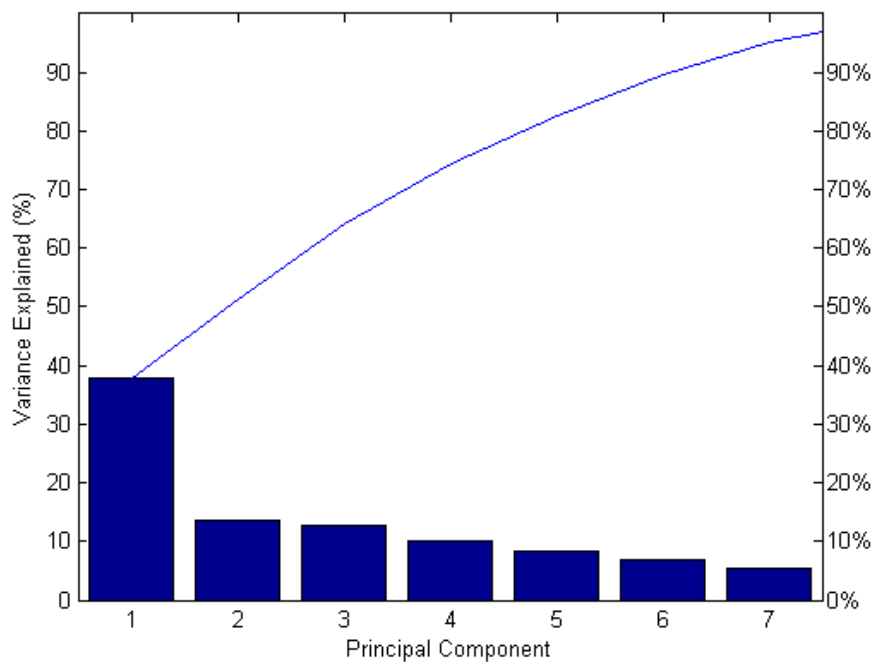


Figure 17. An example of a scree plot used to select principal components (Mathworks, 2021)

2.7.2. Machine Learning

Machine learning can be split into two categories; supervised learning and unsupervised learning. Unsupervised learning includes clustering techniques such as k-means clustering and hierarchical clustering, and probabilistic methods such as Gaussian mixture models. Supervised learning meanwhile is made up of algorithms such as various types of neural networks which need to be trained with relevant training data before being used to classify real data.

Al-Jumaili, et al. (2015) developed the parameter correction technique (PCT) to alter AE features to account for material properties and part geometry. This method successfully improved the performance of source characterisation, however it requires the generation of parameter maps before it can be used. This is a very time consuming process and would need to be repeated with every specimen upon which it is used.

Supervised learning techniques such as support vector machines (SVM) or artificial neural networks (ANN) require large amounts of training data to create a reliable classification process. The challenge of using these kinds of processes with AE data is the extent to which an AE signal is affected by the geometry of the specimen where it is generated. This can mean that similar signals from similar sources but different locations may have very different content and thus be classified separately. Holford, et al. (2017) highlighted some of the associated challenges of classifying AE signals. AE signal parameters are often defined by the user-defined threshold and thus are not universally comparable, and also do not fully capture the signal structure.

Crivelli, et al. (2014) trained a self-organising map (SOM) then clustered the mapped data with the k-means algorithm. This successfully classified failure mechanisms in simple dog-bone shaped specimens. However, this is a far cry from the complex 3D geometry present within the AM500. De Oliveira & Marques (2008) used artificial neural networks (ANNs) to classify AE data recorded from a glass-fibre composite. While this work identified six different signal types, further work was needed to fully link these with physical phenomena conclusively.

3. Experimental Techniques

3.1. Introduction

This chapter aims to introduce the equipment and techniques used to investigate the use of AE within AM. This begins by introducing the Renishaw AM500, the system on which Renishaw wished to implement an AE system, and the geometry of the build plate assembly on which most experimental data was collected. This is followed by sections covering the AE equipment and sensors used in this project and their characteristics. An overview of the signal generation techniques used in this project is then given, followed by a short summary of the couplant methods used to secure sensors to the specimens. An overview of the Polytec 3D scanning laser vibrometer is then given, to lay the groundwork for experimental work presented in Chapter 4 and Chapter 5. Finally, the software used to collect and process data in this project is summarised, alongside overviews of the techniques used to process data for presentation.

3.2. Platform

The focus of this project was developing an Acoustic Emission (AE), damage detection and location system suitable for the Renishaw AM500, shown in Figure 18. Within the AM500 is a chamber containing the 250x250mm print bed on which layers of powder are built up and the part is gradually built, this process is fully described in Section 2.2. For each layer the build plate moves down and more powder is deposited and fused by a scanning laser until all parts are completed. During a build, the chamber is filled with argon gas to prevent oxidation and the build area is lowered incrementally by 20-100 μ m, with a layer being added by a

wiper at each increment. The part is built on the build plate, which is positioned atop of the heater plate as shown in Figure 19. The heater plate conducts heat from the heater attached below, which acts to reduce the temperature gradient through the print and reduce the likelihood of cracking. This is positioned using three rails attached to the underside of the heater plate. The heater can reach up to 200°C, and this combined with the geometry make it necessary to mount the piezoelectric AE sensors on waveguides. This is because AE sensors have a nominal operating range of -50 to 177°C.



Figure 18. The Renishaw AM500 (Renishaw, 2021)

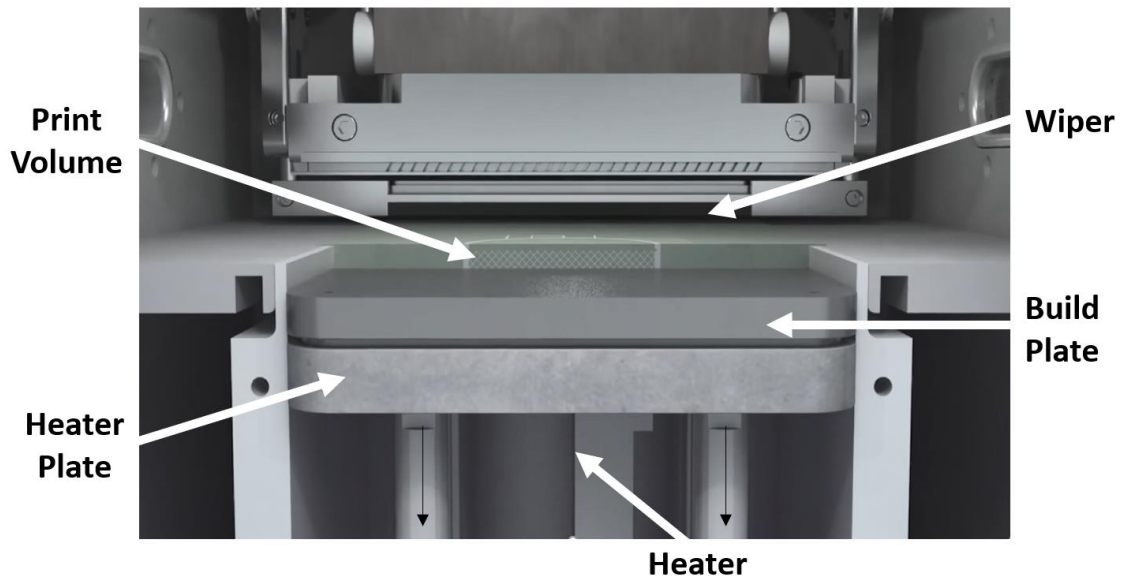


Figure 19. The positioning of the build plate within the AM500

A build plate typically starts at around 20-30mm thick depending on the needs of the customer. After each build, the part is cut from the plate and the plate skimmed to ensure the surface is smooth and flat for the next build. This means that over time the build plate will become significantly thinner. When the plate reaches a thickness of around 10mm it will then be disposed of. This is because the plate will be more susceptible to bending under the mass of powder, which can cause breaks in the build. An exploded view of the build plate assembly is shown in Figure 20.

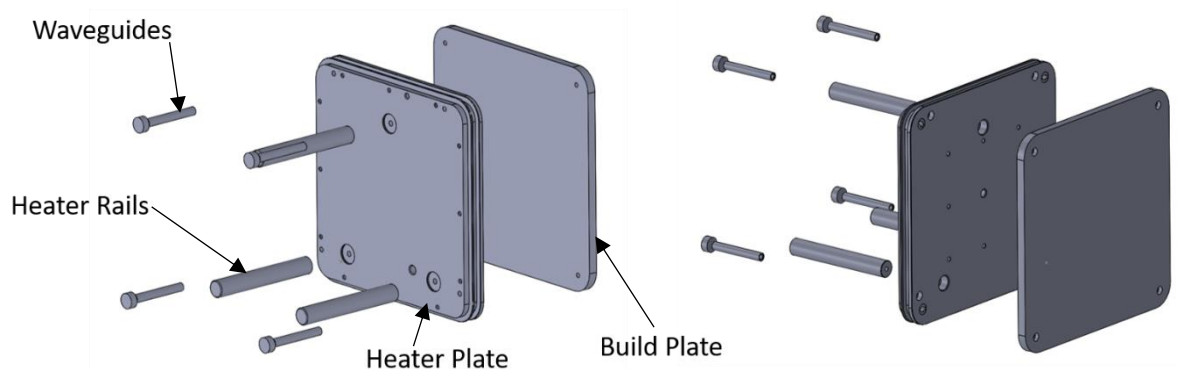


Figure 20. An exploded view of the build plate assembly

As a result of experiments completed as part of this thesis, detailed in later chapters, the design of the waveguides and heater plate were altered to give a clearer propagation path between the build plate and the sensor. A comparison between the designs is shown in Figure 21. The waveguide was redesigned with an external thread at its base with corresponding changes to the heater plate allowing the waveguide to be screwed into the heater plate where it floats until the build plate is affixed. When the build plate is added, the bolts that secure the plate go directly into the waveguide, which tighten up to the build plate.

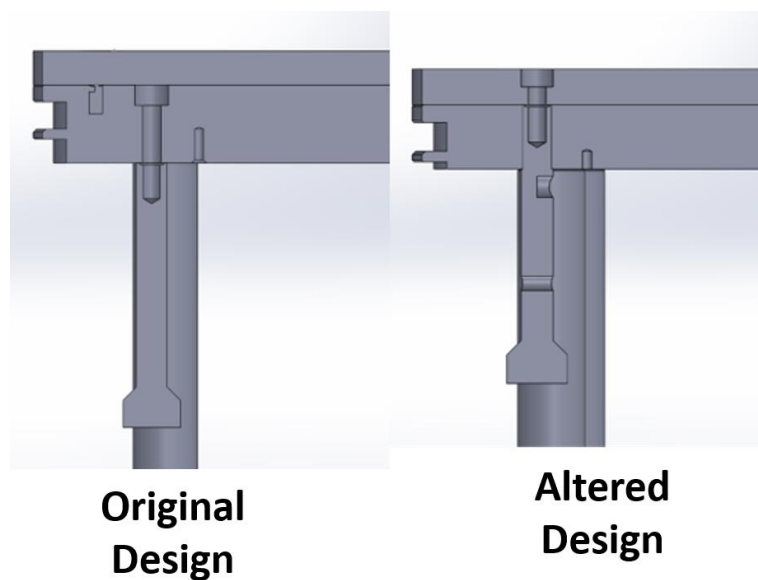


Figure 21. Profile of the original heater plate (left) and the redesigned heater plate and waveguide assembly (right)

Over the course of this project the plates used were 10mm titanium, 15mm stainless steel and 15mm aluminium as they were made available by Renishaw. Most experiments were carried out on a build plate assembly removed from the machine, as any AE signals generated within the structure will propagate through the build plate and into the waveguides.

The design of the waveguides was heavily limited by the geometry of the machine. An ideal waveguide is a long thin rod in order to reduce the modes propagating and maintain the wave shape (Ono and Cho 2004). Unfortunately, the length is limited by the space beneath the heater plate and needs to be thick enough to accommodate the M5 bolt which fixes it to the plate.

3.3. AE System

AE signals were collected using two different Mistras AE systems, a four-channel system and an eight channel system. Additionally, an Adlink system built into the Renishaw AM500 was used to collect in-process signals. The four-channel system is made up of a pair of PCI-2 boards produced by Mistras. These 32-bit boards are capable of data acquisition of up to 40 MHz with real time sampling, making them ideal for collecting AE signals. Additionally, it is capable of simultaneously recording external parameters such as load or temperature, allowing AE data to be correlated with those parameters (MISTRASS 2009). The eight channel Express-8 system operates in much the same way but is much more compact with eight built-in channels and data acquisition of up to 10 MHz (PAC 2013). System choice for an experiment was governed by availability.

The Adlink system used to collect in-process data is a data acquisition system capable of sampling data at up to two Mega samples per second from four channels simultaneously (ADLINK Technology Inc, 2014).

The AE system is connected to the sensors via BNC cables and 2/4/6 preamplifiers. The purpose of the preamplifier is to increase the voltage from the sensor before

reaching the AE system. These provide selectable gains of 20, 40 and 60 dB and provide frequency bandwidth of 20 to 1200kHz.

3.4. Sensors

The primary sensor used during this project was the Mistras WD sensor as selected by Renishaw. This is a wideband piezoelectric sensor, suitable for 100-900kHz and with a 17.8mm diameter ceramic face. This sensor in addition to being effective at temperatures of up to 177°C contains a piezoelectric crystal which converts a mechanical signal into an electrical signal and vice versa. Figure 22 shows the frequency response for the WD sensor, showing that it has a broadly flat response at a broad range of frequencies. This is particularly useful when studying the frequency content of a signal as no specific frequency will be amplified. The WD sensor is a differential sensor, meaning it uses two sensing elements which allows the removal of common noise, resulting in less noise in the recorded waveform.

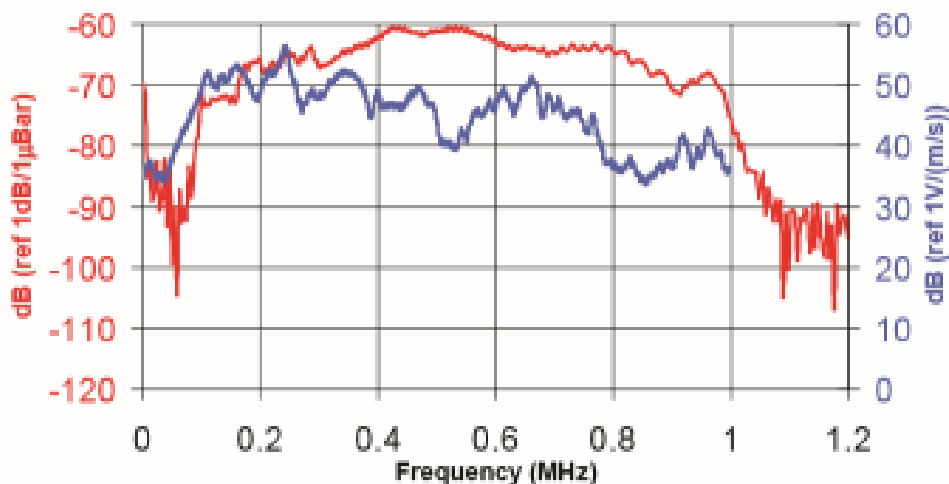


Figure 22. Frequency response diagram for the WD sensor (Mistras, 2011)

Some experiments were also carried out using the Mistras R15A sensor, which is resonant at 150kHz, shown in Figure 23. This was used when the frequency content of the waveform was of less interest than accurately identifying the start of the

signal. The R15A was also used to excite the build plate and waveguides when collecting vibrometry data.

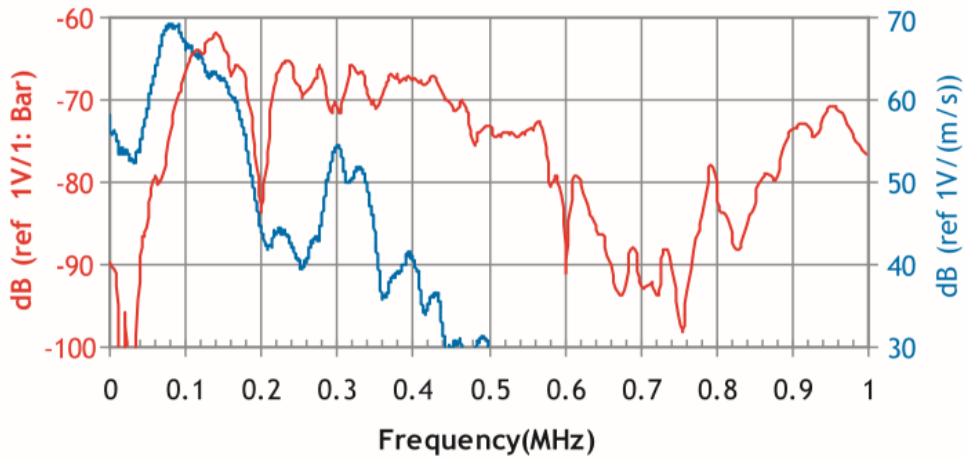


Figure 23. Frequency response diagram for the R15A sensor (Mistras, 2011)

Additionally, when creating multi-frequency signals in order to observe dispersion behaviour of the build plates, the Mistras F15a sensor was used. The F15a produces a relatively flat frequency response, as shown in Figure 24, which made it ideal for producing signals that ranged from 30-350kHz used in Section 4.3. Though the WD sensor is similarly wideband, its differential construction makes it difficult to excite, making the F15a the more suitable.

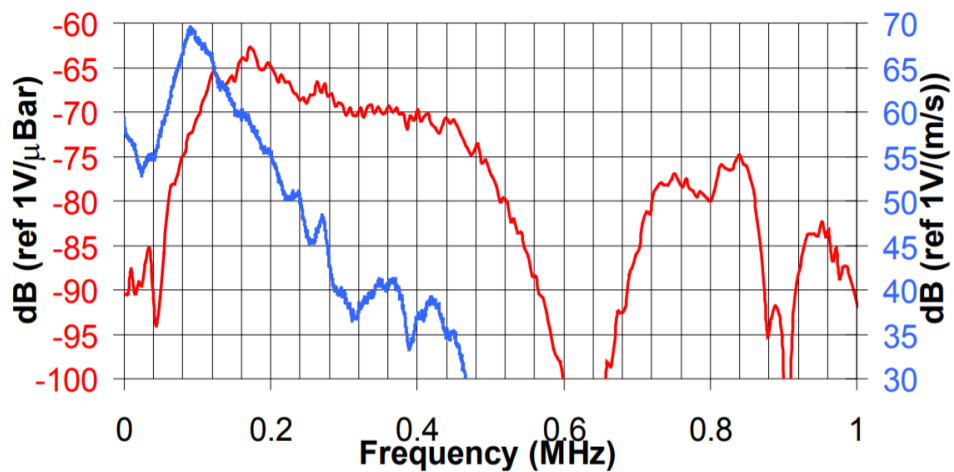


Figure 24. Frequency response of the F15a sensor (Mistras, 2013)

3.5. Signal Generation

The traditional method of generating artificial AE signals is the Hsu-Nielsen source. This is a simple procedure using a mechanical pencil loaded with 0.5mm H2 graphite. The lead is extended 3mm and the pencil is placed at a 30° angle on the surface of interest (often with the assistance of a rocker). This is shown in Figure 25. Pressure is then applied to the surface with the pencil until the lead snaps, with the sudden deformation to the surface causing the release of a wideband elastic wave through the structure (Sause, 2011). This is a very repeatable technique and should give a response between 80 and 100dB each time, making it effective for verifying sensor performance.

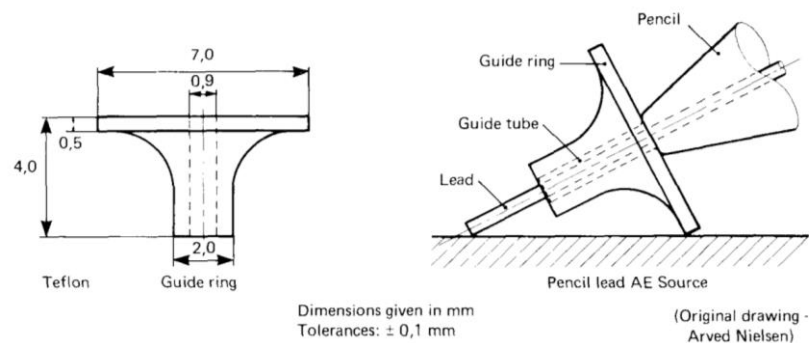


Figure 25. Hsu-Nielsen source method illustrated (Rindorf, 1981)

Signal generation for the vibrometer was carried out using a Teledyne Lecroy Waveform 2012 (Teledyne Lecroy, 2021). This has the capability of producing signals up to 10MHz and a sample rate of 125MHz. It can produce pulses or continuous signals, with a wide range of waveshapes.

However, the signal generator wasn't always able to create the signals needed, its main limitations being the frequency range and lack of flexibility in creating multi-frequency signals. In these cases, the Red Pitaya STEMLab 125-10 development

board (Red Pitaya, 2021) was used instead. This board can create signals up to 125 Mega samples per second, and comes equipped with Python and can be remotely accessed. This Python compatibility allows a huge range of signals to be produced and quickly adjusted. Both the Teledyne Lecroy signal generator and the Red Pitaya were connected to transducers via a Krohn-Hite Model 7500 amplifier, which is capable of amplifying signals of up to 1MHz to up to 200V.

In order to convert these multi-frequency waveforms into a mechanical response, a conical transducer was used. This transducer tapers towards a 1 mm tip in contact with the specimen and was produced by NPL as an alternative to the Hsu-Nielsen source. The frequency response is shown in Figure 26, which shows it produces a largely flat frequency response up to 500kHz with a sharp drop off thereafter.

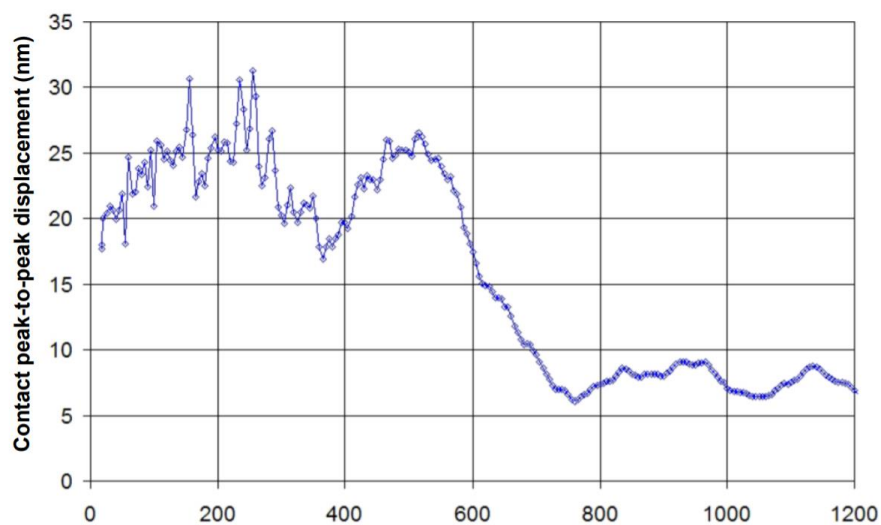


Figure 26. Frequency response of the conical transducer (Al-jumaili, 2016)

3.6. Couplant

There were two types of couplants used during this project; silicone grease and silicone sealant. Each produced an effective seal between surfaces that would allow signals to travel through unimpeded, and were used depending on the situation. Silicone grease was used only when the sensor needed to be quickly switched either for a different sensor or a different specimen.

3.7. Vibrometry

A Polytec PSV-500-3D Scanning Vibrometer (Polytec, 2021) was used extensively to study the acoustic characteristics of the build plate, heater plate and waveguides. The vibrometer operates by directing a laser at the area of interest and measuring the phase difference as it is reflected back. Using the Doppler effect this can then be used to calculate the surface velocity, surface displacement or frequency at each point. Measurements are taken at up to 2.56 MHz and a user defined number of samples are recorded for each point which can then be resampled repeatedly to give an average. This will reduce the effect of any external shocks on the measurement. The vibrometer is made up of three separate laser heads, which allows the vibrometer to record three-dimensional surface velocity data. These are mounted to a fixed bracket to ensure they remain in the same positions relative to each other. An HD camera is then used to track the laser positions. A separate device (detailed in the next section) is used to drive a transducer exciting the specimen. In order to scan across an area, the three laser heads are paired with an HD camera which tracks the laser position. Glass beads can be applied to the scan surface to increase the reflectiveness of the surface. The built-in software allows the lasers to

be calibrated before a scan area is defined. Once the scan has begun, mirrors within the laser heads allow the laser to move to each of the defined scan points to collect data. Additionally, the laser heads and camera are mounted upon a Thorlabs Optical Table (Thor Labs, 2021) to ensure both that external noise is minimised and that the apparatus will remain in the same position between uses. This setup is shown in Figure 27.

Data can then be manipulated and presented using the built-in software or exported as a Universal File Format (UFF) file to be converted for use in external software such as Matlab.

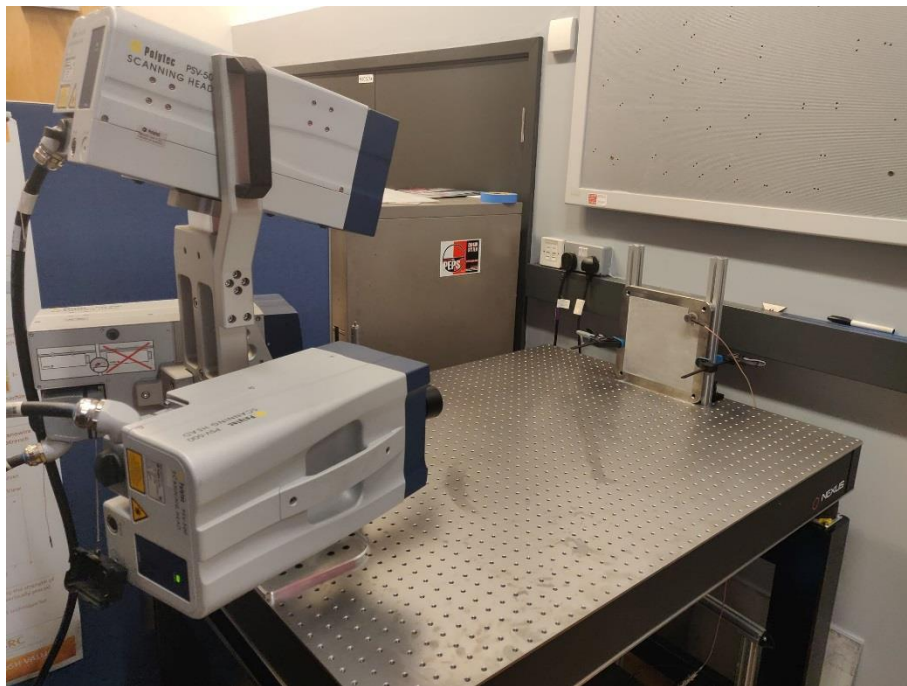


Figure 27. The three vibrometer laser heads mounted on a vibration-isolating table directed at a specimen.

3.8. Software

MathWorks Matlab was the primary tool used for processing data collected in this project. A package of functions developed within Cardiff University were used to extract raw DTA files from AEwin straight into the Matlab environment. These were further developed to be fully integrated with the delta-T process, vastly speeding up the process. Previously all hit data from AEwin had to be exported as txt files and all of the waveform data was exported as CSV files. All data from the vibrometer was also exported into and manipulated in Matlab. Additionally, all data presented graphically in this thesis were produced in Matlab. Matlab packages used include the Wavelet Toolbox, used to create graphical demonstrations of the frequency content of signals, and the Statistics Toolbox for use of functions such as PCA for separating and presenting variables. All wavelet transforms performed were Morse continuous wavelet transforms with a bandwidth of 60 time samples. The Morse wavelet was used due to its suitability for use with signals with varying frequency, as seen in an AE signal.

The Red Pitiya is built upon Python 3 and has a number of built-in functions. Python 3 in conjunction with the Scipy package was used to create the complex signals that were then passed to the conical transducer.

Disperse was used to generate the theoretical dispersion curves through the build plate and waveguides (Lowe, 2021). These could then be exported from Disperse as excel files and imported into Matlab, where they were overlaid over experimental data. This is a purpose-built program that solves the complex Raleigh-Lamb equations for a large range of materials and geometries, including all the build plate materials used in this project.

4. Propagation

4.1. Introduction

Understanding how a signal propagates through a structure is vitally important for locating and characterising signals arising from damage. In the Renishaw AM500 any AE signal produced in the print area will travel into the build plate, heater plate, and then down the waveguide to the sensor. These components were studied in isolation and assembled to investigate how a signal will be altered and how it will disperse.

AE is traditionally used in simple structures such as plates and rods, so it is useful to simplify the problem of the build plate down to a series of plates and rods. It must be established whether the build and heater plate can be modelled as a single plate or as two separate plates, and how far the design details of the waveguides alter their behaviour from that of a simple rod. Another added complexity in this situation is how the thickness of the build plate will reduce over the plate's lifetime, which will result in differences in dispersion and the velocities at which different signal modes propagate. Figure 28 shows some of the potential paths to the sensor. The red arrows illustrate a signal taking the most direct route straight from the source to the top of the waveguide, whilst the blue arrows demonstrate the signal passing straight through the build plate and then through the heater plate to the waveguide. The yellow arrow demonstrates the signal travelling to the fixing point between the heater and build plate where the contact pressure would be highest, before travelling through the build plate to the waveguide.

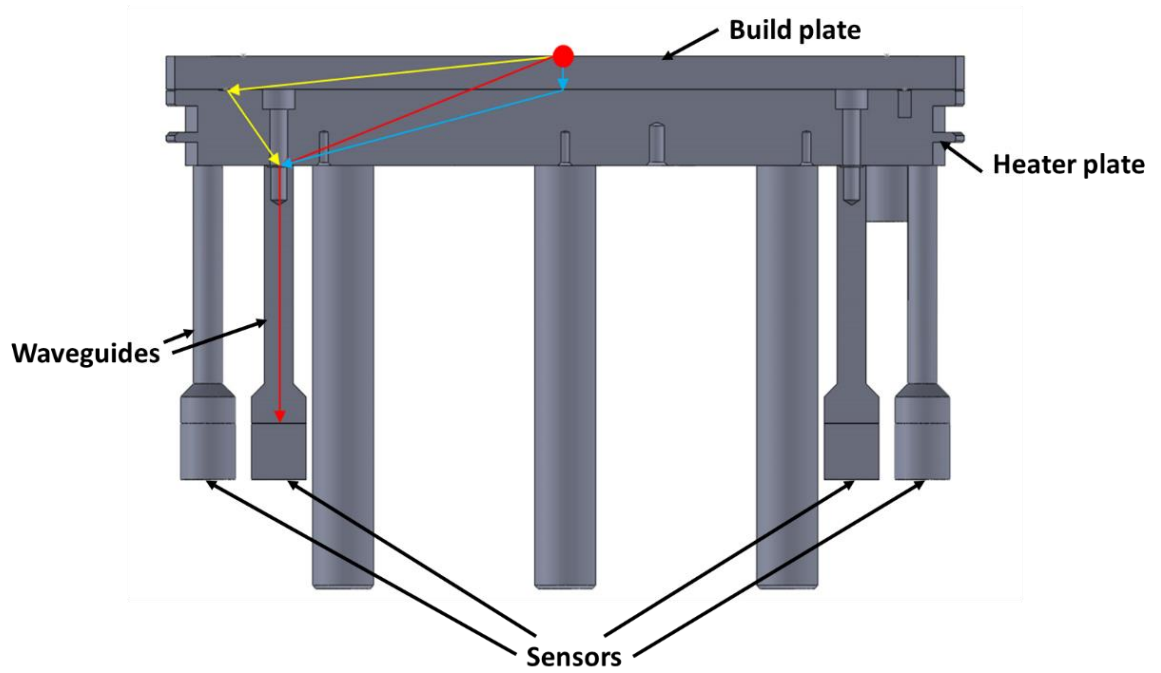


Figure 28. Possible propagation paths from the build plate to the sensor, with potential signal paths marked in red, yellow and blue.

4.2. Propagation through Heater Plate

4.2.1. Experimental Techniques

The 3D scanning laser vibrometer, presented in Section 3.4, was used to study how signals would pass from the build plate into the heater plate. With the build plate securely fastened to the heater plate, an R15A transducer was silicon-bonded to the centre of the build plate and a 100V 150kHz pulse was applied. The transducer was excited for 10 cycles to ensure sufficient energy was imparted into the plate, followed by a 100ms pause to allow energy in the plate to dissipate before the next measurement. This pulse shape was chosen to provide enough energy to allow signals to be clearly recorded on the heater plate and to match the resonant characteristics of the R15A transducer to avoid the signal being overly distorted. A scan area of 100x100mm was then defined on the underside of the heater plate with a grid size of approximately 1mm, with 50 averages taken per point. This setup is

shown below in Figure 29. The build plates available for this were a 10mm titanium plate and a 15mm stainless steel plate, and the experiment was repeated for each.

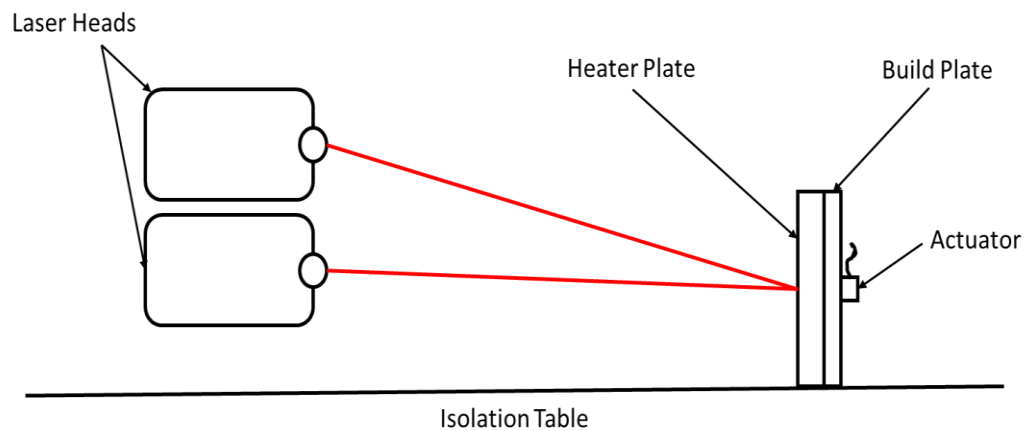


Figure 29. Setup of the vibrometer as it scanned a build plate

4.2.2. Results

The data taken from the vibrometer gives the velocity against time in each of the x,y and z axes for each point. In order to present the displacement across the plate integration was used to transform the data. The movement of the plate was primarily in the out-of-plane z component which was then plotted at a range of times to illustrate the propagation of signals into the heater plate. This is shown in Figure 30 for the 10mm titanium plate and in Figure 31 for the 15mm stainless steel plate. These results demonstrate that signals in the titanium plate took the red path marked in Figure 28, while signals in the stainless steel plate took the yellow path.

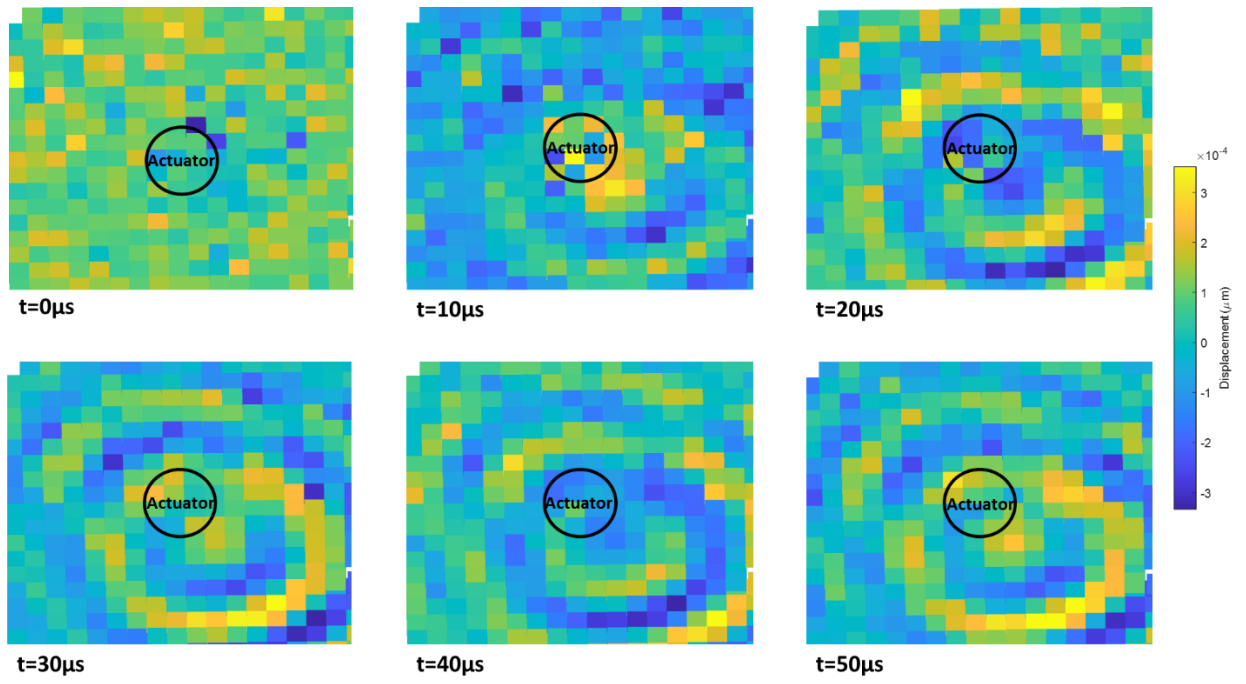


Figure 30. Propagation into the heater plate from the titanium build plate

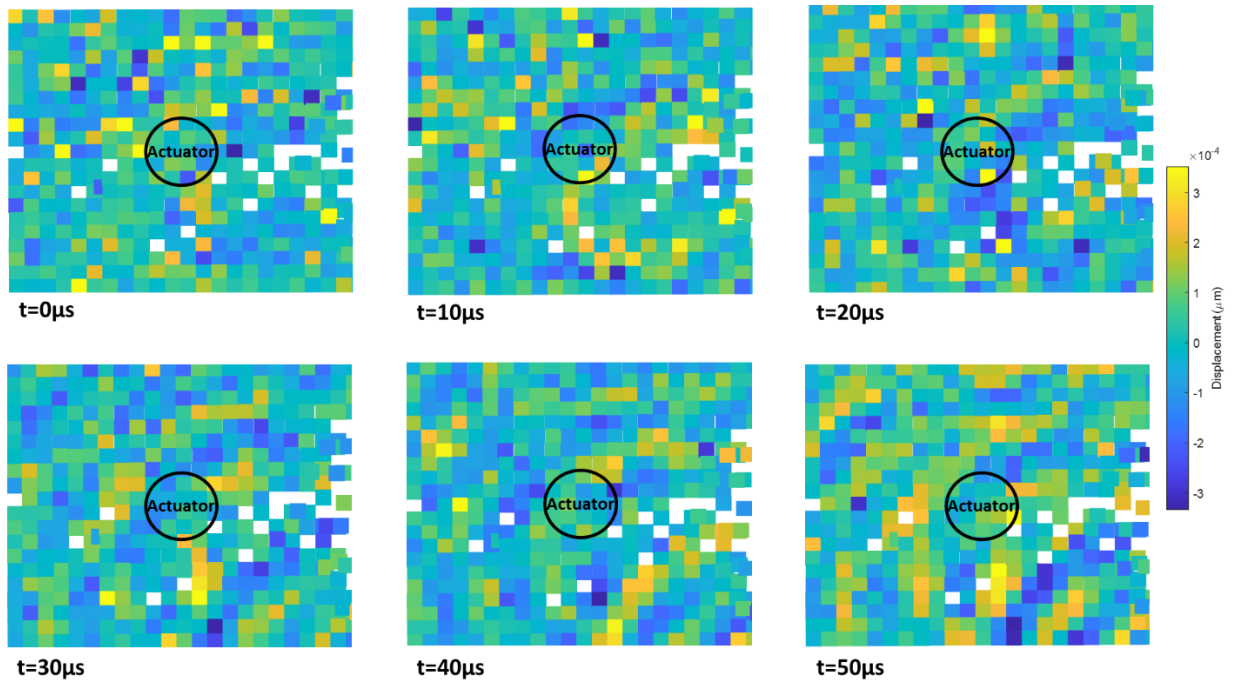


Figure 31. Propagation into the heater plate from the stainless steel build plate. Note that white gaps are due to the vibrometer being unable to resolve those locations

4.2.3. Discussion

These results suggest that the form of each individual plate influences how signals propagate from the build plate towards the waveguide. Within the stainless steel plate, signals travel from the corners where the plates are fixed together towards the centre. This suggests that the greatest contact pressure between the stainless steel plate and heater plate is at the corners, indicating a slightly concave form. Meanwhile, the titanium plate has its greatest contact pressure at the centre despite being fixed in the same way as the steel plate, suggesting a convex form. This would lead to a large variation in the time of arrival to the sensors between two otherwise similar plates. To overcome this, the heater plate and waveguide underwent a significant redesign. To negate the effect of build plate form on the signal path to the waveguide, the waveguides were redesigned to press directly to the underside of the build plate. In order to do this, the outside of the waveguide was threaded to hold it into the heater plate, and the securing points for the build plate were moved in line with the waveguides. This means that when the build plate is fastened down, the waveguides are tightened onto it. This design change is illustrated by Figure 32.

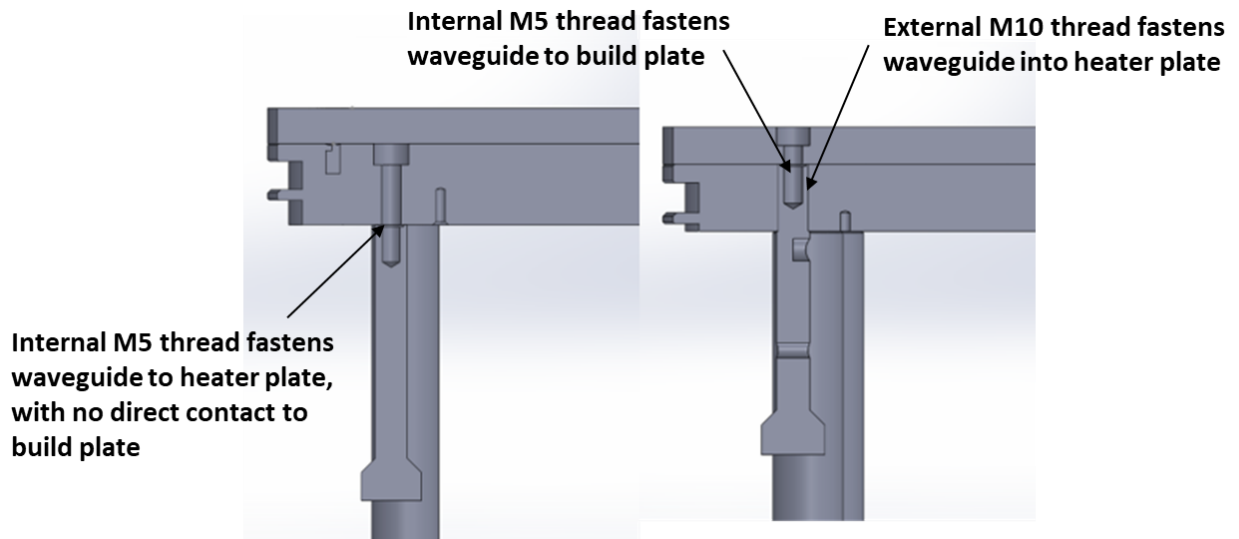


Figure 32. Section View of the original waveguide design (left) and the new design (right)

4.3. Propagation through Build Plate

4.3.1. Experimental Procedure

4.3.1.1. Dispersion Study

The next stage of the propagation study was to investigate how signals propagate through the build plates. The thickness of a build plate can range from 20mm to 10mm during its lifetime, so how signals propagate and disperse will change continuously through a series of builds. This change can be estimated by plotting dispersion curves derived from the Rayleigh-Lamb equations.

The vibrometer, detailed in Section 3.4, was used to study how signals disperse in the two available build plates, the 10mm titanium plate and the 15mm stainless steel plate. F15a transducers were placed on either side of the plate and fixed using silicon sealant. They were placed in the corner offset 50mm from each edge and set using a custom jig to ensure they were lined up identically on either side. These were chosen due to their relatively flat frequency response across the desired frequency range and being able to impart enough energy to be recorded by the vibrometer. A transient signal was created from 30kHz to 350kHz with a 40kHz step, which was produced continuously throughout the recording of data. This signal was produced

by the Teledyne Lecroy waveform generator, with a step of 40kHz allowing each distinct frequency to fully develop across the plate.

The vibrometer was set to record a single line of points diagonally across the plate with 50 samples averaged at each point. This line was made up of 200 points at an approximate spacing of 1mm. This was performed twice, once with the transducer on the build plate front being excited and once with the transducer on the rear. This arrangement is shown in Figure 33.

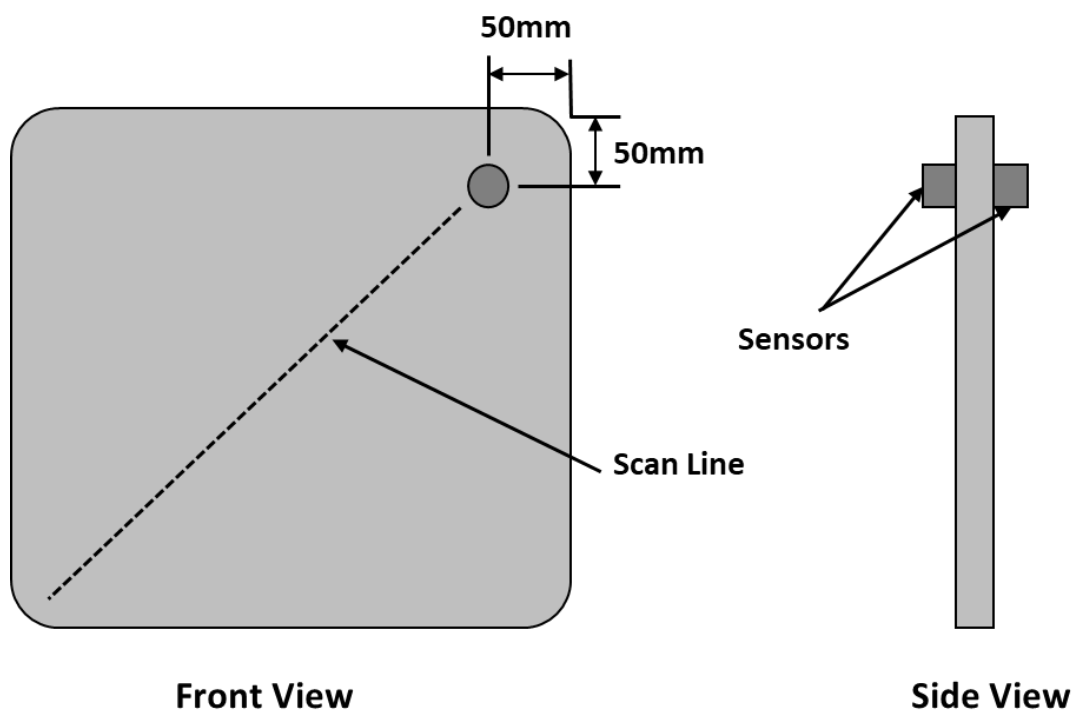


Figure 33. The experimental setup for the dispersion study

4.3.1.2. Reflection Study

In a 250mm wide plate, as used in the AM500, it can take the S_0 wavemode just 80 microseconds to cross from one edge to the other and back again. This is based on wave velocity identified from the relevant dispersion curve. With reflections coming from potentially all 4 edges, this has large effect on the structure of any recorded signal.

In order to better quantify the effect of these reflections on the structure and length of the waveform, a large 1250x1250mm aluminium plate at 15mm thick was acquired. Wideband signals were collected from Hsu-Nielsen sources from various points on the plate and compared with signals collected in a 15mm aluminium build plate.

Four WD sensors were fixed in a row at the centre of the plate, as shown in Figure 34. Hsu-Nielsen sources were then used to generate signals at 11 points along the centre line of the plate towards the plate edge. With each increment towards the edge the distance to the sensor becomes greater and the distance that reflections from the near edge are required to travel becomes smaller and the distance from the sides becomes marginally greater. Five clean breaks were performed at each location, allowing the most representative to be used for analysis, identified using correlation coefficients.

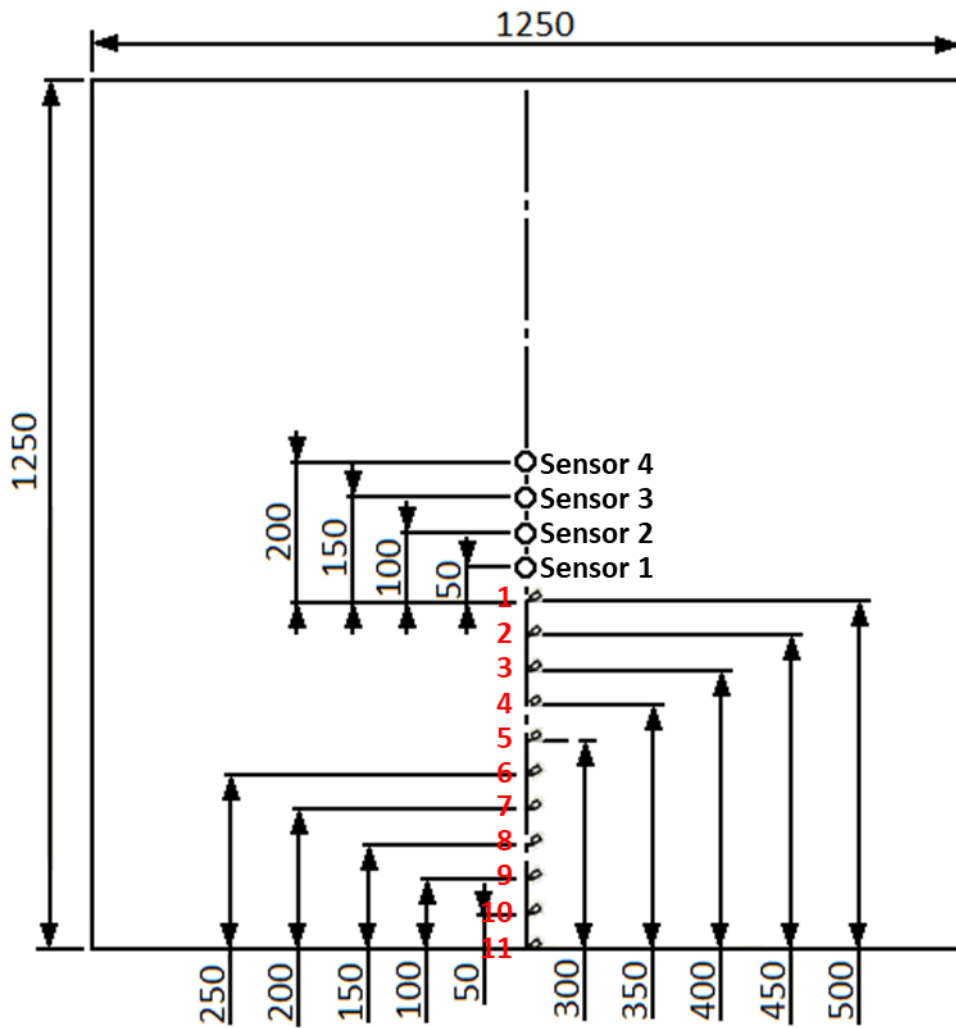


Figure 34. Position of sensors and pencil lead breaks on the large plate

4.3.2. Results

4.3.2.1. Dispersion Study

To assess dispersion in the build plates, the data first needs to be manipulated to provide frequency vs wavenumber. This was done by reordering the data as distance against time, then carrying out a 2D Fourier transform to produce frequency against wavenumber. The results for the 15mm stainless steel plate are presented in Figure 35, with the dispersion curves overlaid upon it. This shows most energy being propagated along S_0 and A_0 with a particularly high intensity region along A_1 . Vertical bars of energy present at 140 and 200kHz can be attributed to the resonant characteristics of the actuator. Figure 36 shows the same signal having travelled

through the thickness of the plate, with energy now more concentrated along the dispersion curves.

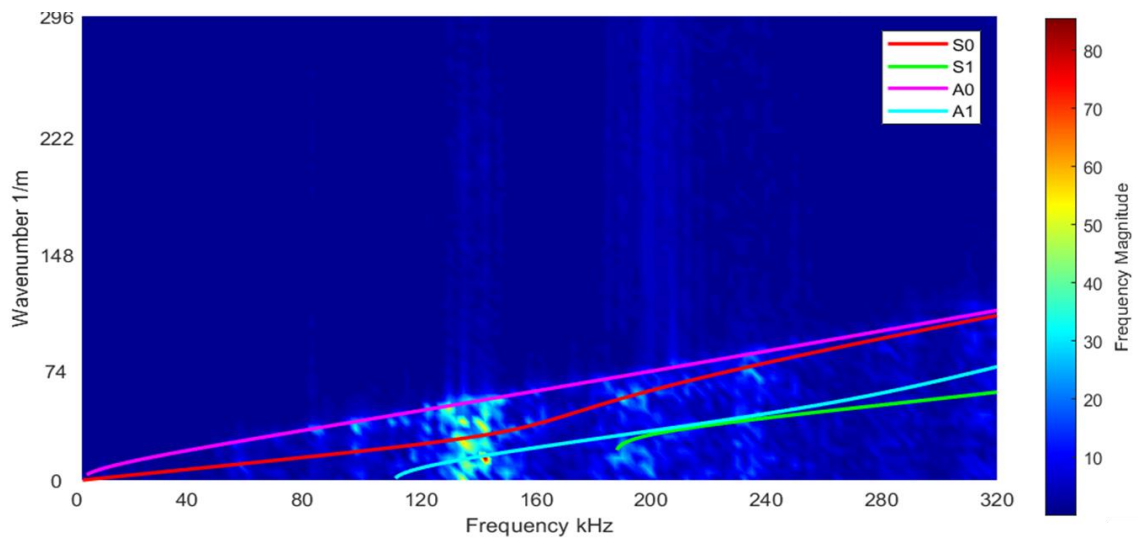


Figure 35. Dispersion of signal from front of stainless steel plate

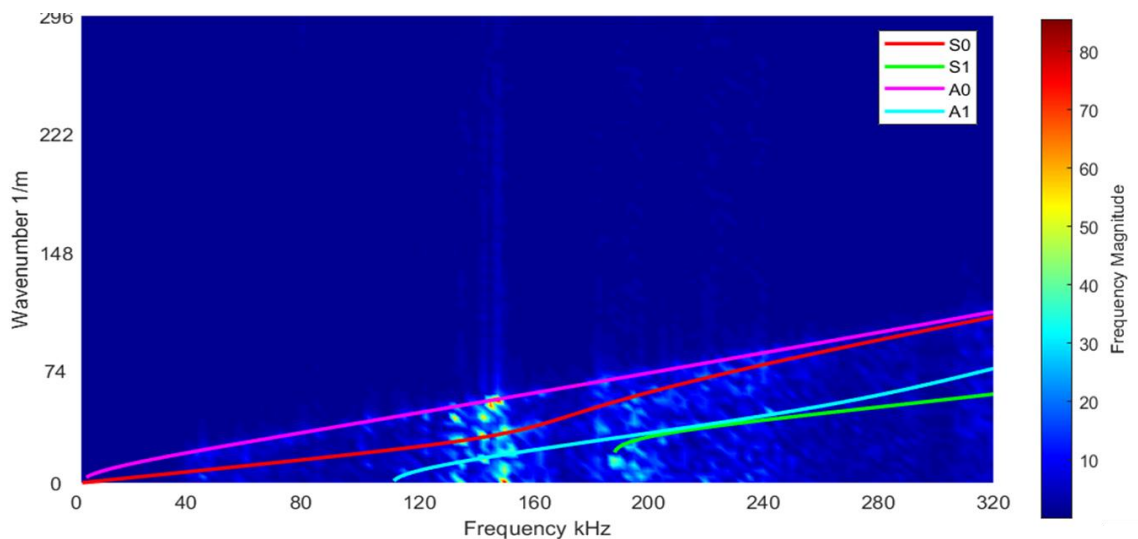


Figure 36. Dispersion of signal from rear of stainless steel plate

Figure 37 shows the dispersion of signals that have travelled along the titanium plate, and Figure 38 shows the dispersion of a signal that has travelled through the build plate. Most of the energy is concentrated along the S_0 and A_0 modes, especially for the signal which has passed through the plate.

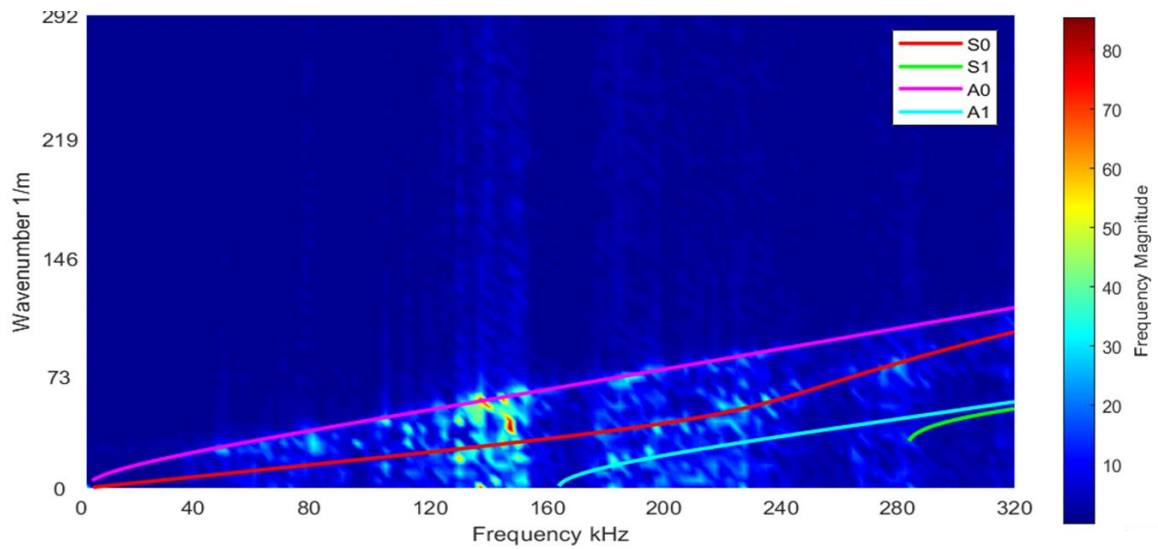


Figure 37. Dispersion of signal from front of titanium plate

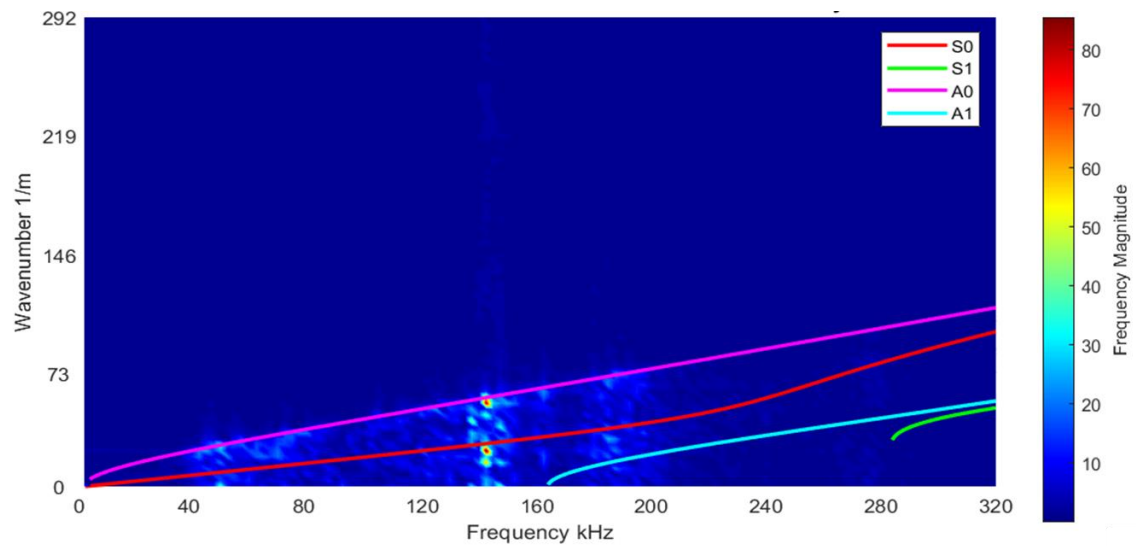


Figure 38. Dispersion of signal from rear of titanium plate

4.3.2.2. Reflection Study

To assess how signals were affected by reflections from plate edges, waveforms from various locations on the 1250x1250mm plate (shown in Figure 34) were plotted and compared, and wavelet transforms were carried out. When plotting waveforms collected in the 1250x1250mm plate, the theoretical arrival of the S_0 and A_0 modes are marked, using AIC to identify the beginning of the signal, assumed to be the bulk P-wave due to the thickness of the plate. In aluminium this is 6320ms^{-1}

from theory (Engineering Toolbox, 2021). The time difference for the S_0 and A_0 modes was then calculated from the distance travelled to the sensor. Figure 39 shows how the S_0 wave coincides with the beginning of a slightly higher amplitude area with the A_0 appearing as the amplitude becomes significantly larger and would likely mark the threshold crossing point.

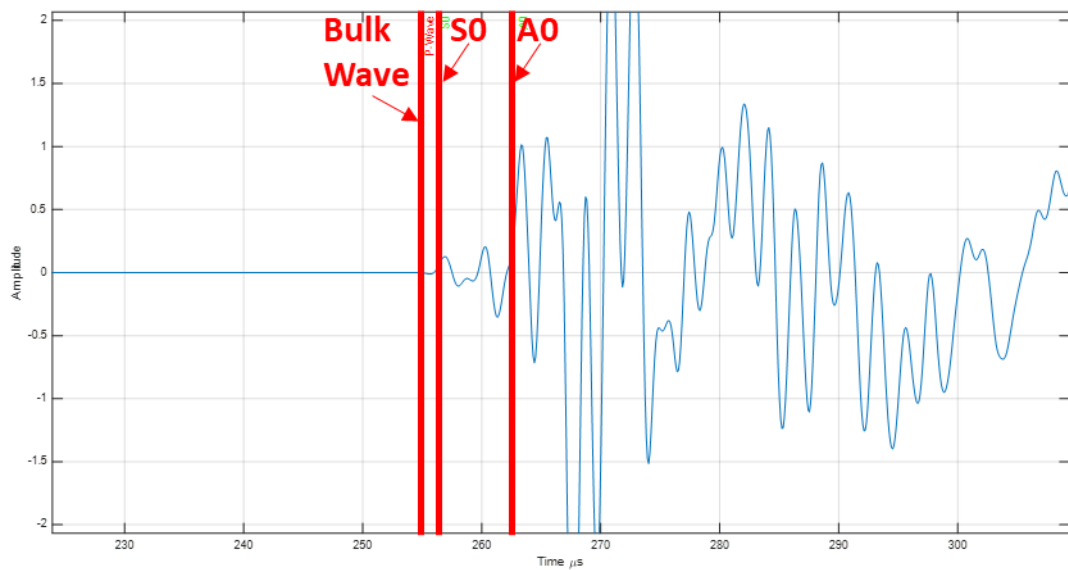


Figure 39. The beginning of a signal collected from the 1250x1250mm plate with the bulk (or P) wave, S_0 and A_0 marked

Figure 40 shows a signal from a Hsu-Nielsen source 500mm from the plate edge, where it will take the first reflections of S_0 and A_0 190 and 330 μ s to arrive respectively. This is with S_0 and A_0 being taken directly from the dispersion curves as 5438 ms^{-1} and 3167 ms^{-1} . The waveforms recorded at sensor 2, 3 and 4 will have travelled an extra 50mm to per sensor, as shown by the sensor positioning in Figure 34, hence the arrival of S_0 , A_0 and their reflections being later.

These waveforms show the majority of energy being carried by the A_0 mode, and the first A_0 reflection heralding an increase in activity following a period of lower frequency activity. As this is merely the first reflection, there are further reflections

after this point, particularly the reflections from the plate sides which should arrive simultaneously. Furthermore, the figure shows how much the amplitude of the signal reduces, essentially halving in magnitude every 50mm.

Figure 41 and Figure 42 show waveforms produced from Hsu-Nielsen sources 350 and then 50mm from the plate edge. When the signal is produced so close to the edge, the A_0 mode carrying the bulk of the energy takes much longer to arrive relative to the S_0 mode, with its reflection having already arrived before A_0 . This leads to reflections of A_0 producing higher amplitudes after the primary first peak which will be a common occurrence in a 250mm square plate where the edge is never more than 125mm away.

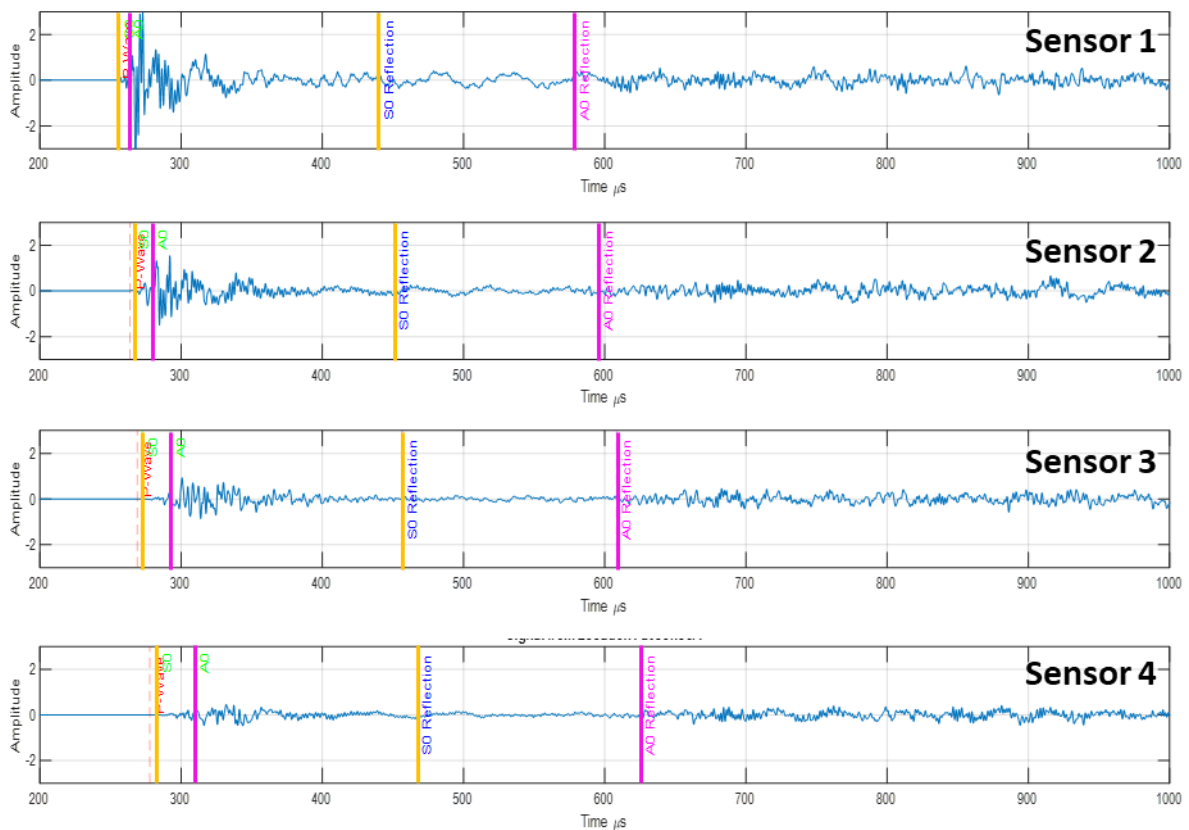


Figure 40. Signals from Location 1 (500mm from the edge and 50mm from Sensor 1) with the S_0 (Magenta) and A_0 (Orange) marked plus their first reflections

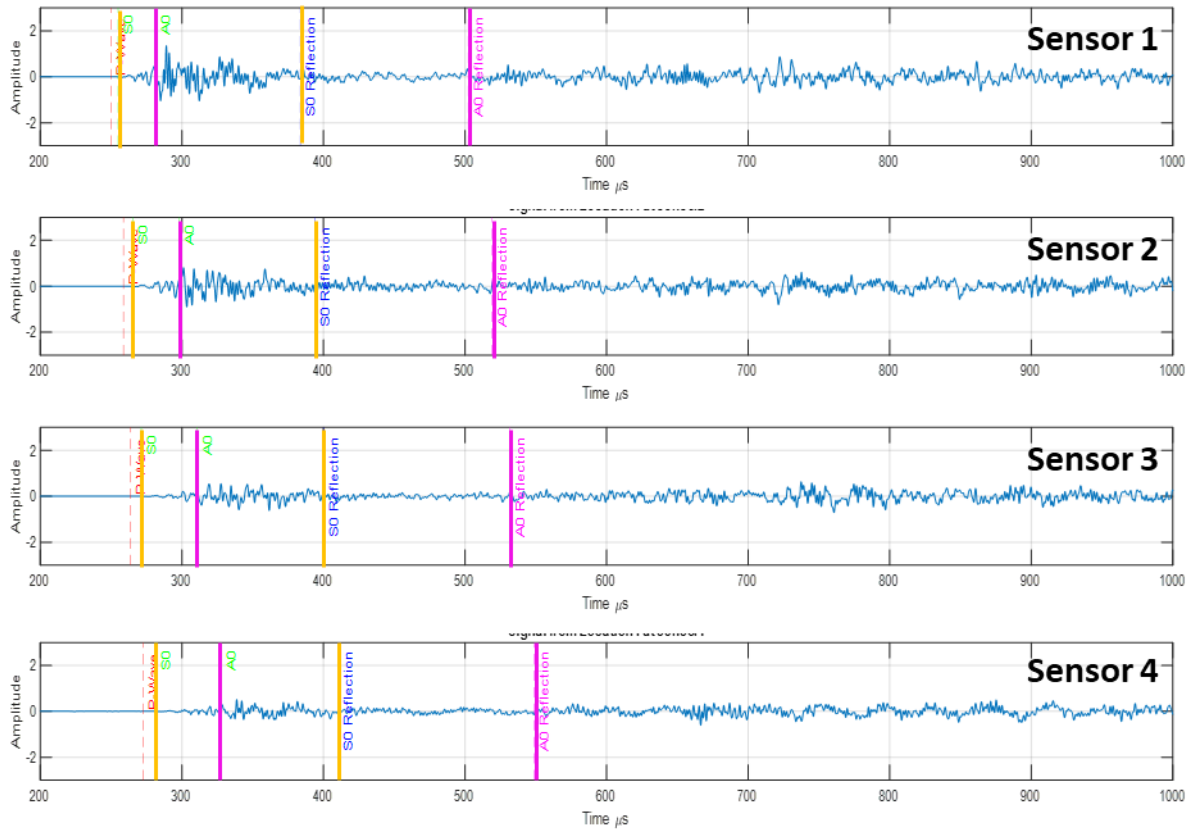


Figure 41. Signals from Location 4 (350mm from the edge and 200mm from Sensor 1) with the S_0 (Magenta) and A_0 (Orange) marked plus their first reflections

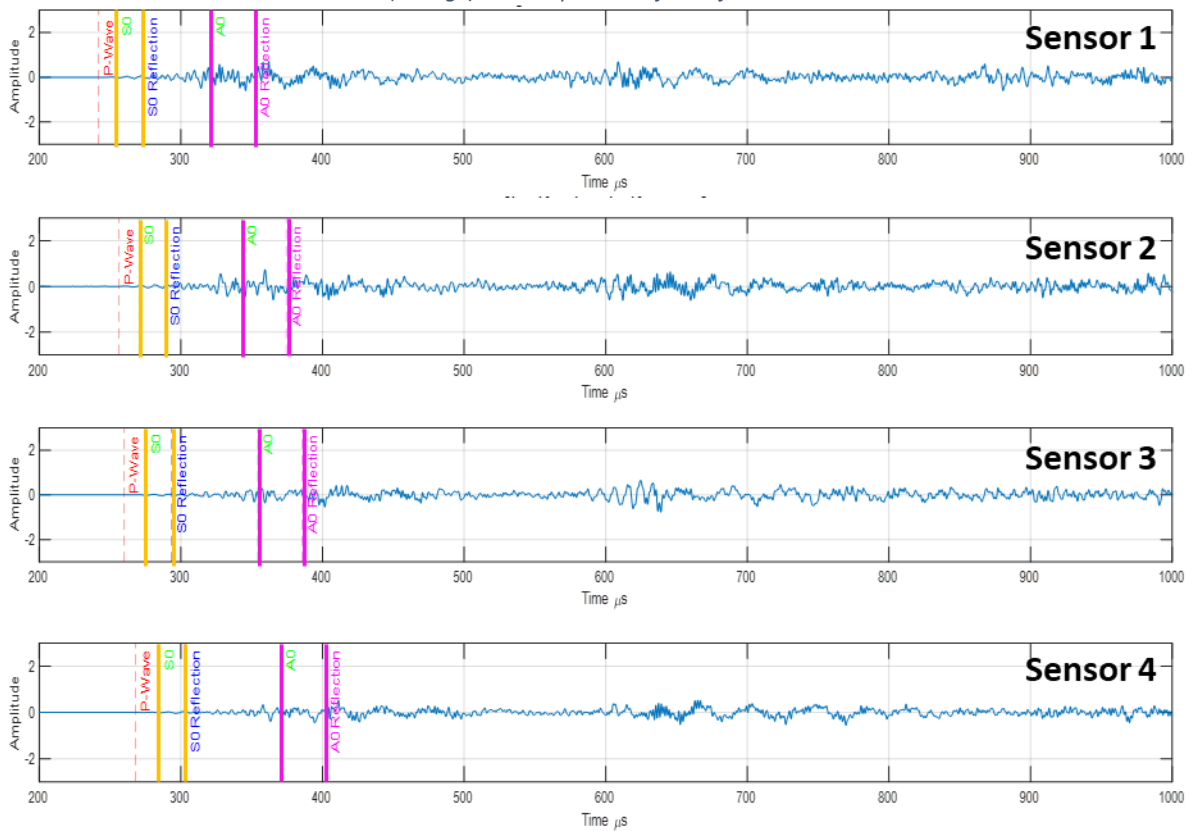


Figure 42. Signals from Location 10 (50mm from the edge and 500mm from Sensor 1) with the S_0 (Magenta) and A_0 (Orange) marked plus their first reflections

To better identify the arrival of reflections in the 1250x1250mm plate, wavelet transforms were plotted for a selection of signals from Hsu-Nielsen sources, with the group velocity dispersion curves for 15mm aluminium overlaid upon them. Figure 43 shows the group velocity dispersion curves for 15mm thick aluminium. These are given as reference for Figure 44 to Figure 55, which show how the dispersion curves line up with a wavelet transform of the signal.

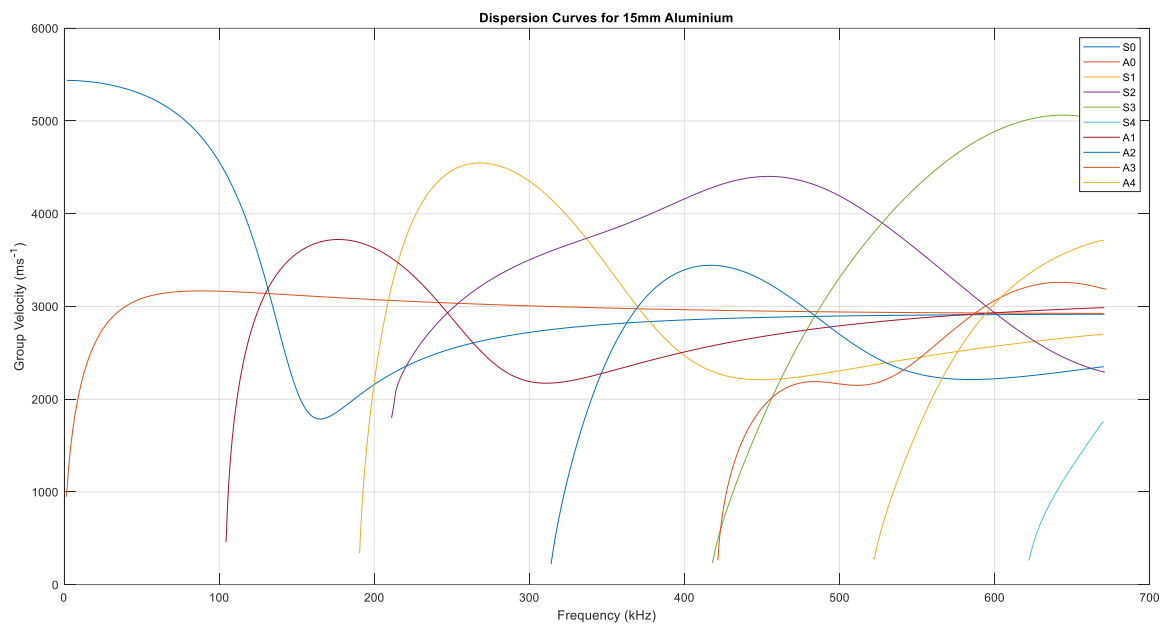


Figure 43. Group Velocity dispersion curves in a 15mm thick aluminium plate

In order to line up the theoretical dispersion curves with a wavelet transform, the dispersion curve needs to be transformed from group velocity to time by using the distance the signal should have travelled to reach the sensor. The start time of the signal was calculated using the AIC method, with the longitudinal velocity in aluminium (6320ms^{-1}) being used to line up the dispersion curves on the wavelet plot. The start times for the dispersion curves were then calculated by calculating how much longer it would take to arrive at the maximum S_0 velocity. The first reflection was plotted by using the additional distance travelled and the additional time taken to travel that distance. Due to the size of the plate, the first reflection

will always come from the near edge and not the sides. Side reflections will have much greater energy when they reach the sensor as reflections from either side will arrive at near identical times and superimpose upon each other.

Figure 44 to Figure 47 are signals taken 350mm from the edge and 350mm from the 1st sensor. The first arrivals of S_0 - S_2 and A_0 - A_2 are plotted, as well as the reflections of S_0 and A_0 . The triple point, where the S_0 , A_0 and A_1 modes converge, is the area of highest intensity with a lot of energy along S_0 and A_0 at higher frequencies. The reflected dispersion curves line up well with the wavelet transform as activity increases with the arrival of the first reflection. After this point activity increases as overlapping reflections arrive at the sensor from all around the plate, with an area of particularly high energy corresponding to the simultaneous arrival of reflections from either side of the plate at around 700 μ s. As the signal progresses at 50mm increments in Figure 45 to Figure 47, energy becomes far more spread out with reflections accounting for more of the total energy of the signal.

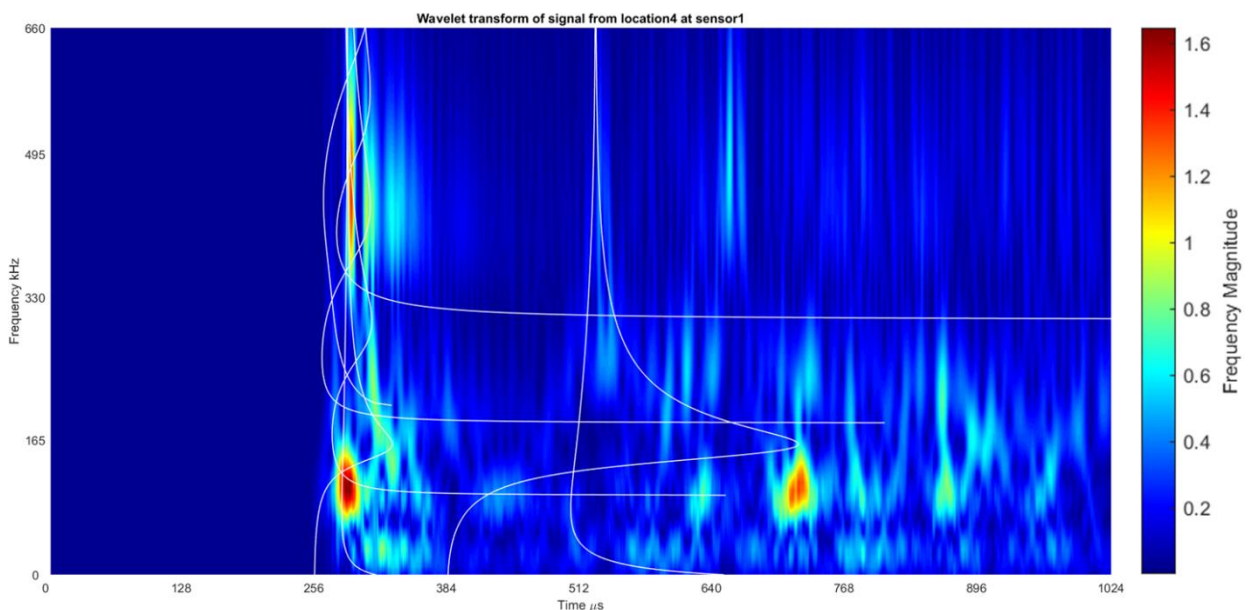


Figure 44. Wavelet transform of a signal originating at location 4 at sensor 1 (350mm from the edge and 350mm from the sensor)

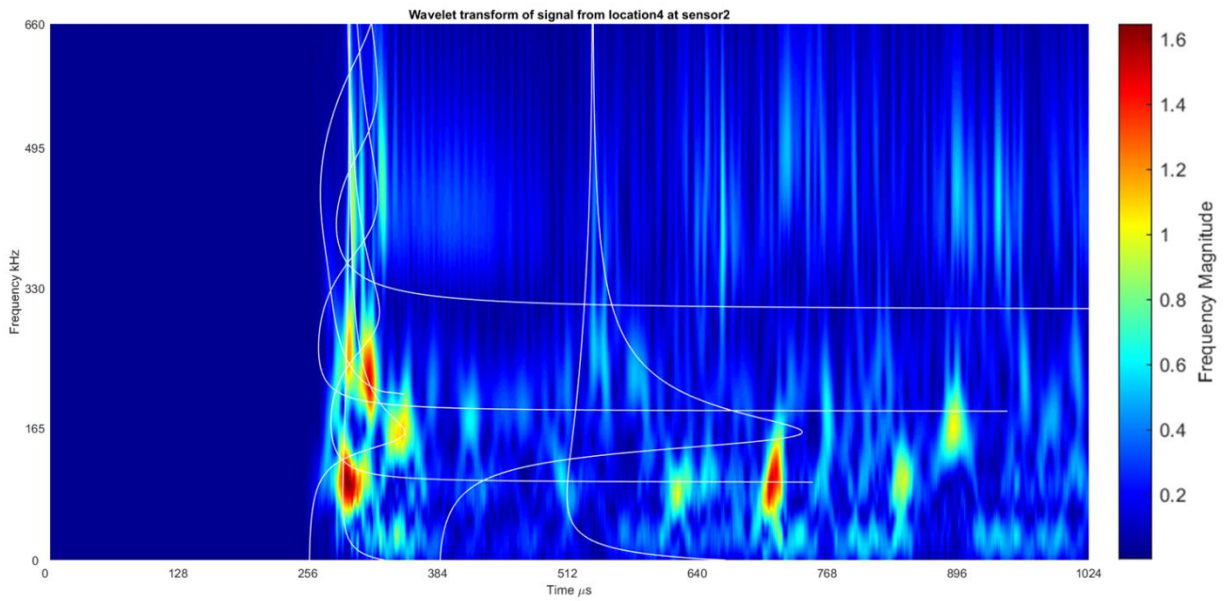


Figure 45. Wavelet transform of a signal originating at location 4 at sensor 2 (350mm from the edge and 400mm from the sensor)

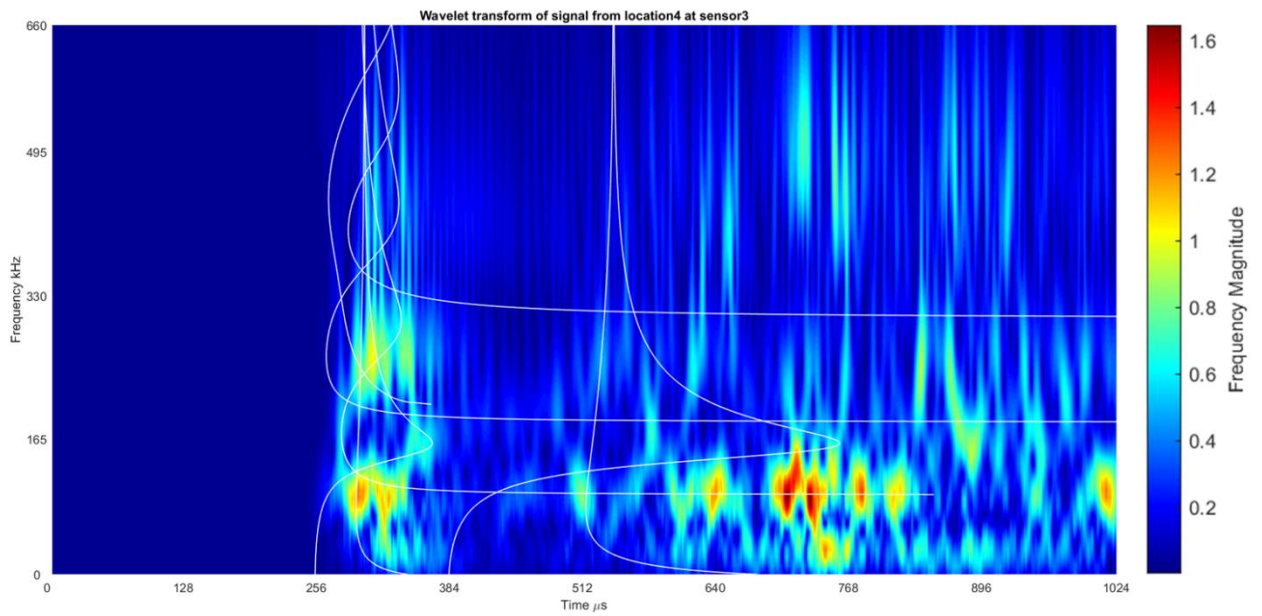


Figure 46. Wavelet transform of a signal originating at location 4 at sensor 3 (350mm from the edge and 450mm from the sensor)

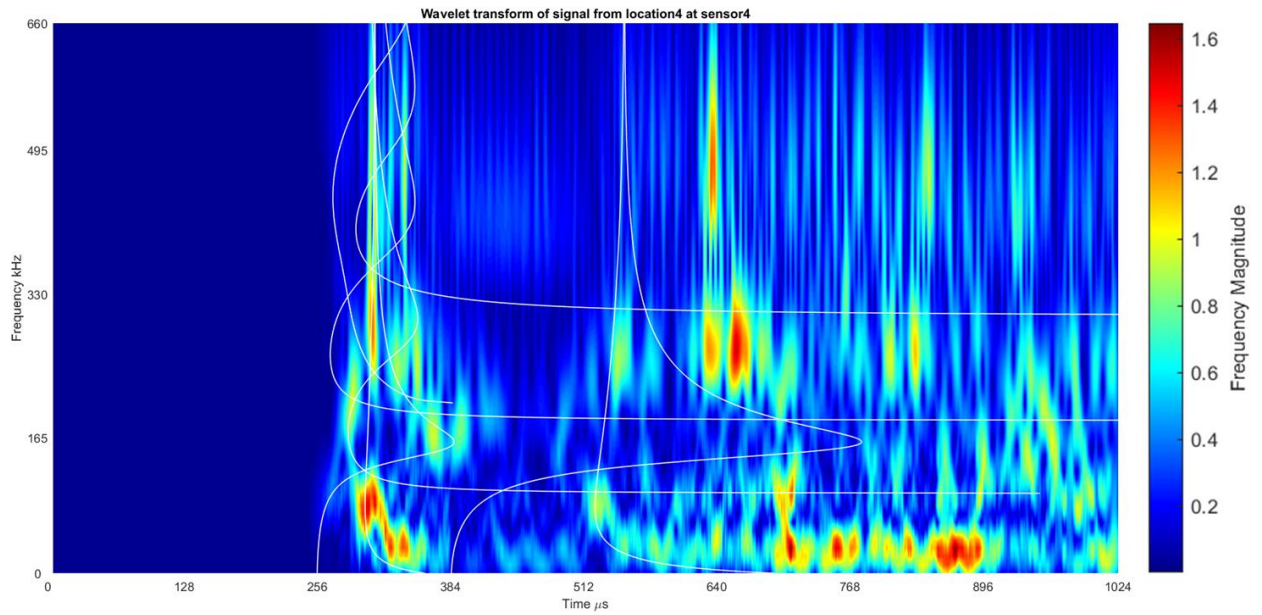


Figure 47. Wavelet transform of a signal originating at location 4 at sensor 4 (350mm from the edge and 500mm from the sensor)

In Figure 48 to Figure 51 the reflections are much more difficult to define making it challenging to observe if the reflection dispersion curves are well lined up. This is likely due to the 1st sensor being just 50mm from the break location meaning the intensity of the 1st arrival skews the colour scale and drowns out any reflections. However, by sensor 4 the reflection arrival is easy to see and lines up well with the dispersion curve, and the first arrival seems to line up well with the dispersion curves, though some modes carry more energy than others.

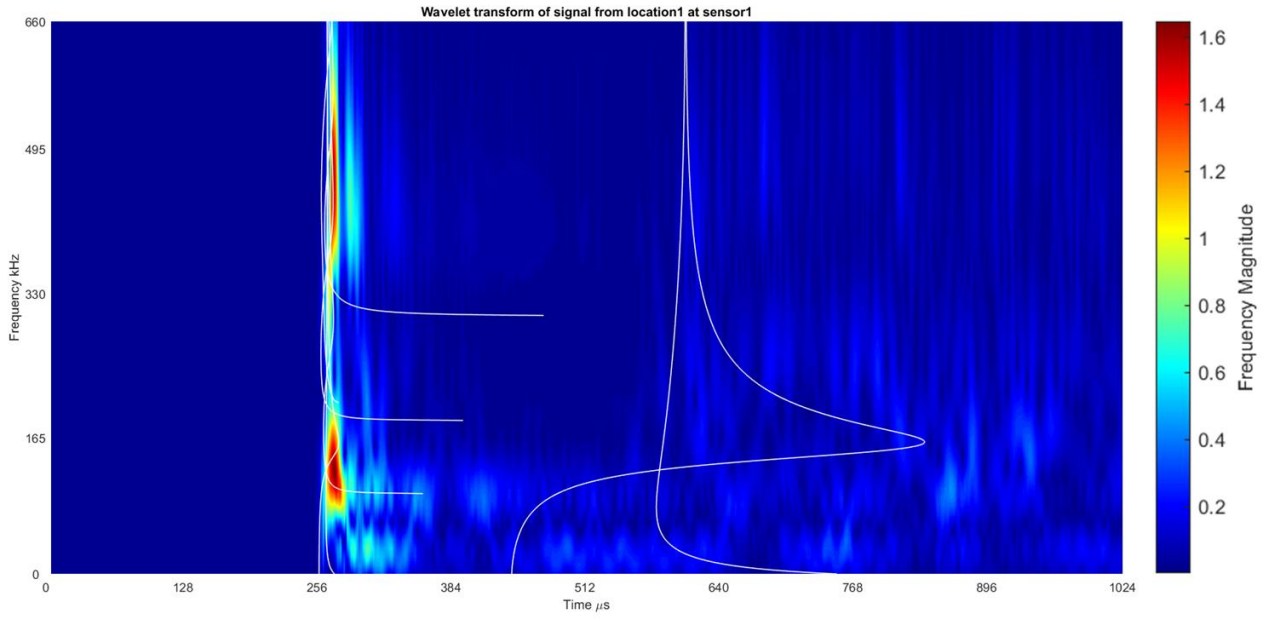


Figure 48. Wavelet transform of a signal originating at location 1 at sensor 1 (500mm from the edge and 50mm from the sensor)

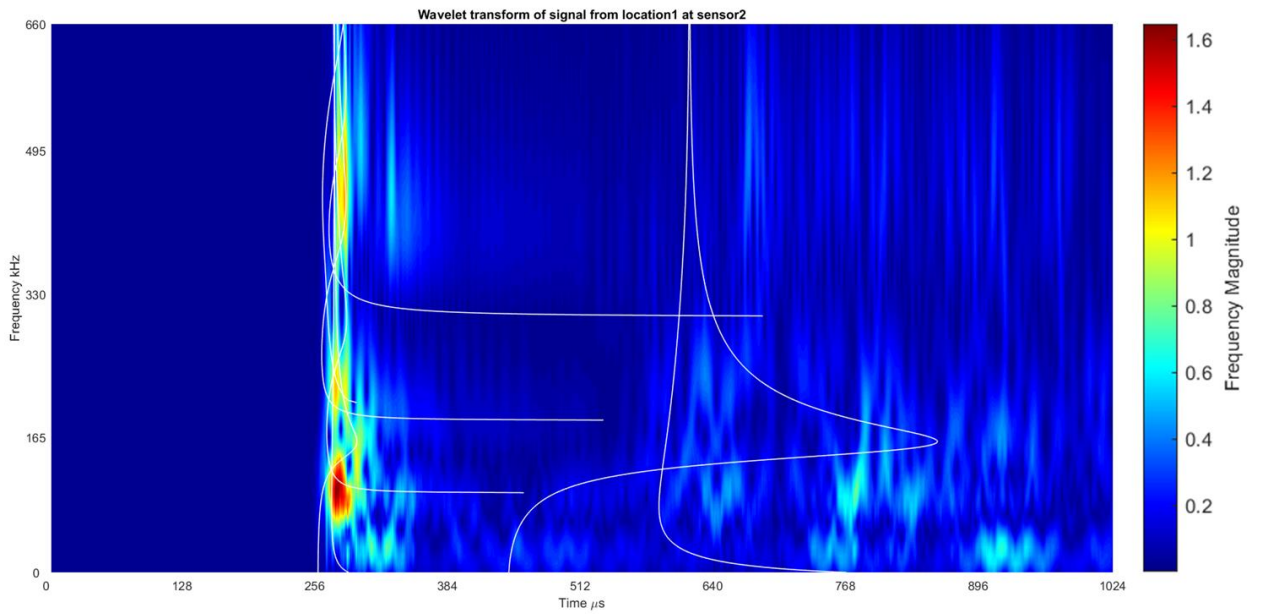


Figure 49. Wavelet transform of a signal originating at location 1 at sensor 2 (500mm from the edge and 100mm from sensor)

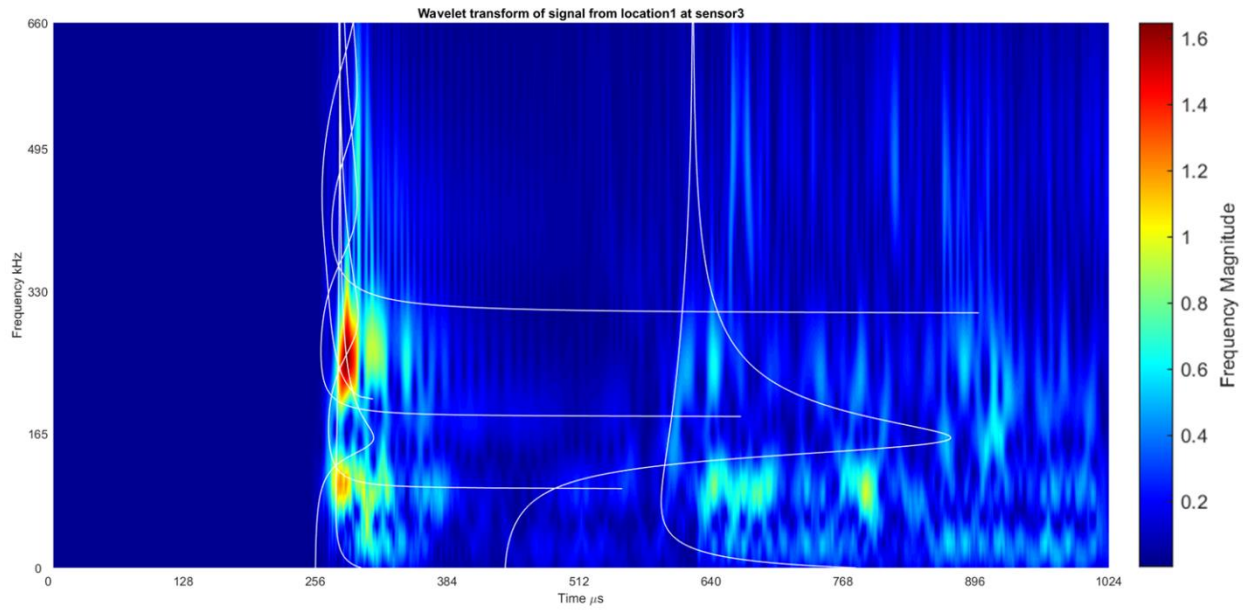


Figure 50. Wavelet transform of a signal originating at location 1 at sensor 3 (500mm from the edge and 150mm from sensor)

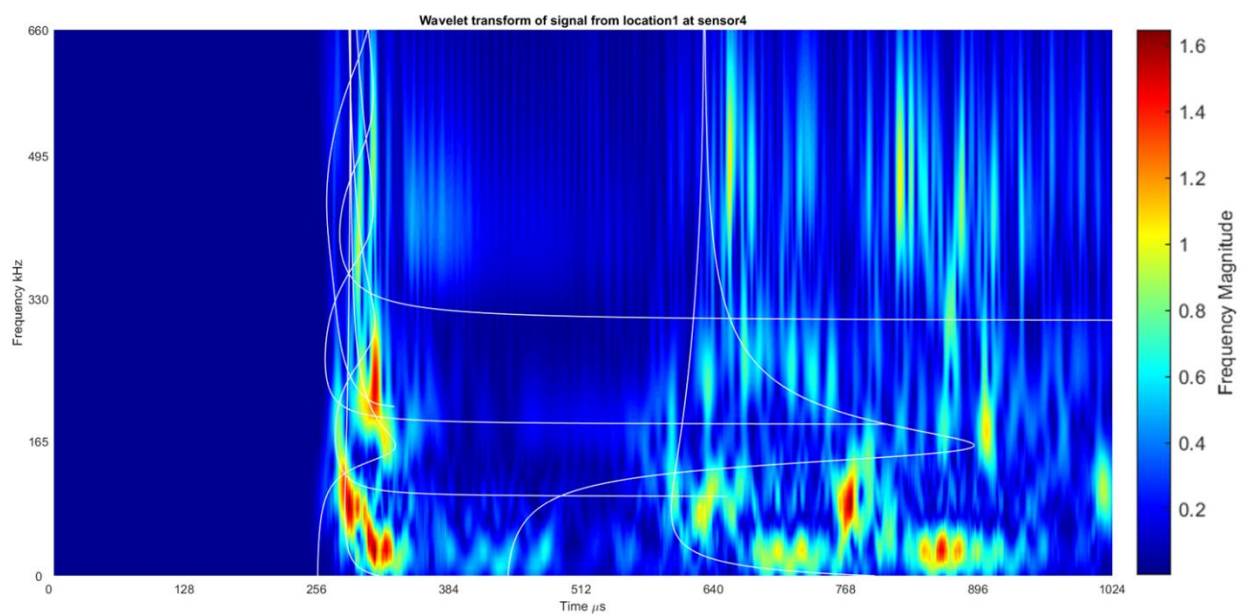


Figure 51. Wavelet transform of a signal originating at location 1 at sensor 4 (500mm from the edge and 200mm from sensor)

Figure 52 to Figure 55 are from a source just 50mm from the edge, so the reflection travels only 100mm further than the first signal. This can be seen by how the dispersion curves for the initial arrival and the reflection arrival overlap significantly.

There is much less energy at the top of the frequency spectrum likely due to the larger distance travelled, and the dispersion curves are heavily stretched by the distance travelled.

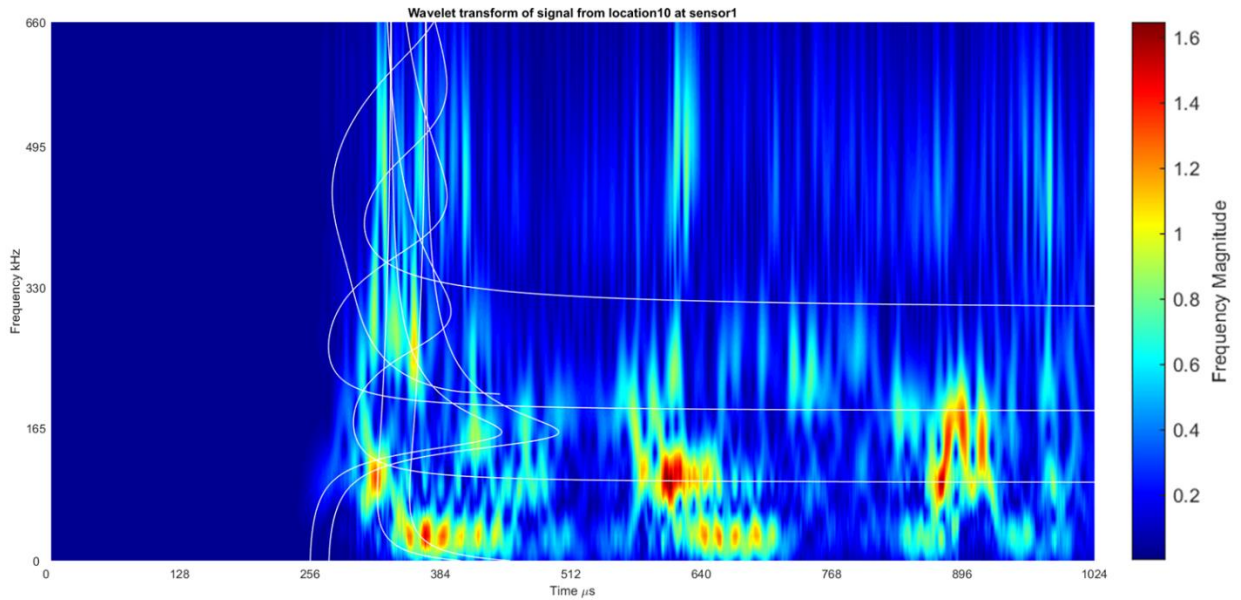


Figure 52. Wavelet transform of a signal originating at location 10 at sensor 1 (50mm from the edge and 500mm from sensor)

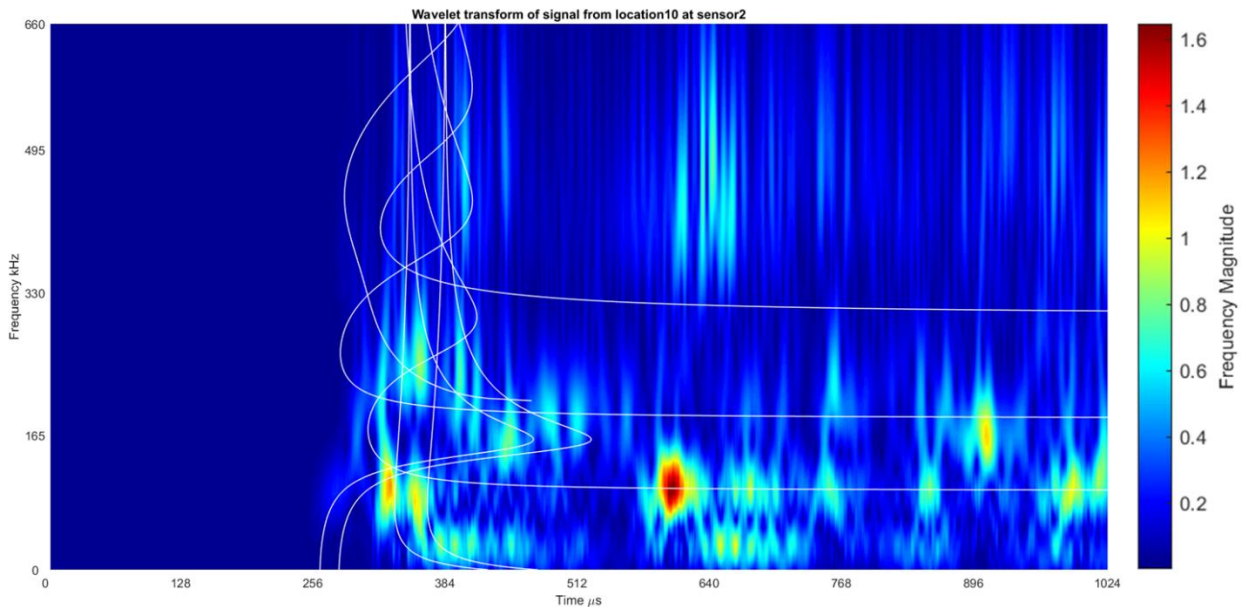


Figure 53. Wavelet transform of a signal originating at location 10 at sensor 2 (50mm from the edge and 550mm from sensor)

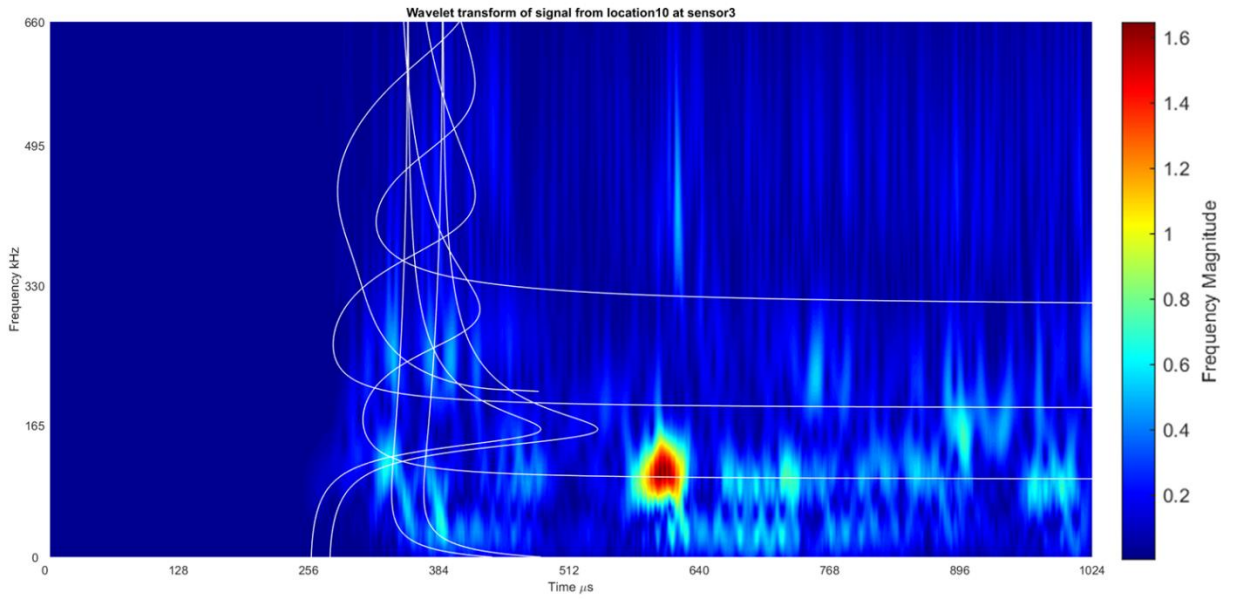


Figure 54. Wavelet transform of a signal originating at location 10 at sensor 3 (50mm from the edge and 600mm from sensor)

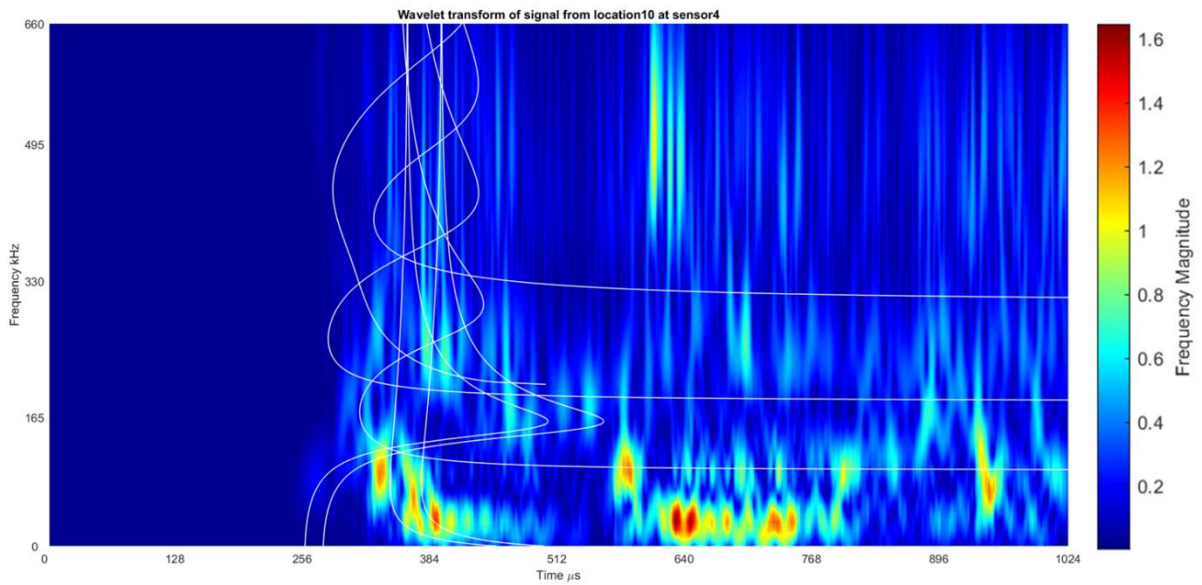


Figure 55. Wavelet transform of a signal originating at location 10 at sensor 4 (50mm from the edge and 650mm from sensor)

Figure 56 shows a direct comparison of signals recorded in a 1250mm plate and a 250mm plate. The sensors were placed in a similar configuration to on the larger plate, with a Hsu-Nielsen source generated 50mm away. The structure of the signal is broadly the same for the first 100 μ s, but from the arrival of the first reflections onwards the signal is largely made up of reflections.

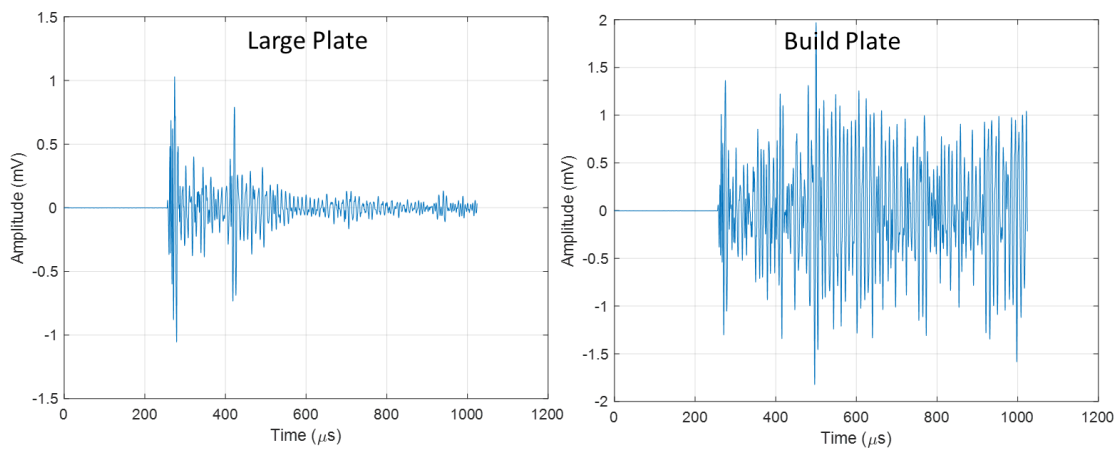


Figure 56. Comparison of similar signals in the large 1250mm plate and a 250mm build plate

4.3.3. Discussion

The study into dispersion in the build plates was carried out to assess how signals disperse in the build plates. These results showed that most energy is distributed along the dispersion curves, especially for a signal that has travelled through the thickness of the plate. This shows that Lamb waves are beginning to develop in the plates, despite the ratio of thickness to length of the plate being relatively high.

The studies into how reflections affect the signal successfully identified when reflections arrive at the sensor. This work, with both waveform plots and wavelet transforms, showed that reflections have a great influence on the waveform, especially the A_0 mode. This was shown to be the dominant mode that was most

likely to trigger the threshold crossing, showing the importance of using AIC to identify the true signal beginning. Additionally, the superposition of reflections later in the signal means that it may recross the threshold and achieve a higher amplitude than the initial signal arrival. This may have implications in trying to characterise signals.

4.4. Propagation through Waveguides

4.4.1. Experimental Procedure

Figure 57 shows the four waveguide shapes tested. Waveguide 1 is the original design that was used predominantly for data collection, whilst waveguide 4 was redesigned to pass through the heater plate and interface directly with the build plate. This retained an identical length of 78mm and primary diameter of 10mm, though it narrows to an 8mm diameter and a with an externally threaded section for the bottom 20mm of the waveguide. This design additionally has a hole at the base of the bolt hole to allow powder egress and a hole 25mm along its length to allow tightening and loosening. Waveguide 3 is identical to waveguide 1 with the exception of a 1mm O-ring 10mm from the base, to investigate how a single change in cross-sectional area affects the signal. Finally, waveguide 2 contains the O-ring groove and powder egress hole, and has a reduced length of 64mm. The top of each waveguide has a diameter of 17mm, though waveguide 2 has an additionally 1mm lip around it to aid with sensor seating. Using Equation 12 from Section 2.5.5 results in resonant frequencies of 38.5kHz for waveguides 1,3 and 4, and of 46kHz for Waveguide 2.

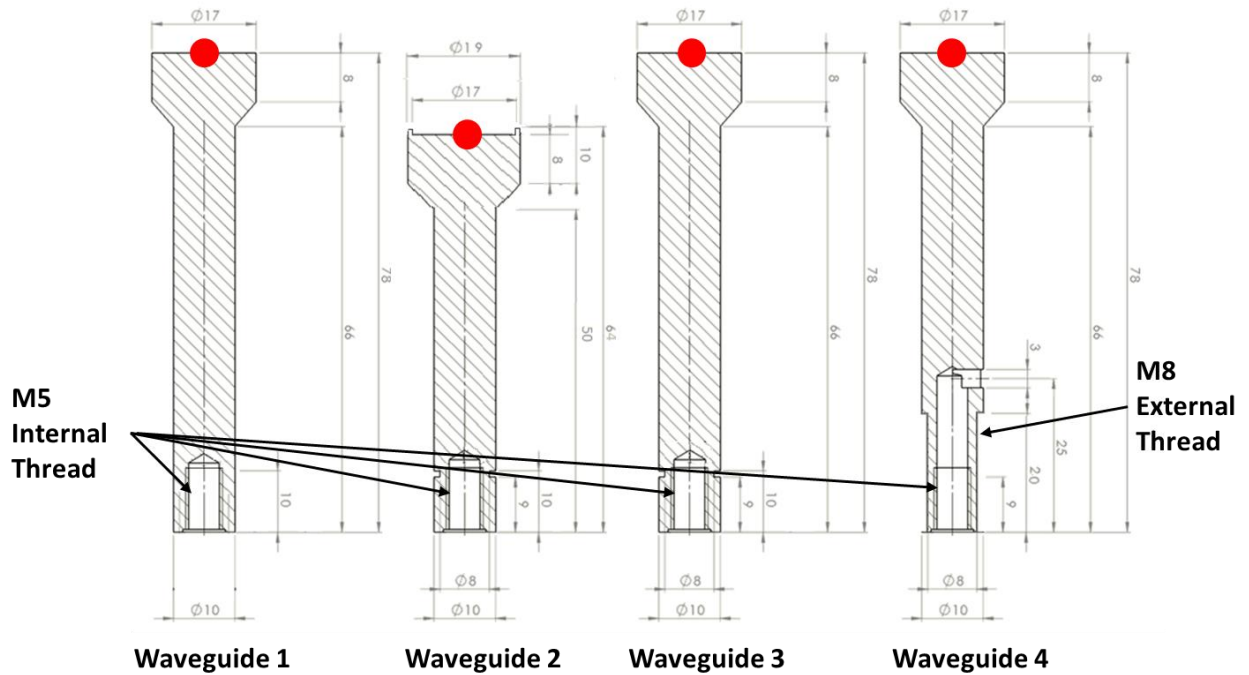


Figure 57. The different designs of waveguide tested, with the red spot indicating the sensor position on each

When collecting vibrometry data from the waveguides, the waveguides were attached to a build plate for stability and to provide a base for signals to be created. An F15A sensor was affixed to wider head of the waveguide and continuously excited with a 100V transient signal, from 30 to 350kHz with a step of 40kHz. The whole length of each waveguide was scanned in a single line of 100 points, with a grid size of around 1mm.

4.4.2. Results

The waveguides also play an important role in the propagation of signals to the sensors. Figure 58 shows energy clustered around L(0,1), F(1,1) and F(1,2). The theory around dispersion in waveguides is presented in Section 2.4.5. However, there appears to be a lot of energy around 320kHz that doesn't conform to the dispersion curve for 10mm diameter steel.

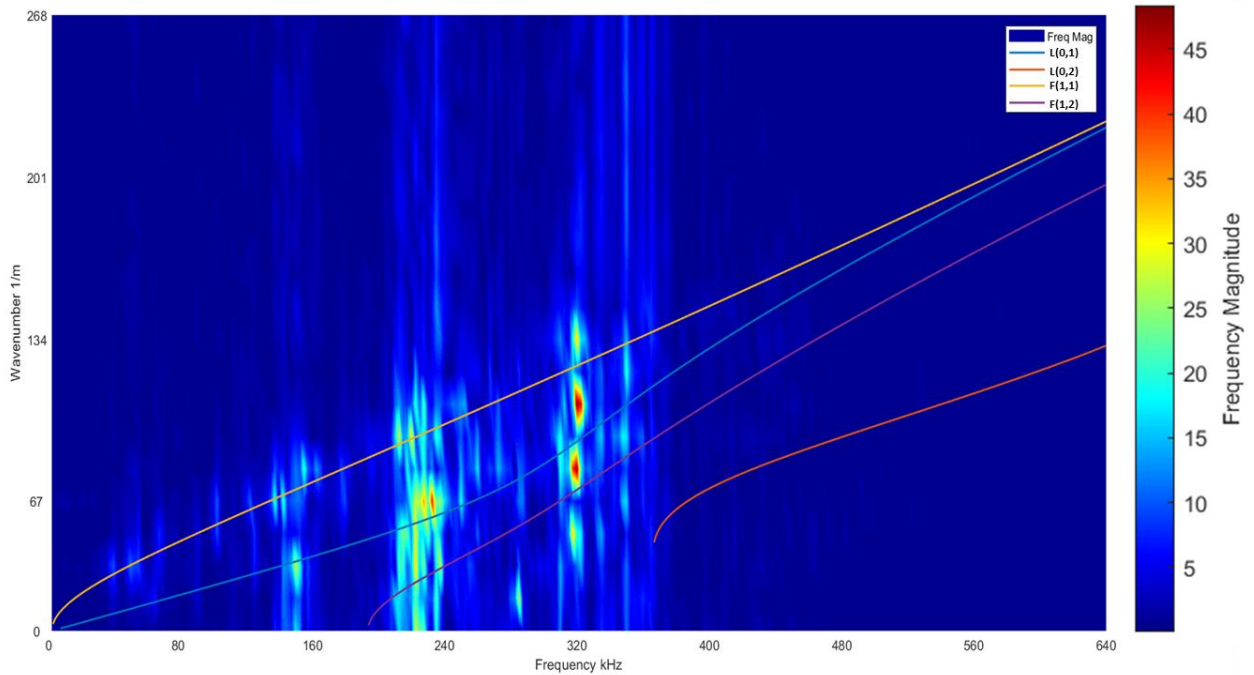


Figure 58. Fourier Transform of vibrometry data of waveguide1 with a bolt with dispersion curves for 10mm diameter steel overlaid

Figure 59 shows the same wavelet transform as Figure 58 but with the dispersion curves of 17mm diameter steel overlaid upon it. This is to show how the changing thickness of the waveguide affects dispersion. The F(1,1) mode lines up with one of the high intensity areas, but not with the others. However, given how the modes have compressed between 10mm and 17mm, it could be assumed that other high intensity areas line up with intermediary dispersion curves between the two. This shows how the thickness changes have an effect on the dispersion and thus the wave propagation.

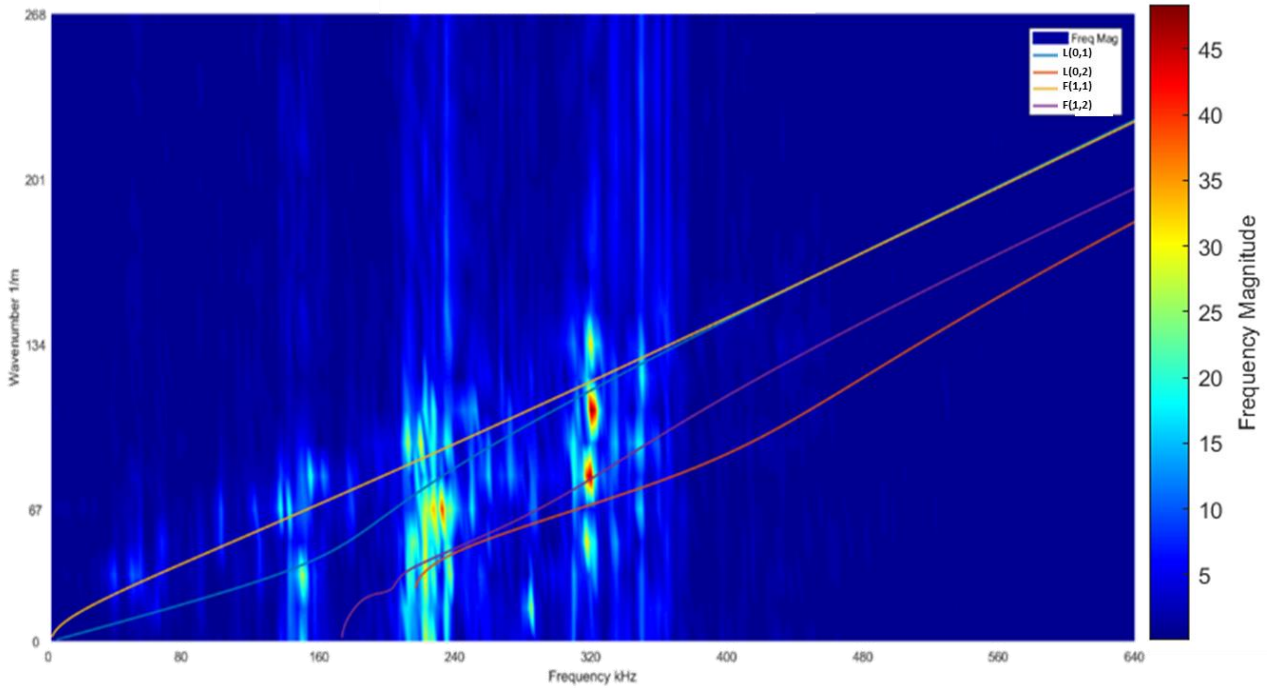


Figure 59. Fourier Transform of vibrometry data of waveguide1 with a bolt with dispersion curves for 17mm diameter steel overlaid

Figure 60 is from Waveguide 2, which was 20mm shorter than the others as well as having a larger diameter as shown in Figure 57. Interestingly, the energy seems to be stretched over the wavenumber domain much more than for waveguide 1, possibly due to its shorter length.

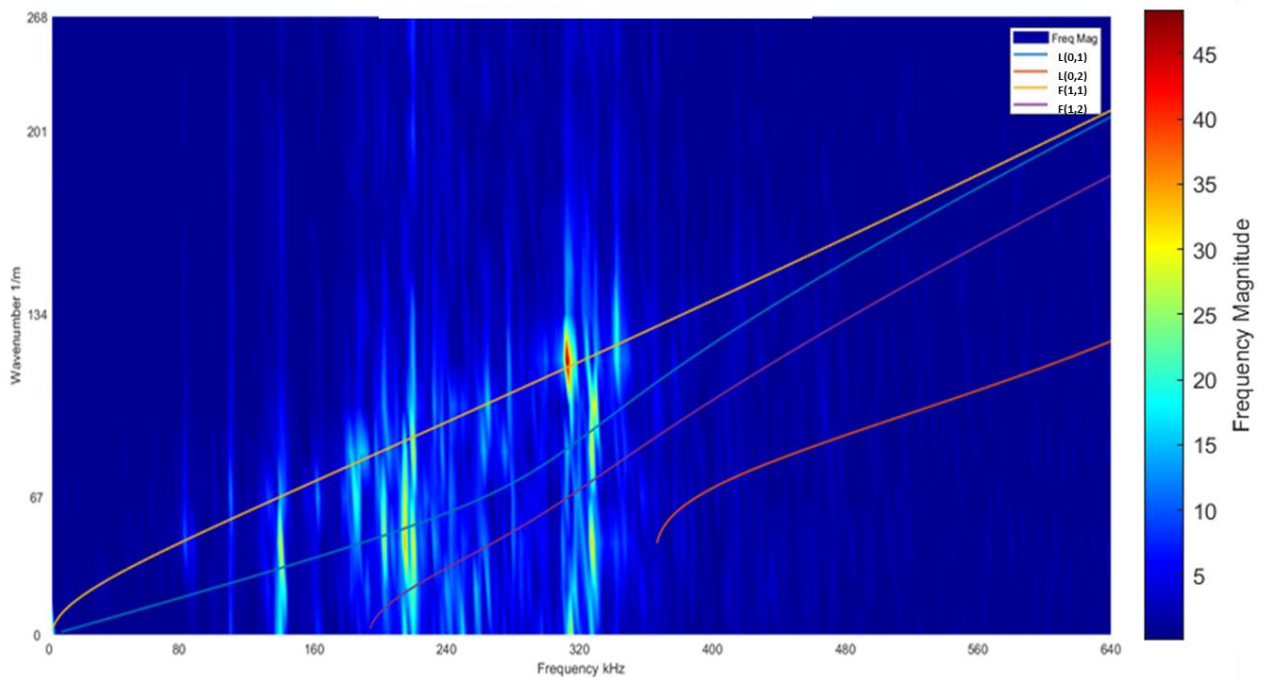


Figure 60. Fourier Transform of vibrometry data of waveguide 2

Figure 61 shows the dispersion through waveguide 3, with the dispersion curves for a 10mm rod. Bearing in mind the only difference from waveguide 1 is a 1mm o-ring groove, it seems that this causes the attenuation of the higher frequency components compared with Figure 6. It also appears that the L(0,1) mode through the 10mm section of the waveguide is clearly dominant. The only difference between Figure 61 and Figure 62 is the lack of a bolt in Figure 34, which amplifies the dominance of the S0 mode.

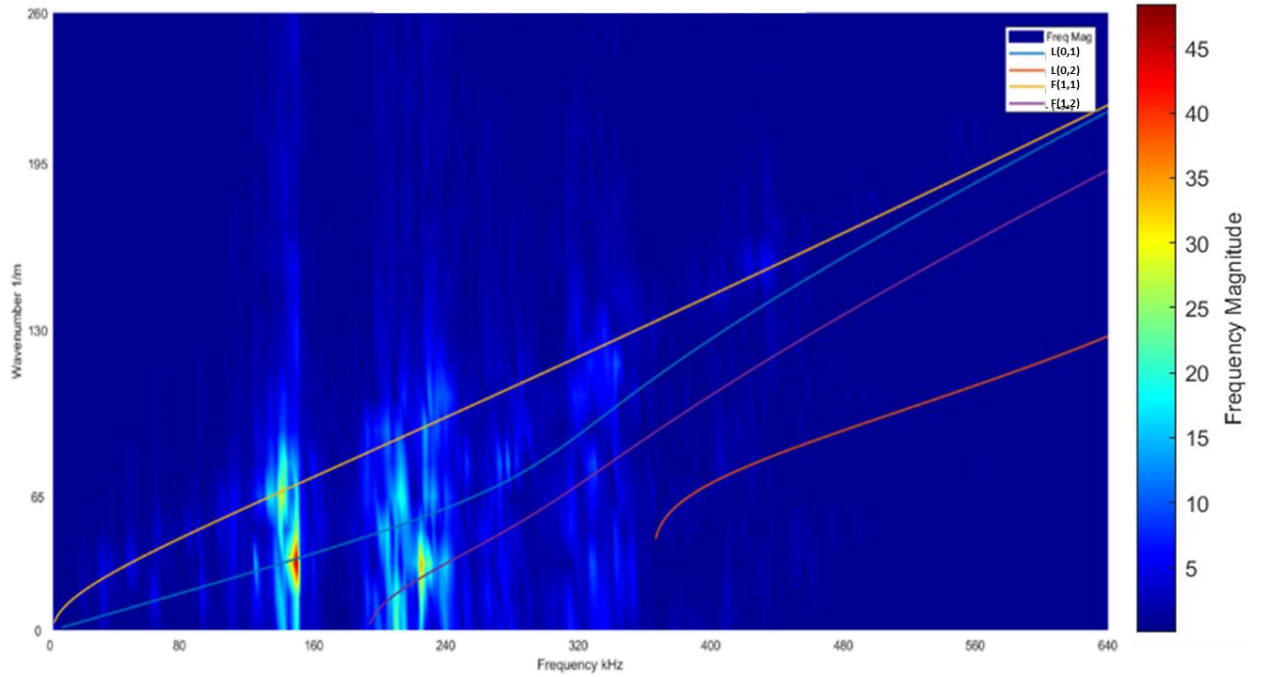


Figure 61. Fourier Transform of vibrometry data of waveguide 3 with a bolt with the dispersion curves for 10mm steel overlaid

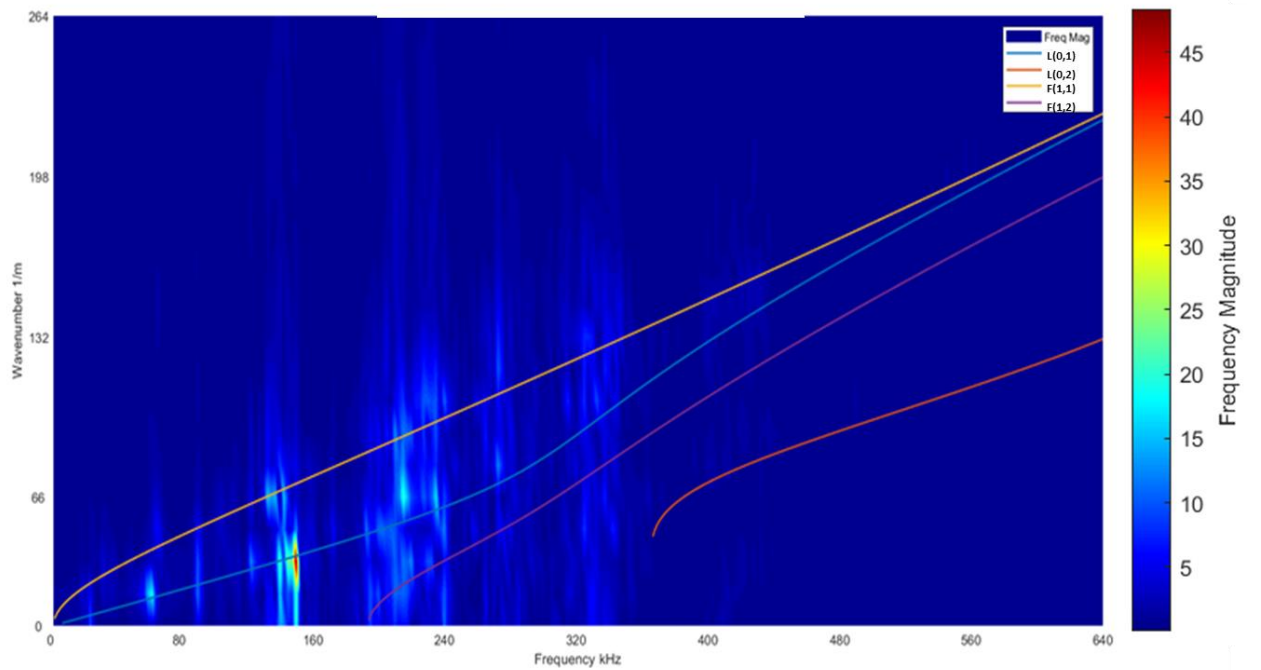


Figure 62. Fourier Transform of vibrometry data of waveguide 3

Figure 63 is the dispersion through waveguide 4, which is by far the most complex of the 4 waveguides. It has an unscrewing hole through it, a powder ejection hole,

and a narrower threaded section. The transform suggests that there a large number of modes propagating through it.

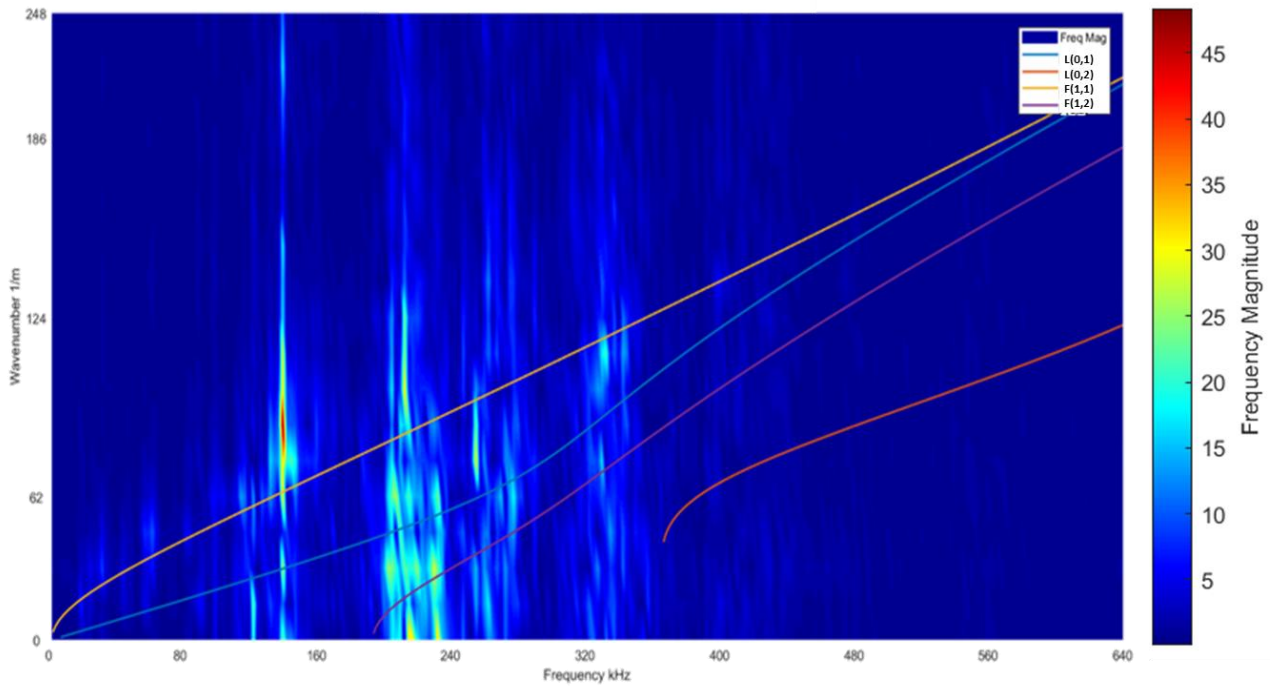


Figure 63. Fourier Transform of vibrometry data of waveguide 4

Figure 64 is the dispersion through waveguide 4 with the dispersion curve for an 8mm steel rod. The $F(1,1)$ is closer to passing through the area of highest intensity, but there is not a strong correlation. This suggests that the wave is being dispersed through an area with an equivalent diameter of much smaller than 8mm.

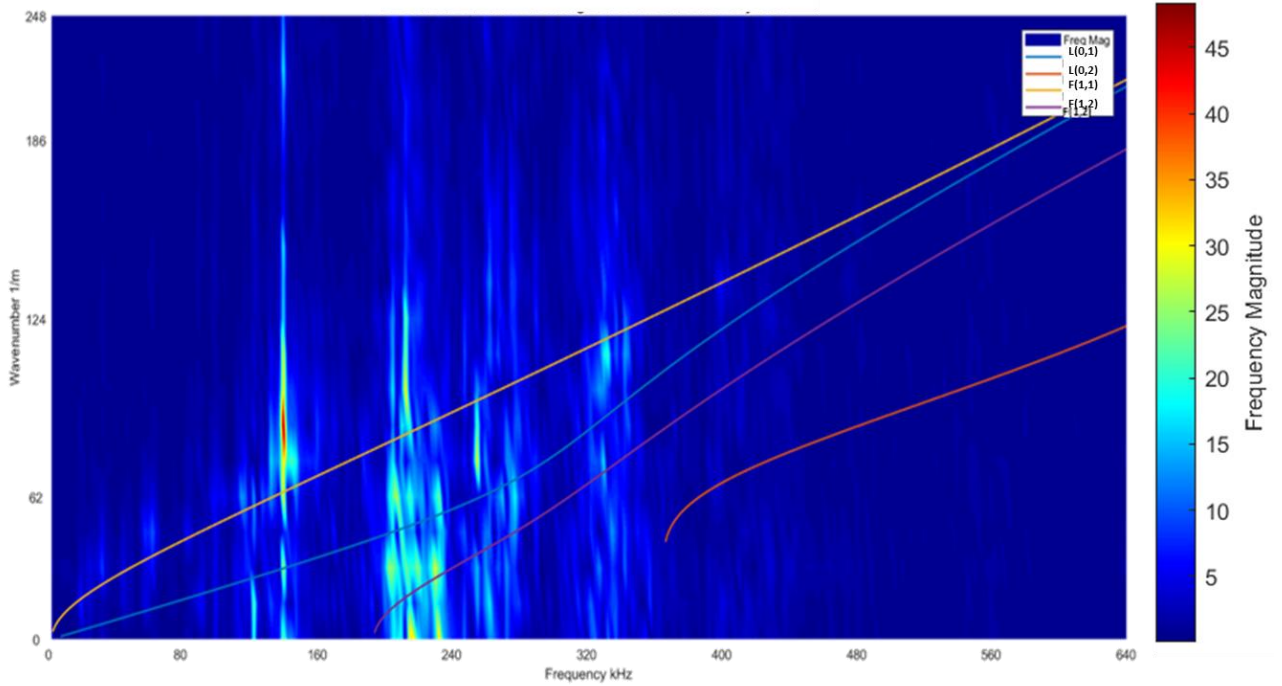


Figure 64. Fourier Transform of vibrometry data of waveguide 4 with a bolt

Figure 65 shows the dispersion through waveguide 4 without a bolt. There is far less energy than in Figure 35 with the high energy area at 150kHz being conspicuously absent. This may be due to the bolt transforming the lower section from a tube to a rod, thus changing the dispersion characteristics. The highest intensity is around 200kHz, and may correlate to an F(1,1) mode.

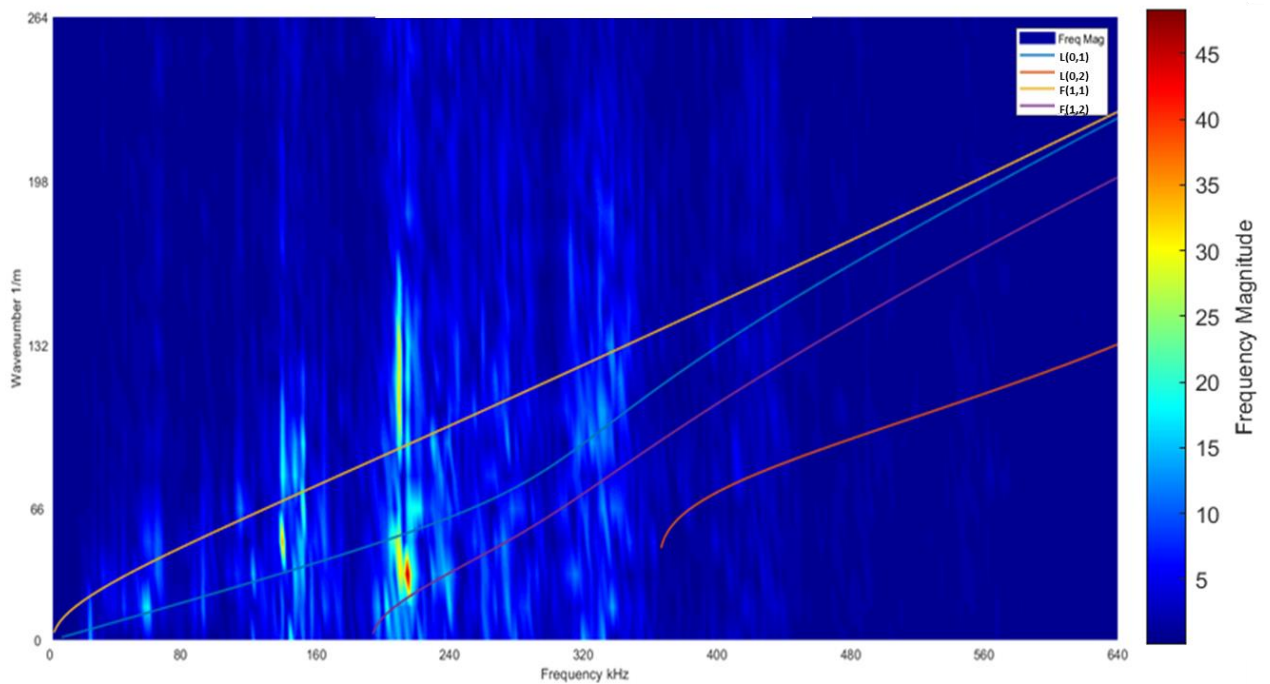


Figure 65. Fourier Transform of vibrometry data of waveguide 4

4.4.3. Discussion

Dispersion has been shown to be present in the simpler original waveguides, however as the waveguide becomes more complex this becomes less clear. Using Equation 12, presented in Section 2.4.5, the harmonic frequencies of a 78mm stainless steel waveguide such as this should occur every 38kHz, which is a likely cause of the repeated vertical bars on each figure. This will lead to a distortion of an AE signal before reaching the sensor, further complicating characterisation.

4.5. Conclusions

This chapter has focused on studying how signals propagate through the build plate, heater plate and the waveguides. Firstly, studies into how signals propagate into the heater plate from the build plate were undertaken. The results of these studies showed that signals passed into the heater plate in different points in different

plates. This means that signals originating from similar source locations on different plates could have very different paths to each sensor. This will result in mismatched arrival times resulting in an inaccurate predicted location. A result of this work led to modifications of the designs of the heater plate and waveguides to create a clearer propagation path, shown in Figure 66. This design change has been carried forward to the Renishaw AM500s.

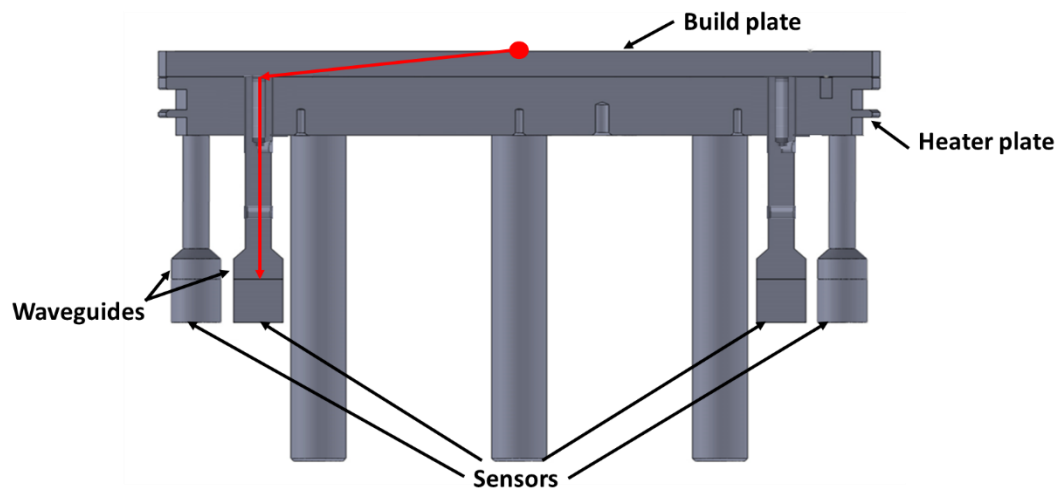


Figure 66. Propagation paths from the build plate to the sensor after the design change

Studies were also carried out into how signals propagate through the build plate. Work carried out using the vibrometer proved dispersion occurs to signals within the build plate, previously Renishaw assumed a bulk wave propagation. Dispersive signals recorded on the opposite side of the build plate to the source suggest that Lamb waves develop despite the relatively high thickness, ideal for recording and locating AE signals. Work done to study reflections in the build plate also showed the presence of dispersion, as well as showing how reflections affect the signal content. A comparison between a signal in the build plate and in a large 1250mm square plate showed that after the first 100 μ s the build plate signal maintains a high

amplitude due to ongoing reflections. This may have implications when it comes to locating and characterising signals.

The work carried out in the waveguides showed that though dispersion is present in them, the relatively complex geometry of the redesigned waveguide means that this becomes less clear. The waveguides were also shown to be highly affected by their harmonic frequencies. The distortion of signals in the waveguides and the repercussions for the characterisation of these signals will be further explored in Section 6.2.

5. Location

5.1. Introduction

The ability to accurately locate the origin of signals is a vital aspect of this project. Builds in the Renishaw AM500 are frequently made up of an array of smaller components being printed concurrently. Being able to locate which component has failed means that that components build can be cancelled before further powder is wasted. AE offers a powerful tool for locating signals quickly as they happen using methods such as Time of Arrival or delta-T as discussed in Section 2.5.

There are several challenges to accurately locating signals within the AM500. As discussed in the Chapter 4.1, the build plate is part of a complex 3D system that includes waveguides and the heater plate. Efforts were made to simplify the propagation paths through the assembly, which should also improve location performance. A further challenge is presented by the thickness of the plate in relation to its width, which leads to large, sustained reflections in the plate as shown in Section 4.3 and can obscure the beginning of the following event.

The aim of this chapter is to investigate the location of signals in a build plate using the TOA and delta-T methods. This work will compare the location accuracy of these two methods, and work on improving accuracy for and useability for each. The TOA work investigated whether dispersion curves could be used to select the wave velocity for that plate thickness, to account for the plate thickness reducing with each build. With delta-T, work was completed with the aim of making delta T data collection more efficient, to make its use in this application more practical. Additionally, work was completed to compare delta-T location accuracy using the same collected maps for different thicknesses. This was completed to replicate the

build plate life cycle, which becomes marginally thinner after each build. It has been assumed that new delta-T training data would be needed before each build, so this work was completed to explore if this was necessary.

5.2. Effect of Poor Plate Fixing

5.2.1. Experimental Procedures

As the build plate is removed and resecured between builds there is a chance the plate is not secured as well as it could be. A reason for this can be due to metal powder remaining within the bolt holes and preventing a full seal. A series of experiments were carried out with different bolt configurations to investigate how this would impact location, which also helped to provide a deeper understanding of how the geometry could be changed to improve location accuracy. For each of the configurations listed below, delta-T training data was collected and sample sources were located for comparison.

- One loose bolt
- Two loose bolts
- Three loose bolts
- Four loose bolts

A further three experiments were carried out with grease and two different arrangements of washers to assess how providing clearer propagation paths to the sensors would improve location performance. This is in continuation of the work carried out in Section 4.2.

- A washer separating a single corner of the build plate from the heater plate
- Washers separating all four corners of the build plate from the heater plate
- A layer of grease between the build plate and heater plate

For each these tests the same 10mm titanium plate was used, with a 200x200mm grid drawn upon it with a 20mm grid spacing, centred about the centre of the plate. This is shown in Figure 67. At each point between five and ten Hsu-Nielsen sources were generated for the production of the delta-T grid. When locating signals with delta-T, a cluster size of 20mm was used, equal to the grid size (Al-Jumaili, et al., 2016). At nine off grid locations, five Hsu-Nielsen sources were generated to assess delta-T accuracy. All delta-T grids and source locations had the onset calculated via the AIC method, detailed in Section 2.5.4. These tests were carried out before the waveguide design was changed, detailed in Section 4.2, and these results show that this had a positive impact on location performance.

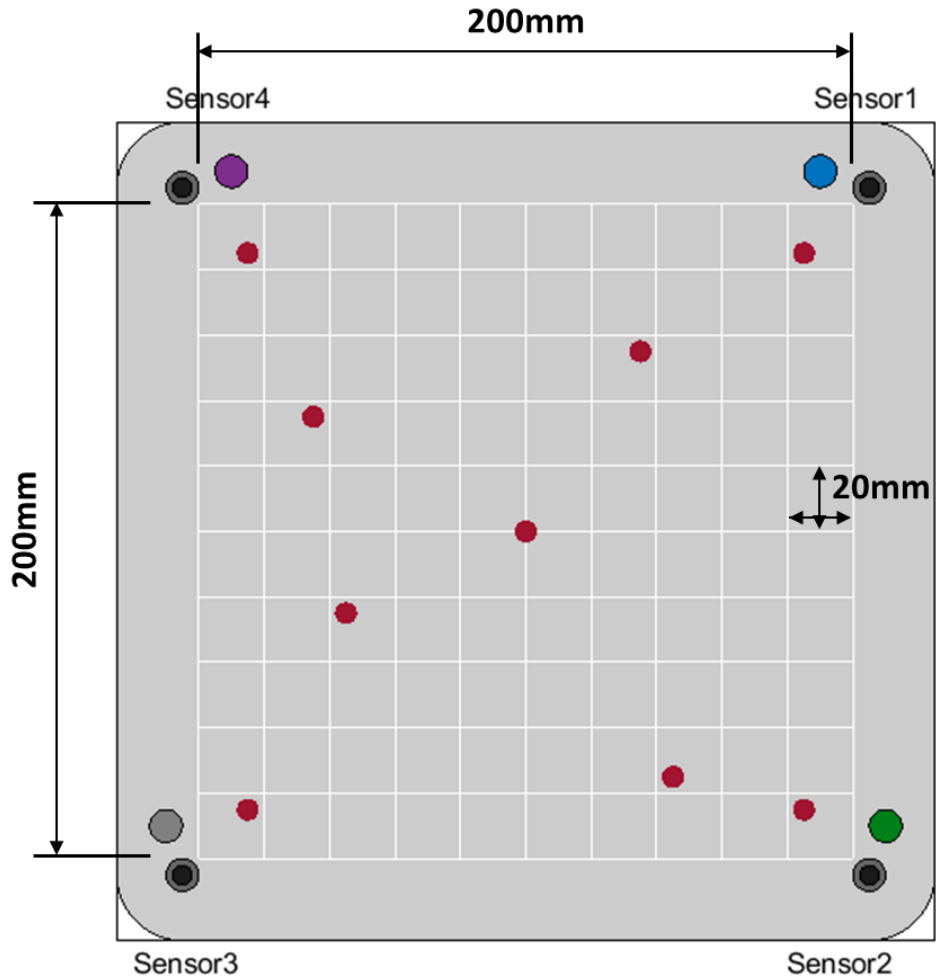


Figure 67. Grid used and with the locations used to collect sample data marked in maroon

5.2.2. Results

Delta-T grids were collected for each configuration in order to show how grids are altered by poor plate fixing as well as showing how location accuracy is affected. Figure 68 shows the baseline delta-T location for when the build plate is fully secured to the heater plate. Although the average error from Table 1 is only 16mm for this configuration, which is a good result, as it is smaller than the grid spacing, some large errors arise. This is especially true in the centre where there are numerous paths to the sensor.

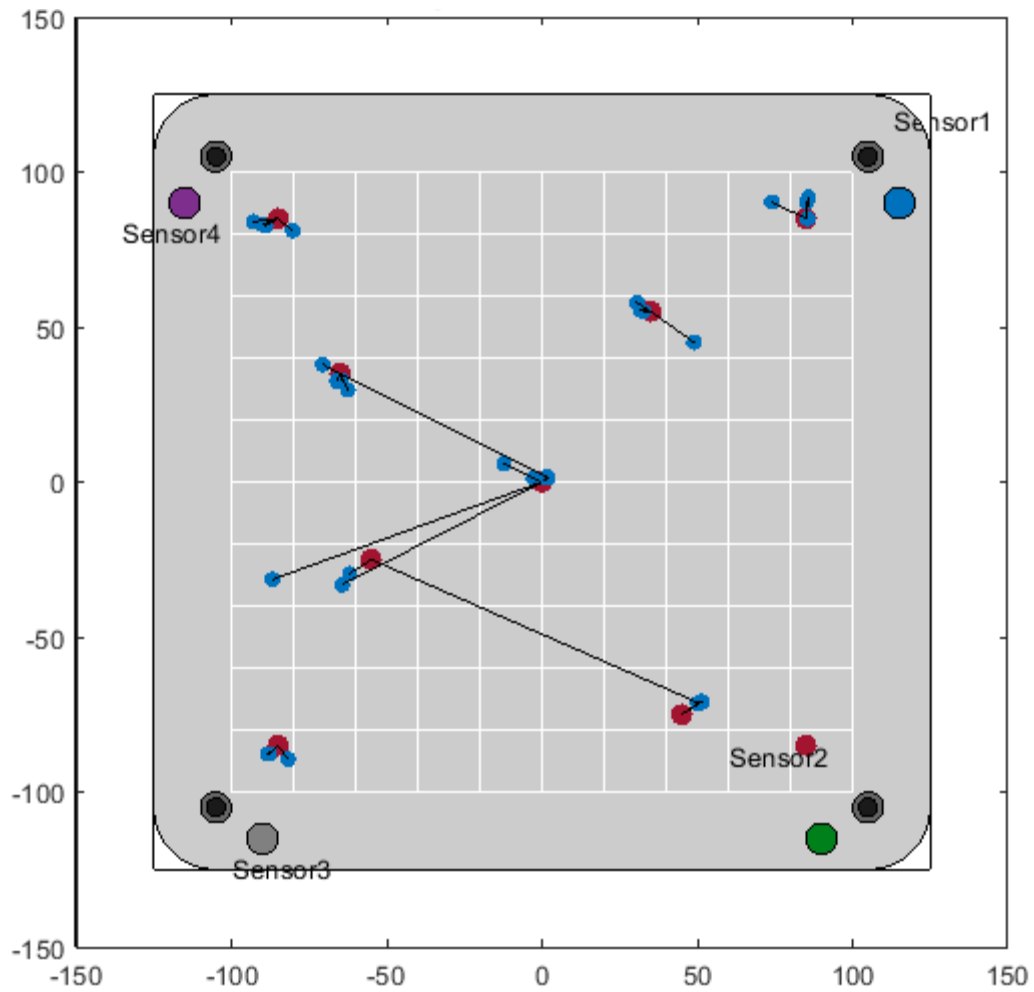


Figure 68. Delta-T results when all bolts are tightened. Red being the actual source location and blue being the located signal. The black lines indicate the distance from the actual source

Figure 69 to Figure 72 present the delta-T location results when one, two, three and all four bolts are loosened. This shows how even with just two bolts not secured, the delta-T becomes unusable for locating signals accurately away from the edges.

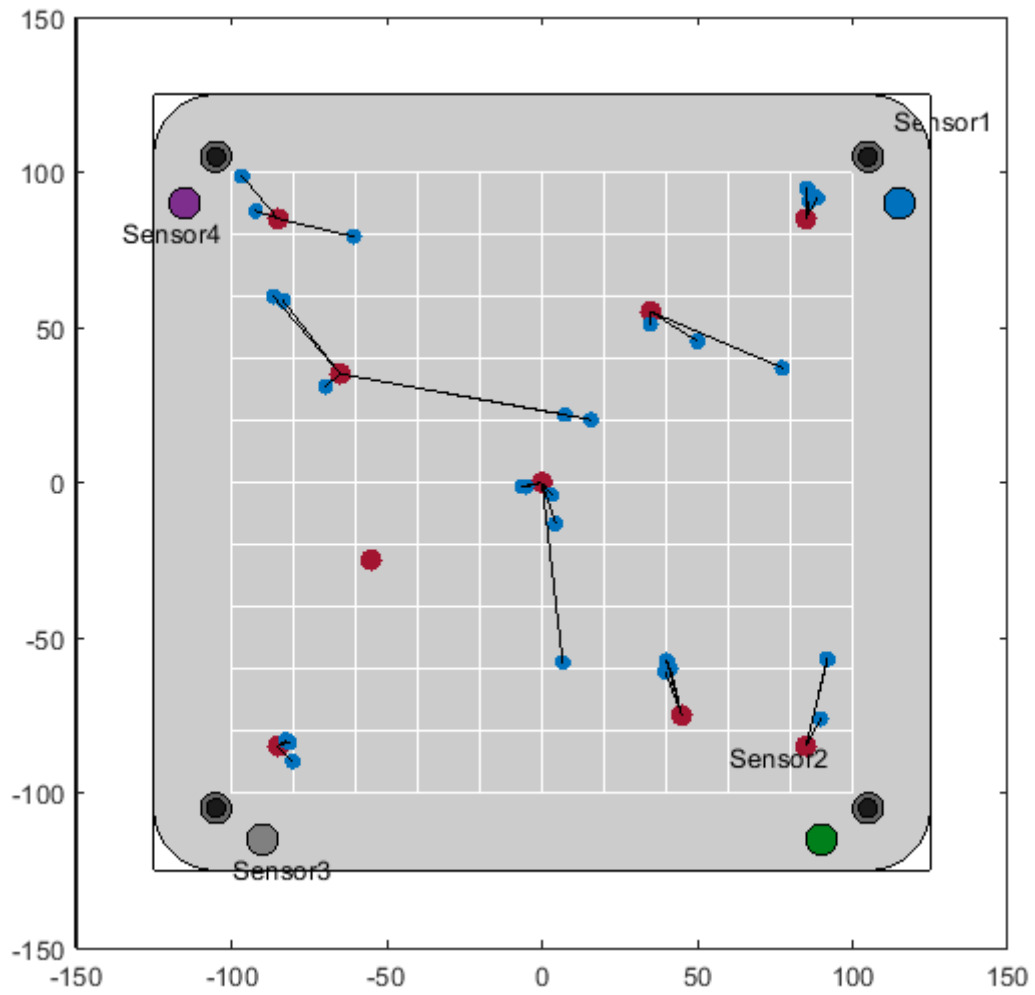


Figure 69. Delta-T results when one bolt is loosened. Red being the actual source location and blue being the located signal. The black lines indicate the distance from the actual source

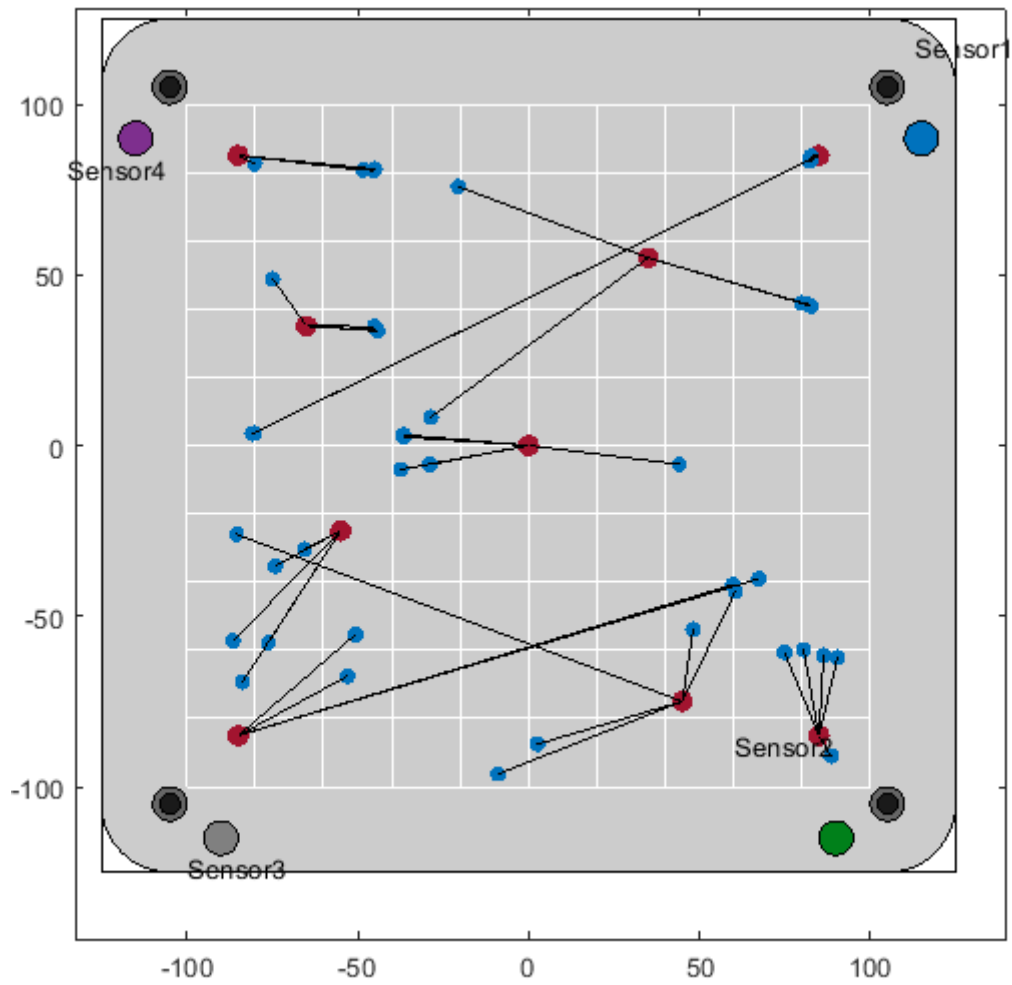


Figure 70. Delta-T results when two bolts are loosened. Red being the actual source location and blue being the located signal. The black lines indicate the distance from the actual source

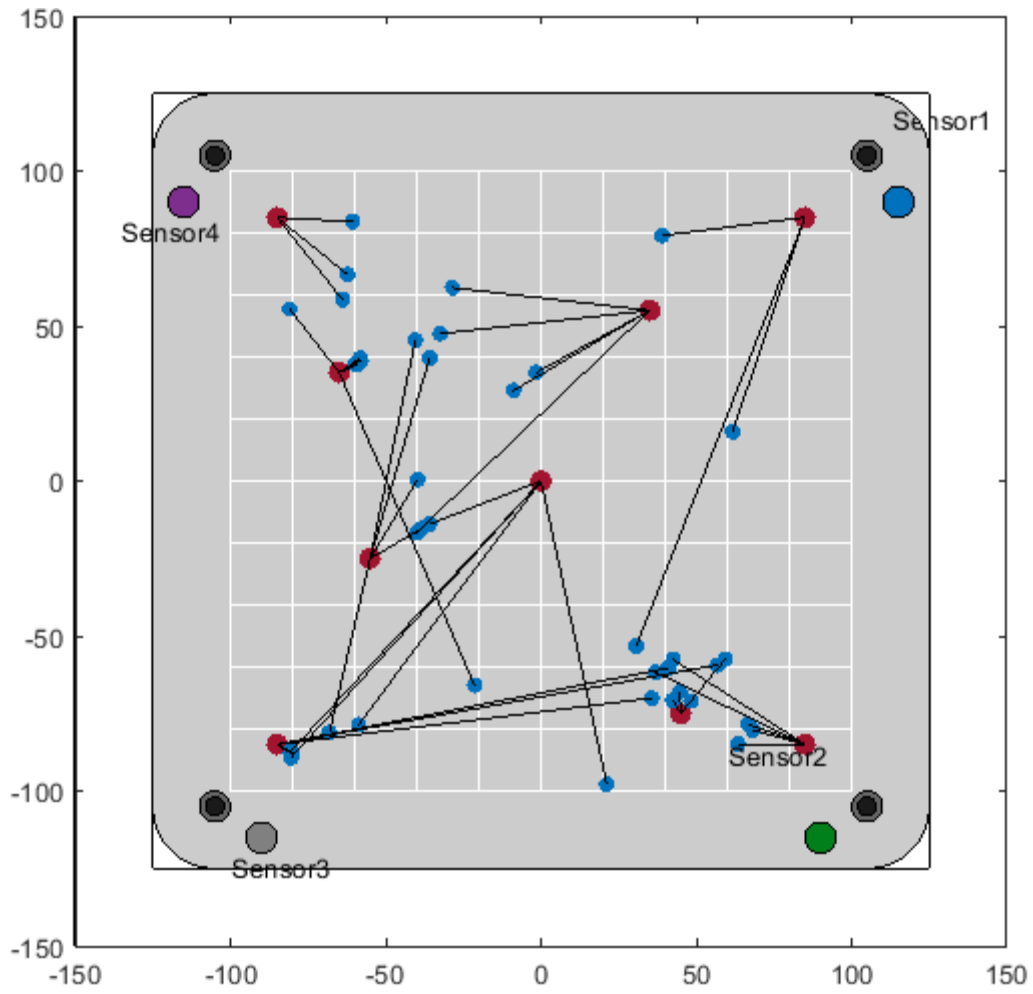


Figure 71. Delta-T results when three bolts are loosened. Red being the actual source location and blue being the located signal. The black lines indicate the distance from the actual source

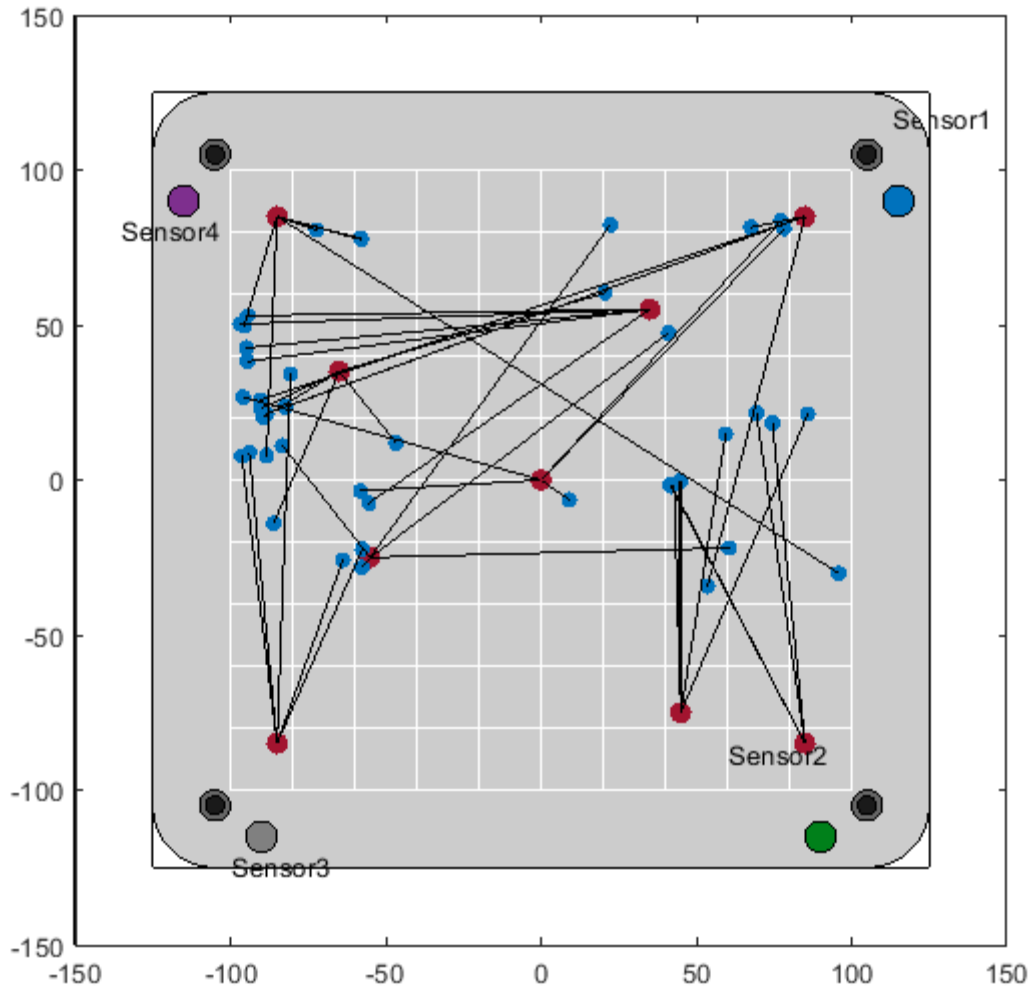


Figure 72. Delta-T results when all bolts are loosened. Red being the actual source location and blue being the located signal. The black lines indicate the distance from the actual source

In Figure 73 a single corner has been spaced on a 1mm washer above sensor 4. This has resulted in far higher accuracy at this corner, likely as a result of the better defined path for the signal to travel in this corner. This is because there is now a space between build and heater plate so the signal has to travel across the plate and into the waveguide and hence sensor. Figure 74 presents the results of separating the build plate from the heater plate at all four corners. Although Table 1 shows that the average error is larger than when the build plate is fastened directly to the

heater plate, there are fewer large errors from central locations and a higher proportion of events are successfully located.

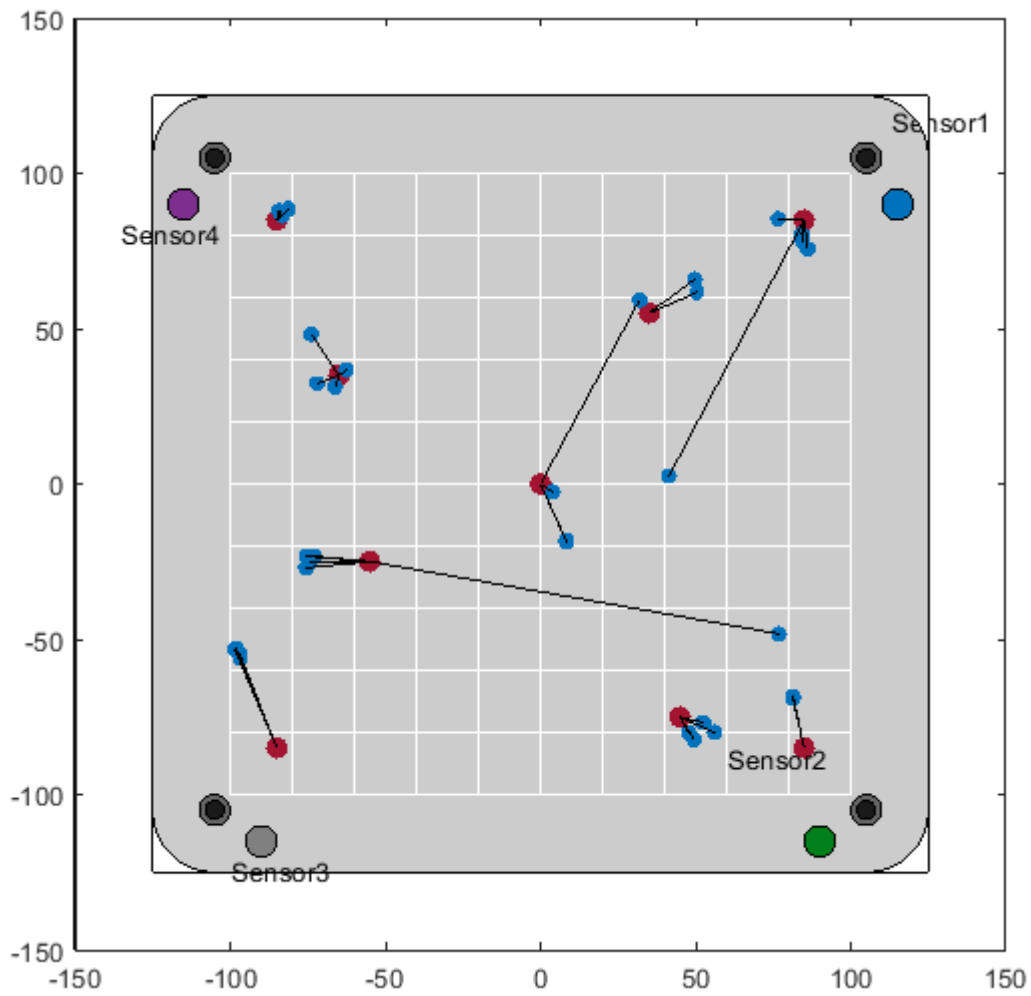


Figure 73. Delta-T results when one corner is spaced on a 1mm washer. Red being the actual source location and blue being the located signal. The black lines indicate the distance from the actual source

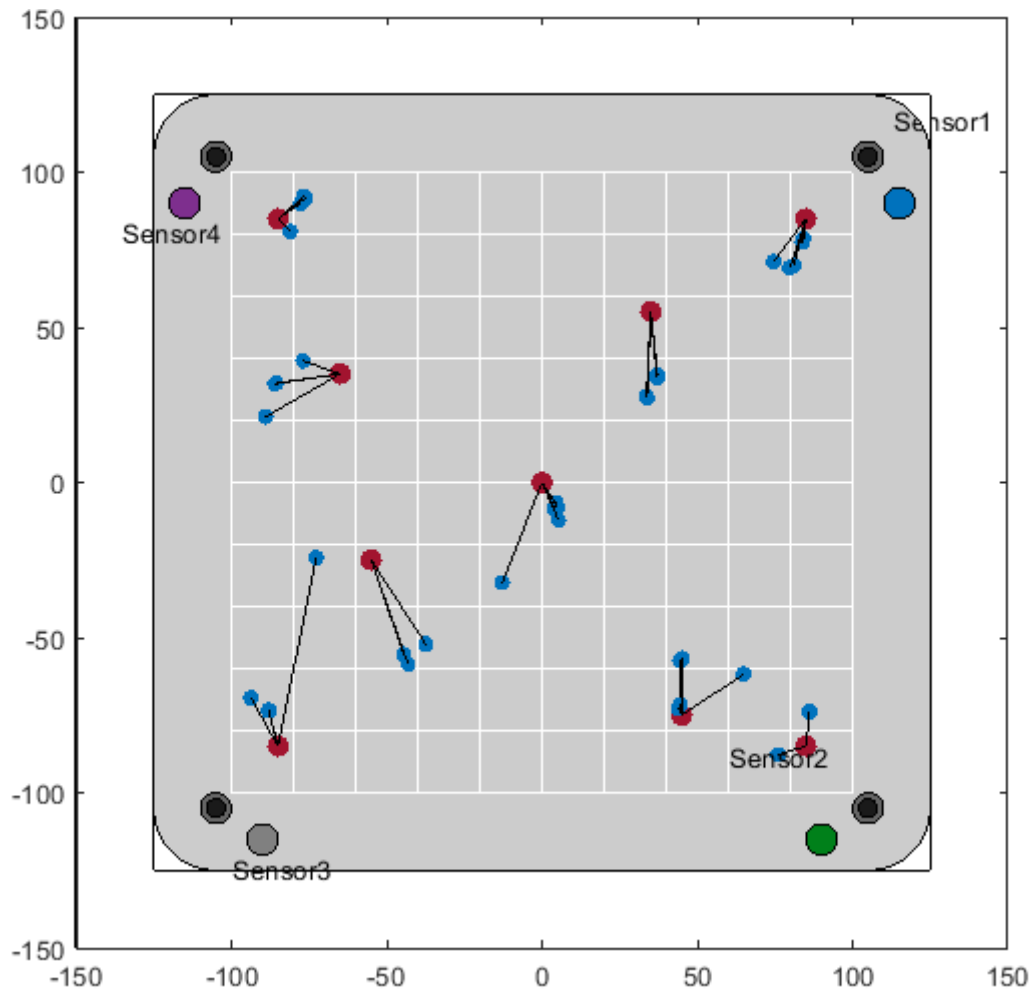


Figure 74. Delta-T results when each corner is spaced on 1mm washers. Red being the actual source location and blue being the located signal. The black lines indicate the distance from the actual source

Figure 75 shows signals located via delta-T with silicon grease between the plates. This effectively fills the gaps between the plates and allows signals to travel directly down to the heater plate and across to the waveguides. Table 1 shows that the error is far lower than without the grease, however a lower proportion of events are located. This suggests that there is still wide variation between signals that is causing many to be filtered out.

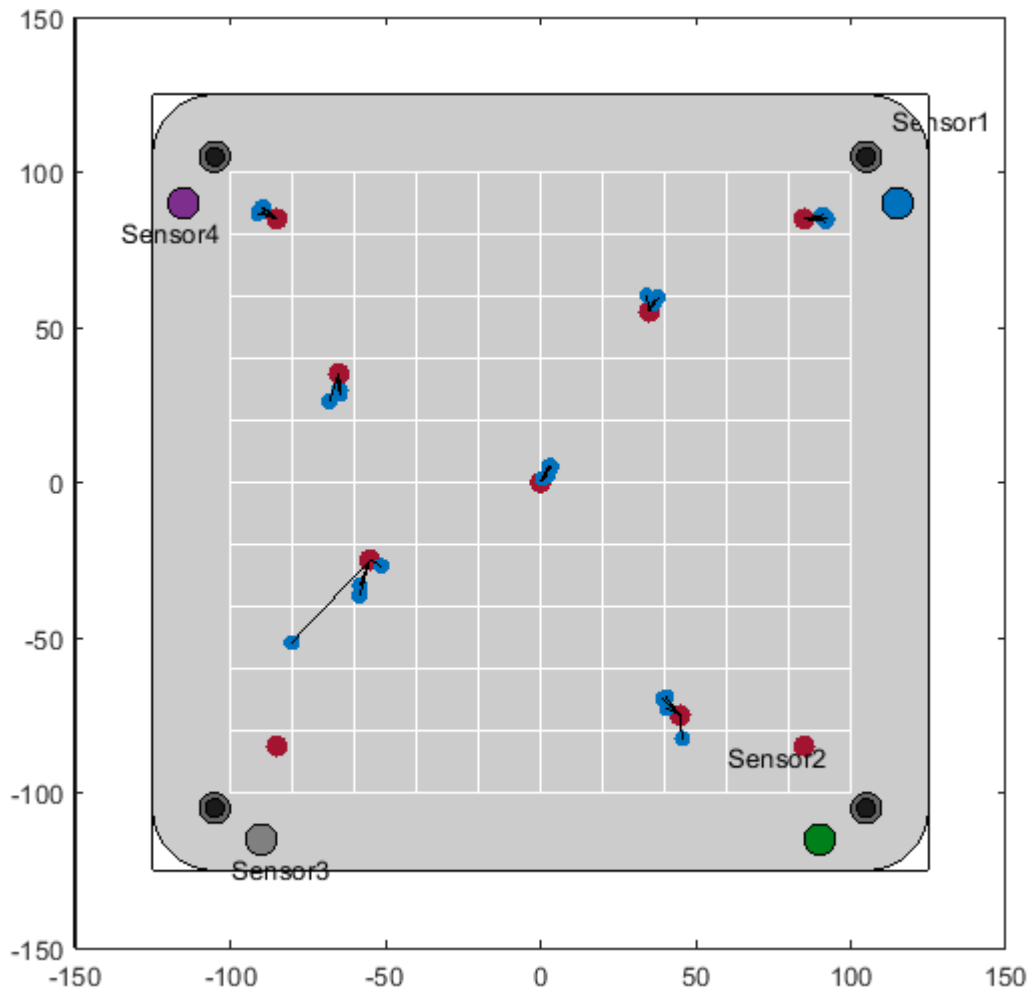


Figure 75. Delta-T results when there is grease between the plates. Red being the actual source location and blue being the located signal. The black lines indicate the distance from the actual source

These results corroborated the findings of analysing signals propagating into the heater plate. If the signal has multiple paths to the sensors, each sensor may be triggered by the signal taking inconsistent paths. This is most pronounced for signals near the centre of the plate which have to travel further to reach any sensor. When the plate is spaced on washers, delta-T locates a higher proportion of signals with similar average error to when it is directly secured to the heater plate. However, it also gives a smaller range of errors than when all bolts are secured directly, with significantly smaller errors at the centre. This is reflected by the much smaller

standard deviation recorded among these locations, with a standard deviation of just 5.8mm when there is grease between the plates and 11.5mm when the build plate is spaced on washers at each corner. This is far lower than the standard deviation of 28.8mm when the build plate is secured directly to the heater plate.

Table 1 provides a summary of the results.

Table 1. Table of average error for each configuration and the standard deviation of events located using delta-T

Configuration	Average Error using delta-T/mm	Average Error using TOA /mm	Standard deviation using delta-T /mm	Standard deviation using TOA /mm
All bolts fully tightened	15.97	51.3	28.8	54.2
1 bolt loosened	21.15	108.7	19.7	83.5
2 bolts loosened	54.60	142.3	52.2	93.2
3 bolts loosened	51.40	161.8	43.5	85.6
4 bolts loosened	88.03	77.6	49.4	64.2
1 bolt spaced	20.46	60.8	25.5	70.8
Whole plate spaced	17.76	73.4	11.5	56.4
Grease between plates	7.35	42.3	5.8	59.1

These signals were also located using the TOA method to assess whether this method copes better with the plate not being fully secured. A longitudinal velocity of 6070ms^{-1} in titanium was used (Engineering Toolbox. 2021). Average errors were found to be very large, with a very large standard deviation. With the fully bolted, spaced and greased configurations this is reflected by some events being well located whilst others are not. This suggests that the TOA method is not always a reliable method of locating events in the build plate, perhaps because of the complex geometry of the build plate assembly.

Figure 76 through to Figure 80 present the TOA results when all bolts are fully tightened through to when all four are loose. TOA gives far worse results in each of these configurations, and frequently fails to locate signals entirely.

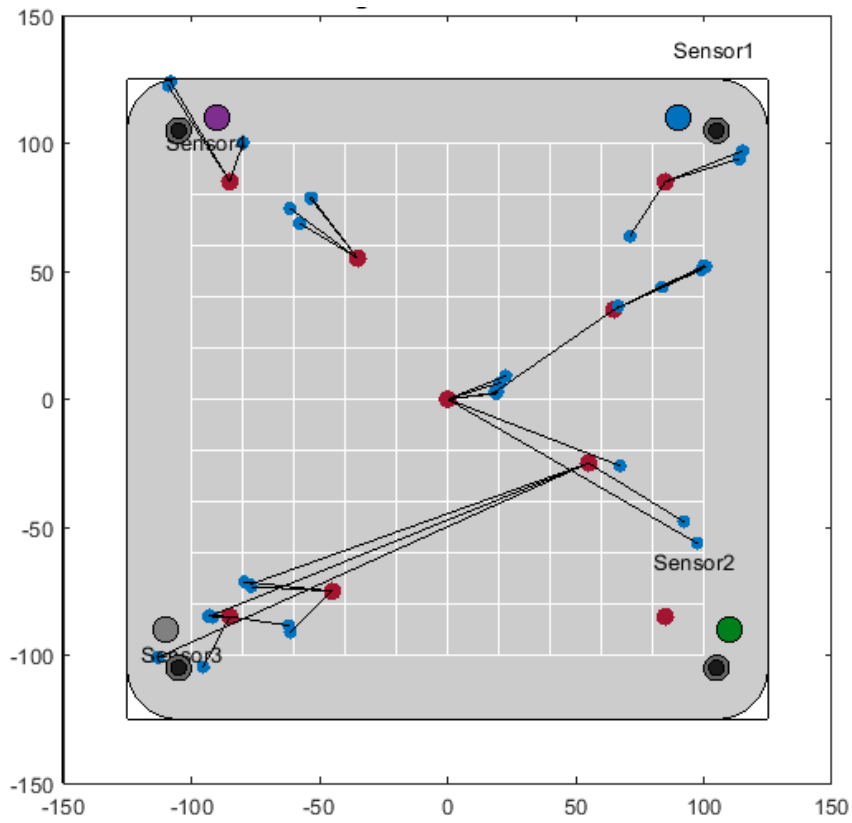


Figure 76. Time of Arrival results when all bolts are fully secured. Red being the actual source location and blue being the located signal. The black lines indicate the distance from the actual source

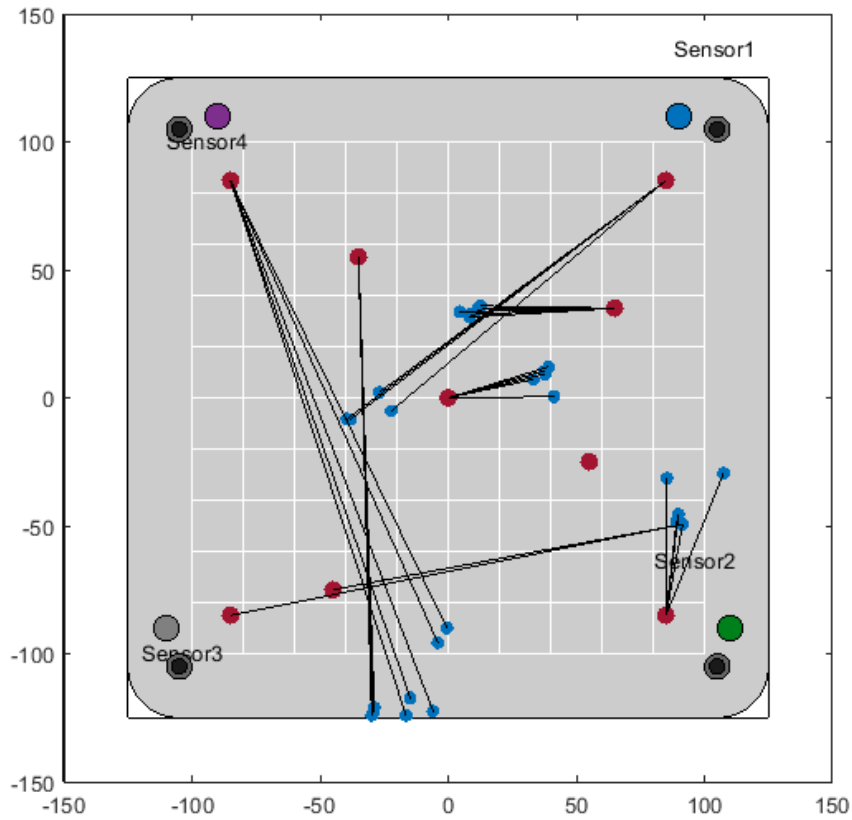


Figure 77. Time of arrival results with one bolt loose. Red being the actual source location and blue being the located signal. The black lines indicate the distance from the actual source

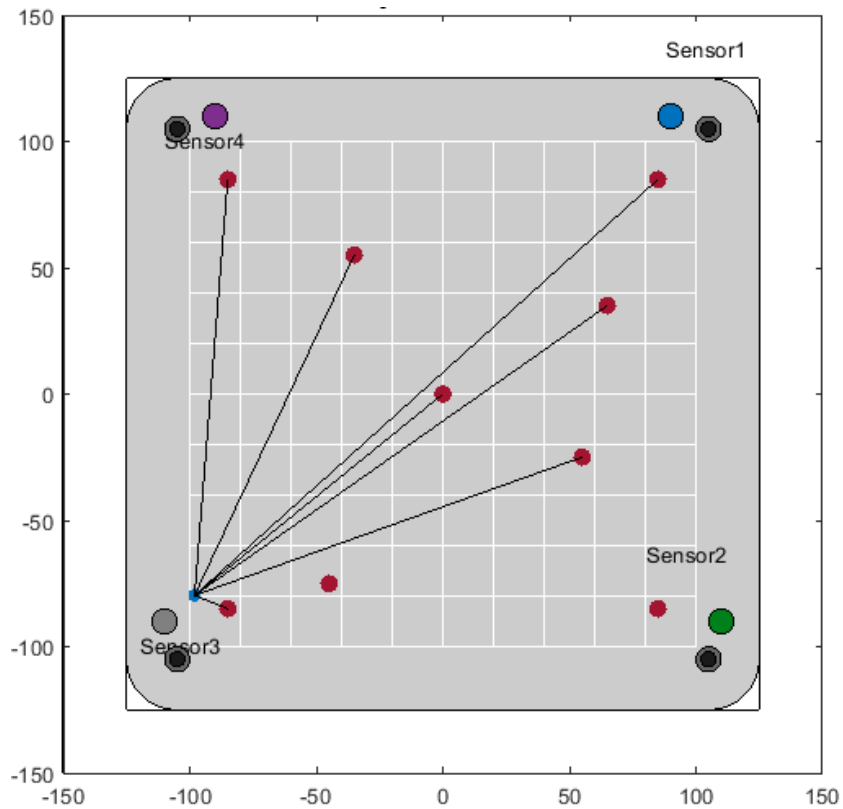


Figure 78. Time of arrival results with two bolts loose. Red being the actual source location and blue being the located signal. The black lines indicate the distance from the actual source

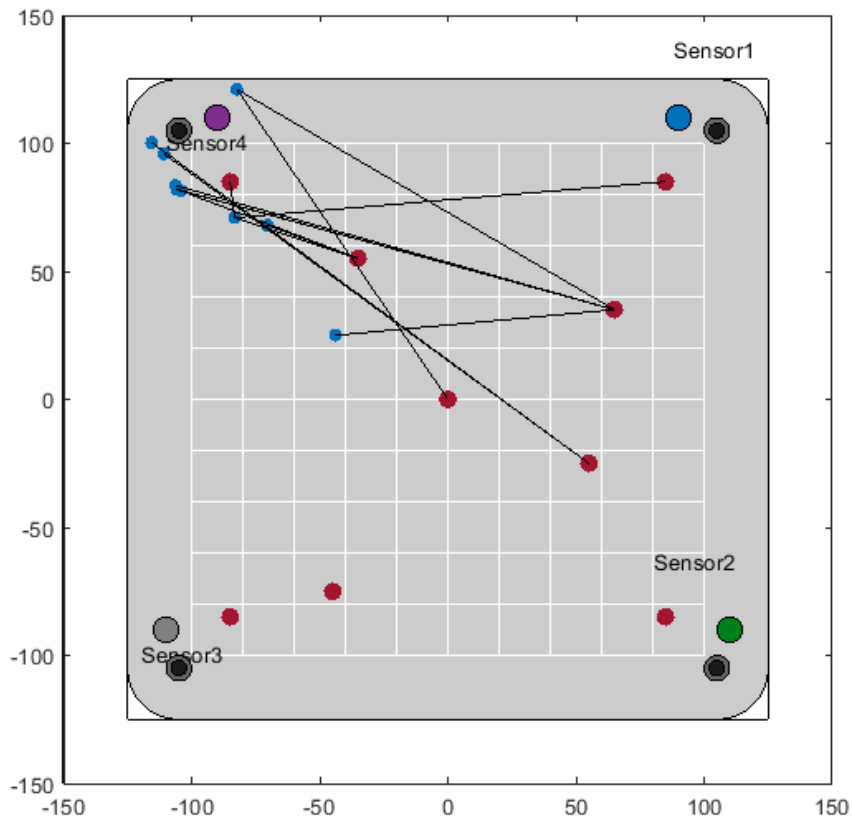


Figure 79. Time of arrival results with three bolts loose. Red being the actual source location and blue being the located signal. The black lines indicate the distance from the actual source

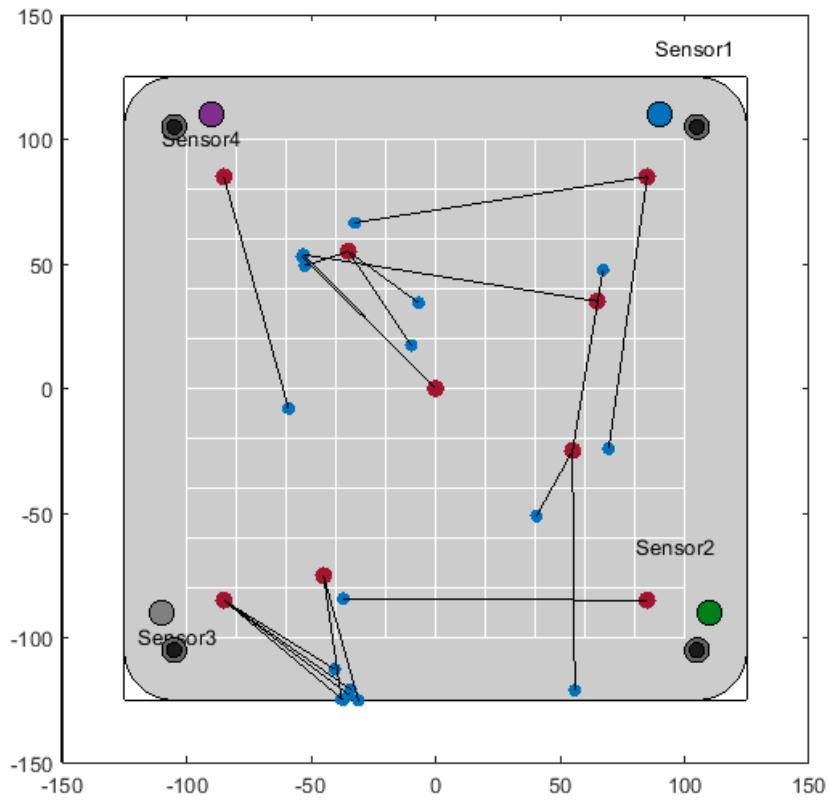


Figure 80. Time of arrival results when all four bolts are loose. Red being the actual source location and blue being the located signal. The black lines indicate the distance from the actual source

Figure 81 and Figure 82 show the results when using TOA when the plate is spaced on one corner, and when the entire build plate is spaced from the build plate. Using delta-T fully spacing the plate provided high accuracy location, which is in contrast to the TOA results presented here. This is likely due to the transition from the build plate to the washer then the heater plate leading to a lower average velocity than if the signal travels directly into the heater plate.

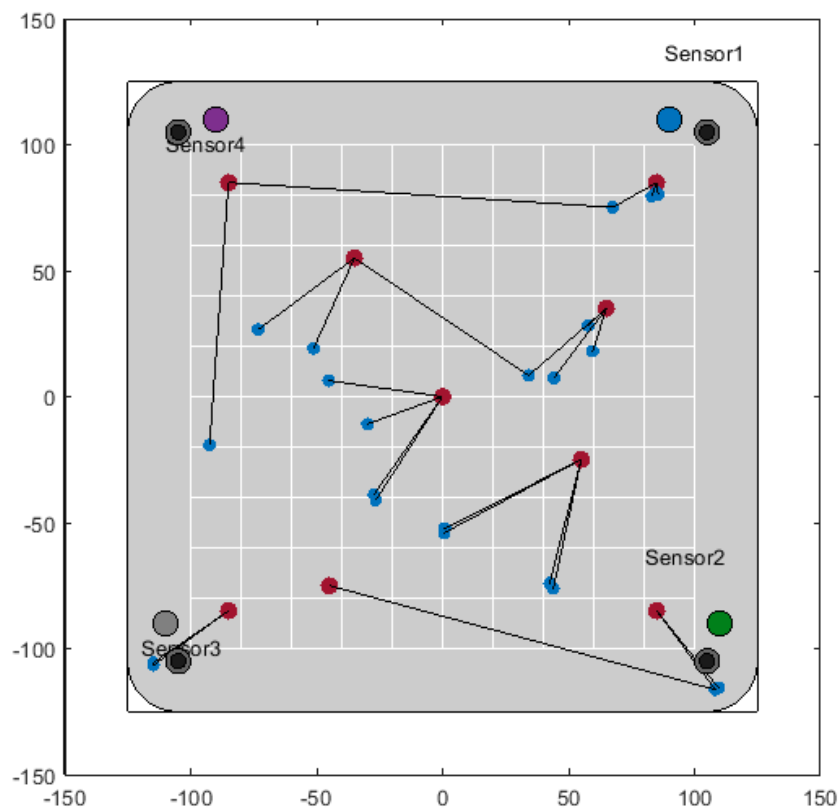


Figure 81. Time of arrival results when one corner is spaced on a 1mm washer. Red being the actual source location and blue being the located signal. The black lines indicate the distance from the actual source

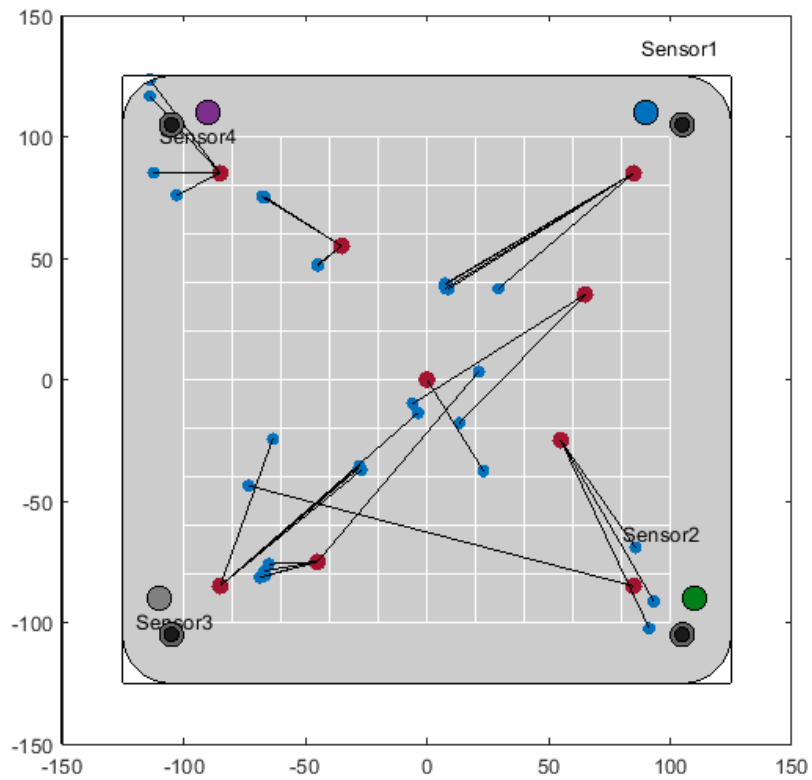


Figure 82. Time of arrival results when the entire plate is spaced on washers. Red being the actual source location and blue being the located signal. The black lines indicate the distance from the actual source

Figure 83 shows TOA results when grease is separating the plates. Once again, this provides less accurate results than delta-T, as the wave velocity through the grease will be different than through the plates and waveguides.

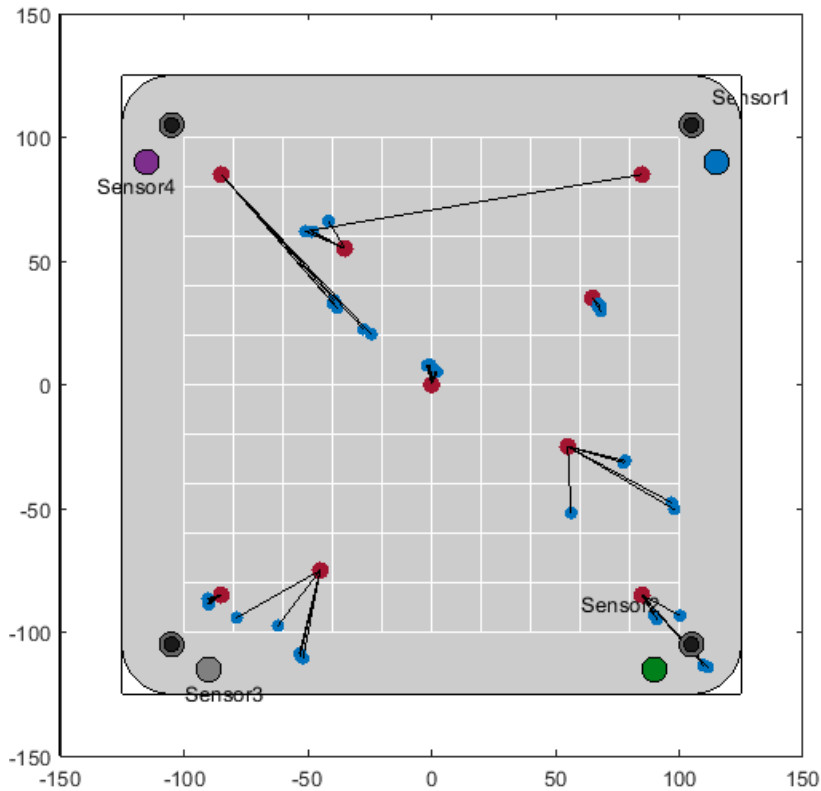


Figure 83. Time of arrival results with grease separating the plates. Red being the actual source location and blue being the located signal. The black lines indicate the distance from the actual source

5.2.3. Discussion

These results show that the delta-T method can be effectively used to locate signals in the Renishaw AM500 build plate, providing the build plate is a uniform tightness all around. However, the results of spacing the build plate on washers shows that this can be improved by providing a clearer signal path.

The delta-T results were far more accurate than those for the TOA method. This shows the strength of the delta-T method when dealing with complex geometries. The lack of accuracy of the TOA results also suggests that the longitudinal velocity selected was not optimal, perhaps due to the mix of materials that the signal travels through towards the sensor. The heater plate and waveguides are made of steel in contrast to the titanium build plate. The optimum wave velocity for TOA will be further explored in the following section.

5.3. Effect of Plate Thickness

5.3.1. Experimental Procedures

In the Renishaw AM500, for each print that is done the build plate is removed from the machine and skimmed to remove material fused to it. This means that the thickness of the plate and the path to the sensors will be slightly different each time. Over the lifetime of the build plate this leads to a radical reduction in thickness and would mean that a new delta-T map is required each time. Unfortunately, producing a delta-T map is a time intensive task which it isn't necessarily viable to do for every single print. However, TOA may not be suitable either, as despite its shorter processing time, dispersion characteristics change with plate thickness, effecting wave velocity in the plate. Therefore, a modified version of TOA was developed that used the dispersion curves of that material to compensate for the changing thickness of the plate.

The process is as follows:

- Load dispersion curves of **group velocity** against **frequency-thickness**
- Divide by the buildplate **thickness** to give **group velocity** against **frequency**
- Decide which wave mode (S_0 , A_0 etc) to use to select the velocity
- Use a Fourier transform to select the dominant frequency from the signal being analysed
- Interpolate from the graph the velocity corresponding to that frequency along the chosen dispersion curve, as shown in Figure 84

- Use traditional time of arrival using the selected velocity to predict a source location

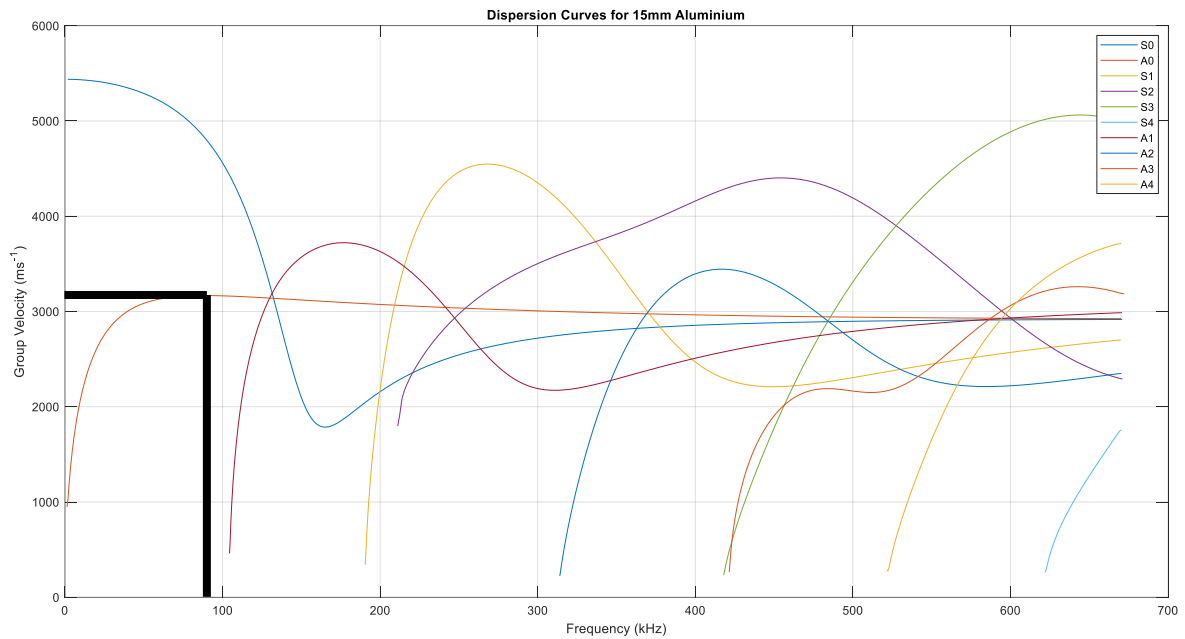


Figure 84. Selecting a wave velocity from the dispersion curve at a particular frequency

To establish a relationship between ΔT and thickness and investigate dispersion-based TOA, a series of plates of different thicknesses were acquired. Due to availability, plates of thicknesses 3, 6, 8, 10, 12 and 15mm were selected, with 5mm holes drilled to match waveguide placement on a build plate. These are shown in Figure 85.

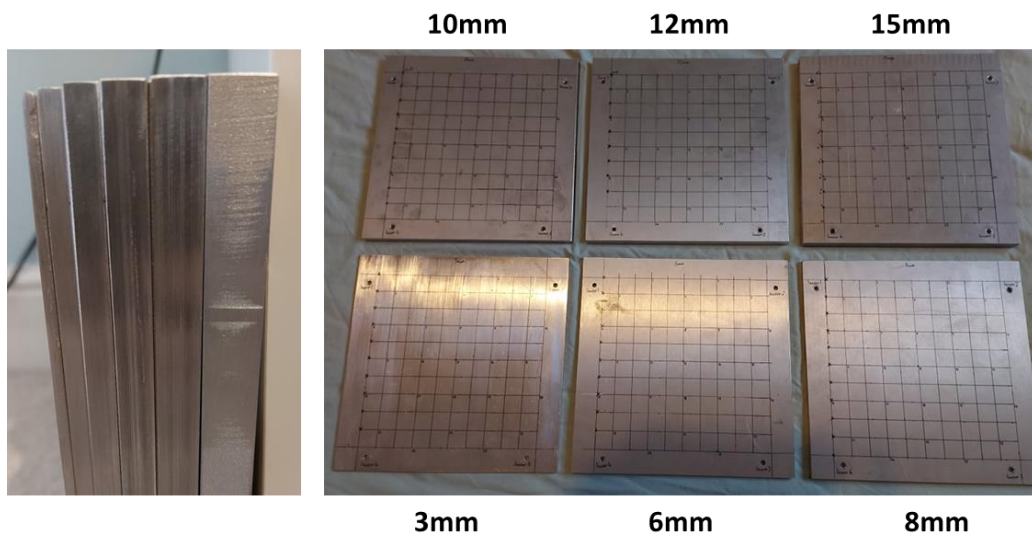


Figure 85. The six different thickness plates used

Although plate thicknesses in the build process would not go below 10mm it was important to establish extremes of size to establish meaningful relationships. Grids of 200x200mm and 20mm spacing were then drawn on the plates. Training data was collected from every node on this grid, and 25 locations were chosen across the grid to collect sample sources, as shown in Figure 86. Hsu-Nielsen sources were used across the entire grid for each plate to create the delta-T maps, and ten sources were generated at each of the marked points to collect sample data. Each of these was also located using TOA and the dispersion-adjusted TOA method outlined above.

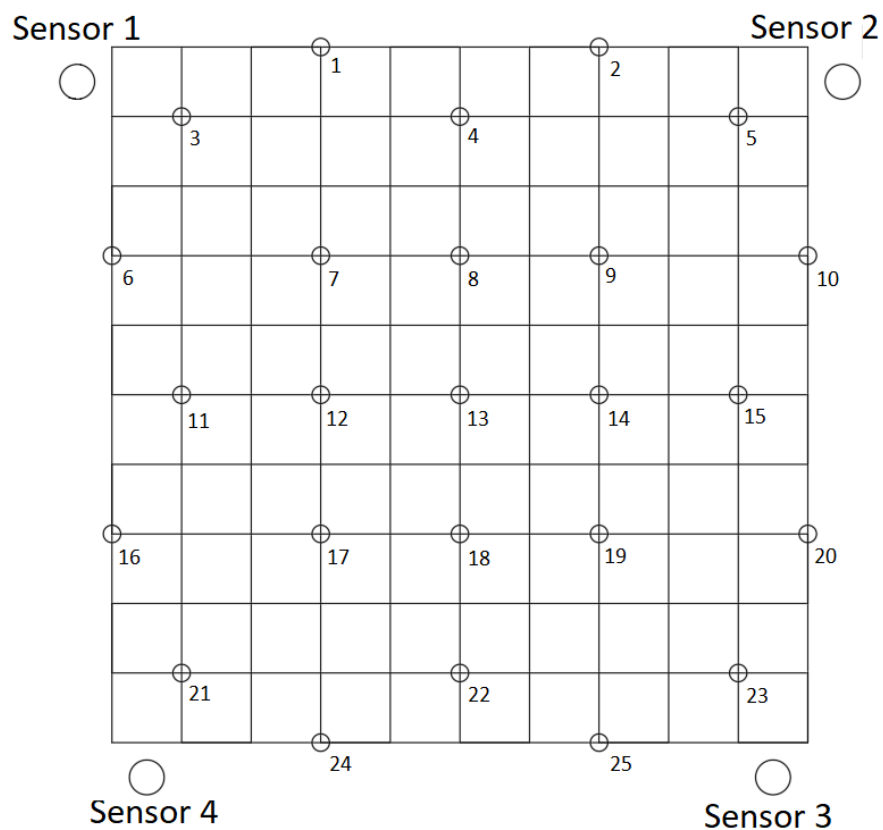


Figure 86. The grid drawn on the plates and positions of sample locations

These were chosen to compare how accurately signals can be located on the edges and nearer the centre. Sensors were bonded to the waveguides and used in the same positions for each plate, with washers used to ensure bolts were secured to

the same depth in the plate for each plate. A torque wrench was used to ensure all bolts were at the same tightness of 4Nm. The onset of the signal was selected when locating sources and creating delta-T grids using the AIC method detailed in Section 2.5.4. Waveguides were secured directly to the build plate to reflect design changes carried out following the results of Section 4.2 and Section 5.2, which determined that having AE signals travel through the heater plate before reaching the waveguide was having an adverse effect on location and propagation.

5.3.2. Results

When locating signals using the TOA method, the greatest challenge is in selecting an appropriate wave velocity. This will usually be the longitudinal velocity or shear velocity, which are independent of frequency and material thickness unlike the S_0 and A_0 modes. In aluminium, these will be 6000m/s and 3040m/s respectively (Engineering Toolbox, 2004). In Figure 87, the figure on the right shows signals located using the longitudinal velocity, and the figure on the left shows signals located using the shear velocity through 12mm aluminium.

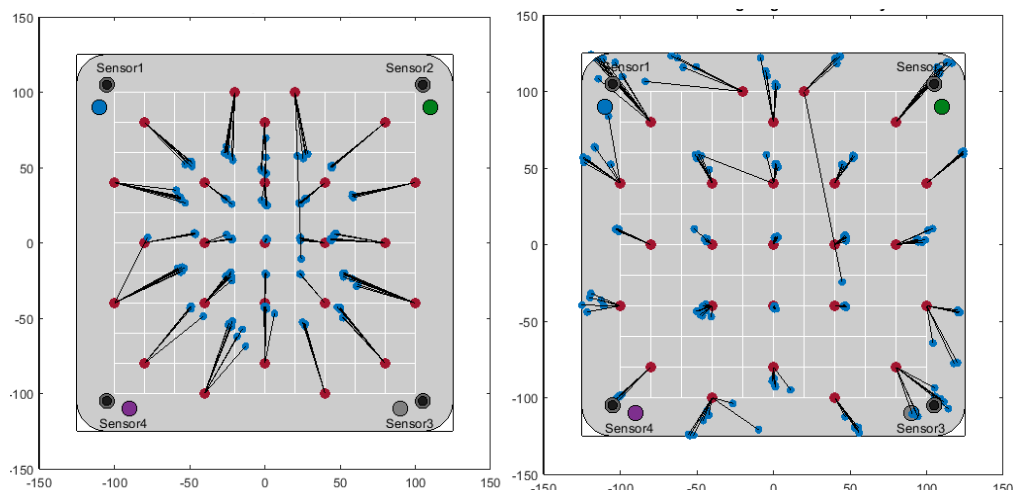


Figure 87. Time of arrival results on a 12mm plate using the shear velocity (left) and longitudinal velocity (right). Red being the actual source location and blue being the located signal. The black lines indicate the distance from the actual source

Table 2 shows the average error for each thickness when using the shear and longitudinal velocity for aluminium.

Table 2. A table of average error for a range of different thickness plates using the shear and longitudinal velocities

Plate Thickness /mm	Shear Velocity Average Error /mm	Longitudinal Velocity Average Error /mm
3	31.3	22.4
6	30.6	18.8
8	29.8	21.0
10	24.4	18.3
12	21.0	29.2

Using the shear velocity leads to locations drifting towards the centre, and the longitudinal velocity gives results towards the edge, so the optimum speed must be somewhere between. This may be due to the transition to and propagation of the signal down the waveguide.

A Matlab script was developed to use the TOA method to locate signals from each of the sources shown in Figure 86, and compute the average accuracy from a range of speeds from 3000 to 6000m/s at an interval of 100m/s. A graph of speed against average error is shown below in Figure 88.

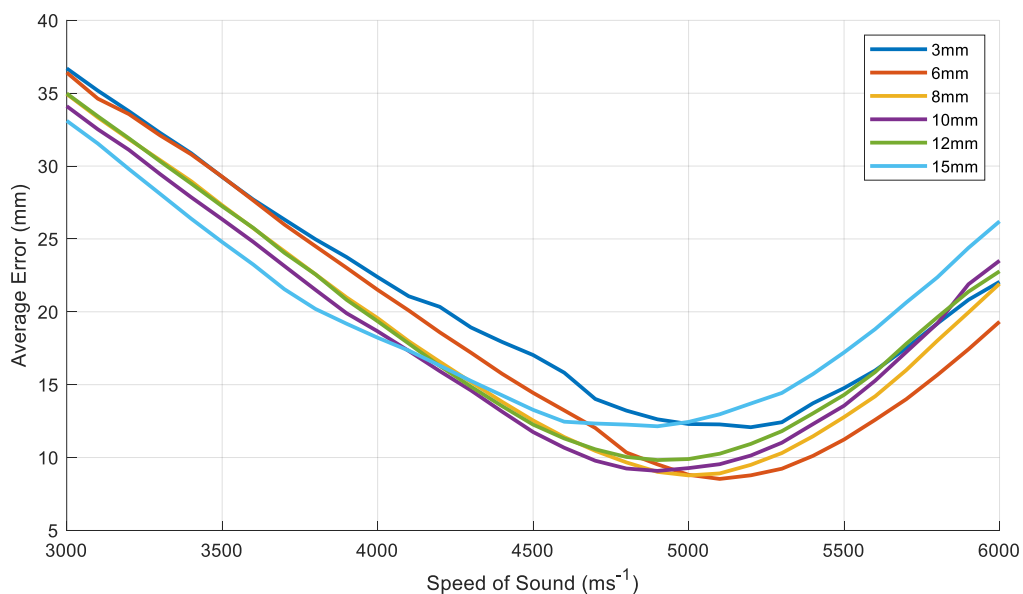


Figure 88. Graph of Average Error against speed of sound for each plate thickness

The minimum points of each of these graphs marks where the average error is lowest for each plate thickness. Table 3 below shows speed that gives the minimum error for each plate thickness. These are derived from the turning points of the lines plotted in Figure 88. It can be seen that the optimum speed reduces as the thickness increases. This is in line with dispersion curves, where frequency components the fastest S_0 mode will travel slower as the plate becomes thicker.

Table 3. Optimum wave velocity for each thickness of plate

Thickness (mm)	Optimum Speed (m/s)
3	5200
6	5100
8	5000
10	4900
12	4900
15	4900

Having shown that the optimum speed to locate signals does change with plate thickness, the effectiveness of dispersion-adjusted TOA location can now be tested. Figure 89 to Figure 93 show the located signals for plate thicknesses 3 to 15mm, with S_0 on the left and A_0 on the right.

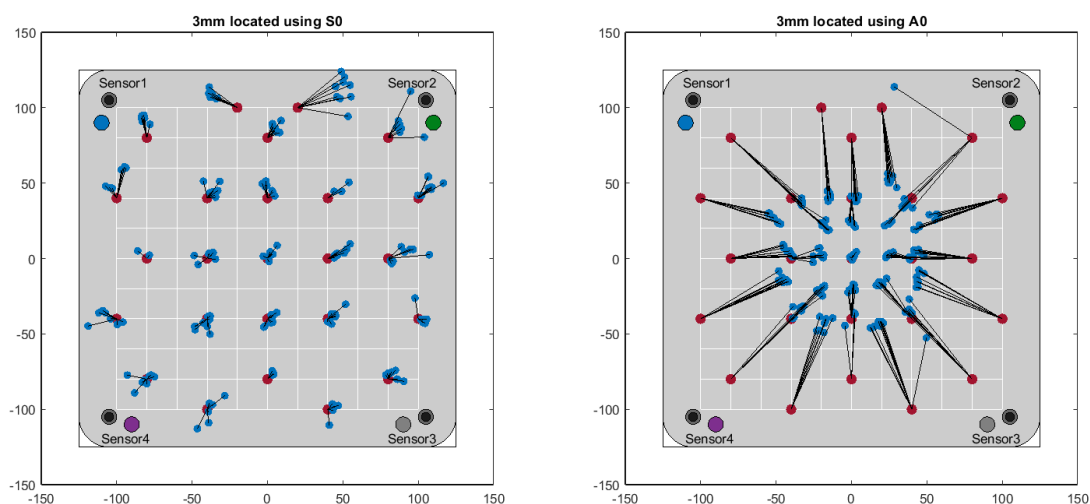


Figure 89. Signals located in the 3mm plate using the S_0 mode (left) and the A_0 mode (right). Red being the actual source location and blue being the located signal. The black lines indicate the distance from the actual source

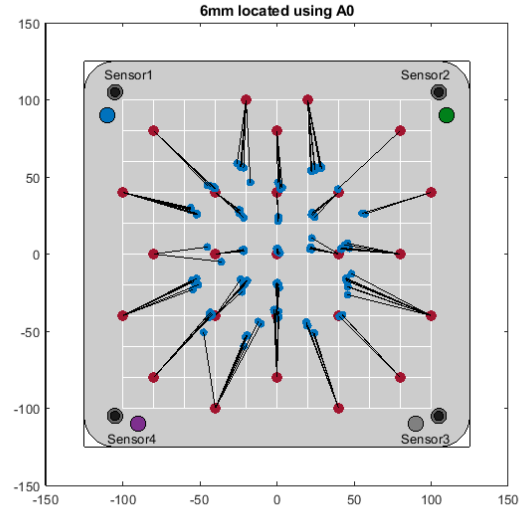
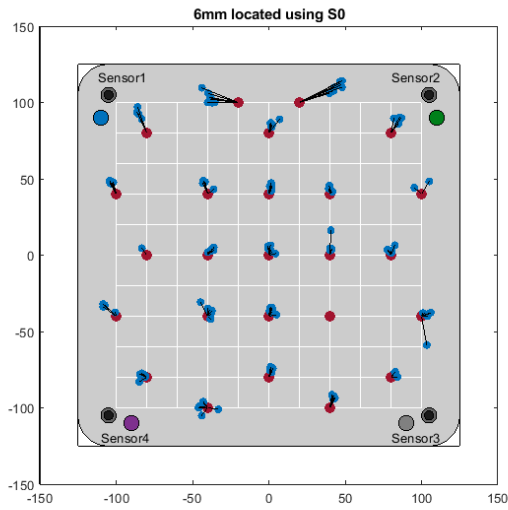


Figure 90. Signals located in the 6mm plate using the S0 mode (left) and the A0 mode (right). Red being the actual source location and blue being the located signal. The black lines indicate the distance from the actual source

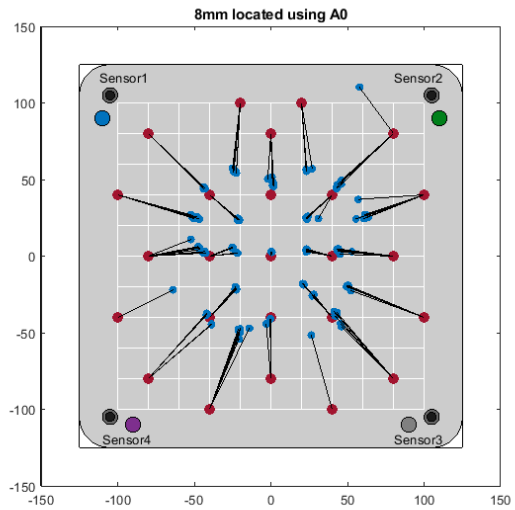
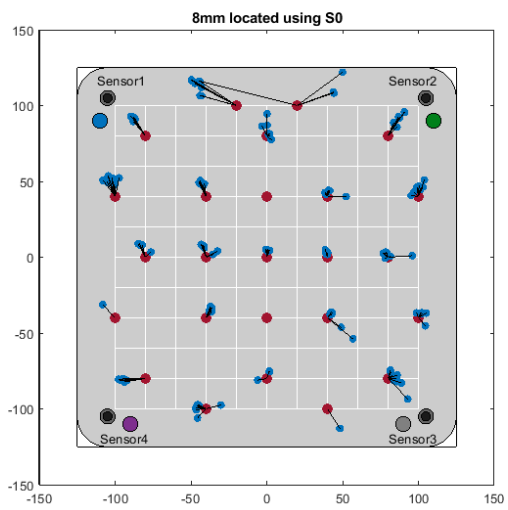


Figure 91. Signals located in the 8mm plate using the S0 mode (left) and the A0 mode (right). Red being the actual source location and blue being the located signal. The black lines indicate the distance from the actual source

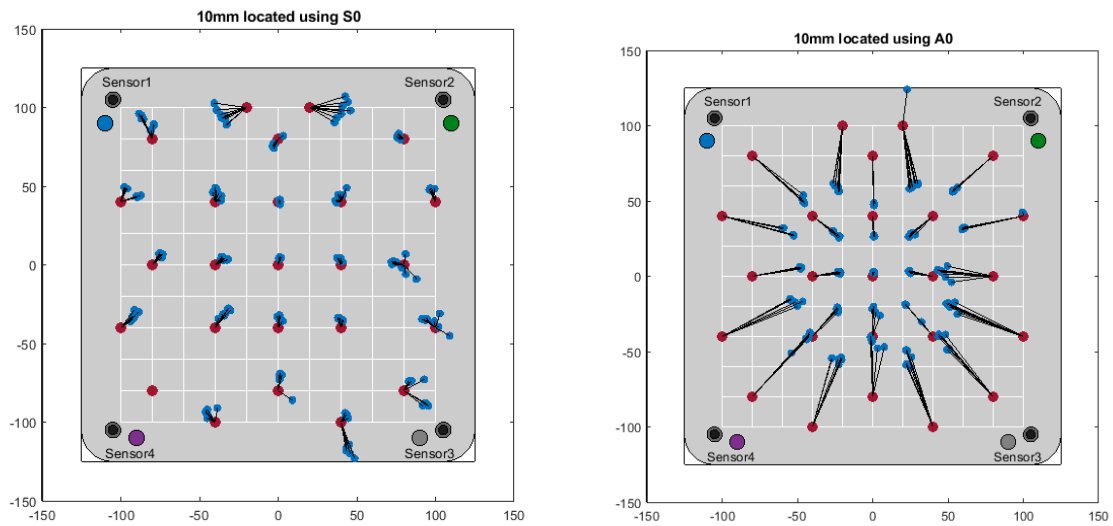


Figure 92. Signals located in the 10mm plate using the S0 mode (left) and the A0 mode (right). Red being the actual source location and blue being the located signal. The black lines indicate the distance from the actual source

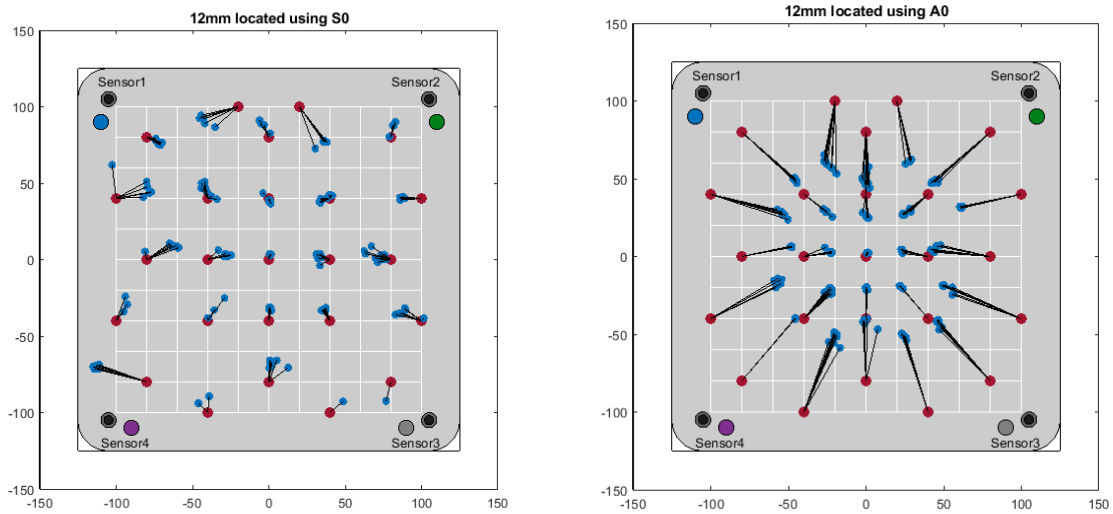


Figure 93. Signals located in the 12mm plate using the S0 mode (left) and the A0 mode (right). Red being the actual source location and blue being the located signal. The black lines indicate the distance from the actual source

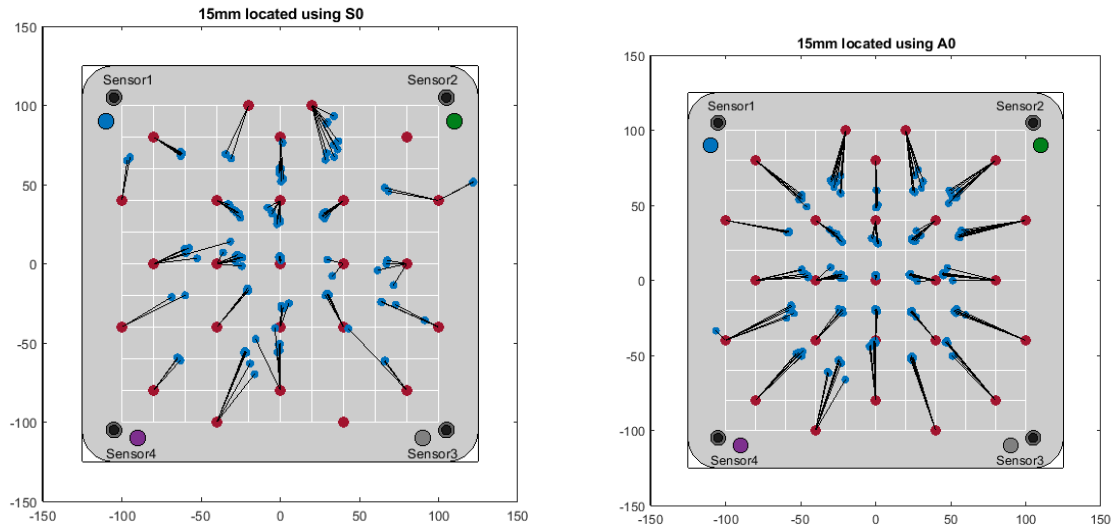


Figure 94. Signals located in the 15mm plate using the S_0 mode (left) and the A_0 mode (right). Red being the actual source location and blue being the located signal. The black lines indicate the distance from the actual source

It can be seen that this method presents more accurate results than using the Longitudinal or shear velocities, especially when using the S_0 curve. Table 4 shows the average error for each plate thickness using S_0 and A_0 dispersion curves to select appropriate speeds.

Table 4. Table of average error for each thickness using S_0 and A_0 modes

Plate Thickness /mm	S_0 Mode average error /mm	A_0 Mode average error /mm	S_0 Mode standard deviation /mm	A_0 Mode standard deviation /mm
3	9.6	37.6	18.7	26.5
6	6.2	29.4	9.4	24.7
8	8.3	35.8	11.4	20.8
10	7.2	29.3	9.4	21.7
12	12.6	29.5	12.8	21.8
15	17.6	27.7	16.0	20.3

Though errors are small for thicknesses up to 10mm, errors become larger as the plate becomes thicker. This is likely due to there not being sufficient length for plate waves to develop in these higher thicknesses, combined with the effect of reflections established in Section 4.3. There is also a considerably higher standard

deviation for events located using the A_0 mode, though the standard deviation when using the S_0 mode rises with the thickness.

When locating signals using the delta-T method, the wave velocity cannot be adjusted with thickness as it is not used as part of the location algorithm (Baxter, et al., 2007). Ideally, the delta-T grids would be recollected each time the thickness changes. Though delta-T generally gives more accurate results than TOA it is far more time consuming due to the need to collect data from across the plate and uncertainty about whether a delta-T map is still usable after the plate is skimmed, or if a new map is required.

Figure 95 to Figure 100 show signals located using delta-T on the plates from thickness of 3mm to 15mm. Each of these plates had their own set of delta-T training data collected which was used to locate these sources.

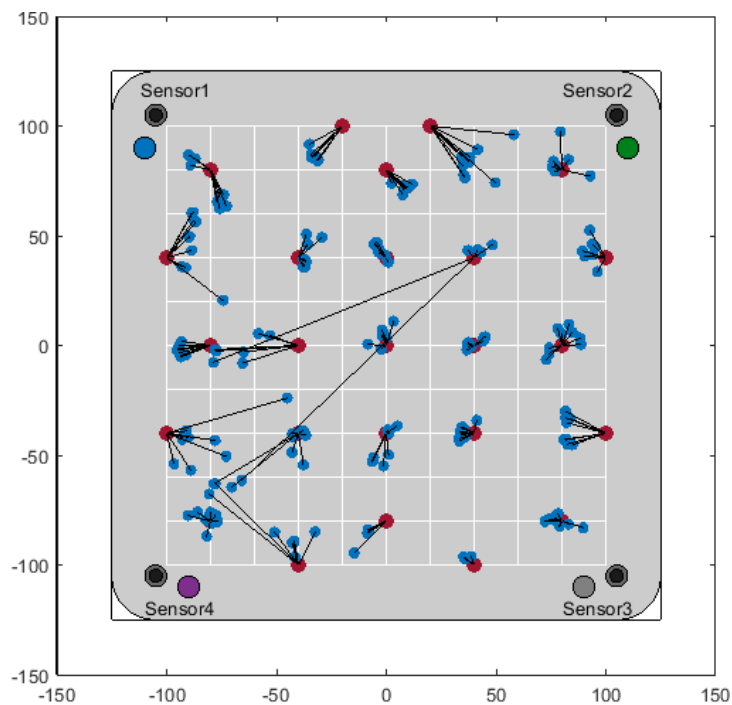


Figure 95. Signals located in a 3mm plate using delta-T. Red being the actual source location and blue being the located signal. The black lines indicate the distance from the actual source

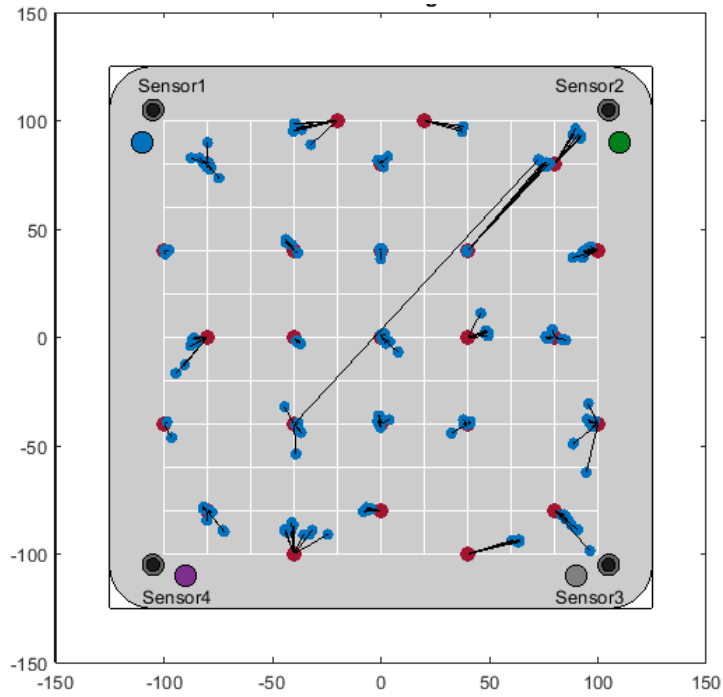


Figure 96. Signals located in a 6mm plate using delta-T. Red being the actual source location and blue being the located signal. The black lines indicate the distance from the actual source

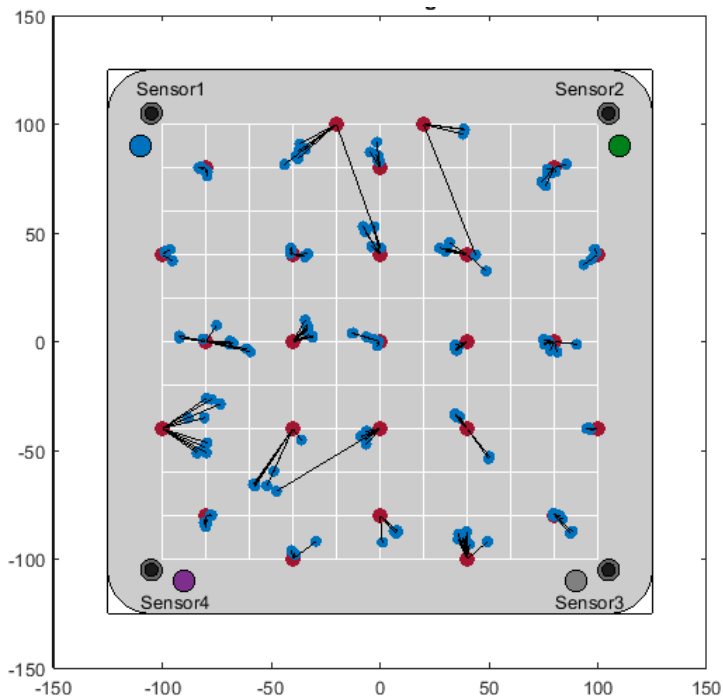


Figure 97. Signals located in an 8mm plate using delta-T. Red being the actual source location and blue being the located signal. The black lines indicate the distance from the actual source

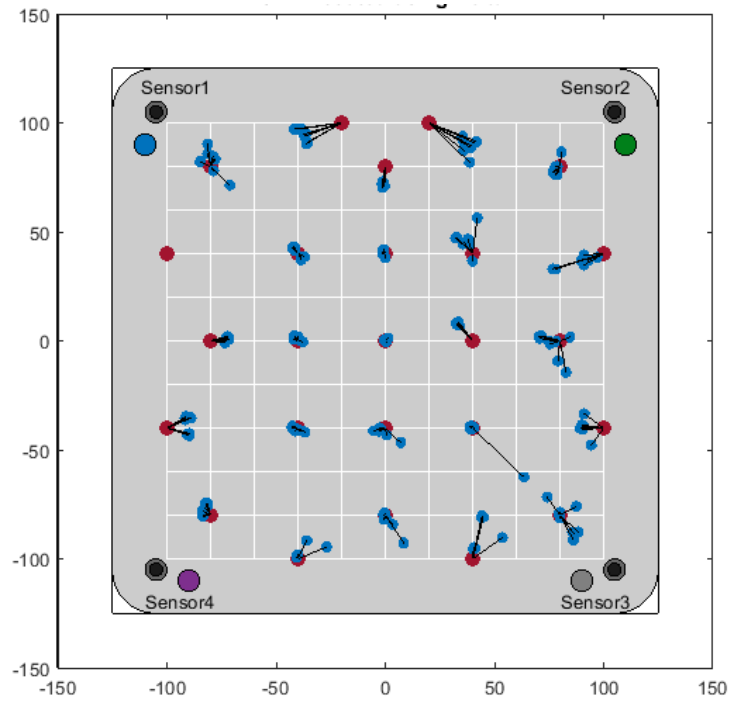


Figure 98. Signals located in a 10mm plate using delta-T. Red being the actual source location and blue being the located signal. The black lines indicate the distance from the actual source

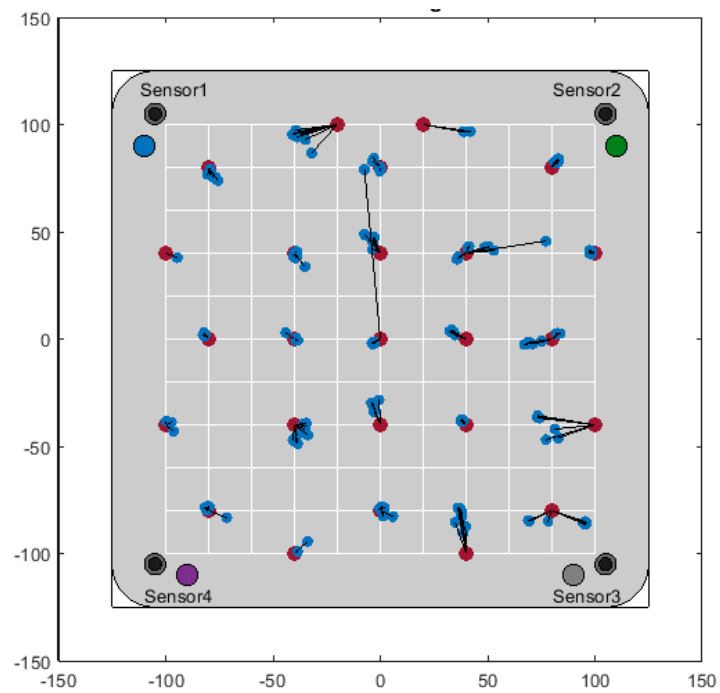


Figure 99. Signals located in a 12mm plate using delta-T. Red being the actual source location and blue being the located signal. The black lines indicate the distance from the actual source

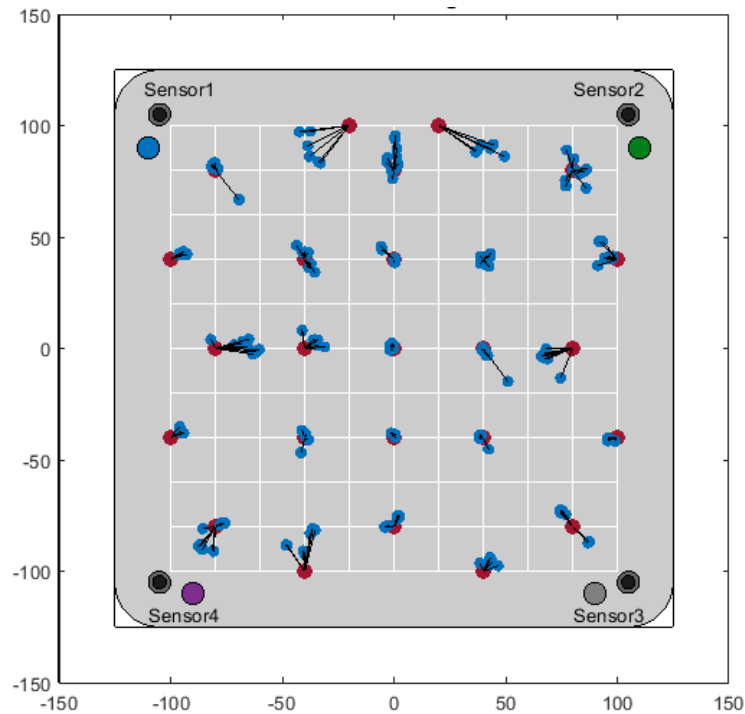


Figure 100. Signals located in a 15mm plate using delta-T. Red being the actual source location and blue being the located signal. The black lines indicate the distance from the actual source

The average error from each of these is then shown in

Table 5, showing that the average error for each plate is lower when using delta-T.

Additionally, the standard deviation of this data is fairly small, much smaller than for events located using delta-T in Section 5.2. This shows that redesigning the waveguide to interface directly with the build plate was an effective way of increasing location accuracy.

Table 5. Table of average errors when using delta-T

Plate Thickness /mm	Average Error /mm	Standard Deviation /mm
3	13.2	15.5
6	9.9	15.6
8	10.0	9.8
10	7.3	6.3
12	8.1	8.9
15	6.6	7.0

The differences between delta-T grids were found to be negligible, shown in Figure 101, so before attempts were made to estimate intermediary delta-T grids, data was located on a range of plate thicknesses using grids collected on the 15mm plate.

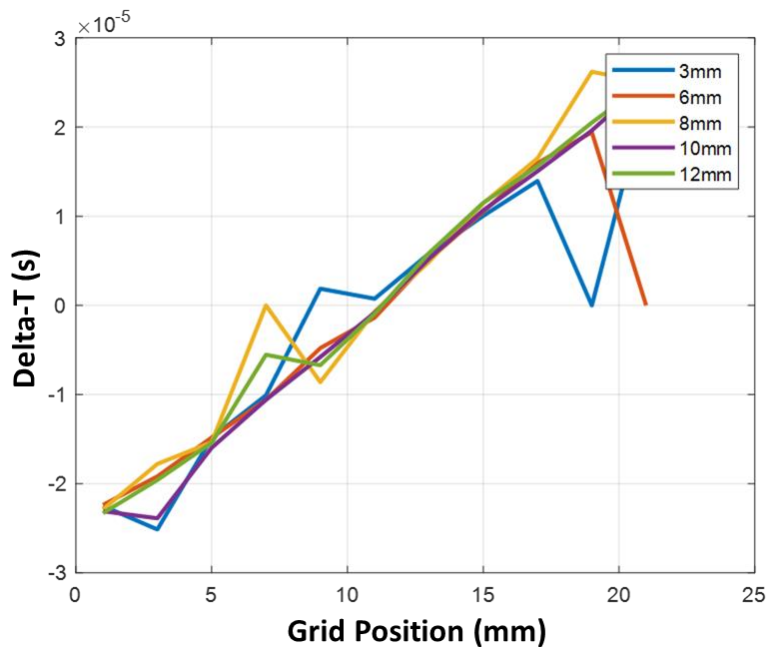


Figure 101. A graph of grid position against delta-T for each of the plate thicknesses

In a manufacturing setting, it is not possible to collect data from a plate at its thickest and thinnest and interpolate from there, so it's important to establish a relationship between thickness change and delta-T change. This could be done by looking at the relationship between the distance to the sensors, the thickness and the delta-T for each node.

The average errors of locating signals from each thickness plate using the delta-T training data from the 15mm plate are shown in Table 6. The average error remains small throughout, showing that the small differences between the grids mean that delta-t data does not change significantly enough with thickness to require new training data to be collected for every build.

Table 6. Table of average errors for each plate thickness using delta-T data from a 15mm plate

Plate Thickness /mm	Average Error /mm	Standard Deviation /mm
3	10.5	6.7
6	8.9	7.3
8	8.9	8.6
10	7.6	6.9
12	7.9	8.4

Figure 102 to Figure 106 show the results for attempting to locate on 3 to 12mm thick plates using delta-T data from a 15mm plate.

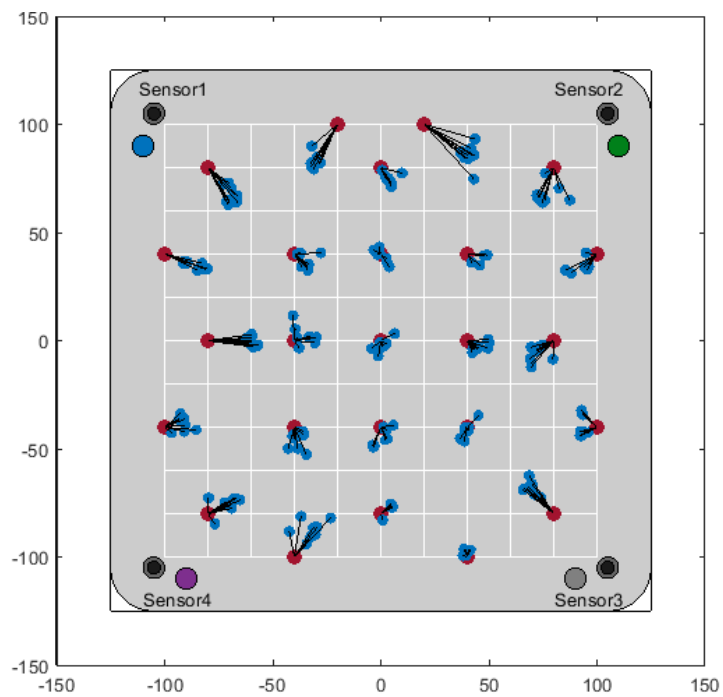


Figure 102. Events located in a 3mm plate using delta-T data from a 15mm plate. Red being the actual source location and blue being the located signal. The black lines indicate the distance from the actual source

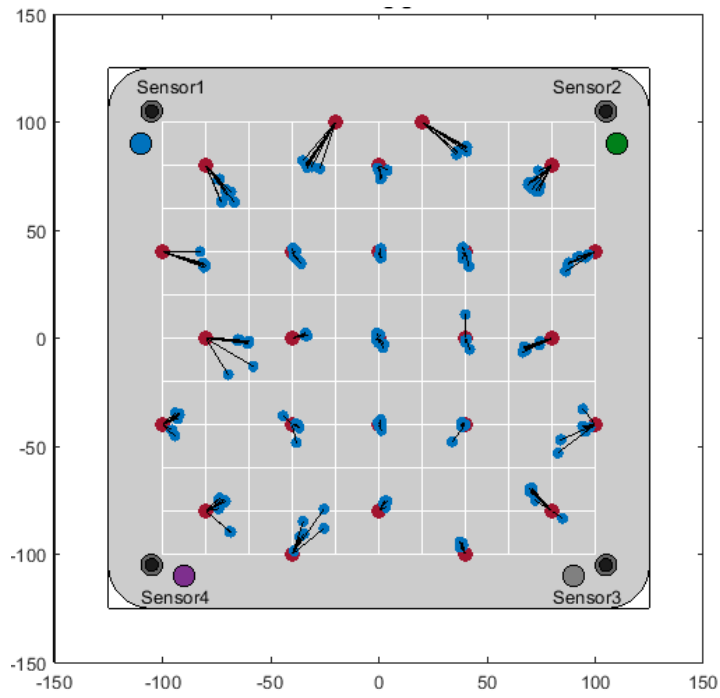


Figure 103. Events located in a 6mm plate using delta-T data from a 15mm plate. Red being the actual source location and blue being the located signal. The black lines indicate the distance from the actual source

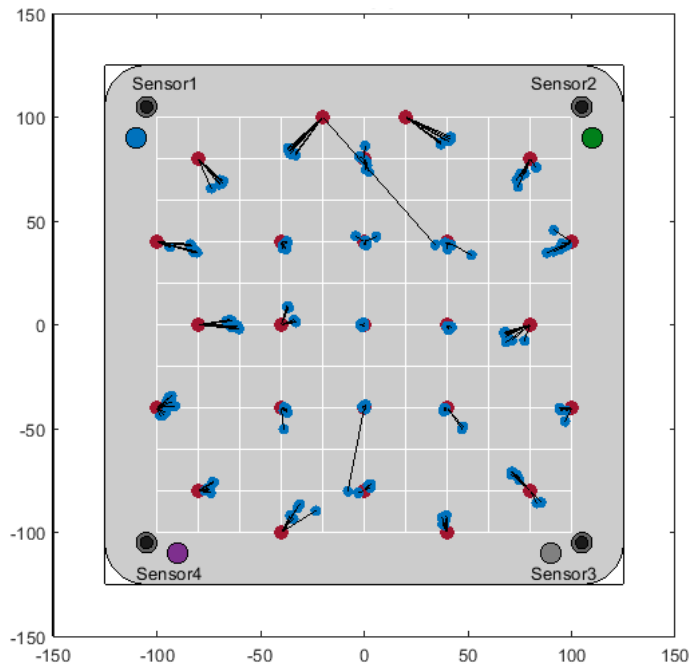


Figure 104. Events located in a 8mm plate using delta-T data from a 15mm plate. Red being the actual source location and blue being the located signal. The black lines indicate the distance from the actual source

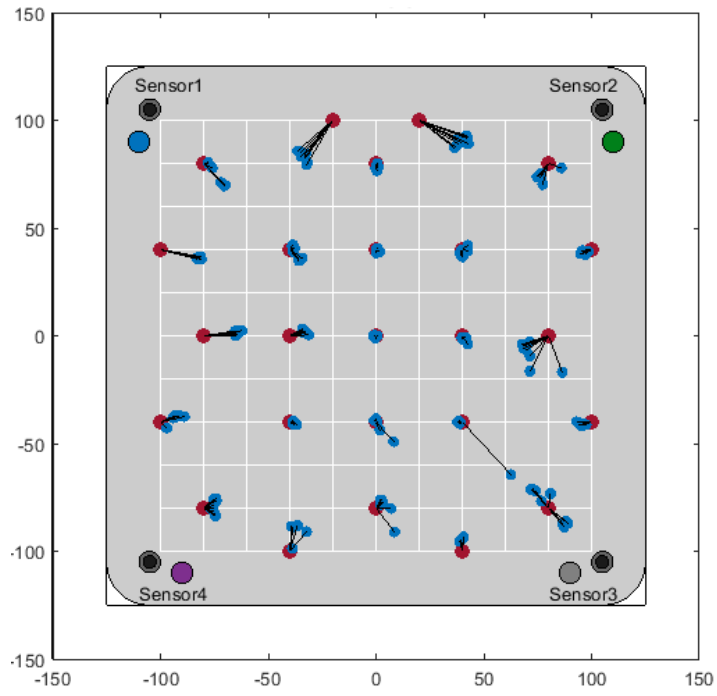


Figure 105. Events located in a 10mm plate using delta-T data from a 15mm plate. Red being the actual source location and blue being the located signal. The black lines indicate the distance from the actual source

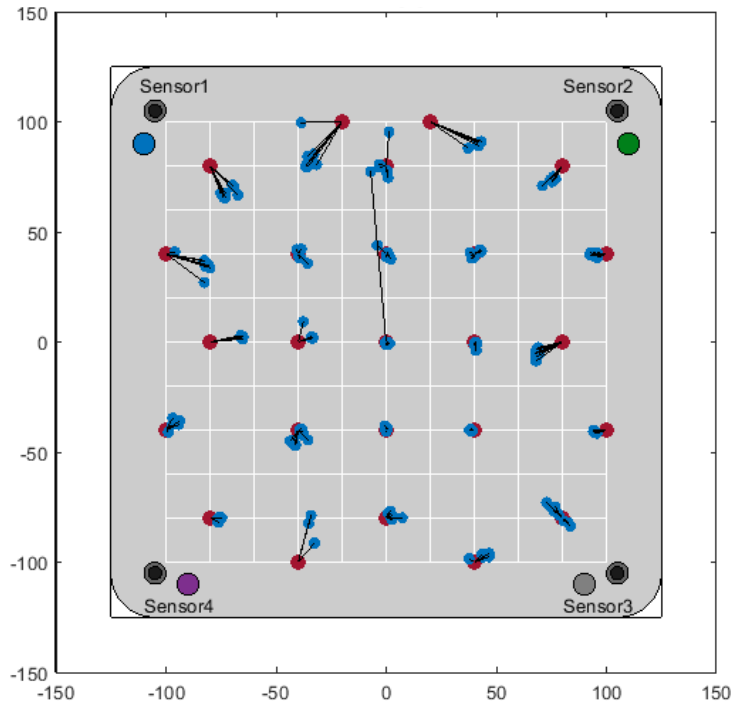


Figure 106. Events located in a 12mm plate using delta-T data from a 15mm plate. Red being the actual source location and blue being the located signal. The black lines indicate the distance from the actual source

Figure 107 shows the percentage difference in delta-T values between a grid from the 3mm plate and from a 15mm plate. Differences are less than 10% across most of the plates, with the exception of the area at the centre of the plate where delta-T tends towards zero so percentage differences become large. This shows why signals can still be accurately located despite thickness changes.

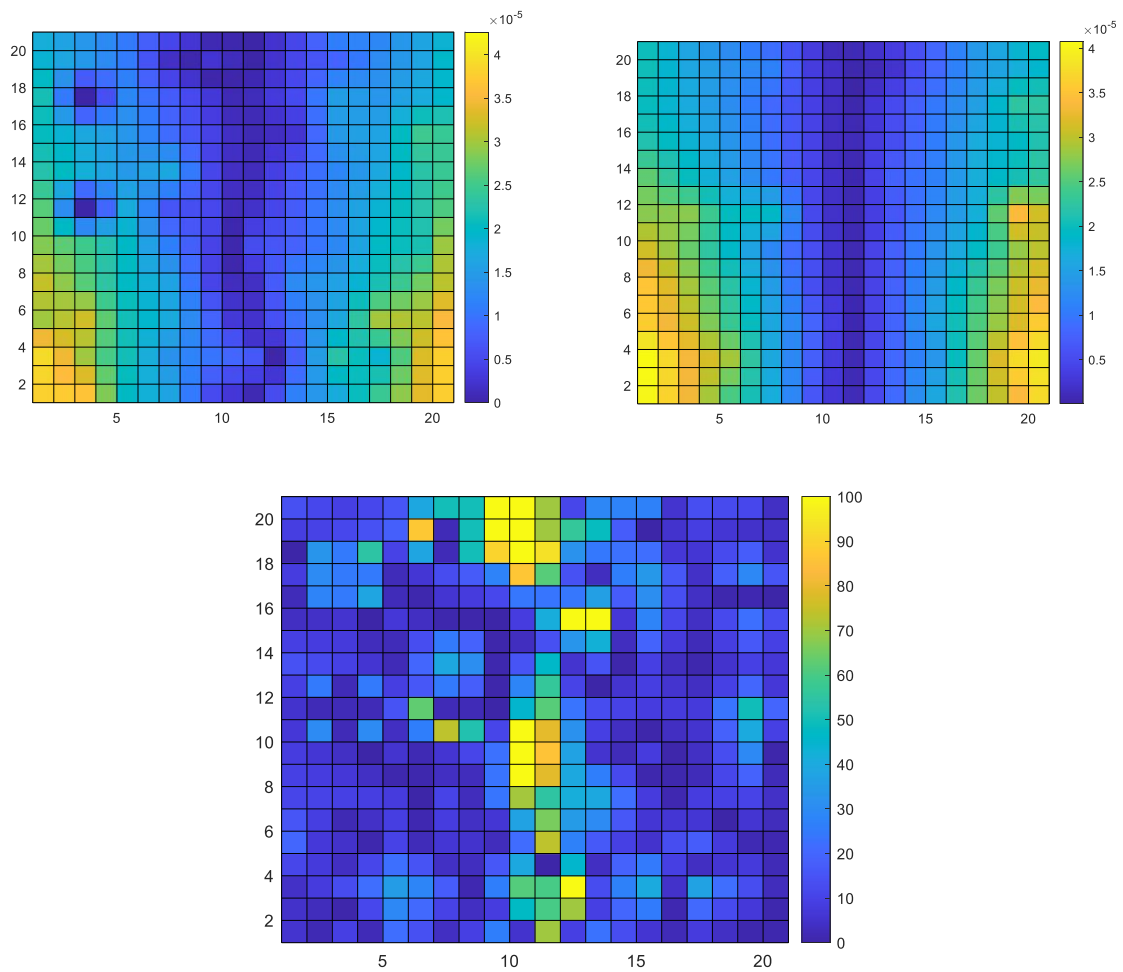


Figure 107. Delta-T grids for the 3mm plate (top left), 15mm (top right) and the percentage difference between them (bottom)

5.3.3. Discussion

The initial work in this section was to assess how accurately the S_0 and A_0 modes could be used to locate signals with the TOA method. The results of this showed that neither was optimum, with an optimum velocity somewhere between. Work was then completed to calculate the optimum wave velocity for each thickness. This showed that the optimum velocity ranged from 5200ms^{-1} for the 3mm plate to 4900ms^{-1} for the 15mm plate. As expected, this lies between the S_0 and A_0 mode. Further work using dispersion curves to adjust TOA provided errors around 10mm and less for the smaller thicknesses, though when the thickness reached 12 and 15mm the accuracy became substantially worse. This may be due to the thickness meaning that Lamb waves lack the space to fully develop, and is a limitation of this approach. The optimum velocity doesn't line up perfectly with the dispersion curves, however this could be due to the influence of the waveguide where the wave is limited to the bar velocity of steel, which is 5000ms^{-1} (Engineering Toolbox, 2021) .

The delta-T work carried out showed that as an approach it remained a more accurate method of locating sources than TOA, though when the optimal TOA velocity is used the difference is small. This work also showed that the change in the delta-T grid is very small when changing the thickness as signals continued to be accurately located on the 12mm to 3mm plate, despite using training data for the 15mm plate. This means that delta-T grids would not necessarily need to be recollected before every build, making the delta-T more viable for use within an industrial setting.

5.4. Optimising Delta-T Collection

5.4.1. Experimental Procedures

As previously mentioned, a major issue with the delta-T method is the need to collect large amounts of training data. Previous delta-T grids presented in this chapter used grid spacings of 20mm, which on a 200mm x 200mm grid means collecting data from 121 separate grid points. Using a coarser collection grid would increase the speed of data collection. However, in non-homogeneous materials and complex geometries this may lead to inaccuracies, and any erroneous signals would have a larger impact on the final grids.

In order to test the effectiveness of using coarser grid spacings, grids were created by selecting a limited amount of data to produce grids with grid spacing of 40, 100 and 200mm. These were selected as they all fit within the 200mm x200mm area within the envelope of the waveguide fixtures on the build plate. These require the collection of data at 36, 9 and 4 points respectively, whilst the original 20mm spacing requires data from 121 points. These grids are shown in Figure 108. To collect this data, delta-T training data was collected across the whole 11x11 20mm grid, and then filtered down to the required points for each configuration. Grids of 21x21 points were then created by interpolating from these points. Sensors were positioned as in Section 5.3.1., and sample data was collected in the same points as shown previously in Figure 86.

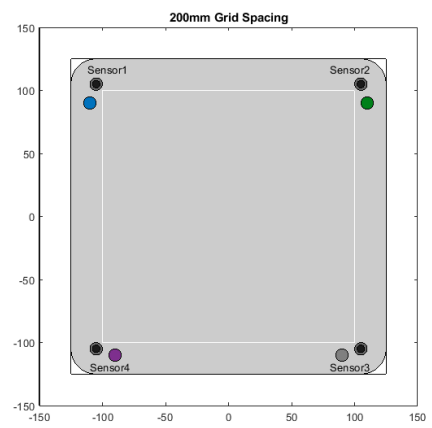
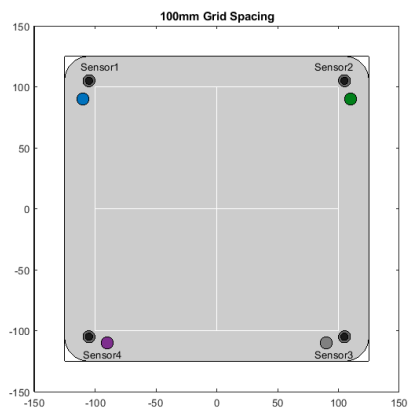
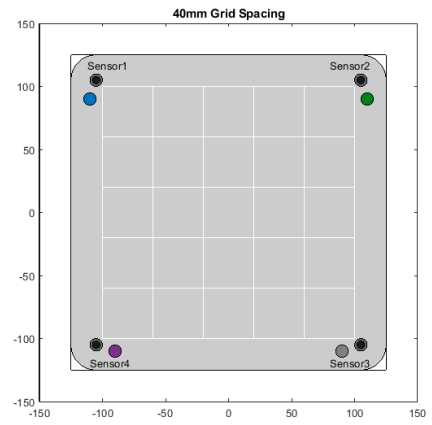
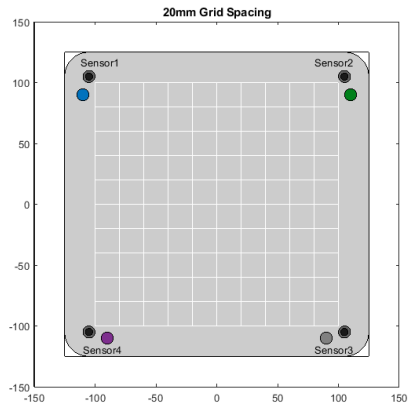
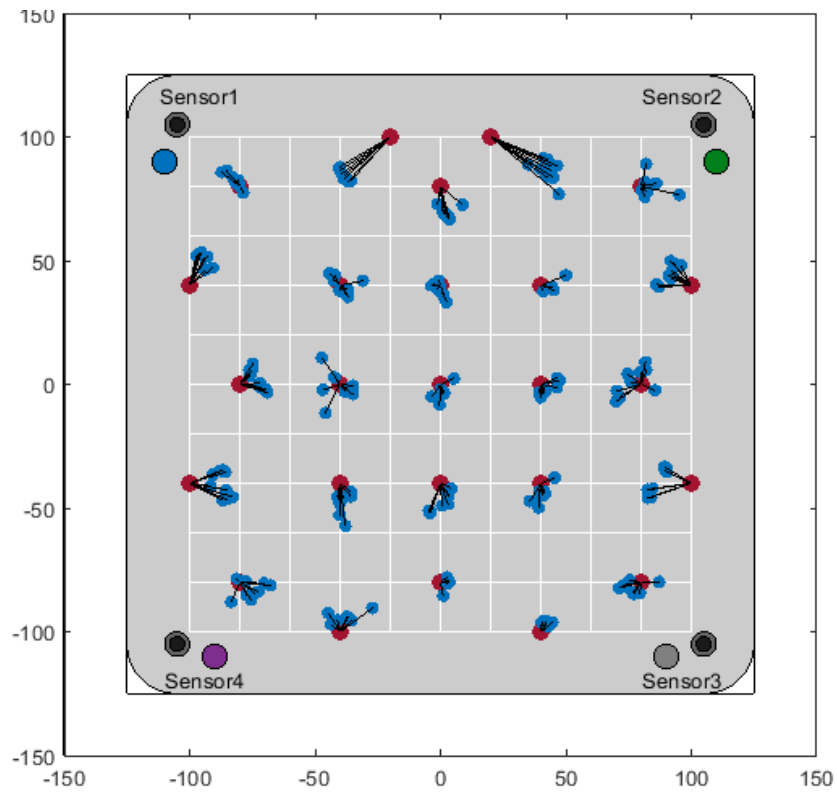


Figure 108. (clockwise from top-left) 20, 40, 100 and 200mm grid spacings

5.4.2. Results

Figure 109 to Figure 114 present the results of using each of the coarser grids for each different thickness plate used in a previous section. It can be seen that accuracy remains high even as the grid is reduced to just four points.



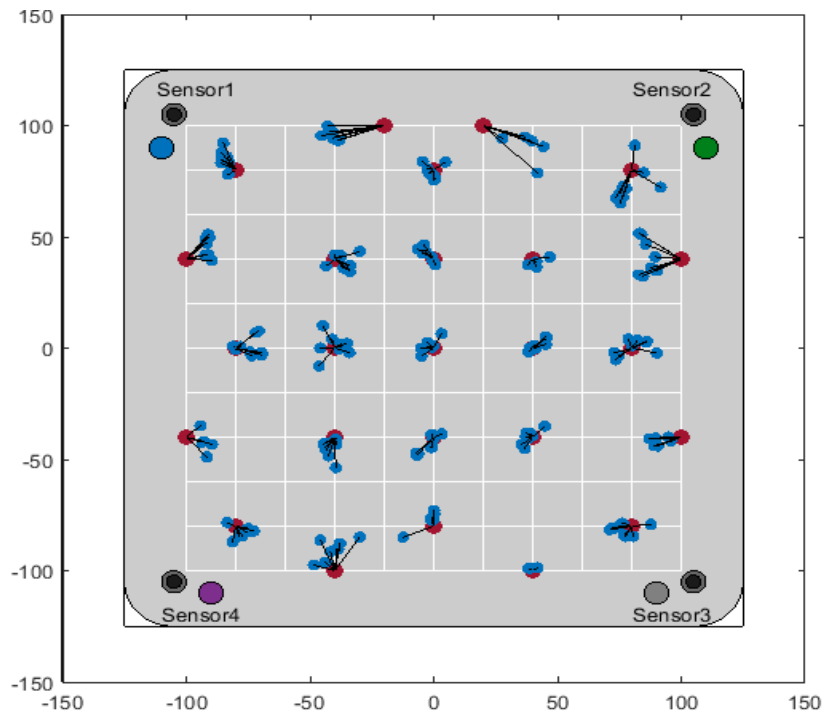
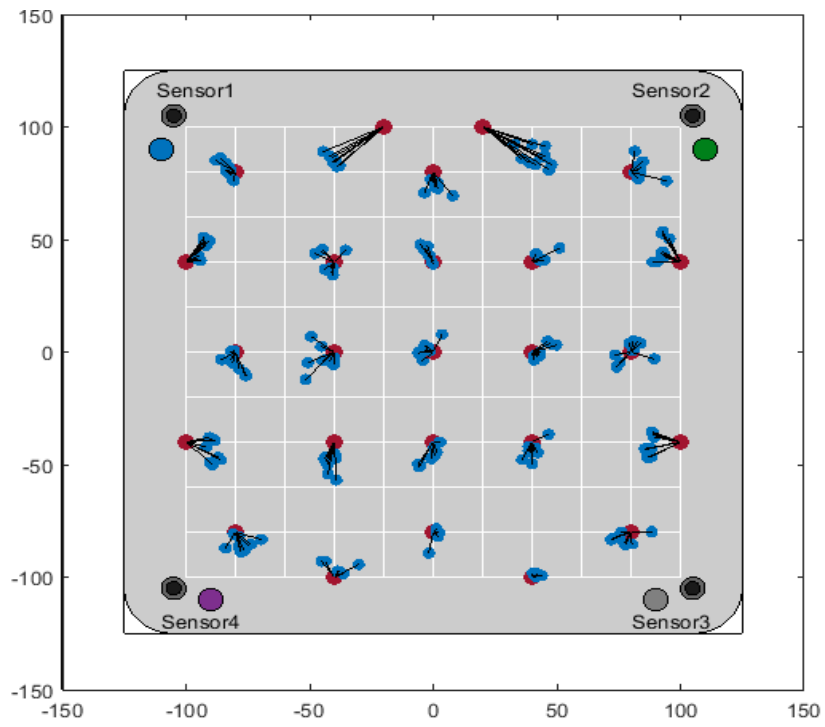
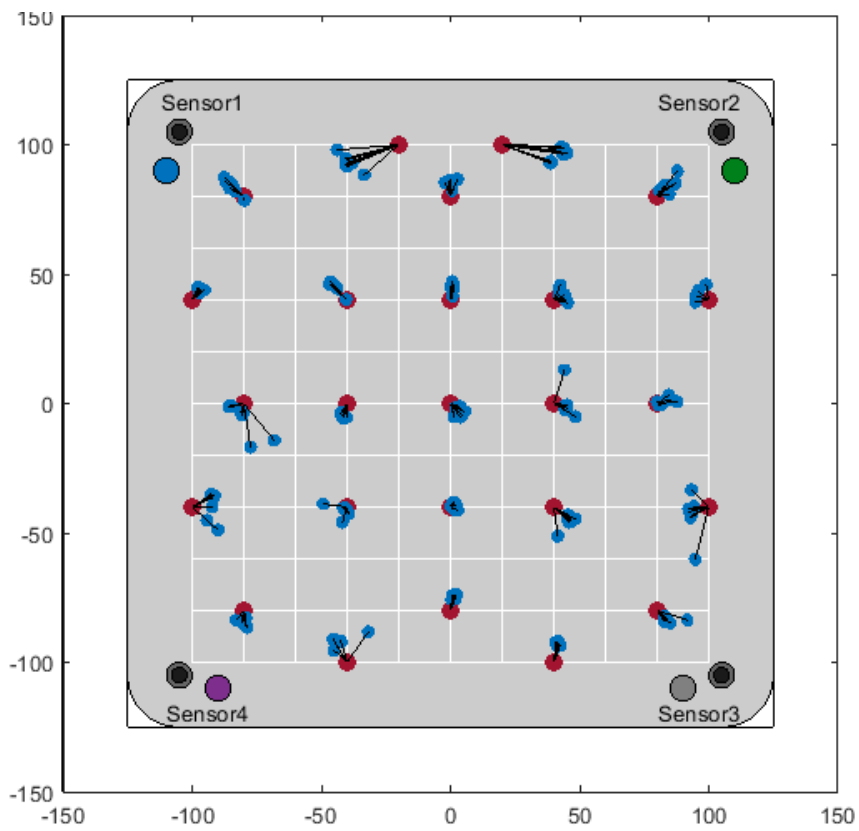
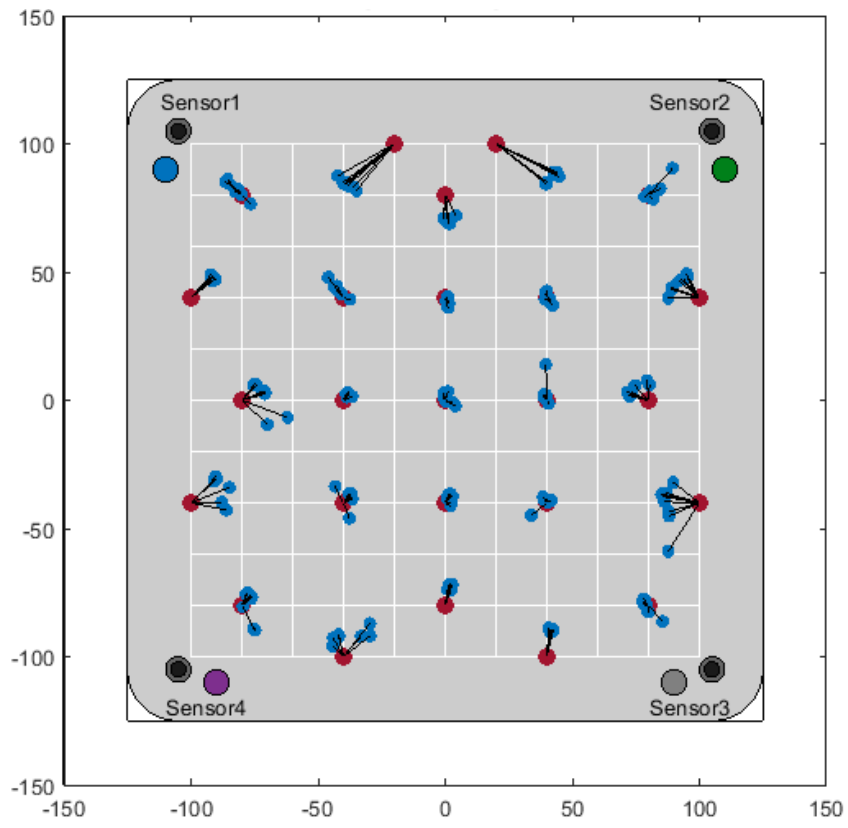


Figure 109. Results of using 200mm spacing (top), 100mm spacing (middle) and 40mm spacing (bottom) on 3mm thickness plate. Red being the actual source location and blue being the located signal. The black lines indicate the distance from the actual source



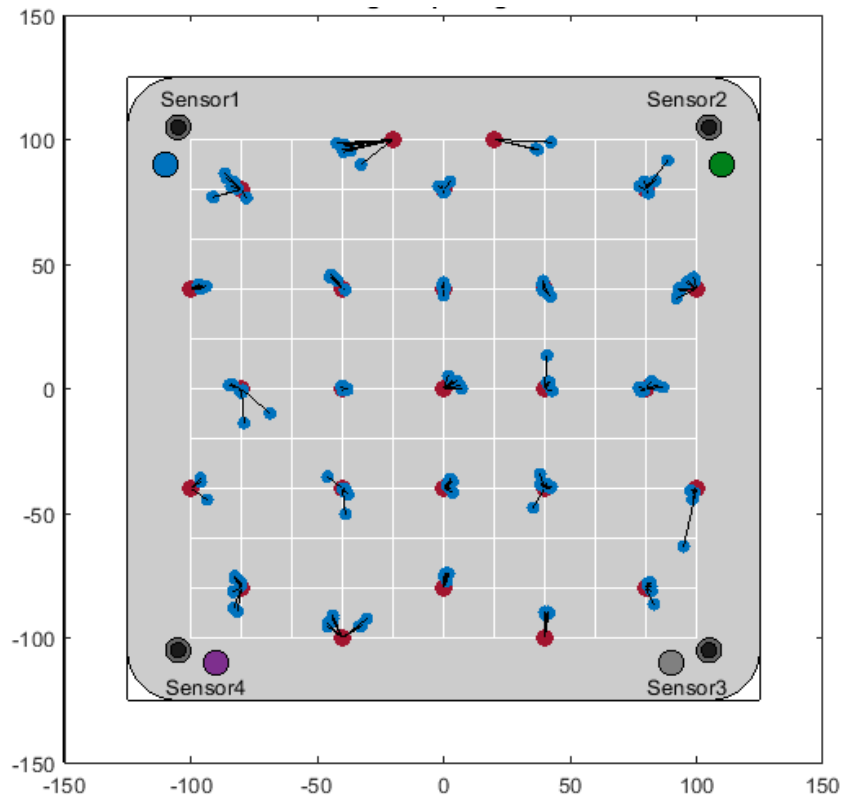
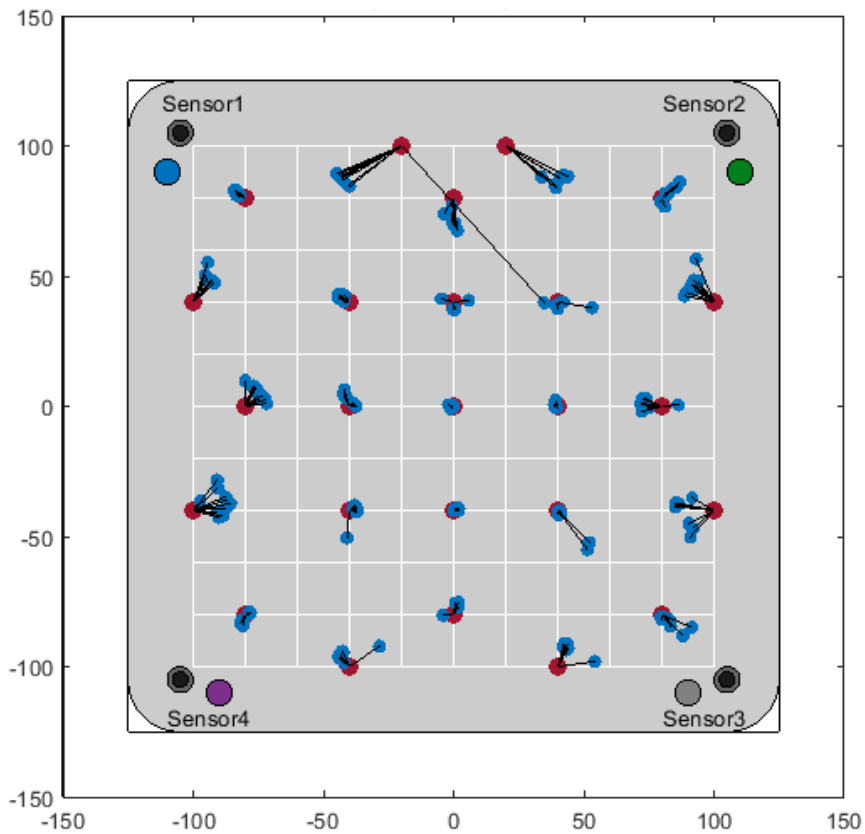


Figure 110. Results of using 200mm spacing (top), 100mm spacing (middle) and 40mm spacing (bottom) on 6mm thickness plate. Red being the actual source location and blue being the located signal. The black lines indicate the distance from the actual source



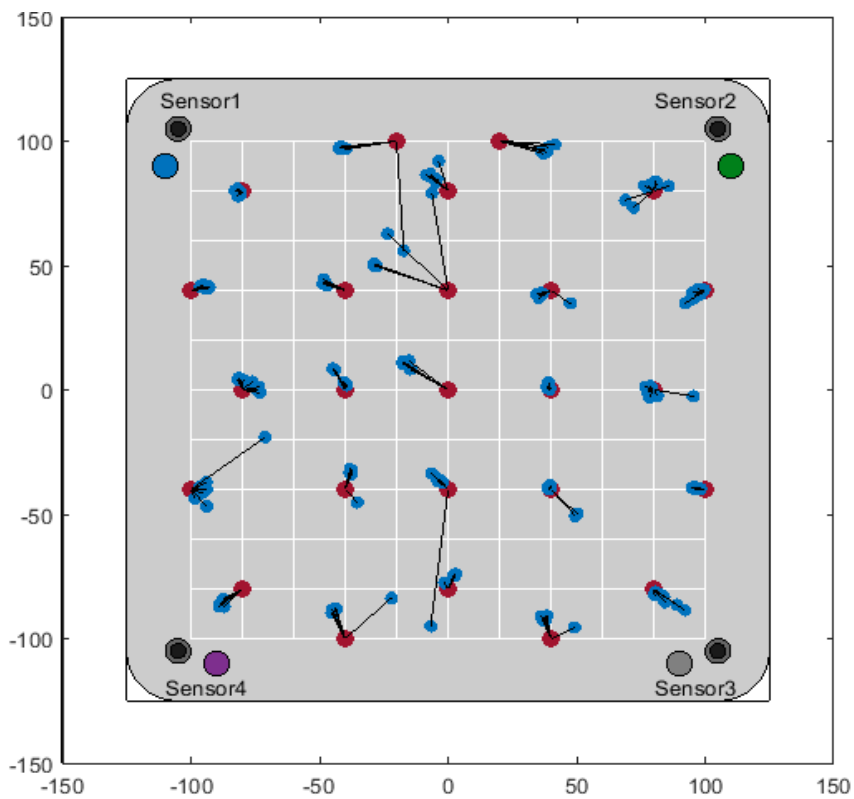
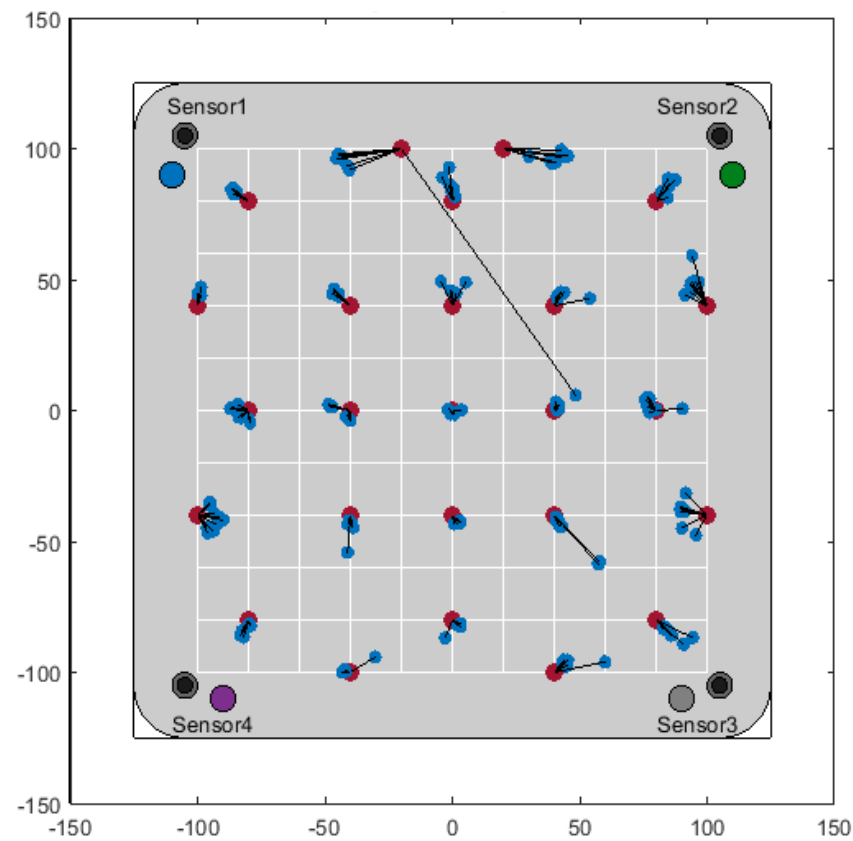
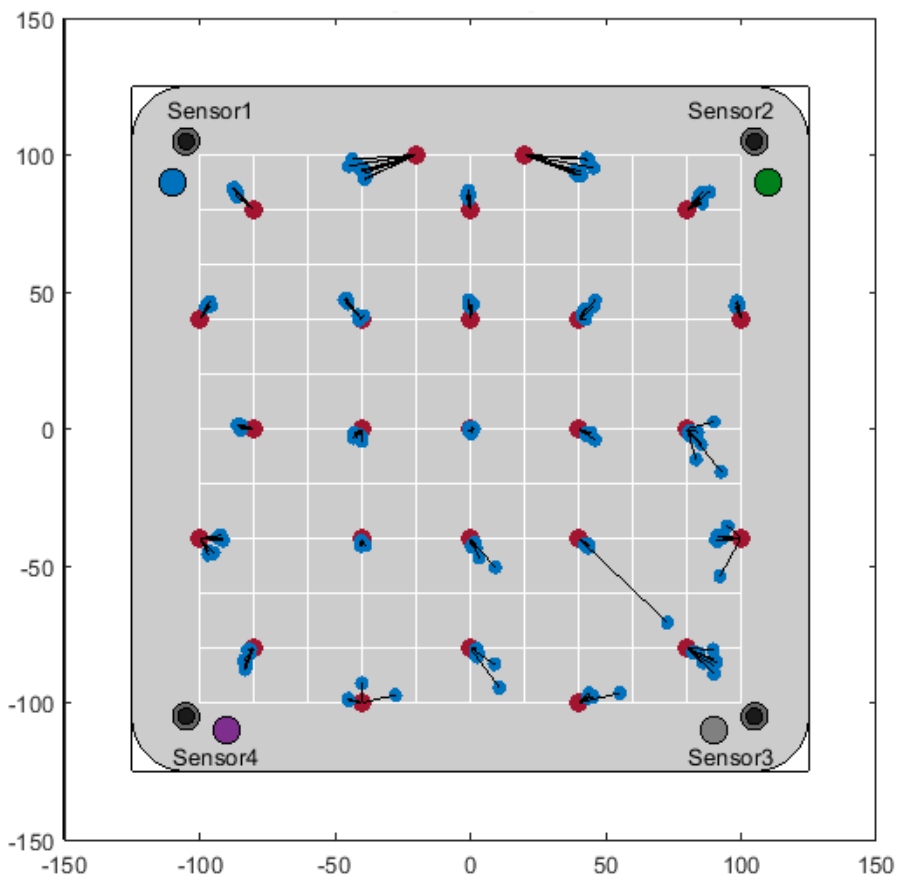
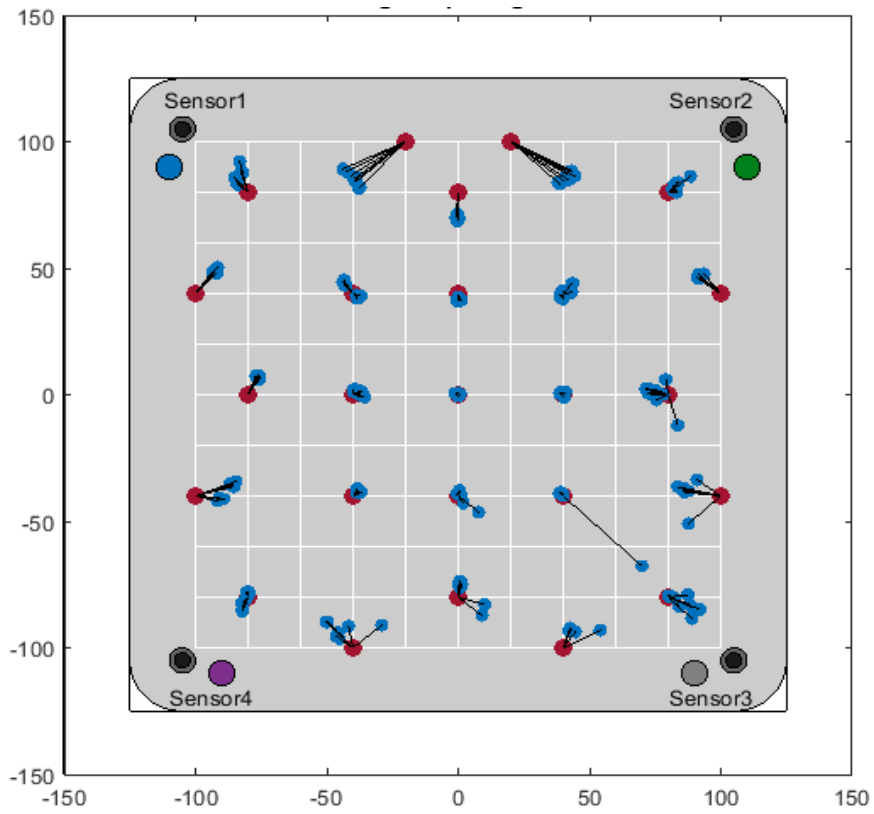


Figure 111. Results of using 200mm spacing (top), 100mm spacing (middle) and 40mm spacing (bottom) on 8mm thickness plate. Red being the actual source location and blue being the located signal. The black lines indicate the distance from the actual source



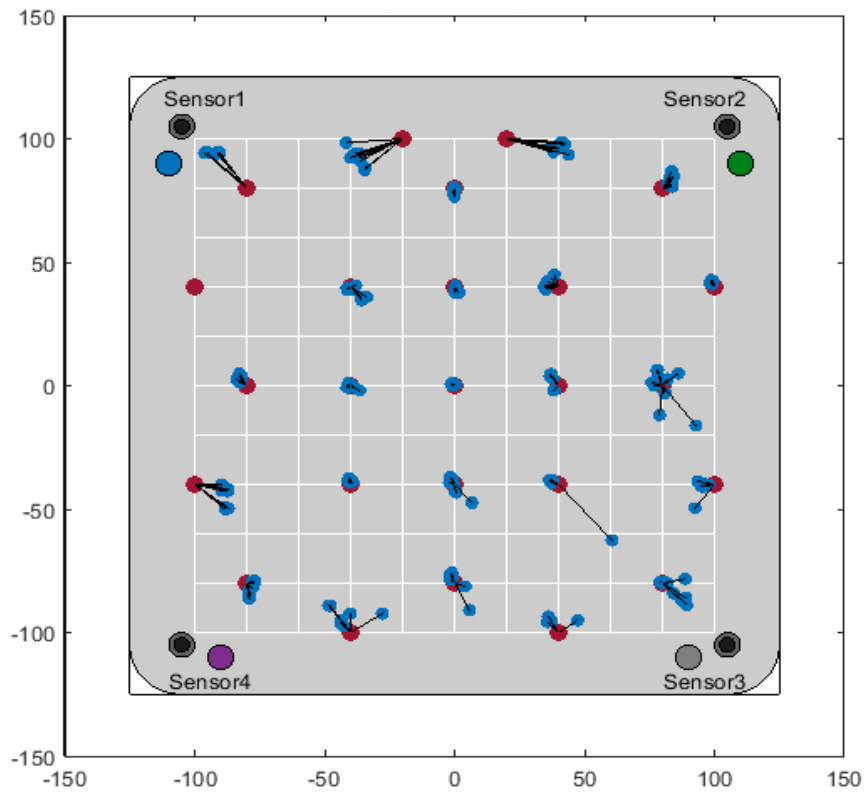
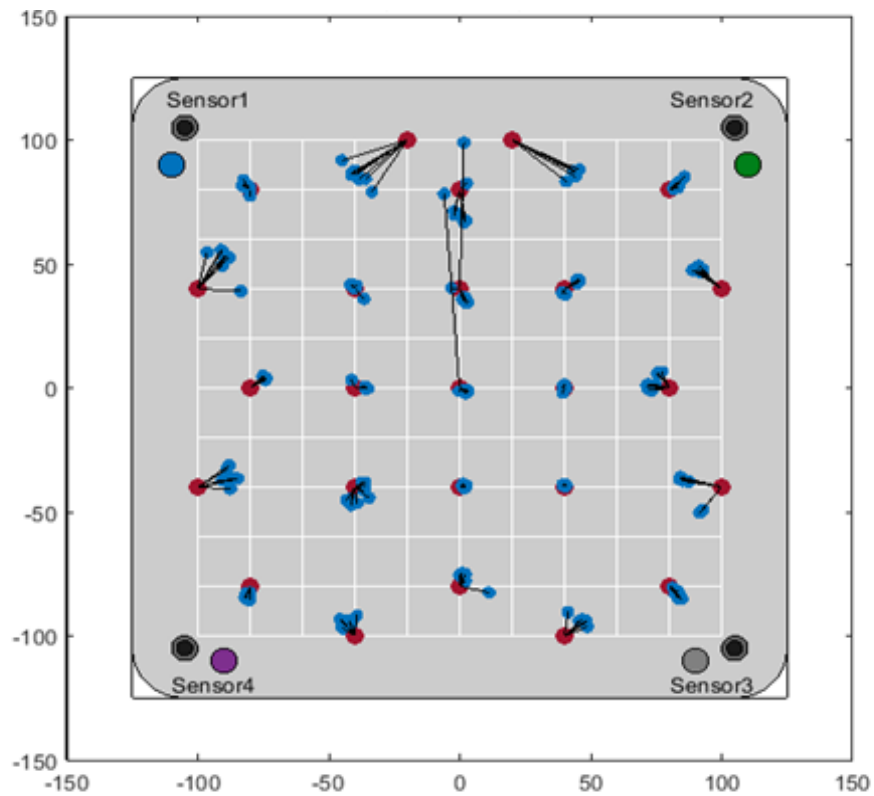


Figure 112. Results of using 200mm spacing (top), 100mm spacing (middle) and 40mm spacing (bottom) on 10mm thickness plate. Red being the actual source location and blue being the located signal. The black lines indicate the distance from the actual source



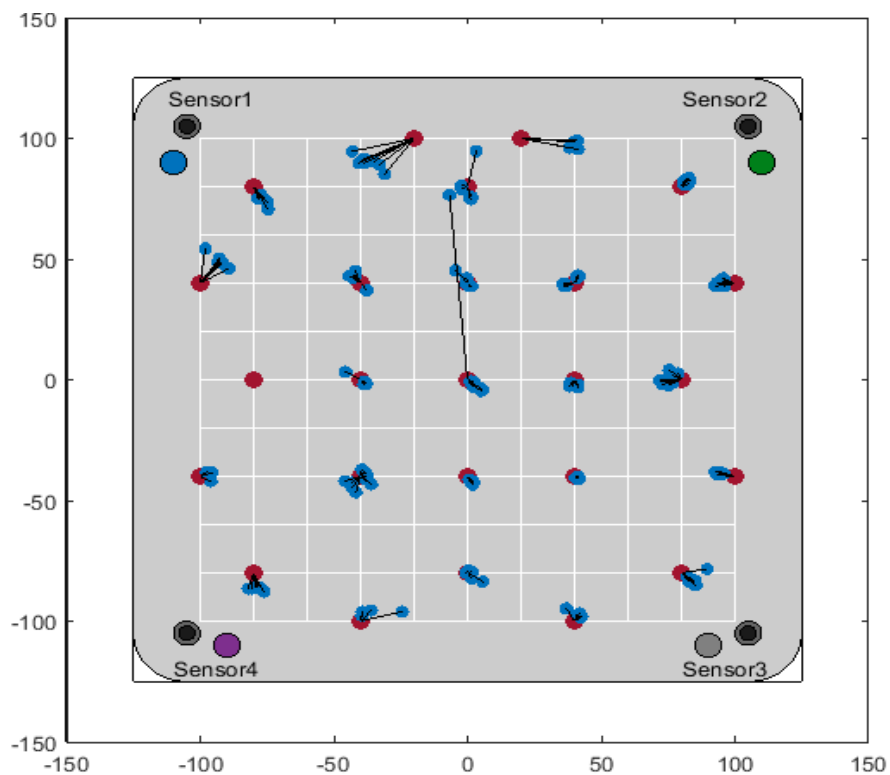
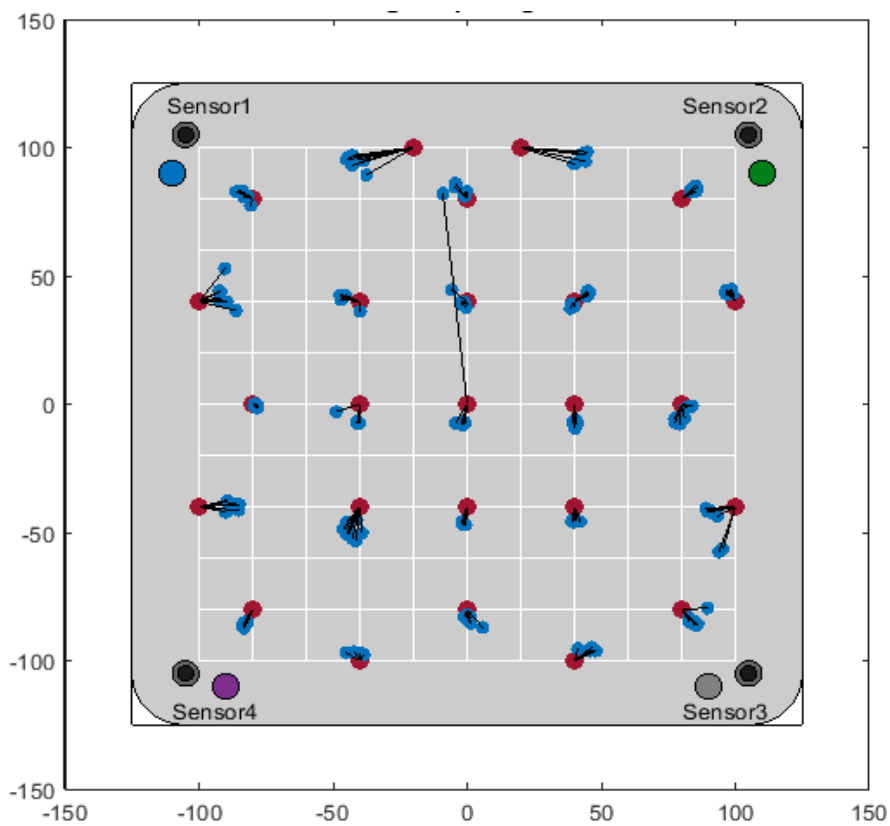
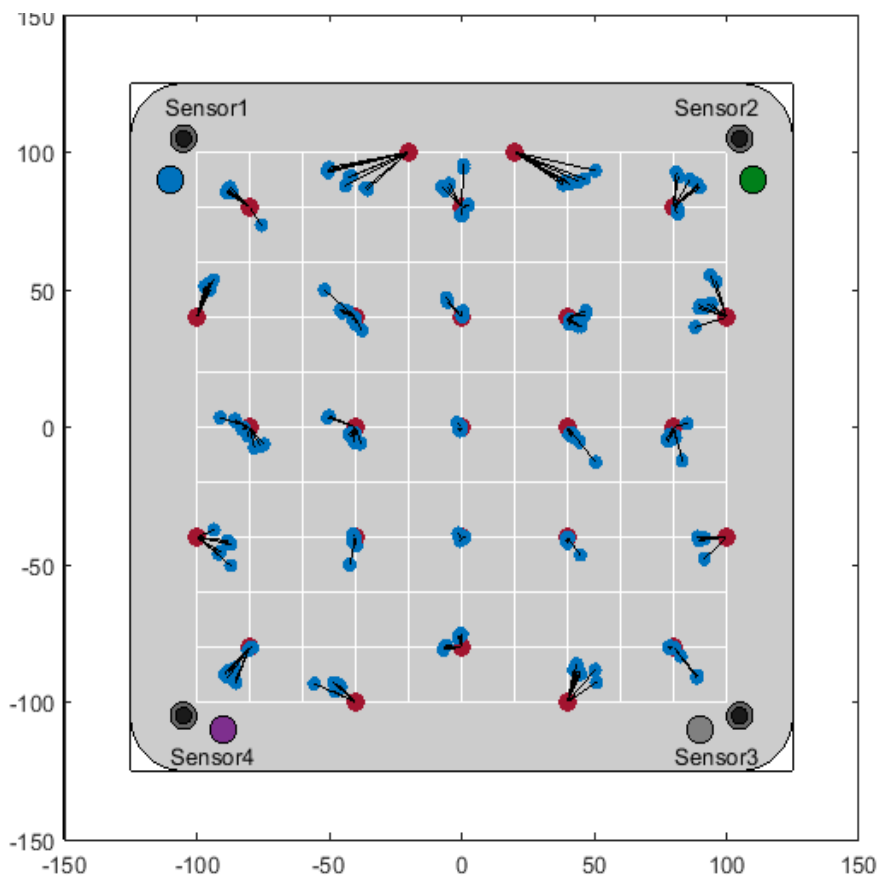
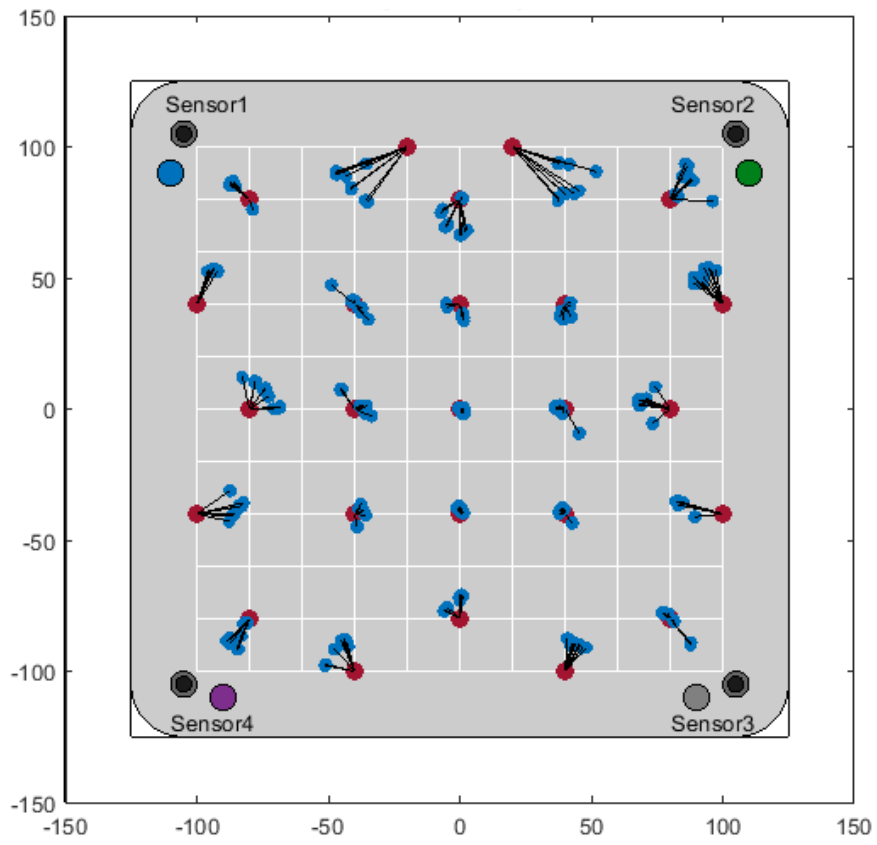


Figure 113. Results of using 200mm spacing (top), 100mm spacing (middle) and 40mm spacing (bottom) on 12mm thickness plate. Red being the actual source location and blue being the located signal. The black lines indicate the distance from the actual source



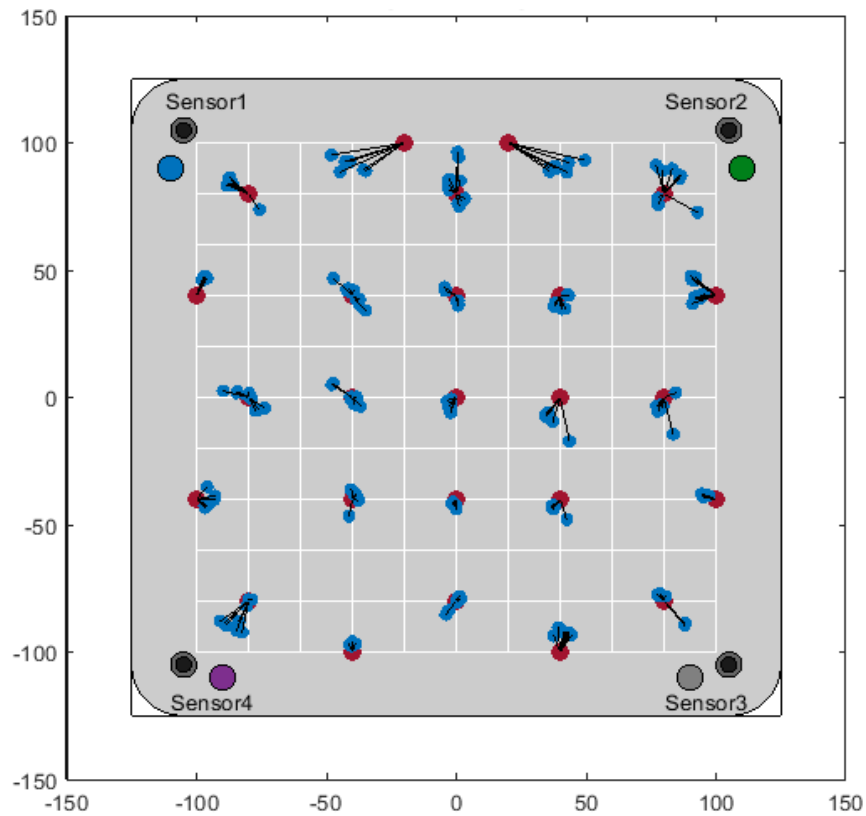


Figure 114. Results of using 200mm spacing (top), 100mm spacing (middle) and 40mm spacing (bottom) on 15mm thickness plate. Red being the actual source location and blue being the located signal. The black lines indicate the distance from the actual source

Table 7 gives the average error in mm for each plate thickness with each grid configuration. It can be seen that accuracy remains high and even improves as the grid becomes coarser.

Table 7. Table of average error for each grid size and thickness

Plate Thickness /mm	Grid Size /mm			
	20	40	100	200
3	13.2	7.5	8.4	9.0
6	9.9	5.2	7.2	7.8
8	10.0	8.9	7.9	7.6
10	7.3	6.5	7.2	7.8
12	8.1	6.1	8.0	8.2
15	6.6	6.7	8.0	9.5

5.4.3. Discussion

This results of this work showed that despite an increase in the coarseness of the grid, the average error remained small and in some cases even decreased. Delta-T is best suited for use with non-homogeneous materials such as carbon fibre, where collecting data across a fine grid accounts for different directional velocities. However, the AM500 build plates are generally homogeneous meaning that only a few points are needed to accurately interpolate a delta-T grid. A finer grid may be slightly less accurate because small variations in the collected data are effectively amplified, resulting in a much less smooth grid than using fewer points.

5.5. Locating In-Process Signals

5.5.1. Experimental Procedures

In-process signals were acquired from a build containing five sample tokens, which had been selected as they had previously been observed at Renishaw plc to produce substantial amounts of AE data. These tokens were made up of an upper and lower bar, with narrow supporting bars between them designed to be likely to break. The build plate geometry used was the heater and build plate design produced following the results of Section 4.2. The build material and build plate used were titanium. Signals recorded by the WD sensors are recorded by an Adlink system, detailed in Section 3.2. These were recorded with a threshold of 40dB, with long wavestreams of 1ms recorded. These are then processed into separate waveforms automatically depending upon if further events are detected in that signal.

5.5.2. Results

Figure 115 shows signals located from a build using TOA. A wave velocity of 4100ms^{-1} was arrived at as an appropriate value in a similar fashion to Section 5.3.2 when the optimum velocity for aluminium was found. The five parts being built are outlined along the centre of the plate. It can be seen that a number of signals are located close to the parts being built, however a large amount are located around the edges. This figure gives no information either on the magnitude of the event, nor on the number of crossing points used to ascertain that location.

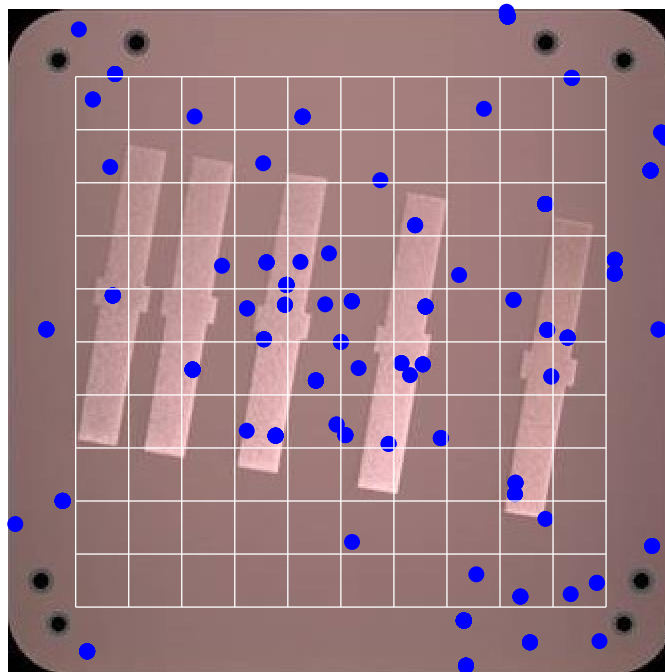


Figure 115. In-Process signals located using TOA at 4100m/s

All location results thus far have been presented primarily as scatter plots, however this may not be ideal when presenting data to the final user. When locating events, using a scatter plot can give an impression that data is precisely located. A way of overcoming this is a 'binned' approach, meaning the plate area is split into squares and the number of events in each square presented. Figure 116 shows how this may look on a build using a grid size of 20mm. Alternatively, a grid spacing of 10mm is

presented in Figure 117. However, a 20mm grid size is more suitable as events can be expected to be located to within 20mm.

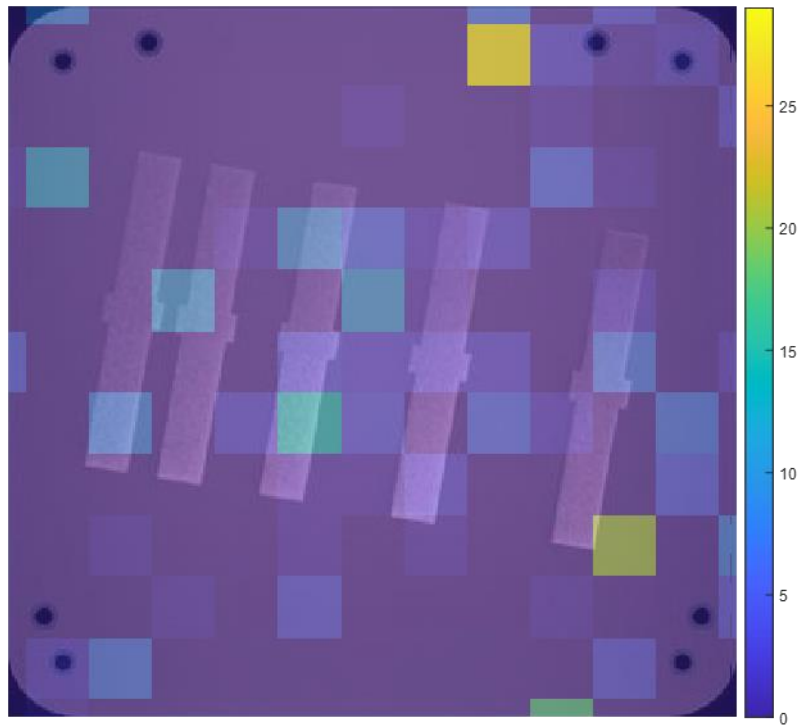


Figure 116. Using a 20mm grid to indicate where the highest number of events occur

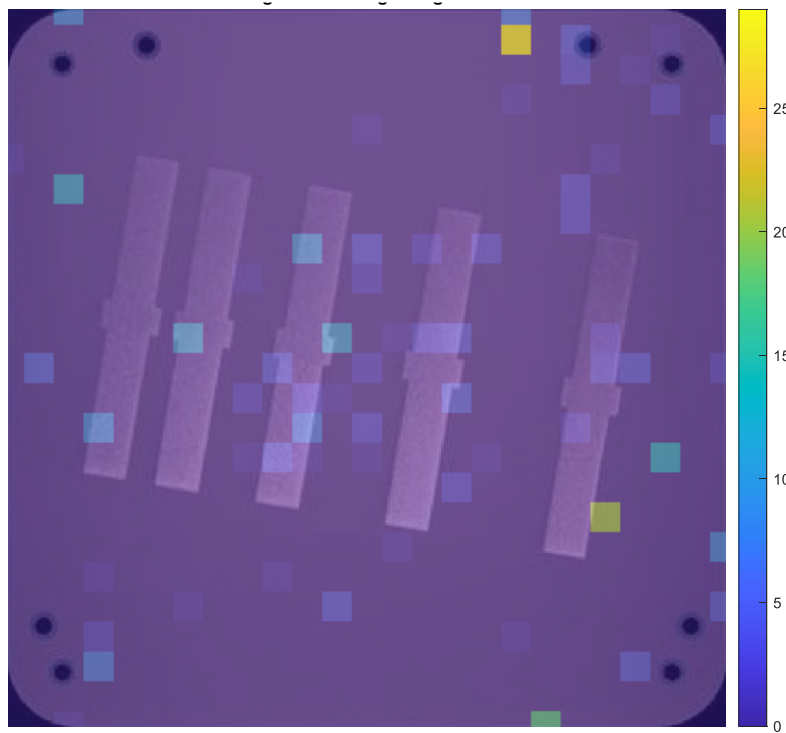


Figure 117. Using a 10mm grid to indicate where the highest number of events occur

This purely presents the number of events occurring in each grid square and does not account for the magnitude or certainty of them. A refinement of this method gives signals a weighting based upon magnitude and certainty, meaning that a large amplitude signal located with a higher number of crossing points would have a much larger value than a low amplitude signal that is more likely to be noise.

The TOA Matlab script used gives a certainty value based upon the number of crossing points between calculated hyperbolae, with 1 meaning all hyperbolae converged at that point and zero meaning that no hyperbolae fully crossed. Figure 118 gives the data previously displayed a weighting by summing the certainties of all sources on that square. This reduces the influence of signals located away from the printed parts whilst also making it easier to see where AE has been released by a part.

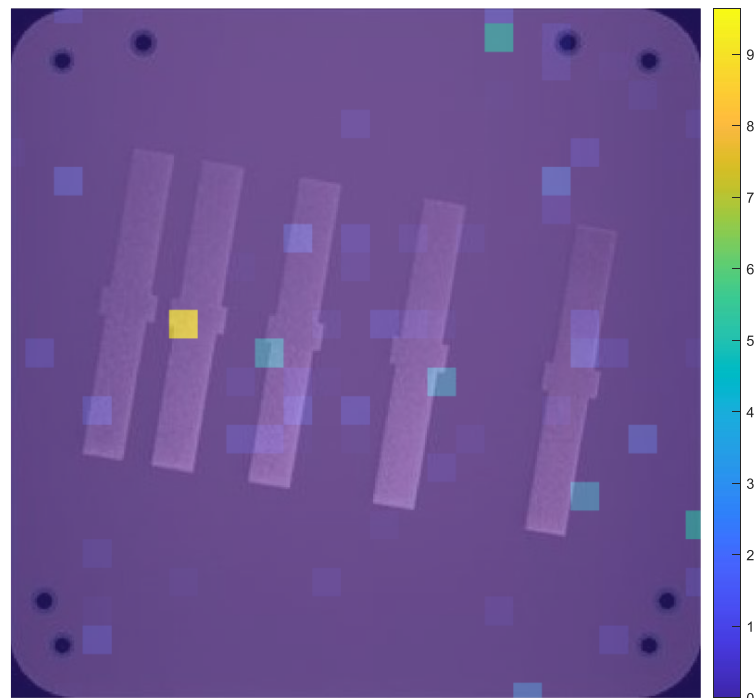


Figure 118. Using a 10mm grid to indicate where the highest number of events occur with a weighting towards sources with a higher certainty

5.4.3. Discussion

In-process signals offer a different challenge to locating sample signals. Sample signals are all produced by the same mechanism and aimed to be consistent with each other. In-process signals will differ based on their mechanism and the size of that defect, leading to a large range of frequencies and peak amplitudes. Out of 276 events, a total of 136 (49.3%) were located around the central area around the built parts. However, when reducing to only those with a certainty of over 0.5, this increases to 80% being located around the parts. This shows that signals are being effectively located around the parts being monitored.

5.6. Conclusion

This chapter was split into four sections; assessing how build plate fastenings affect the ability to accurately locate sources, how the changing thickness of a build plate through its lifespan affects location accuracy, how effectively in-process sources can be located and whether a more efficient delta-T grid training data collection method can be used.

Using delta-T to locate signals in plates with differing numbers of bolts loosened showed the importance of ensuring a uniform tightness across the bolts, as well as showing the effectiveness of the delta-T method versus the TOA method. Work to simplify the propagation paths using washers between the build plate and heater plate showed that this can effectively improve location accuracy. This with the work presented in Section 4.2 contributed to the design change to the heater plate and waveguides previously summarised.

The changing thickness of the plate throughout its lifespan was shown to not require the recollecting of delta-T training data after every build, as the changes in delta-T

values were negligible across a range of plates from 15mm to 3mm. This combined with work to optimise delta-T data collection showing just four points are needed makes it a more viable location method than previously thought. Additionally, dispersion-adjusted TOA was shown to be effective using the S_0 mode, though it became less effective at higher thicknesses. The optimum velocity increased marginally as the thickness was reduced, though not to the extent predicted by dispersion curves.

Finally, in-process signals were effectively located using TOA, proving the useability of AE as a method of locating defects within an active build. Certainty values attained by recording crossing points gave the highest values around the built parts. This could be furthered by giving weightings according to amplitude or signal energy to identify significant signals.

6. Characterisation

6.1. Introduction

The final section of this project was to look into whether it was possible to characterise signals occurring during an ALM build. This work was split into two parts; assessing how signals are altered on their transition to the sensor and looking into whether different signals could still be differentiated after reaching the sensor. Work into how the signal changes was focused on the waveguides and the build plates. The waveguide design was altered over the course of the project, and it was established in the Chapter 3 that this had a major impact on the frequency content of the signal, while this Chapter will further explore whether the waveguides have a 'tuning' effect on the signal leading different signals to have similar features. As discussed previously, the build plates' thickness will change through its lifecycle, so how the shape of signals will be altered was also investigated. Characterisation efforts are based upon training a system to recognise signals, which is made far more difficult if these signals change form with every build.

The second section of this chapter focuses on methods of separating in-process signals. The first part of this was to devise a suitable method of feature extraction, with features taken from traditional AE features, wavelet transforms and statistical methods. The suitability of these features was then assessed using correlation coefficients between all feature pairs, as features that are overly similar can skew the results. Data from a build could be separated based upon when the laser is active, allowing signals caused by the wiper to be distinguished and removed.

6.2. Effect of Waveguide Geometry on Signals

6.2.1. Experimental Procedure

As previously discussed in Section 4.4.1, there are four different waveguide designs that have been used in this project. These are shown in Figure 119. Designs one and four are the designs used before and after the heater plate redesign, while designs 2 and 3 have a few features for comparison. Design four is by far the most complex of the four, with multiple thicknesses and through holes.

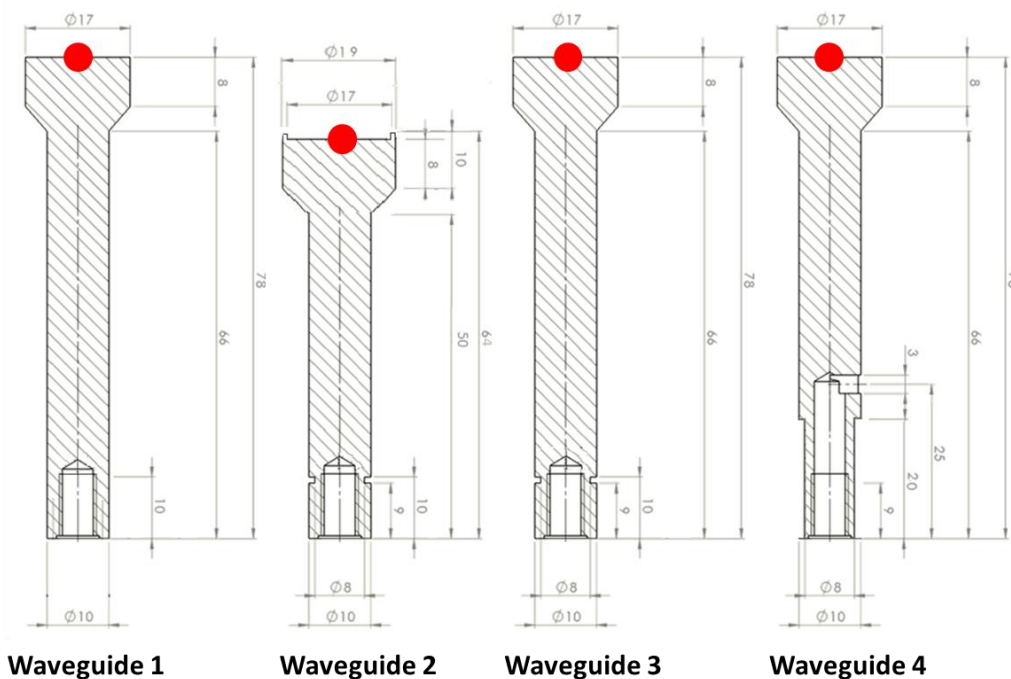


Figure 119. The four waveguide designs

An experiment was conducted in which Mistras WD sensors were silicone bonded to each waveguide and the waveguides were bolted at the four corners of the build plate. A conical transducer was used to produce a signal at the centre of the plate. This is a transducer that was specially designed to produce wideband signals similar to a Hsu-Nielsen source. A fifth WD sensor was placed on the build plate adjacent to the conical transducer to record an in-plate signal to compare to the waveguide signals. This setup is shown in Figure 120.

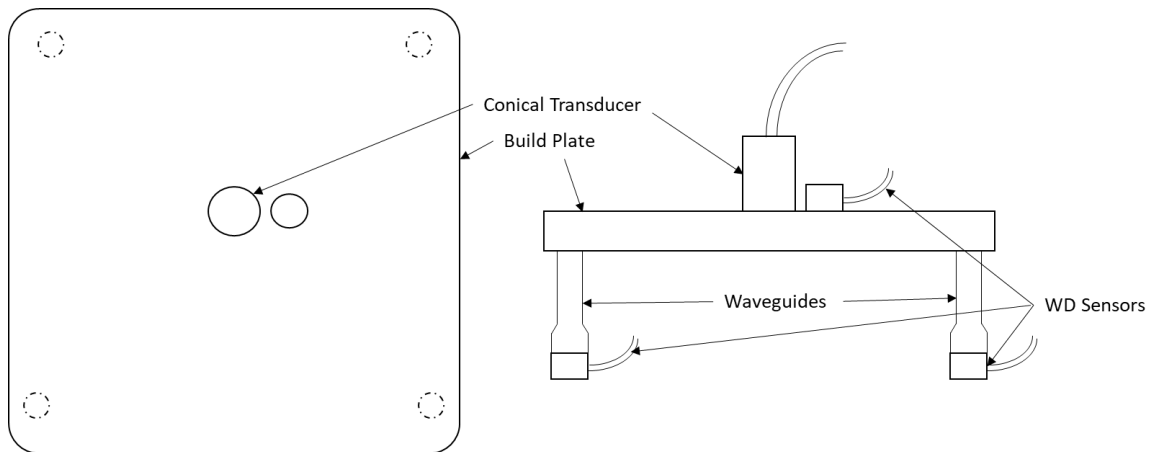


Figure 120. The setup used to generate signals for comparison in the waveguides

The signals used to excite the plate and waveguides were carefully selected. A key part of this experiment was to look at how frequency content would be altered by the propagation down the waveguide. At first, a short sharp square wave was considered in order to excite the broadest range of frequencies, however this came with a few issues. Firstly, the result at the actuator would have been closer to a sinusoidal signal due to a ramping effect at the edges of the signal. Also, it was found that a single pulse was not sufficient to produce a signal with high signal to noise ratio at the waveguide sensor. A five pulse signal was chosen as sufficient to excite the sensors, and this was windowed to smooth discontinuities and allow a natural ramping up of the signal. Using a five pulse signal means that the amplitude can gradually increase in a way that the actuator can accurately reproduce. A Hann Window was used as this best preserves the frequency content of the input signal. However, windowing would radically change the frequency composition of the square wave so it was decided to use sine, sawtooth and triangle waves where input frequency structure is more well-defined. The shapes and frequency spectrums of these three input signals are shown in Figure 121, Figure 122 and Figure 123.

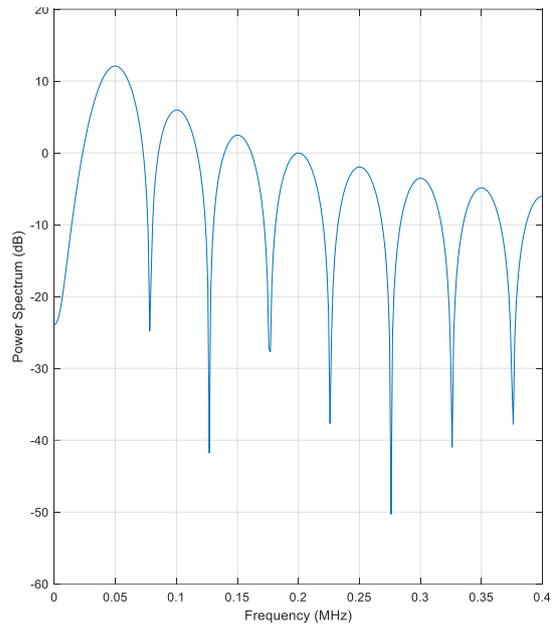
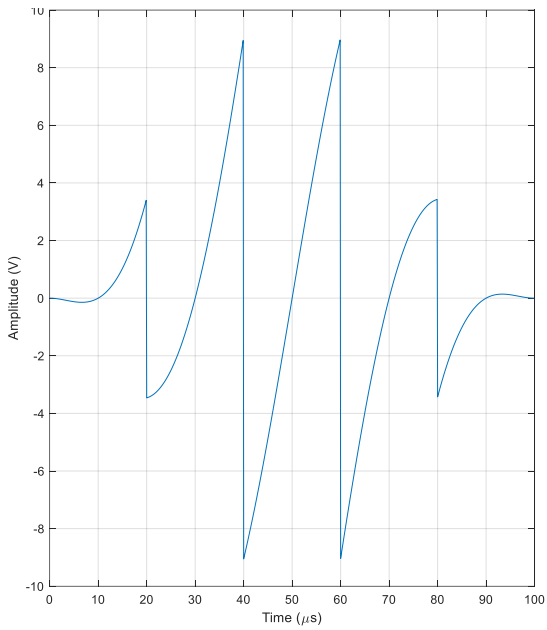


Figure 121. A 50kHz sawtooth signal (left) and the associated frequency spectrum (right)

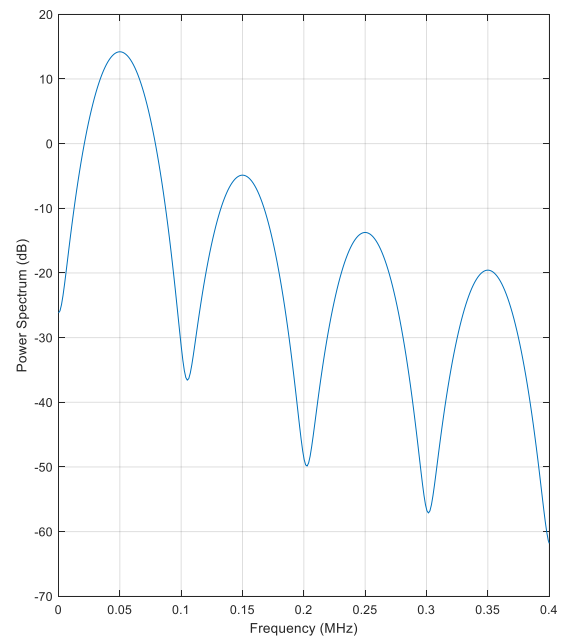
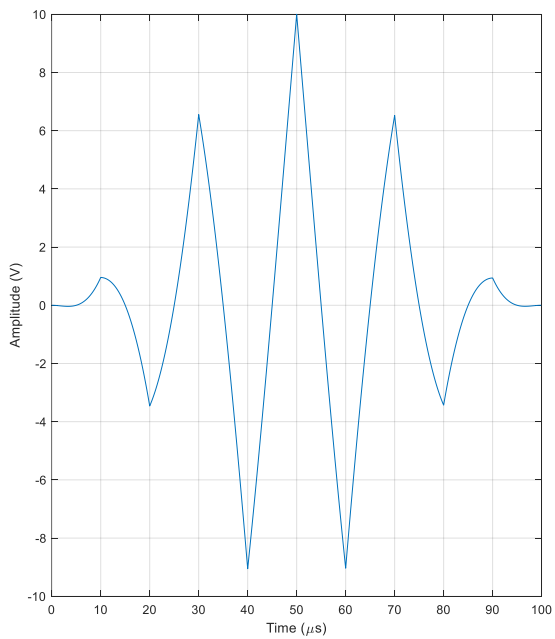


Figure 122. A 50kHz triangle signal (left) and the associated frequency spectrum (right)

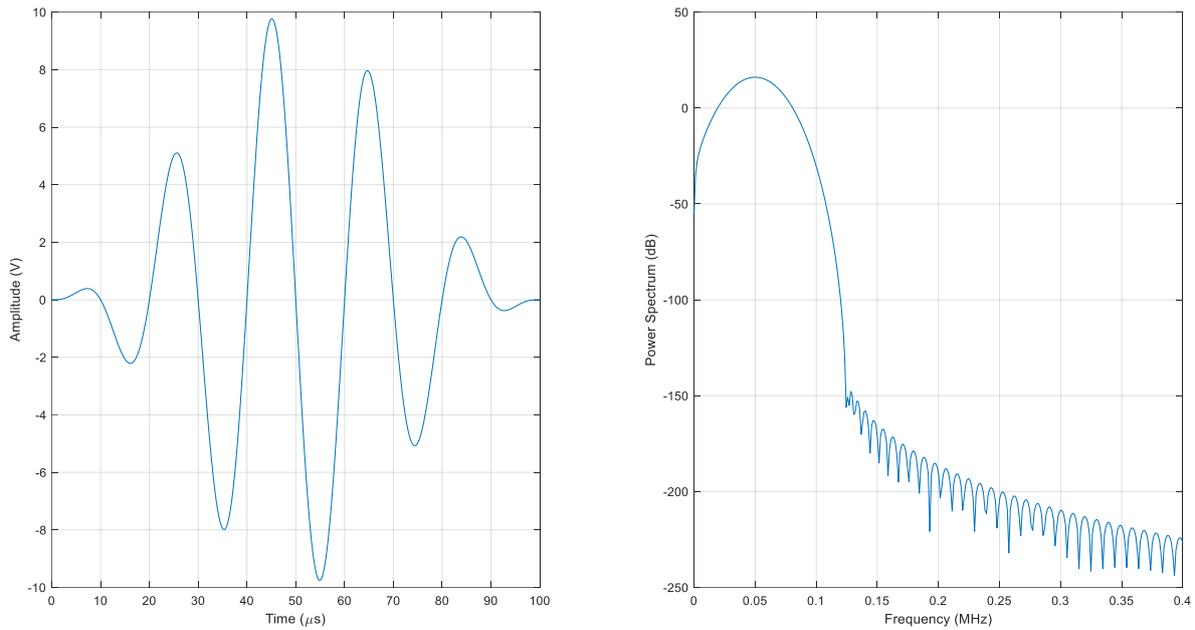


Figure 123. A 50kHz sinusoidal signal (left) and the associated frequency spectrum (right)

Each of these signals were created by the Red Pitya and used to excite the plate through the conical transducer. The frequency was changed between 50 and 400kHz at intervals of 50kHz whilst the amplitude was changed from 10 to 100V at intervals of 10V using 100x amplification from the Krohn-Hite Amplifier. Each shape/frequency/ amplitude combination was repeated 10 times with a 3 second interval between each pulse.

6.2.2. Results

Before serious efforts can be made to characterise signals from a build, it is important to understand how the structure of a signal is altered before it reaches the sensor. A key question was whether signals from demonstrably different sources were separable, or does the amplification and attenuation of different frequencies mean that different signals converge on a similar result.

Figure 124 shows the peak amplitude results for signals recorded at each of the 4 waveguides, with each section being the frequency from 50kHz up to 400kHz. It can

be seen the consistently largest amplitude response occurred at 100kHz for each waveguide design.

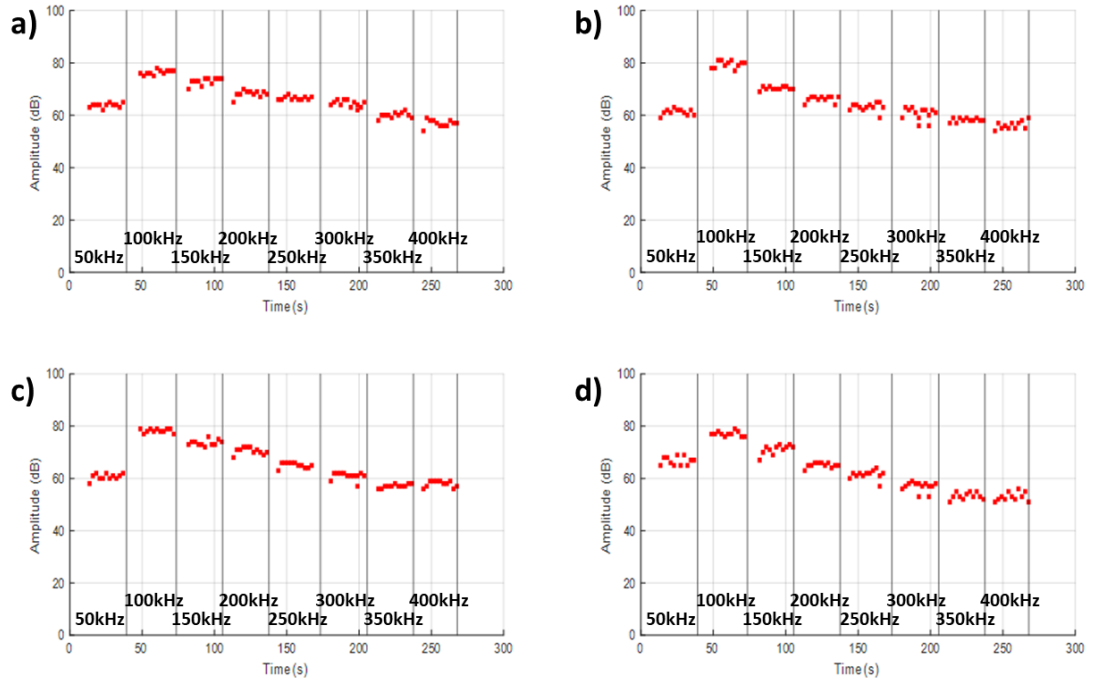


Figure 124. Amplitude of 70V sine wave signals that have travelled along a) Waveguide 1, b) Waveguide 2, c) Waveguide 3, d) Waveguide 4

Figure 125 is a similar plot for the signals recorded on the build plate which shows that the peak at 100kHz is specific to the waveguides as the same signals have a relatively low response at 100kHz and instead peak around 250kHz. This also means that the high response at 100kHz is not due to the conical transducer.

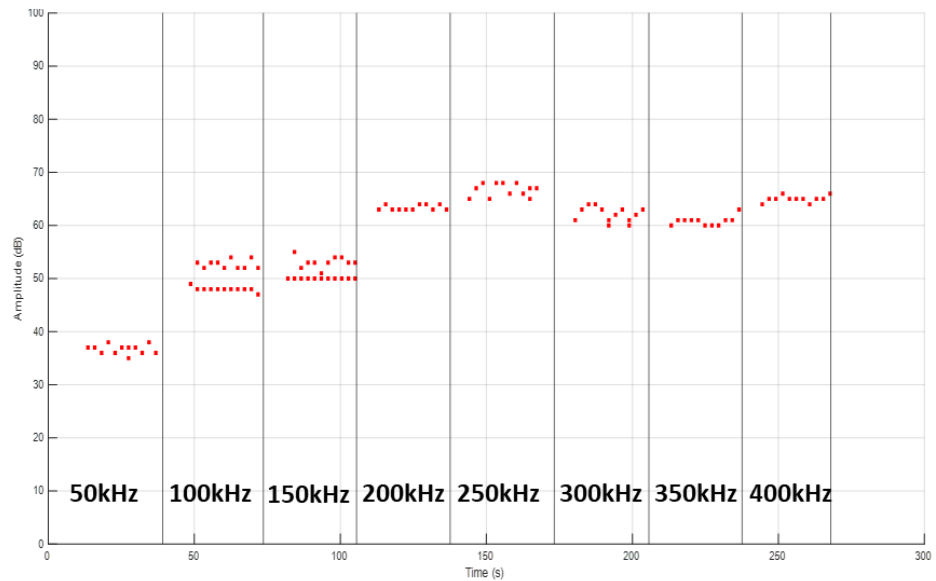


Figure 125. Amplitude of 70V sine waves at 50-400kHz recorded in a sensor on the build plate adjacent to the actuator

Figure 126 to Figure 128 show waves of each shape that have travelled down the length of the waveguide. It shows that after the initial arrival reflections begin to arrive around 80 microseconds later, which is in line with the time taken for the A_0 signal to reflect back along the waveguide and off the waveguide base back to the sensor. The peak amplitude of the full signal can also be seen after this point, likely due to the superposition of multiple reflections. This means that in order to get features representative of the initial arrival the signals needed to be altered to cut out the reflections.

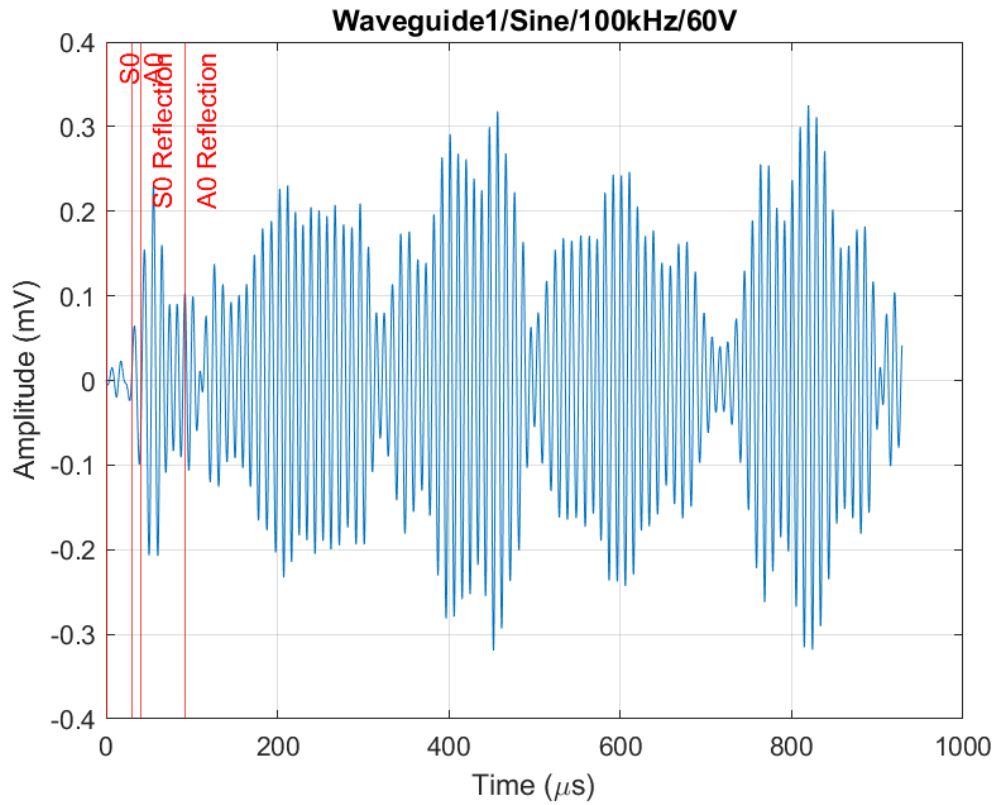


Figure 126. Waveform of Sine wave that has travelled through waveguide 1

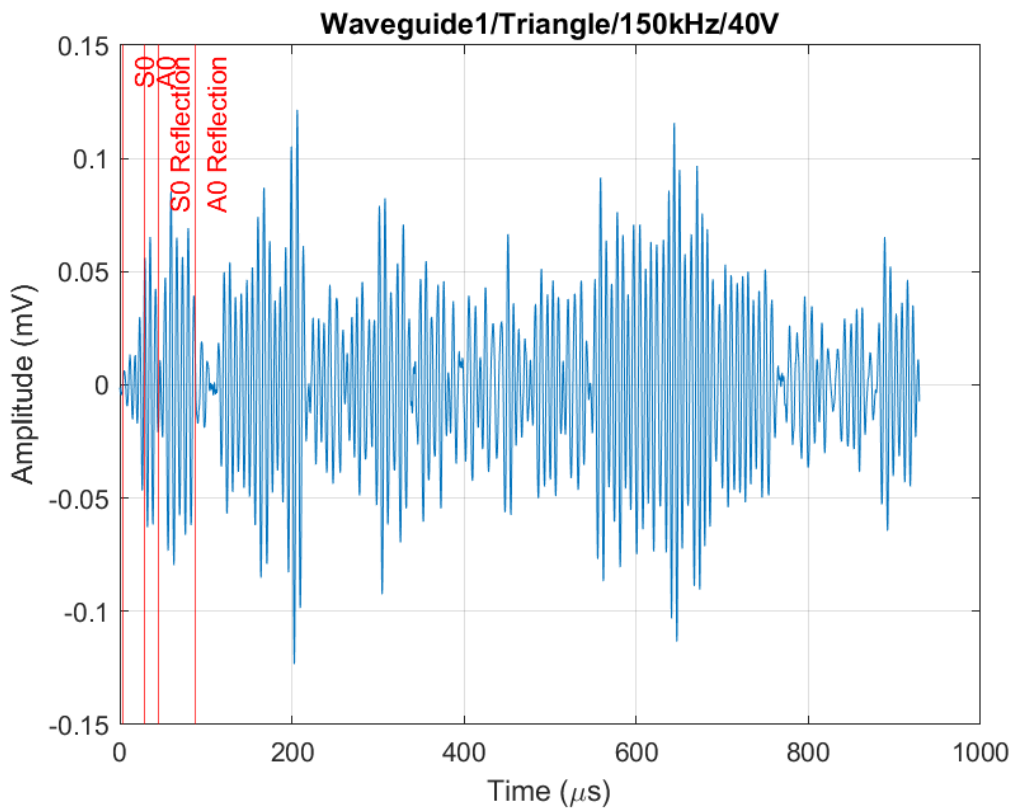


Figure 127. Waveform of a triangle wave that has travelled through waveguide 1

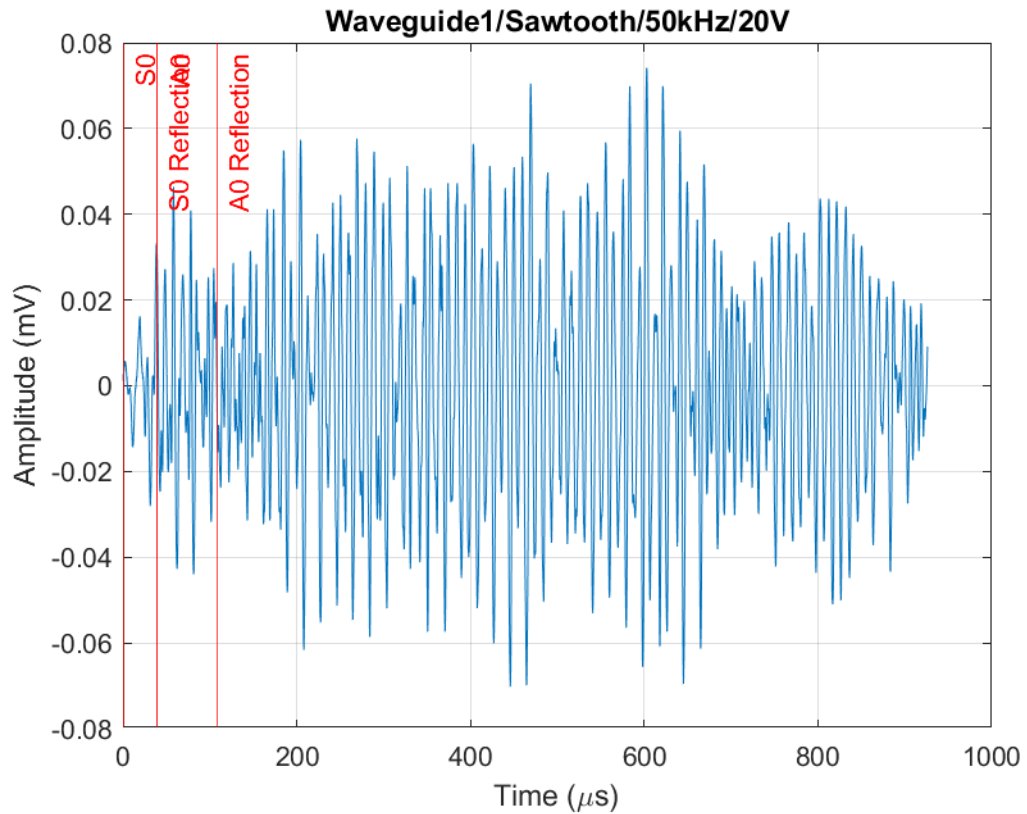


Figure 128. Waveform of a sawtooth wave that has travelled through waveguide 1

The waveforms were cut by using AIC to identify the beginning of the signal, and then cutting it off 80 microseconds later when the first reflections arrive. Before beginning feature extraction, the frequency content was observed as this would give a good idea of any shifts that occur along the waveguide. Figure 129 to Figure 131 are a selection of Fourier transforms of different shaped signals along the waveguide. These have been clipped so that the spectrum is not affected by reflections.

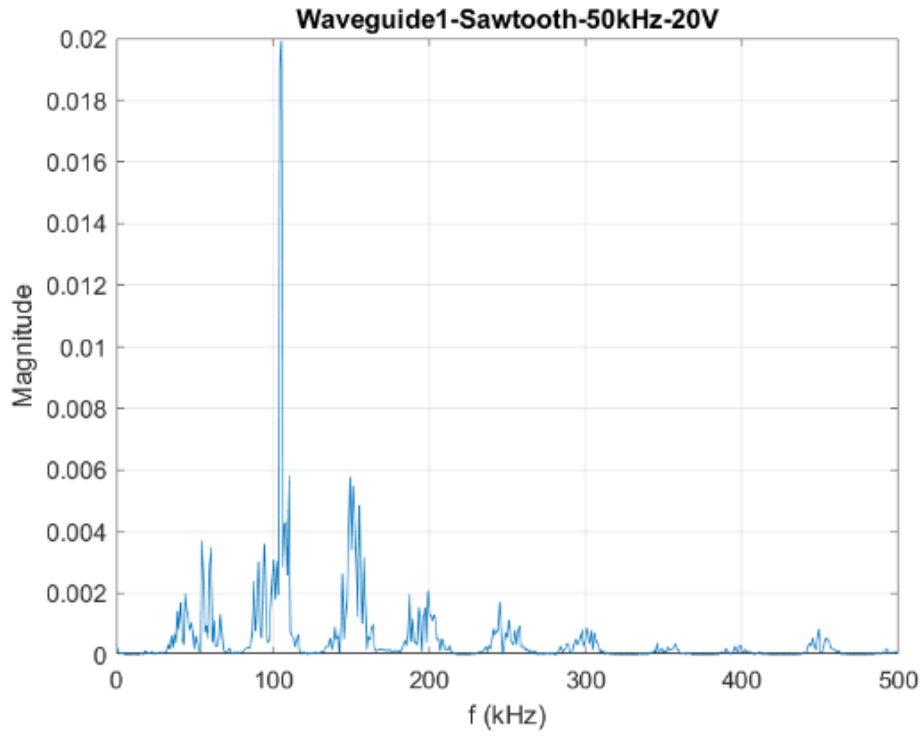


Figure 129. Fourier transform of a 50kHz sawtooth signal that has travelled along waveguide 1

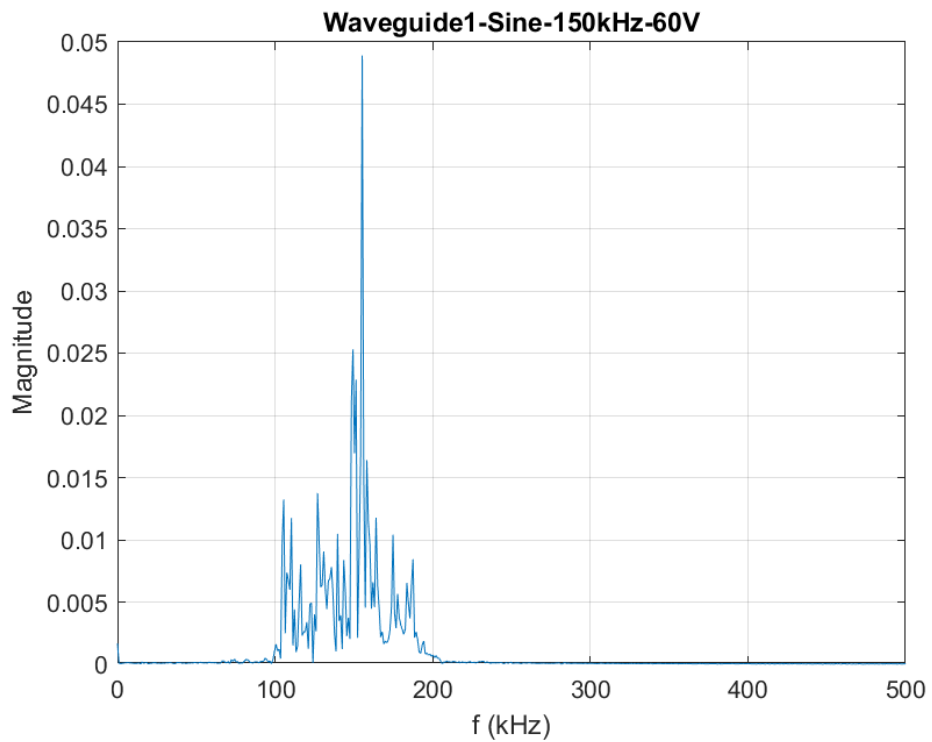


Figure 130. Fourier transform of a 150kHz sine signal that has travelled along waveguide 1

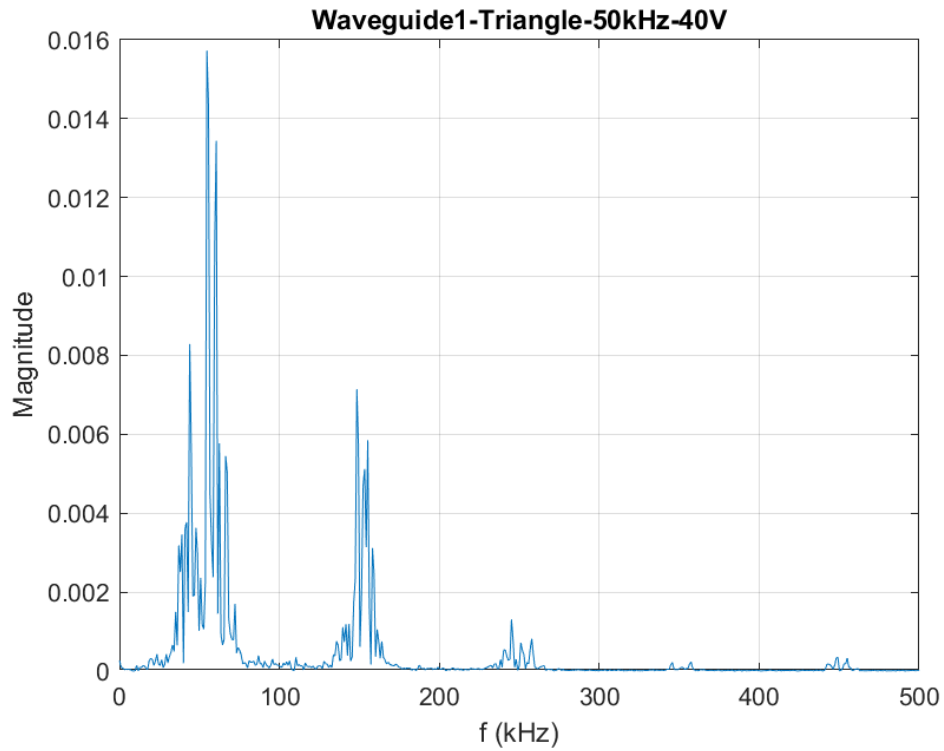


Figure 131. Fourier transform of a 50kHz triangle signal that has travelled along waveguide 1

Figure 132 to Figure 134 are Fourier transforms of the same signals as shown previously, but recorded in the build plate before the signal has reached the waveguide. The frequency content of each is similar, showing that no particular frequency is amplified by the reflections.

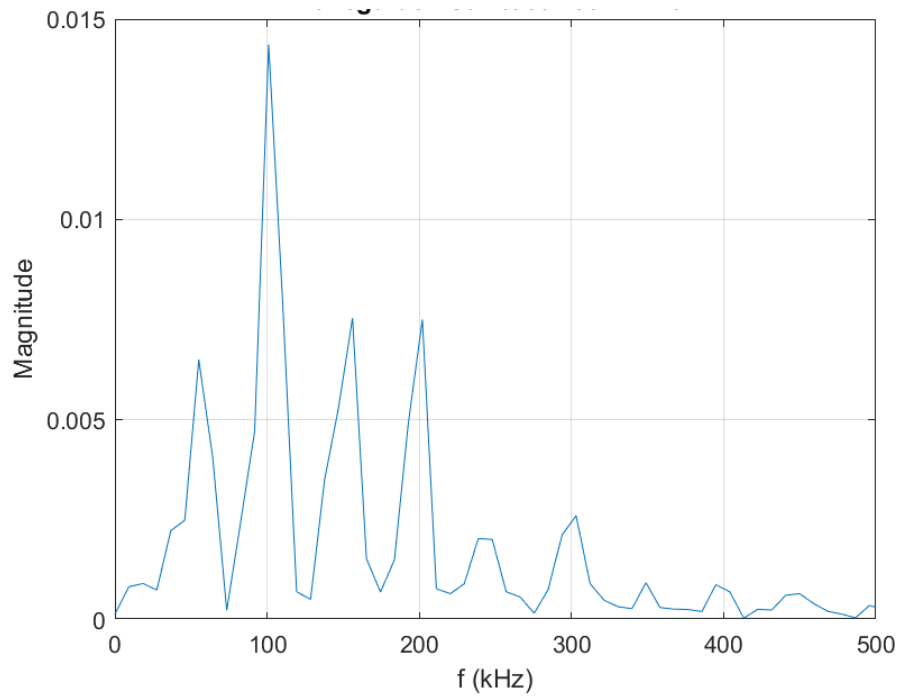


Figure 132. Fourier transform of a 20V 50kHz sawtooth signal in plate

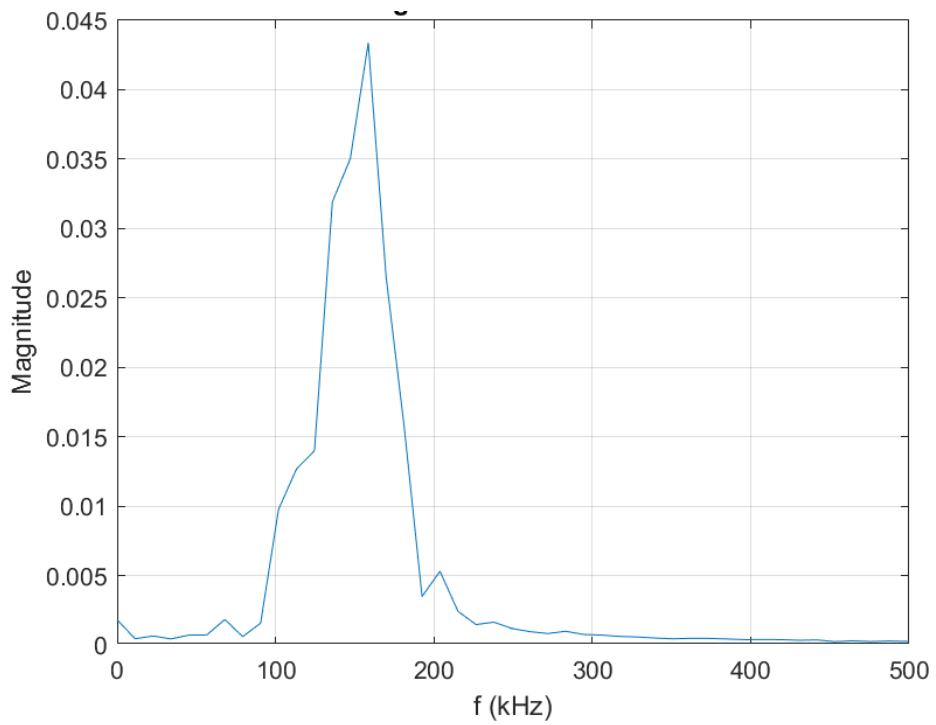


Figure 133. Fourier transform of a 60V 150kHz sine signal in plate

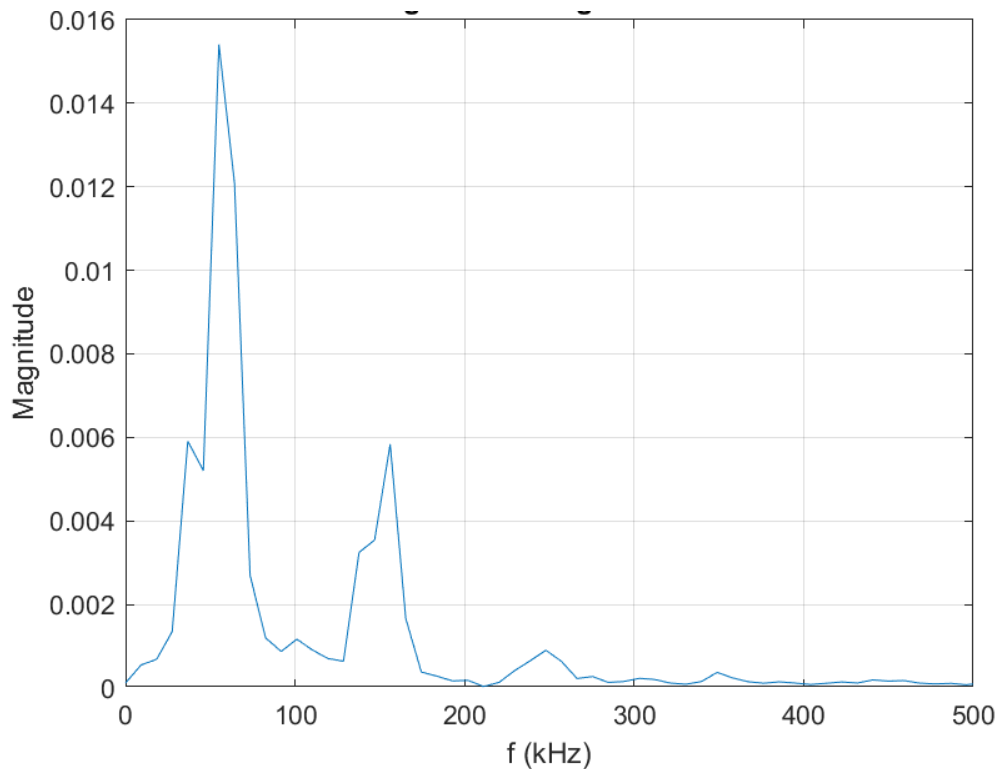


Figure 134. Fourier transform of a 40V 50kHz triangle signal in plate

A principal component analysis was then carried out on the data collected, combining all of the input amplitudes and frequencies for each waveshape and waveguide. To do this 26 separate features were extracted from the data:

- **AE Features-** Rise time, counts to peak, counts, energy, duration, amplitude, average signal level, average frequency, RMS, initiation frequency, reverberation frequency, signal strength, absolute energy, frequency centroid and peak frequency
- **Statistical Features-** Mean, skewness, kurtosis
- **Wavelet Features-** peak frequency at 20, 40 and 60 μ s from signal onset, peak magnitude at 100, 200, 300, 400 and 500kHz

Feature reduction using correlation coefficients with a threshold of 0.75 was then carried out, and these remaining features were normalised to give a mean of zero and a standard deviation of 1. The remaining 14 features were:

- **AE Features**- Rise time, counts, average signal level, absolute energy, frequency centroid
- **Statistical Features**- Mean, skewness, kurtosis
- **Wavelet Features**- peak frequency at 60 μ s from signal onset, peak magnitude at 100, 200, 300, 400 and 500kHz

A PCA was then carried out to transform these 14 features to a new variable set, with the aim being for the variance of the data to become more concentrated in two plottable principal components. As shown in Figure 135, the two primary principal components account for over 50% of the variance of the data.

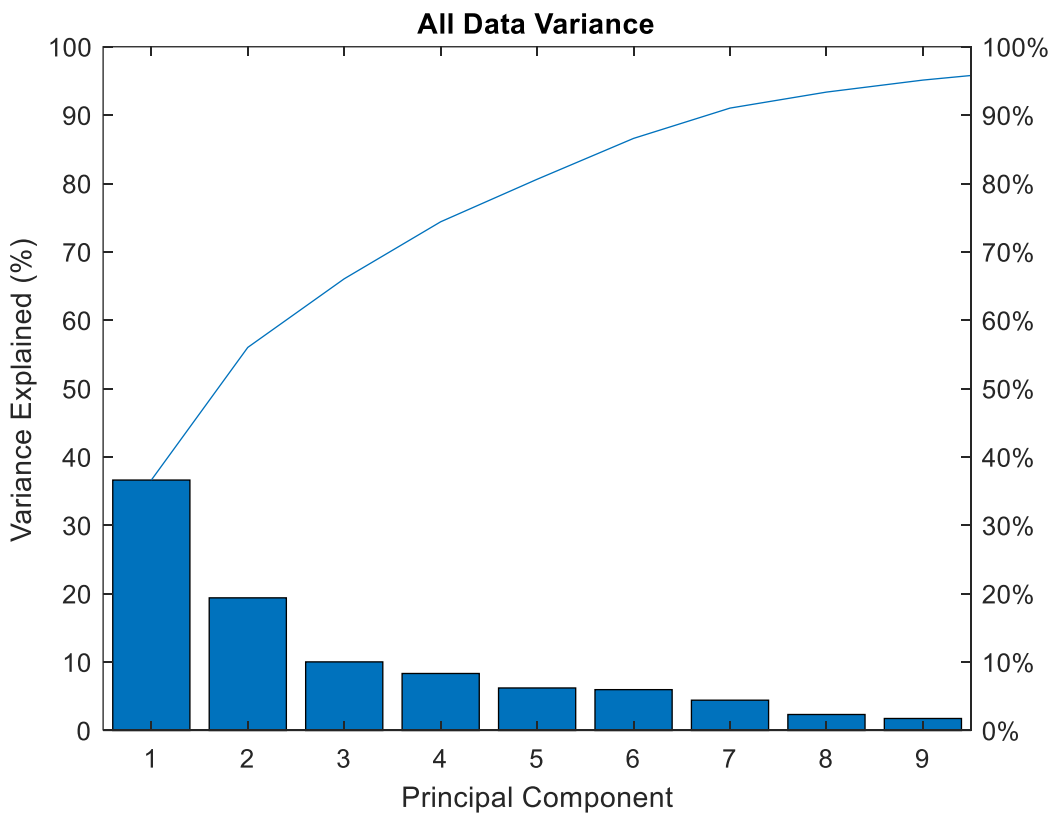


Figure 135. A scree graph of the data variance accounted for by each principal component

The breakdown of the top two principal components that were used to plot data is given in Table 8. All values are between -1 and 1, and are a measure of the variation that each variable gives to that principal component. This shows that the

rise time and the skewness variables have the greatest influence over principal component 1, whilst principal component 2 is most dependent upon counts and average signal level. Interestingly, though the wavelet features were independent of each other they have very little affect on the variance of the data.

Table 8. Table showing the contribution of each feature to the top two components of the principal component analysis

Variables		Principal Component 1	Principal Component 2
AE Features	Rise time	0.509	-0.284
	Counts	0.395	0.546
	Average Signal Level	0.042	0.573
	Absolute Energy	0.073	0.062
	Frequency Centroid	0.026	-0.197
Statistical Features	Mean	0.006	-0.363
	Skewness	-0.495	-0.033
	Kurtosis	0.482	-0.229
Wavelet Features	Peak Frequency at 60 μ s from onset	-0.115	0.235
	Peak Magnitude at 100kHz	-0.129	-0.043
	Peak Magnitude at 200kHz	-0.191	-0.057
	Peak Magnitude at 300kHz	-0.182	-0.070
	Peak Magnitude at 400kHz	-0.156	-0.068
	Peak Magnitude at 500kHz	0.048	0.035

These two principal components were then plotted as scatter plots, shown in Figure 136. This plot highlights each of the three waveshapes applied. This shows little separation between the waveshapes, which shows a despite different input signals the signals are indistinguishable with the selected features at the sensor.

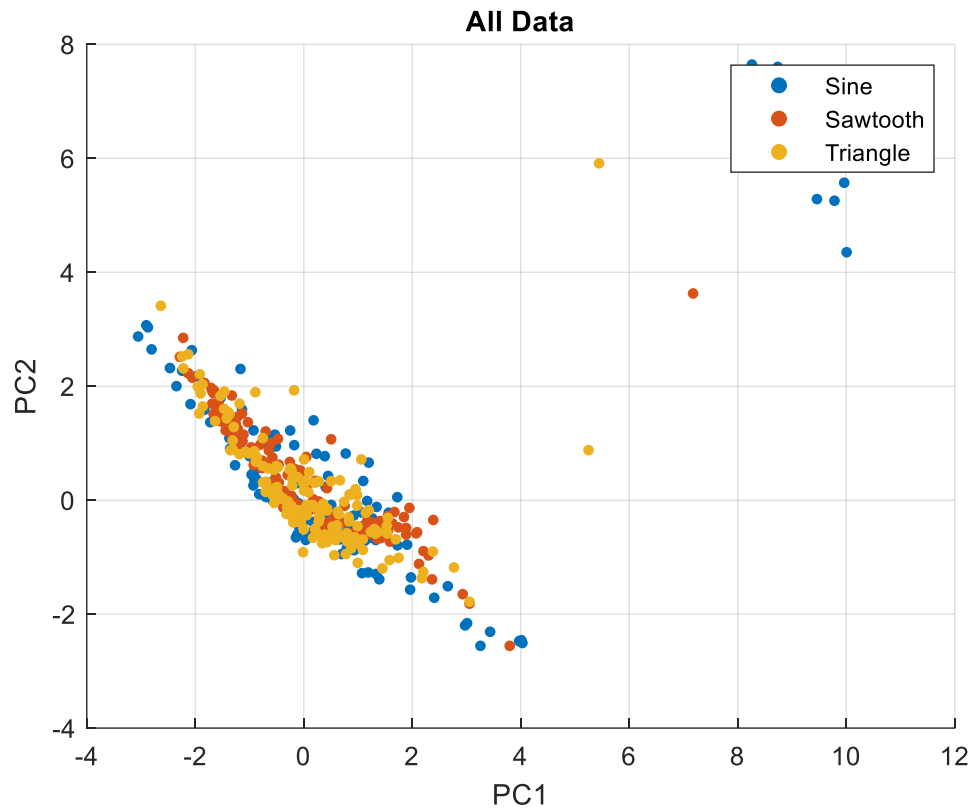


Figure 136. Scatter plot of the two primary principal components, with the different waveshapes highlighted

Figure 137 shows this same data with the different waveguide geometries highlighted instead of waveshape. It seems that each waveguide geometry also produces very little separation between the signals.

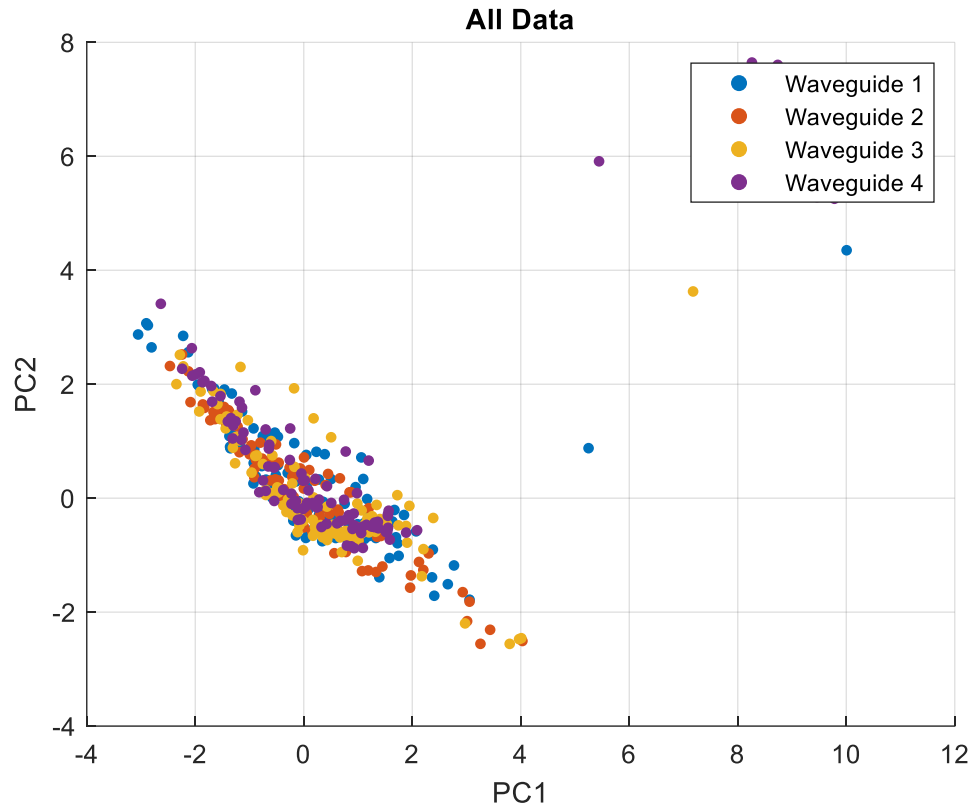


Figure 137. Scatter plot of the two primary principal components, with the different waveguide geometries highlighted

6.2.3. Discussion

This study has shown that the waveguides have a significant impact on the frequency content of the signal, with certain frequencies amplified over others. This is shown by the comparing Figure 124 and Figure 125 where the frequencies producing the highest amplitudes in the plate are different from the from the frequencies producing the highest amplitudes in the waveguides. Extracting AE, statistical and wavelet-derived features for presenting with PCA gave little separation between the signal groups, either when separating by waveguide geometry or waveshape. This indicates that the signals are undergoing a significant amount of tuning as they travel along the waveguide, which may present a challenge when classifying defect types.

6.3. Effect of Plate Thickness on Signals

6.3.1. Experimental Procedure

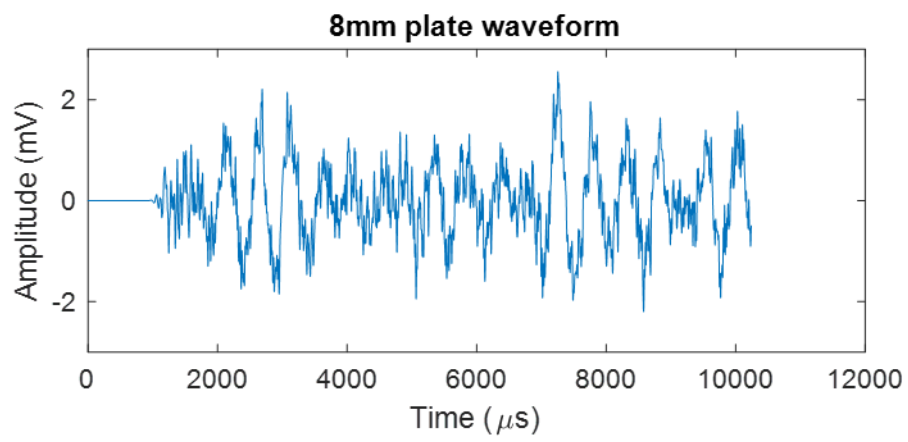
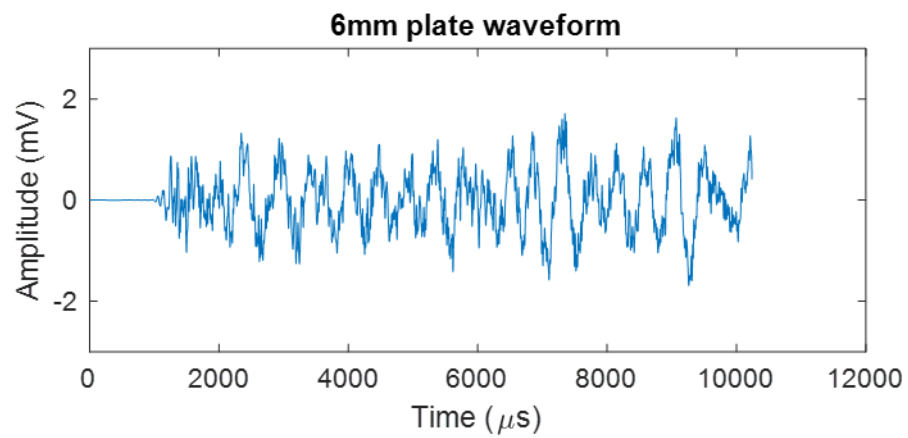
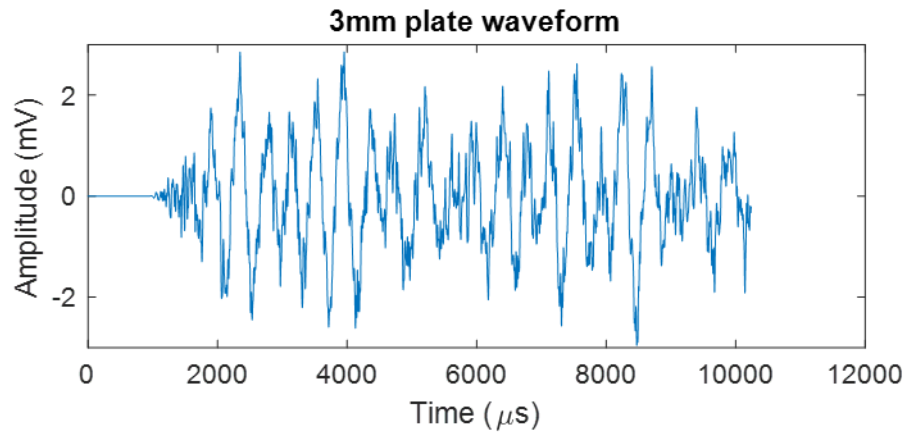
In Section 5.3, work was undertaken to investigate how the thickness of the build plate affects location. In this chapter, the waveforms produced in different thicknesses are compared to examine how the features of a waveform change with thickness. As described in Section 5.2.1., delta-T data collection meant that there were a large number of waveforms collected from each thickness that could be used to identify waveform differences across thicknesses. Standard AE features were extracted, as well as features extracted by statistical and wavelet methods for comparison. The mean, skewness and kurtosis were calculated from each waveform. Wavelet transforms were carried out for each waveform, and used to take the maximum frequency at 20, 40 and 60 μ s through the signal. The peak magnitude at 100, 200, 300, 400 and 500kHz were also extracted. These features were then reduced to only features with a high degree of independence from each other so that dependent variables wouldn't skew the results. This was completed by calculating the correlation coefficient between all pairs of variables, and removing any variable with a correlation coefficient greater than 0.75. The principal components analysis method was then used to further reduce this to two components that can be easily presented graphically to highlight groupings.

6.3.2. Results

The characterisation of signals using either supervised or unsupervised learning relies on collecting large amounts of data for each possible defect type and using this to train a machine learning algorithm. However, this requires signals of a similar origin to have a similar form after propagation to the recording sensor, so that the

algorithm can properly characterise them. With the plate thickness changing with each build a situation may arise where similar origins produce very different waveforms, making characterisation impossible.

Figure 138 to Figure 140 present waveforms from each thickness adjacent to the sensor, at the plate centre, and at the opposite corner to the sensor. Each signal is collected via a simple Hsu-Nielsen source. These show how the waveform changes with thickness, with amplitude generally falling as the plate thickness increases.



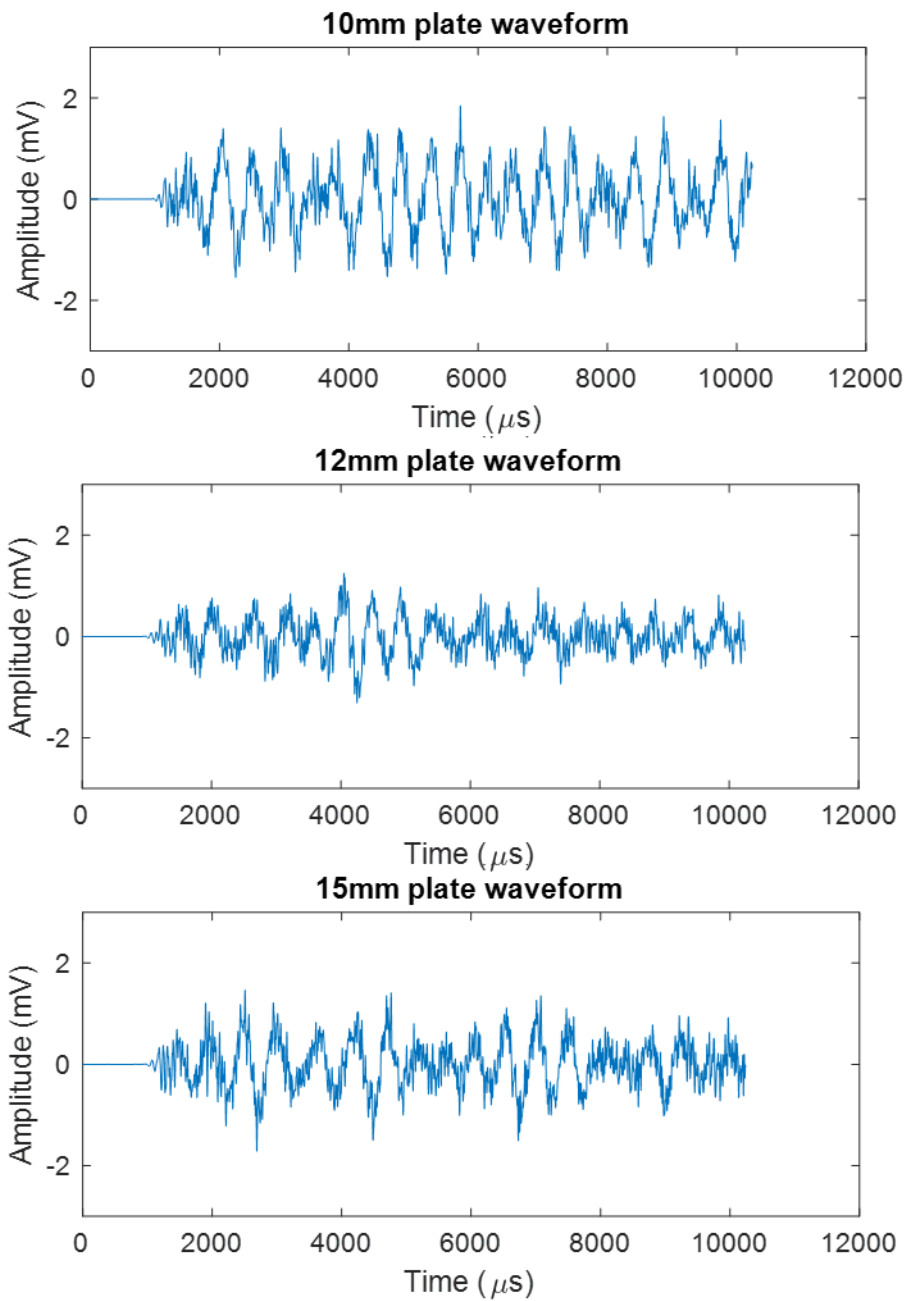
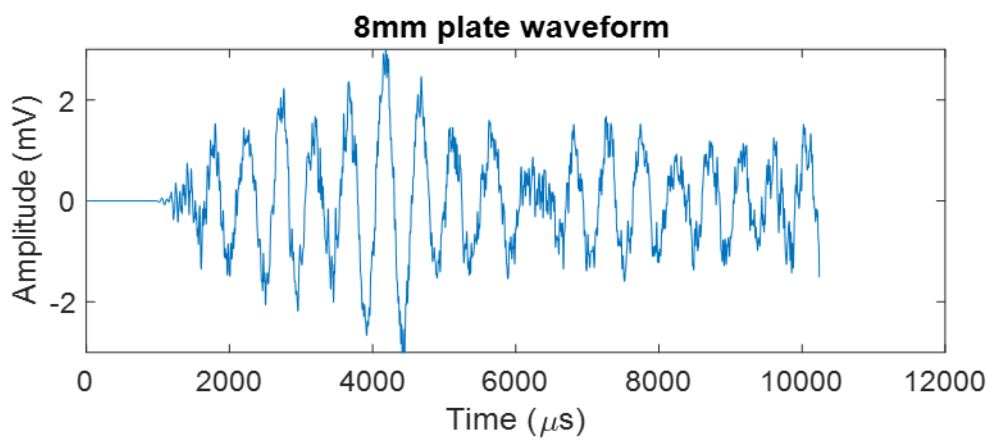
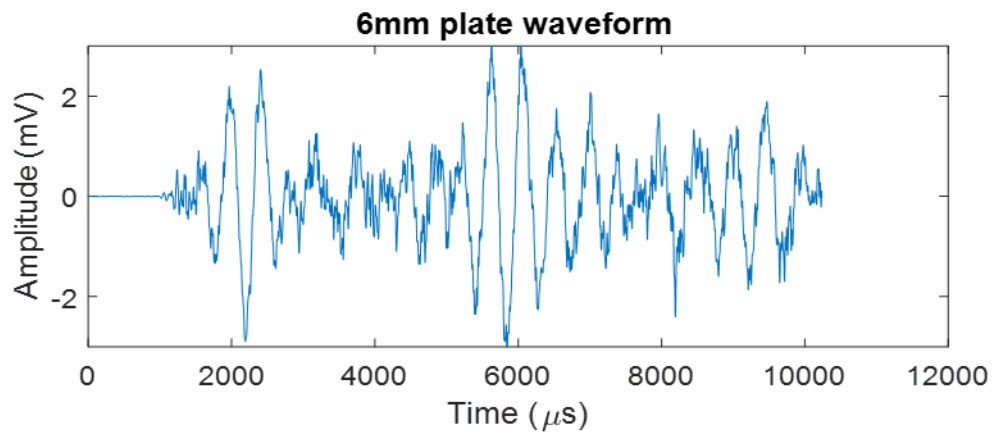
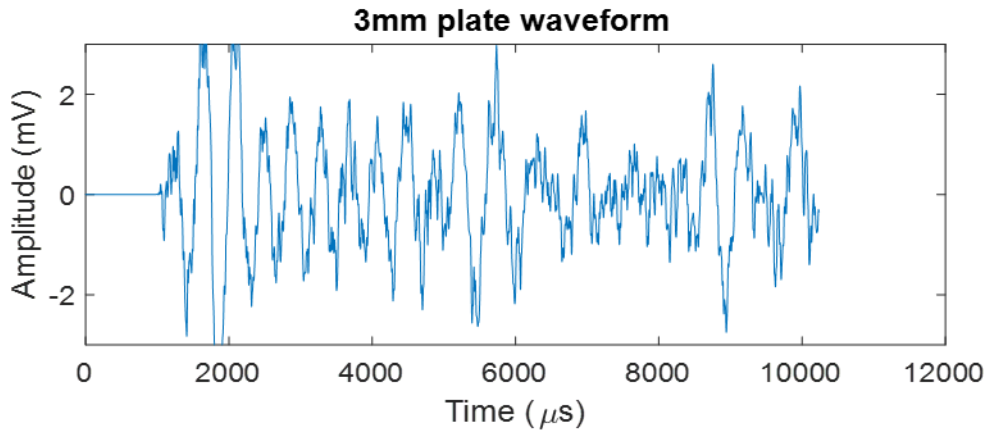


Figure 138. Waveforms from each thickness that were generated adjacent to the top of the waveguide



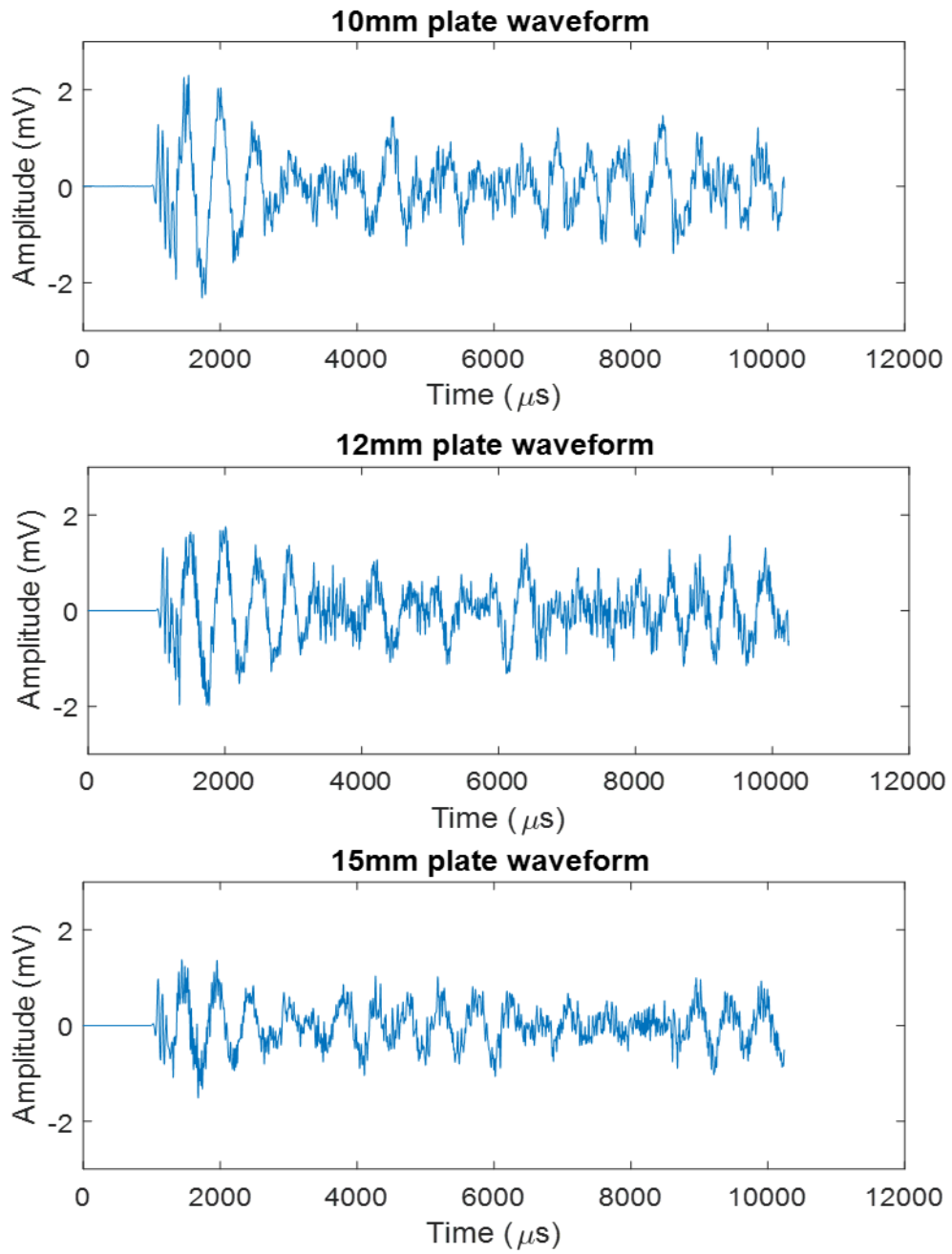
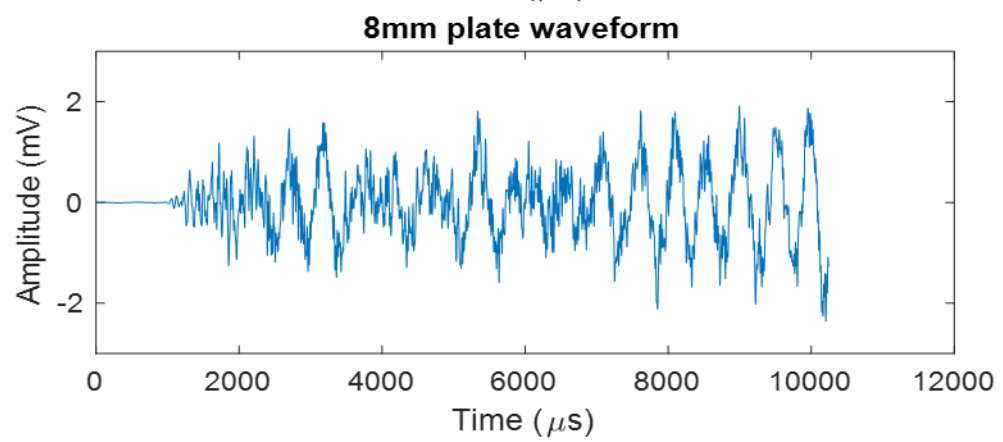
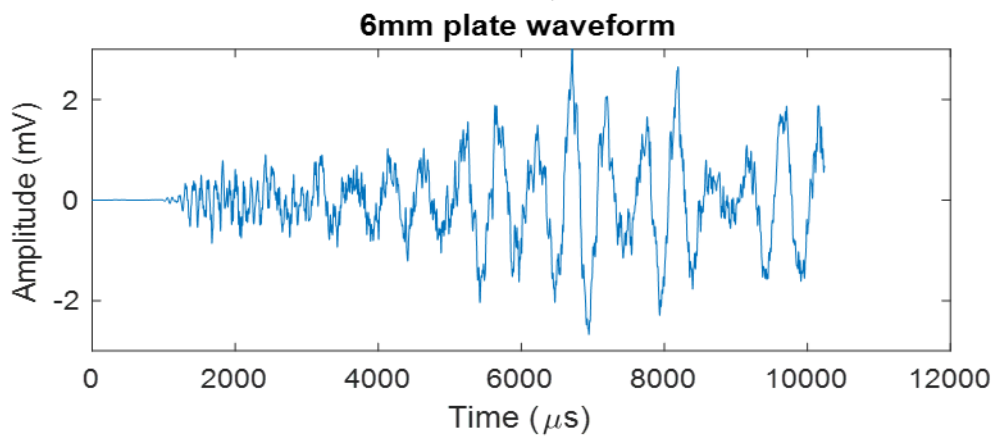
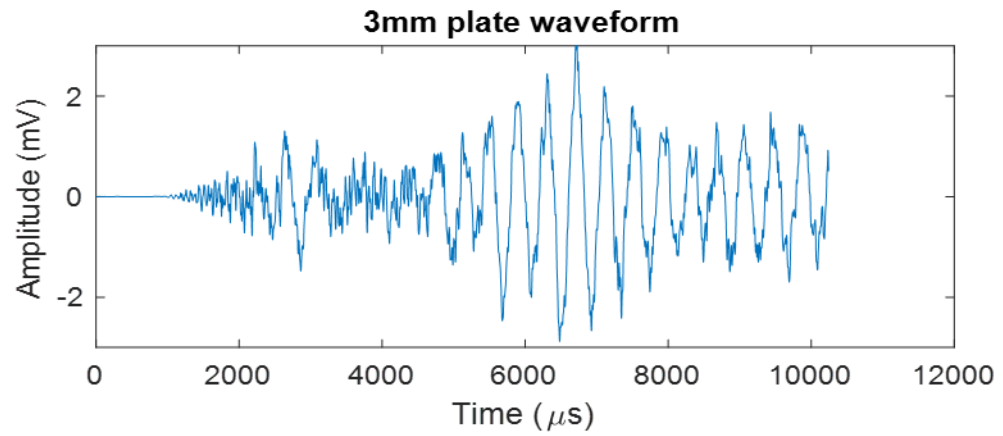


Figure 139. Waveforms for each thickness that were generated at the centre of the build plate



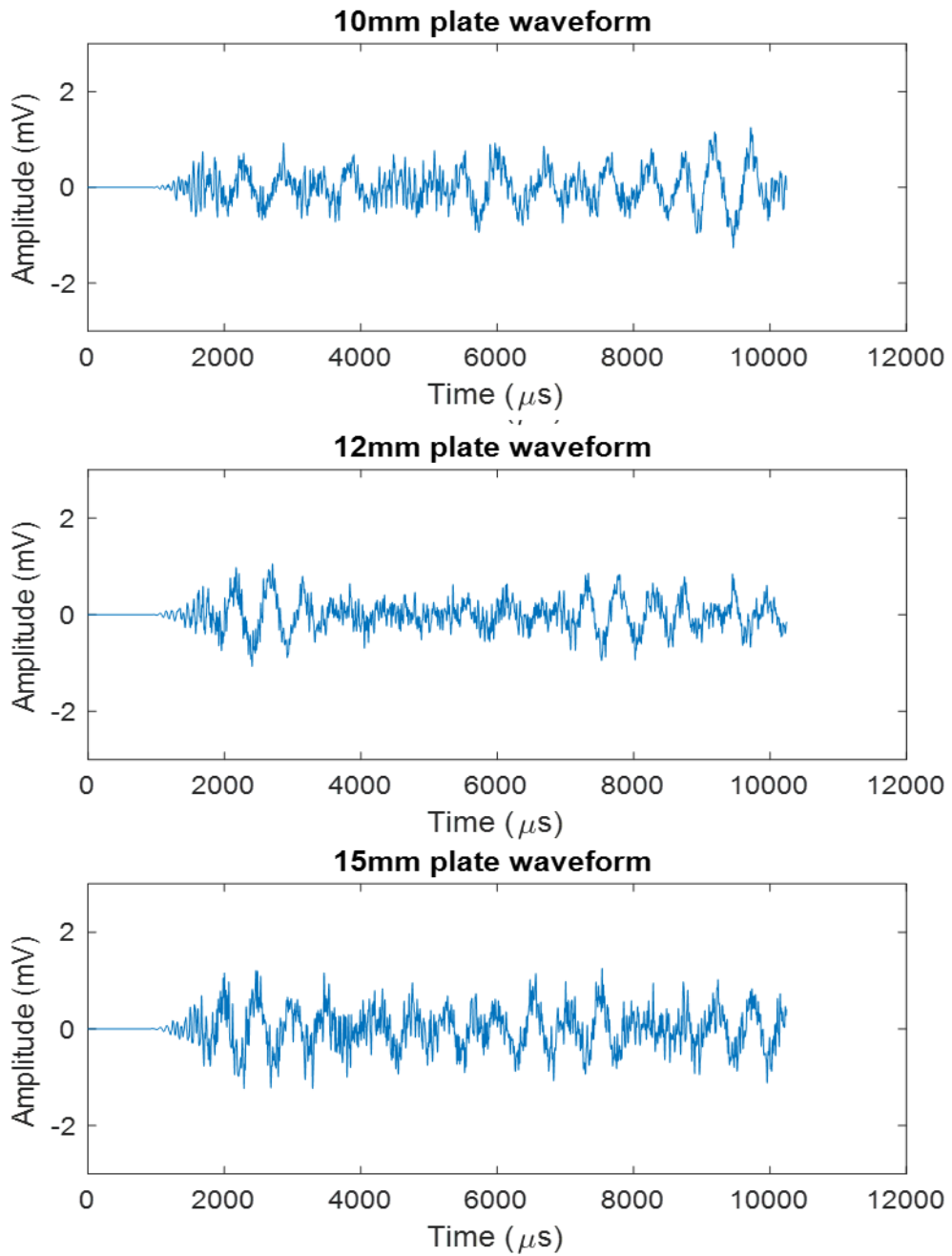


Figure 140. Waveforms for each thickness that were generated at the opposite corner of the build plate to the sensor

Differences in the signals for each thickness can also be illustrated by the frequency content from wavelet transforms, as shown by Figure 141 to Figure 146. As the thickness increases, the intensity at lower frequencies (around 50kHz) reduces likely due to the effects of dispersion. Based on the reflection study carried out in Section

4.3, these signals can be seen to be largely made up of reflections which continue to propagate for the full 1ms length of the signal for every thickness.

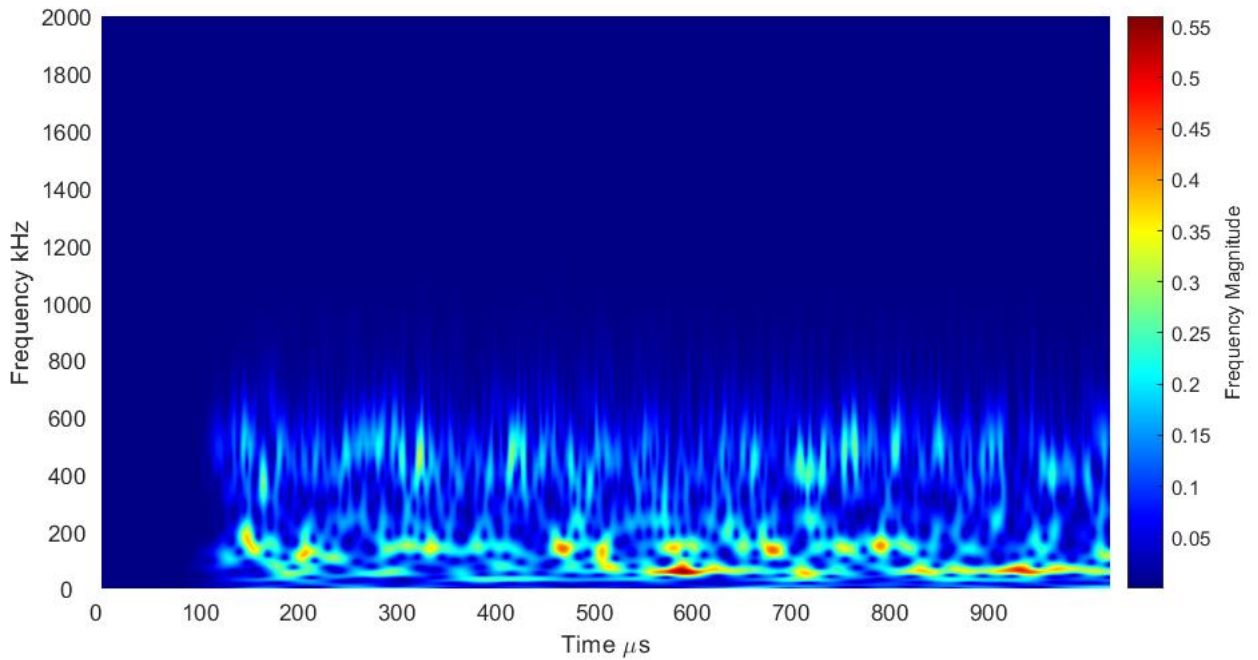


Figure 141. Wavelet transform of a signal originating from the centre of the 3mm plate

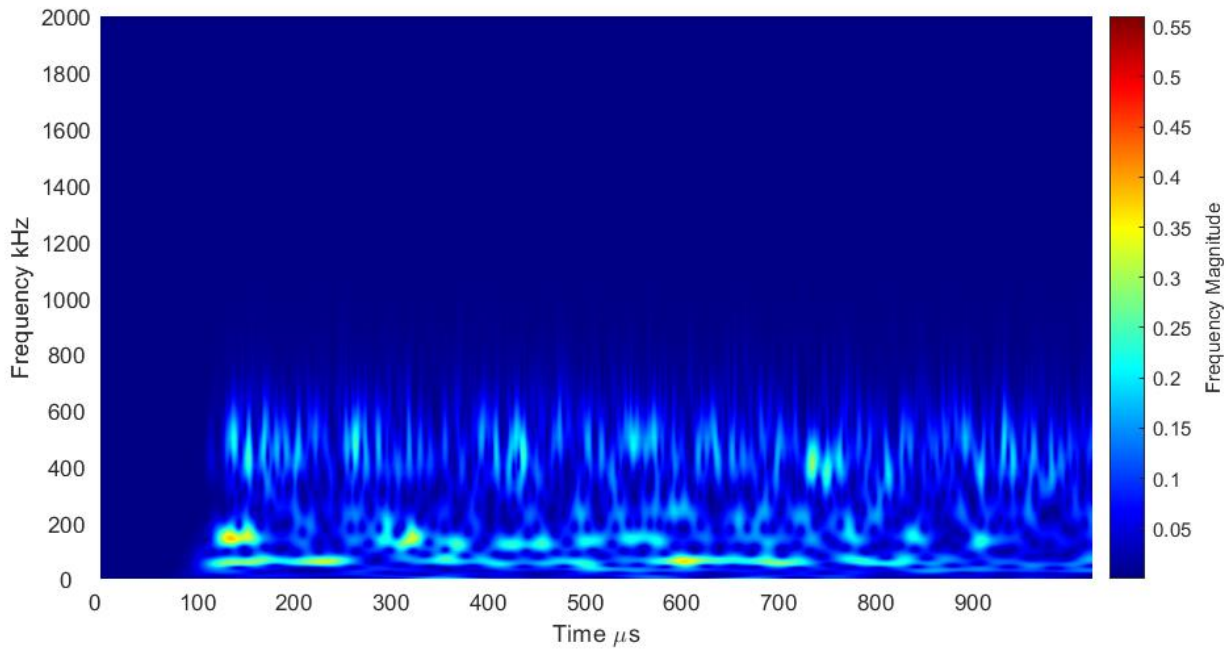


Figure 142. Wavelet transform of a signal originating from the centre of the 6mm plate

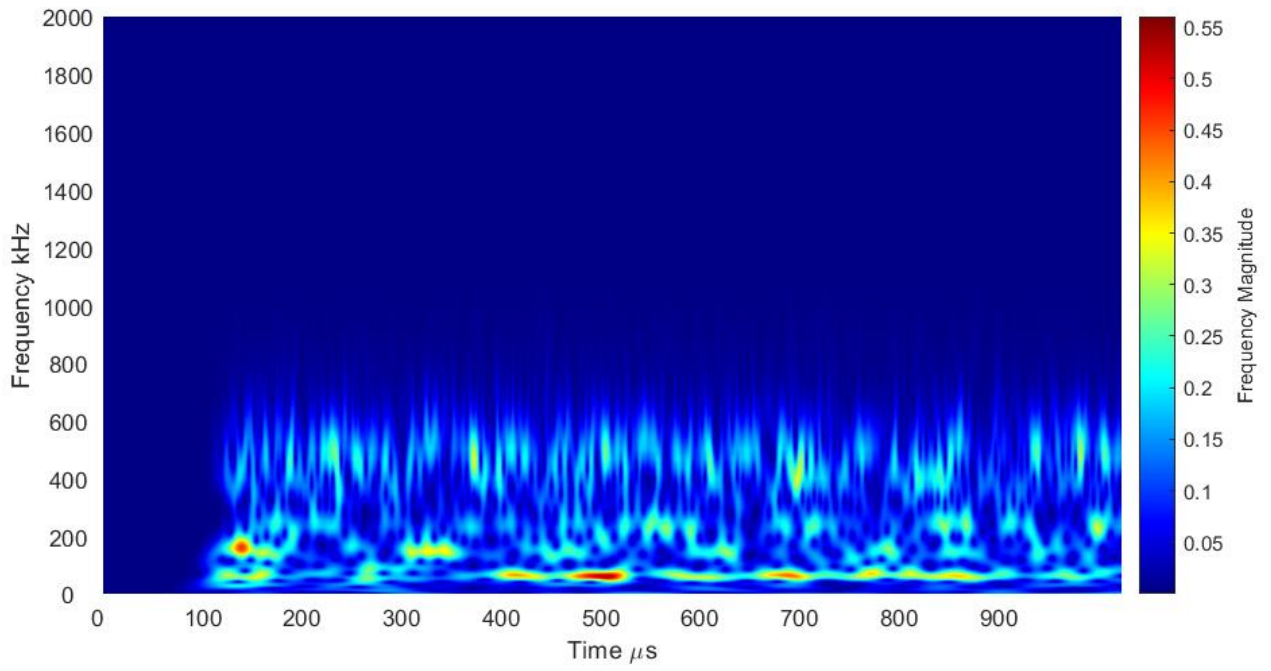


Figure 143. Wavelet transform of a signal originating from the centre of the 8mm plate

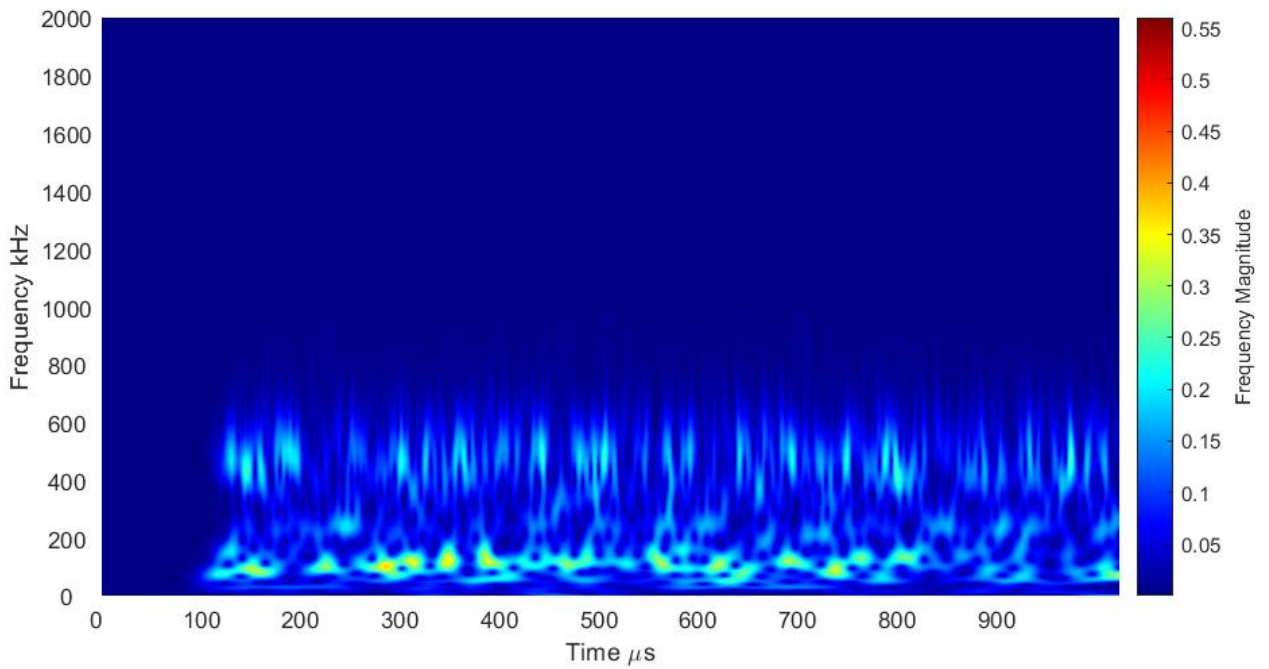


Figure 144. Wavelet transform of a signal originating from the centre of the 10mm plate

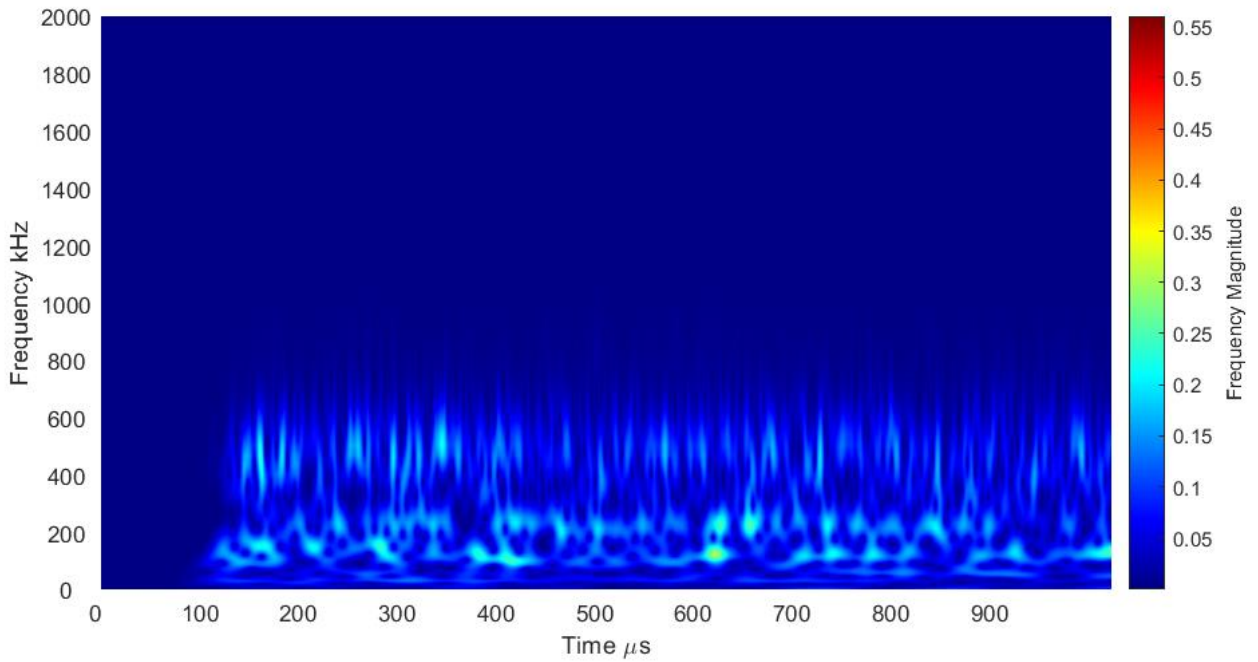


Figure 145. Wavelet transform of a signal originating from the centre of the 12mm plate

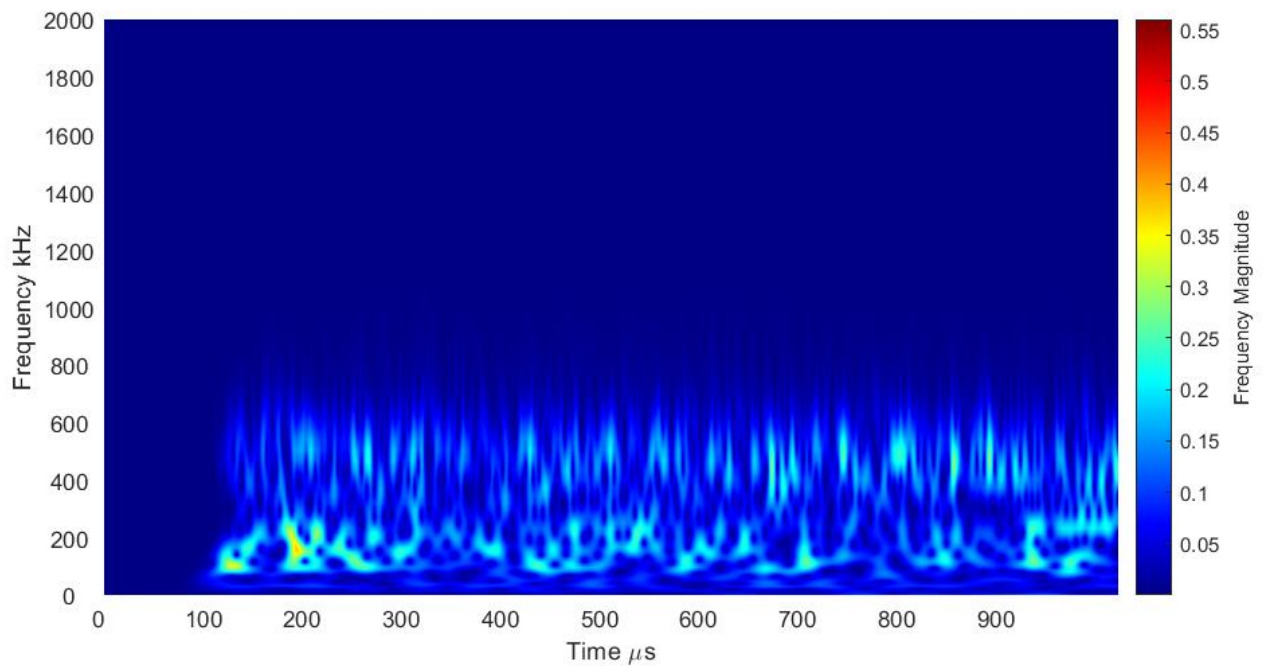


Figure 146. Wavelet transform of a signal originating from the centre of the 15mm plate

In order to characterise the signals, features need to be extracted to represent each signal. This was performed in the same way as described for waveguide comparison in Section 6.2.2, with the same 26 features extracted. The correlation between these features is then used to reduce to the most independent features, and they are

mean and standard deviation adjusted. This still left the same 14 features, so PCA was used to reduce this to two plottable variables. The breakdown of which variables contribute to these principal components is shown in Table 9. This shows that the first principal component is most greatly influenced by rise time, counts, average signal level and peak magnitude at 200 and 300kHz. Meanwhile, the second principal component is most greatly affected by rise time, average signal level, skewness and peak magnitude at 200kHz. However, as seen in Figure 147, these two principal components only account for around 35% of the variance of the data.

Table 9. Table showing the contribution of each feature to the top two components of the principal component analysis

Variables		Principal Component 1	Principal Component 2
AE Features	Rise time	0.437	0.413
	Counts	-0.434	0.284
	Average Signal Level	-0.427	0.472
	Absolute Energy	0.076	-0.227
	Frequency Centroid	0.114	0.275
Statistical Features	Mean	-0.052	-0.048
	Skewness	0.226	-0.459
	Kurtosis	-0.102	0.009
Wavelet Features	Peak Frequency at 60 μ s from onset	-0.020	0.019
	Peak Magnitude at 100kHz	0.000	-0.004
	Peak Magnitude at 200kHz	0.408	0.400
	Peak Magnitude at 300kHz	0.434	0.160
	Peak Magnitude at 400kHz	0.210	0.144
	Peak Magnitude at 500kHz	0.204	0.098

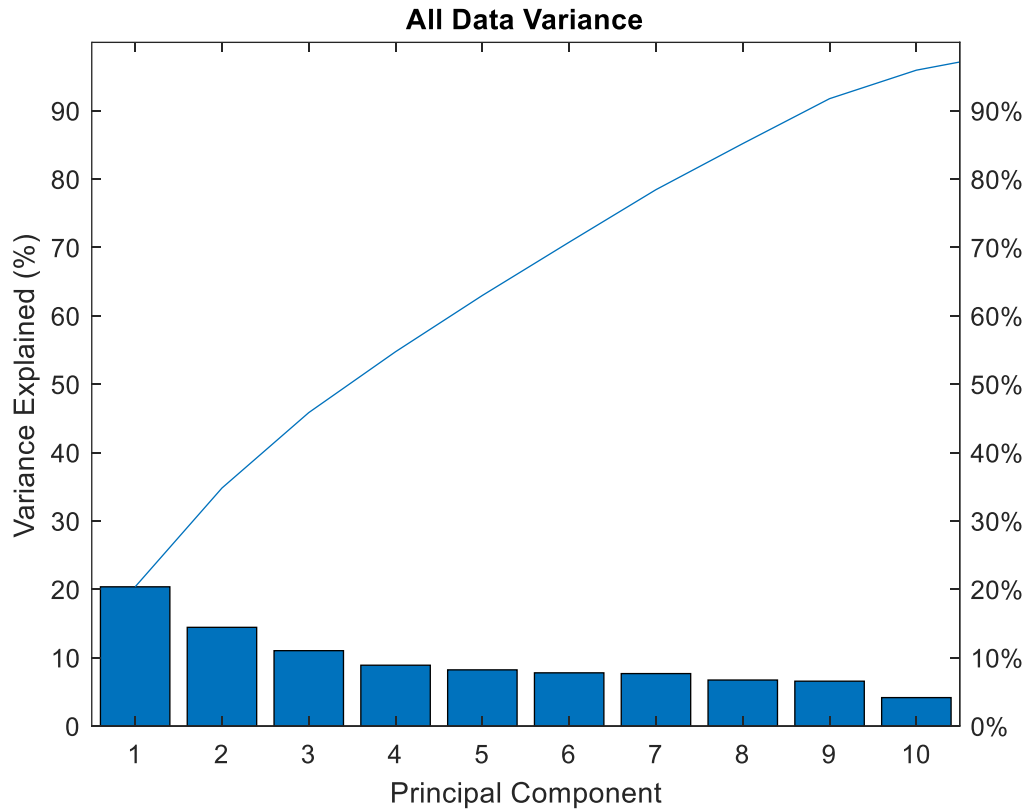


Figure 147. A scree graph of the data variance accounted for by each principal component

The results of plotting the top two principal components are shown in Figure 148. This shows that the chosen variable does not show any separation despite the differences previously shown. This suggests that characterisation may be possible with the appropriate feature selection.

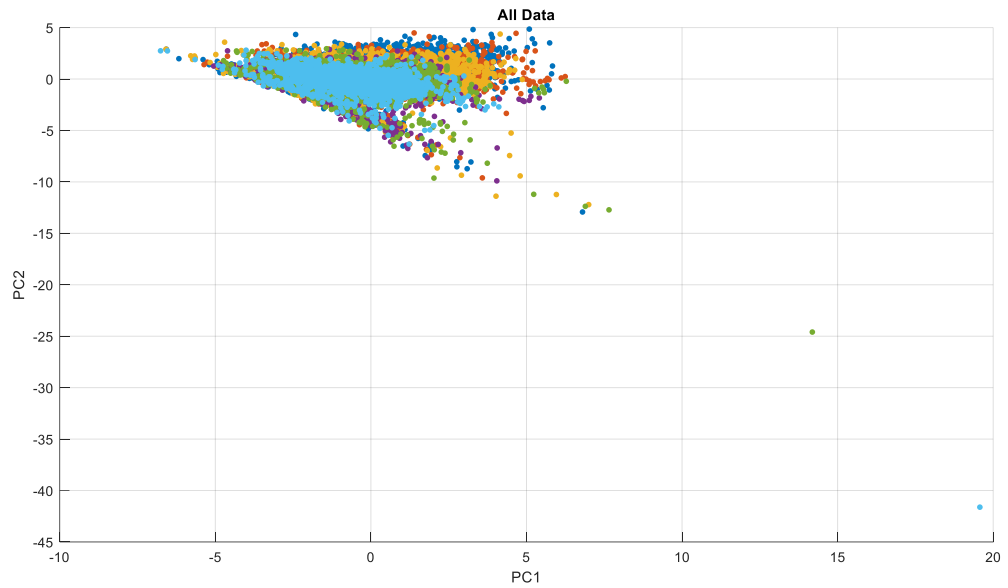


Figure 148. The two principal components of all data collected from the plates, each colour representing a different thickness

6.3.3. Discussion

The results of the principal components analysis showed very little separation between all of the thicknesses, despite the large number of features used. This is a positive outcome when it comes to classifying signal in the AM500. This means that throughout the lifetime of a build plate, similar defects will continue to be grouped together despite the change in geometry.

6.4. Separating In-Process Signals

6.4.1. Experimental Procedure

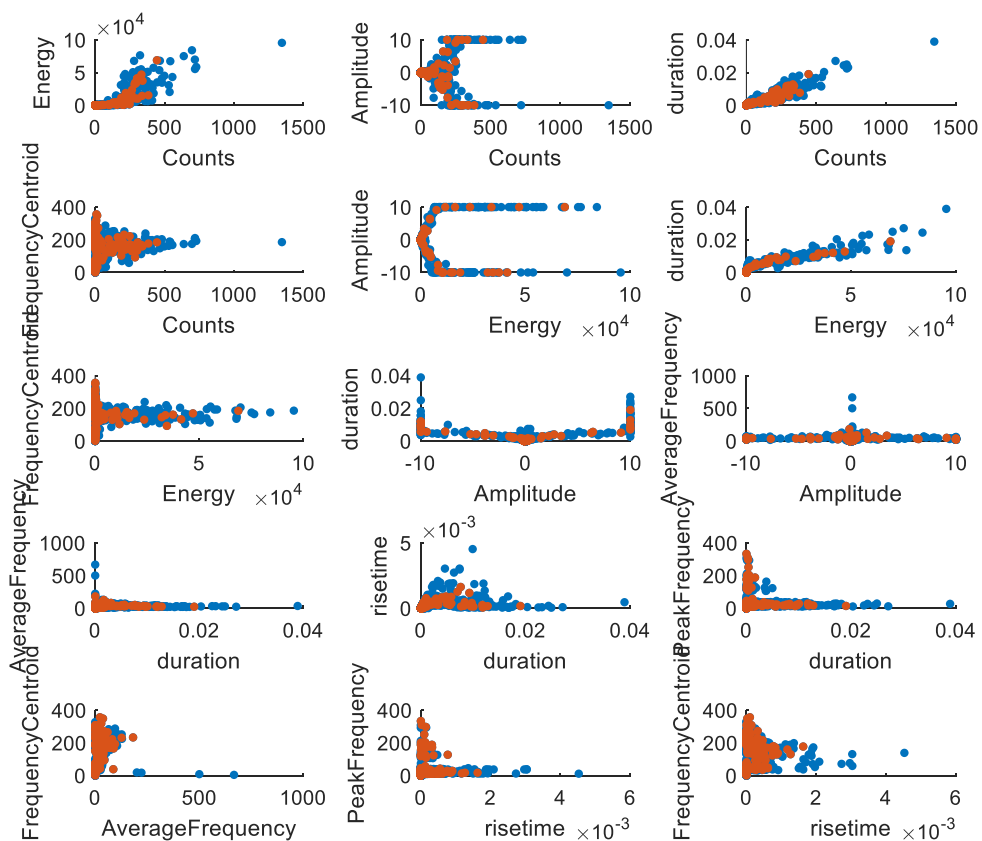
All in-process signals were collected from titanium builds within a Renishaw AM500 fitted with WD sensors. Signals were collected using an Adlink system built into the machine, that are then split into individual AE waveforms. Features were then extracted from these in the way previously described in Section 6.3.1. When the wiper is adding powder for the next layer, a pump cycles the argon atmosphere within the build chamber. Timestamps of pump activity can then be used to isolate signals which occur during the laser phase and during the wiper phase.

These were separated, and the same features used in Section 6.2.2 were extracted and reduced to 14 independent features. A principal components analysis was then carried out to see how signals recorded when the wiper is and isn't active was then carried out. A principal component analysis was then also carried out with multiple in-process data-sets pooled together to look at whether different but similar builds produce similar enough signals to train a classification model. Each of these builds was using titanium powder and build plate, however each contained different components.

6.4.2. Results

In-process signals must travel from a defect source in the print volume, through the printed material before going through the build plate and then the waveguide before reaching the sensor. This path will be different for each signal, meaning that similar defects in different parts of the build volume may produce signals that may not be grouped together by a classification algorithm. In addition, it is difficult to identify defect mechanisms around which to group signals.

One possible way to separate signals is based upon when the wiper is and isn't spreading powder across the powder bed. For one of the in-process data-sets, the timestamps of when the wiper is active and inactive were recorded and synced with AE data. The wiper is known to impact with the printed part as it deposits further powder on the bed, so signals occurring during this time were separated. Figure 149 is a scatter matrix of AE features taken from in-process signals, with red representing signals occurring during the wiper phase and blue representing the rest of the signals. These scatter graphs show little variation between wiper phase and non-wiper phase signals, and few groupings forming.



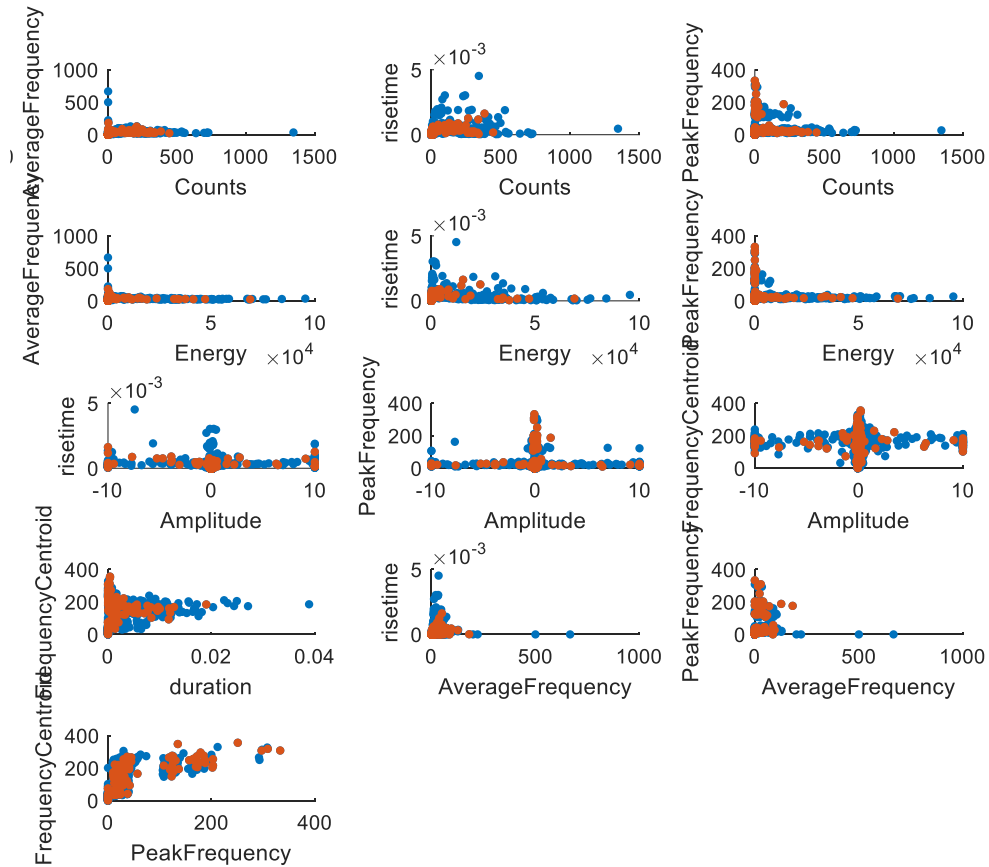


Figure 149. Scatter matrix of features taken from in-process signals

To further look into whether signals can be separated around the wiper phase, Figure 150 and Figure 151 show the distribution for each feature for wiper phase (red) and non-wiper phase (blue). For each feature the distribution is similar for both phases, suggesting that the majority of AE signals being recorded are related to neither the laser nor the wiper. Therefore it can be assumed that these signals are derived from defect mechanisms within the build volume and the laser and wiper do not produce significant AE signals.

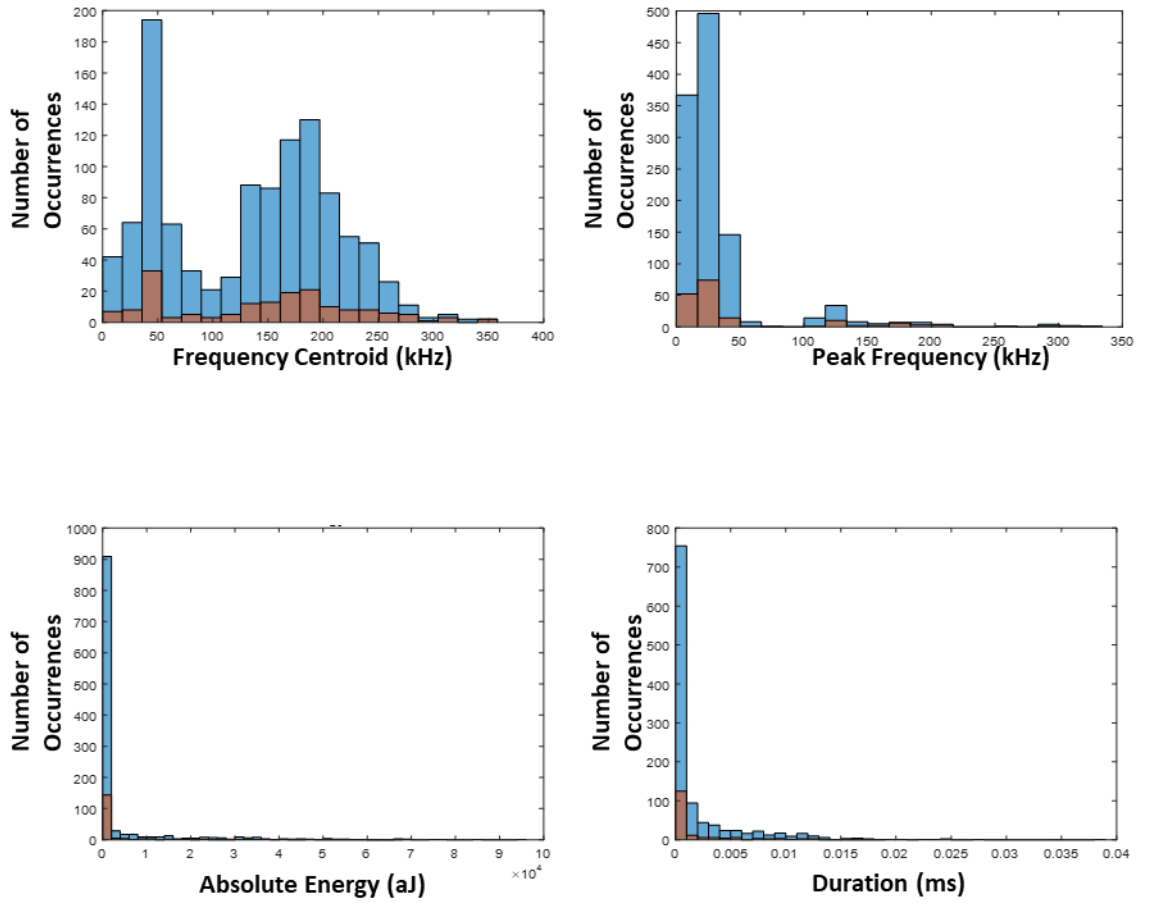


Figure 150. Bar chart distribution of frequency centroid, peak frequency, energy and duration for wiper phase hits (red) and non-wiper phase hits (blue)

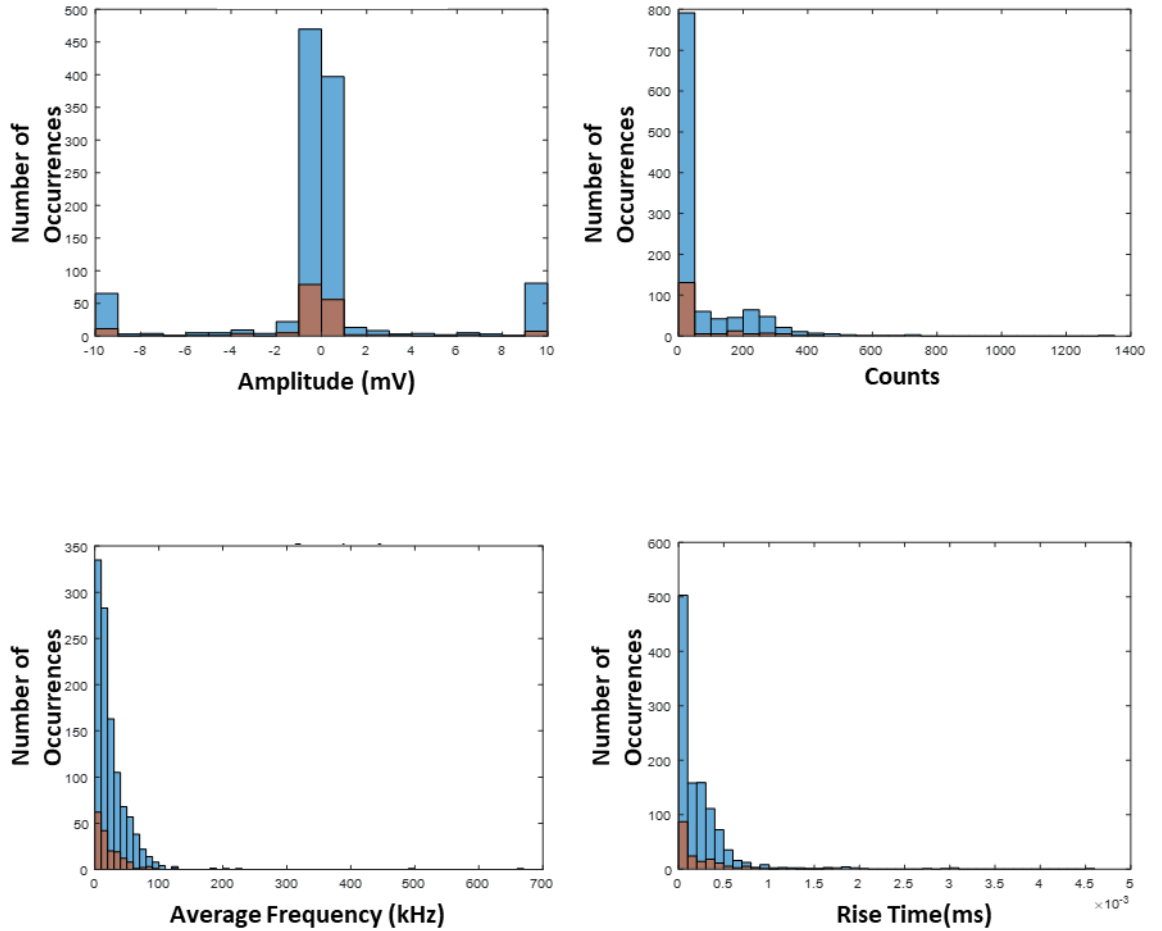


Figure 151. Bar chart distribution of amplitude, counts, average frequency and rise time for wiper phase hits (red) and non-wiper phase hits (blue)

Large numbers of signals are derived from the build volume, with a large range of amplitudes. The most notable signals recorded from the build volume are those with extremely large amplitudes. An example is shown in Figure 152. It can be seen that the amplitude is ‘clipped’, meaning that the magnitude is limited by what the Adlink acquisition system can capture. Defects releasing such large amounts of energy are more likely to be a print failure cause.

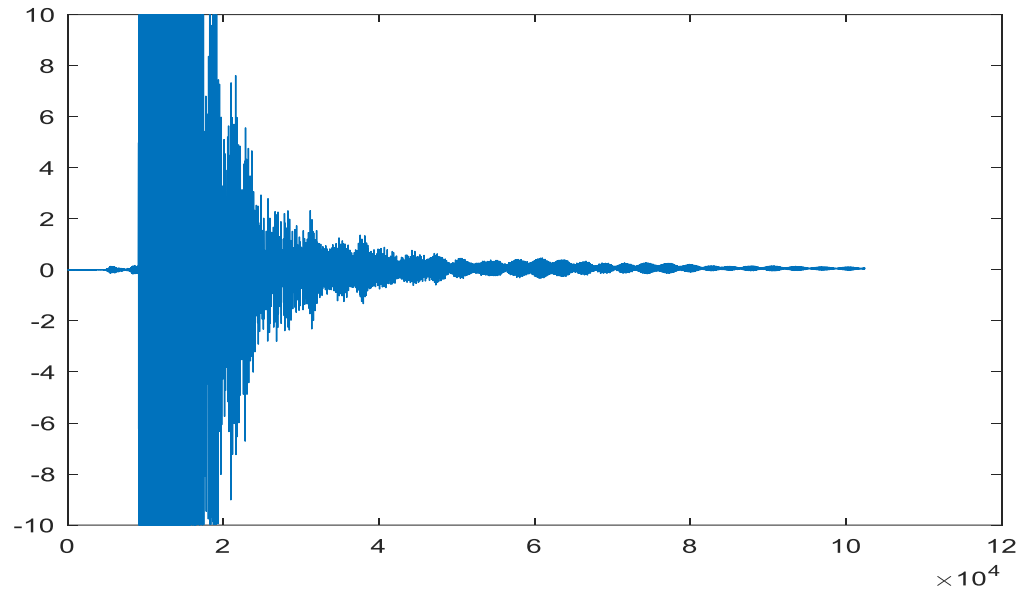


Figure 152. An example of a high amplitude signal

As previously completed in Section 6.2.2, additional features were extracted from the in-process signals, using wavelet and statistical methods. This wide range of features were then reduced to those with a correlation coefficient below 0.75 and a PCA was performed. The features used are shown in Table 10 and Table 11 for signals from a single build and multiple combined builds respectively. For signals from a single build, the first principal component is most strongly influenced by the duration and counts, whilst the second component is strongly influenced by the peak frequency above all other features. The principal components of the combined build signals are influenced by a more diverse range of features than only the AE features. The first principal component is strongly influenced by the duration, mean, and the peak magnitude at 200 and 500kHz, all to similar extents. The second principal component is most strongly influenced by the wavelet features related to the peak frequency at 20, 40 and 60 μ s from the signal onset.

Table 10. Table showing the contribution of each feature to the top two components of the principal component analysis for signals from a single build

Variables		Principal Component 1	Principal Component 2
AE Features	Duration	0.633	0.051
	Counts	0.515	-0.295
	Peak Frequency	-0.062	0.693
Statistical Features	Mean	0.402	-0.131
	Kurtosis	-0.256	-0.069
Wavelet Features	Peak Frequency at 20 μ s from onset	0.107	0.035
	Peak Frequency at 20 μ s from onset	0.061	0.151
	Peak Frequency at 20 μ s from onset	0.062	0.142
	Peak Magnitude at 500kHz	0.292	0.604

Table 11. Table showing the contribution of each feature to the top two components of the principal component analysis for signals from multiple builds

Variables		Principal Component 1	Principal Component 2
AE Features	Duration	0.487	0.223
	Counts	0.093	0.294
	Peak Frequency	0.001	0.251
Statistical Features	Mean	-0.482	0.040
	Skewness	-0.033	-0.001
	Kurtosis	-0.101	-0.046
Wavelet Features	Peak Frequency at 20 μ s from onset	-0.086	0.507
	Peak Frequency at 40 μ s from onset	-0.090	0.528
	Peak Frequency at 60 μ s from onset	-0.077	0.495
	Peak Magnitude at 200kHz	0.488	-0.081
	Peak Magnitude at 500kHz	0.501	0.094

The scree plots shown in Figure 153 demonstrate that the main two principal components from the single build only account for around 35% of the variance of the data, whilst the two principal components of the combined in-process data account for 50% of the data variance.

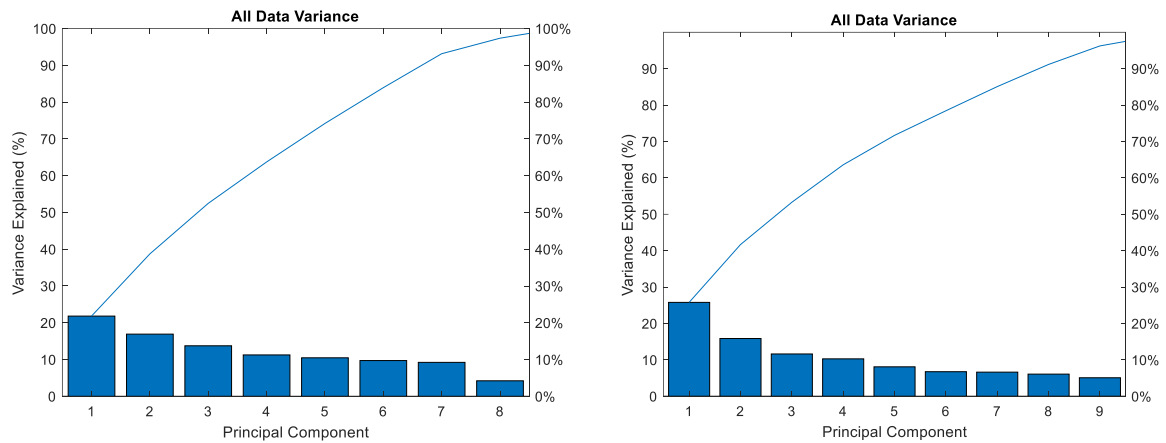


Figure 153. Scree plot of principal components from signals from a single build (Left) and multiple combined builds (right)

The results of plotting the two primary principal components is shown in Figure 154 for data from a single build and in Figure 155 for data from multiple builds combined. Figure 154 shows most signals in a single grouping with some smaller groupings. However, further work would be needed to identify whether these signals are grouped by defect mechanisms and to determine what those defect mechanisms are. Figure 155 shows the separation between similar but separate builds. This is likely due to small differences in plate fixings or variations in build parameters and shows how complicated characterising signals from the build volume will be.

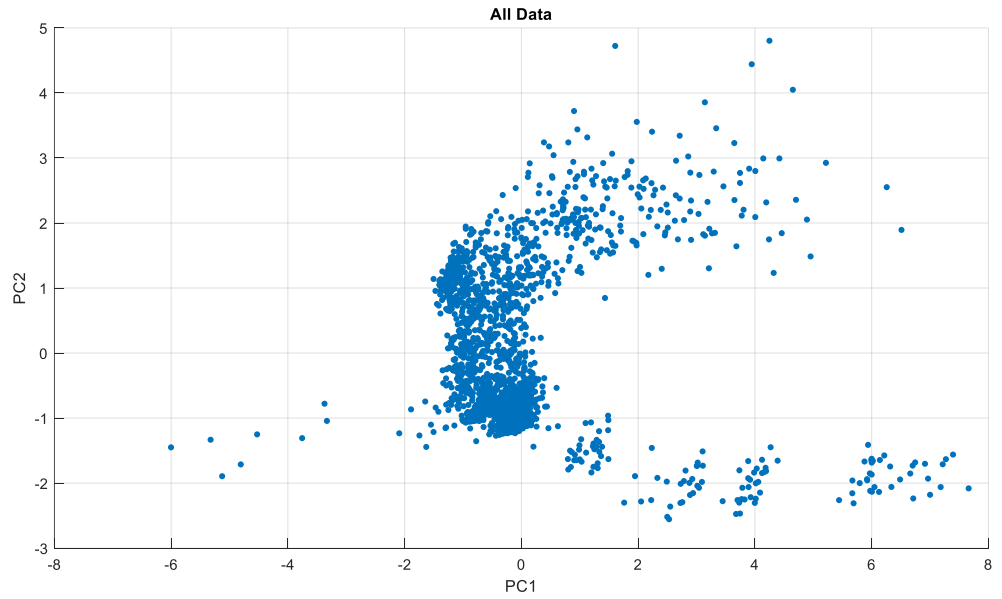


Figure 154. Graph of two primary principal components of data taken from a single build

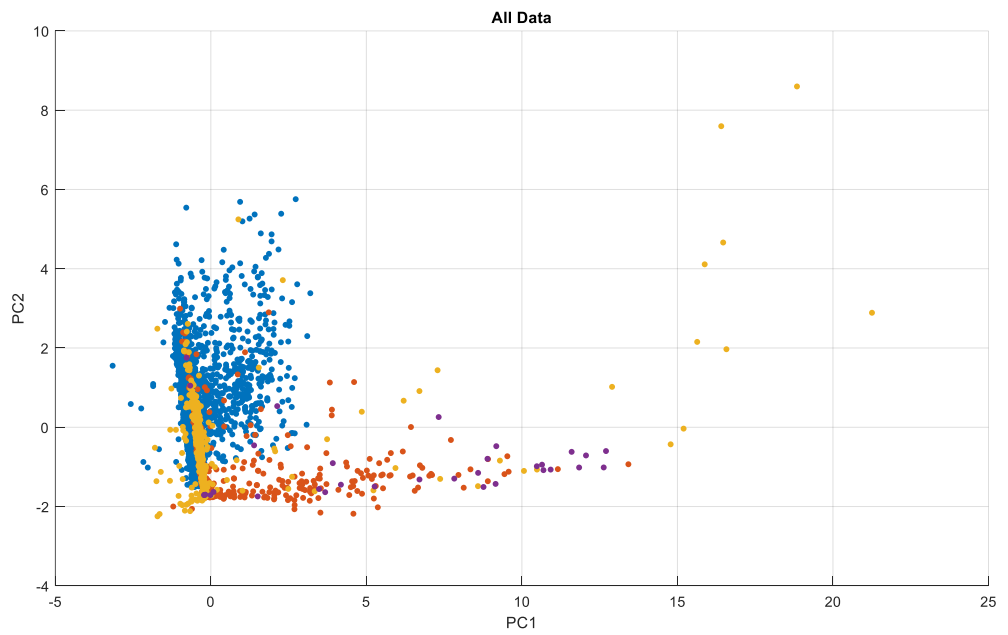


Figure 155. Graph of two primary principal components of data taken from multiple builds, with each colour representing a different build

6.4.3. Discussion

The two main parts of this section are whether sources from within a single build can be separated, and whether sources from builds of similar build setting but different parts can be grouped. Work into whether signals could be extracted when the wiper is active and thus no fusion is taking place showed that these features followed a similar feature profile to when the wiper is inactive. This suggests that very few signals are linked to wiper impacting the partially built component or to laser activity, and most signals are generated in the bulk material. This was followed by a principal components analysis for a single in-process data-set, which resulted in most signals being grouped together with some smaller groupings being present. Further work would be needed to link these groupings to physical phenomena. However, when three in-process data-sets were pooled there was significant variation between them. This has large repercussions for future efforts to classify in-process signals. Unsupervised learning techniques such as ANNs rely on huge volumes of reliable training data to successfully classify it. However, this will not be possible if every individual AM build produces a unique AE feature set.

6.5. Conclusion

The three sections of this chapter were looking into how signals are altered by the waveguide, how signals are changed by using different plate thicknesses and separable in-process signals are. Waveguides were tested using triangular, sawtooth and sinusoidal waves of 50 to 400kHz to assess the degree to which signals are altered by the transition down the waveguide and what effect this would have upon characterisation. Similarly, signals originating from plates of different thicknesses were compared to investigate how the change in thickness may affect attempts to

characterise signals. Finally, principal components analysis was used to investigate how in-process signals can be separated to investigate both whether different defect types can be identified within a build, and whether it would be practical to build a large dataset of signals for training a machine learning algorithm.

Studies into how signals differ across different build plates showed little separation between them. Though the amplitude and features linked to amplitude change with thickness, the lack of separation in the PCA plot show that this should not be an issue that means that similar defects recorded at different thicknesses cannot be grouped together.

However, studies into signals along the waveguide indicate a significant amount of tuning occurs, which complicates efforts to classify signals. This is further complicated by findings from in-process data. Though separation can be seen of signals from the same build, the fact that there is significant variation across build in their feature profile means that training of learning algorithms would be very challenging.

7. Conclusion and Future Work

7.1. Conclusion

This project was supported by Renishaw with the aim of implementing an AE system within the AM500 that would be capable of identifying, locating and characterising signals originating from defects within the build volume. Using AE would provide the advantage of identifying defects throughout the volume, compared to most visual and thermal methods which only identify defects forming on the top layer and require the build to stop while the layer is checked.

The first part of this project was to identify how signals propagate through the build plate, heater plate and waveguides. This work was performed show how a signal reaches the sensor, and if there were any obstacles to providing an accurate location. The use of 3D vibrometry upon the heater plate demonstrated how the primary path from the source on the build plate to sensor differed between different plates. This led to the implementation of changes, by Renishaw, to the heater plate and waveguide designs on all AM500s going forward to assist with producing a clear propagation path. The design change introduced a direct contact between the build plate and waveguides, which simplified signal propagation paths giving more consistent arrival times thus leading to improved location performance. Other work carried out in this chapter included a study into how signals travel through the build plate, specifically with relation to dispersion and reflections. Experiments comparing signals in a build plate and a plate of equal thickness but much larger area showed that reflections arrive very quickly after the initial signal onset and due to a coupling effect often have a much larger amplitude. These findings may carry implications

when attempting to characterise events as reflections arrive from different angles for similar signals. Furthermore, experiments performed on the 3D vibrometer established the dispersive nature of the build plates. This work showed that the changing thickness through the lifecycle of the build plate has an influence on the dispersion of signals and importantly the propagation velocity.

The next chapter was made up of a series of studies into the most effective methods of locating defects with the AM500, as well as how plate thickness changes will affect location performance and how well in-process events could be located. Further work was also done to optimise the data collection for the previously established delta-T method, which is time consuming, and hence not necessarily practical from a commercial viewpoint. Initial experiments were performed on the original heater plate and waveguide configuration (prior to the changes introduced due to the propagation study), which highlighted some of the propagation path issues shown by the vibrometry work. This included a study looking at how the build plate not being properly secured, by the four corner bolts, affects the accuracy of locating AE events. Delta-T data was collected for seven tests, with one through to four bolts loose, and with grease and then one or four washers separating the build and heater plate. This work established the importance of ensuring that the plate is properly secured to collect accurate location data, which can be an issue when manufacturing powder is trapped in the bolt holes when a build is removed. Grease between the plates provided more accurate results, whilst spacing the plates on washers at each corner improved accuracy even further and gave very little spread from each sample location. This provided further evidence that the design needed to be altered in order to facilitate the use of AE to accurately locate defects.

In continuation of work into dispersion in plates carried out in the propagation chapter, a study was carried out into whether using dispersion curves to select wave speeds for TOA would improve accuracy. This would allow for the changing thickness of the build plate throughout its lifecycle, while also not giving the customer the task of collecting delta-T maps between every build. Though it was found that the optimum wave velocity does increase as the plate becomes thinner, as per theory, the optimum speed lies between the A_0 and S_0 speeds and so using dispersion curves was not the optimum approach. However, the optimum wave velocity was found to be close to the bar velocity of the steel waveguides, perhaps due to the signal travelling a similar distance in the waveguide as through the build plate depending upon where the event occurs.

As mentioned previously, a disadvantage of using delta-T in a commercial setting compared to TOA is the need for the customer to collect new delta-T training data between each build. However, delta-T had been proven to provide more accurate location results than TOA, so work was carried out to make it a more feasible option commercially by studying how the required amount of training data can be reduced. By locating signals on progressively thinner plates using only delta-T data collected from a 15mm plate, it was shown that small differences in wave velocity due to thickness had only a negligible effect on the location accuracy. This work suggested that it may be possible to produce a single delta-T map for the full lifecycle of a build plate, though further work is needed on a range of plates to verify this fully. Beyond this, work was carried to produce grids with a smaller number of nodes, from 121 with a grid size of 20mm down to four with a grid size of 200mm. This study found that events were accurately located consistently, and in some cases improved. This

is likely due to an overfitting of the data when using a large amount of training data and reflects the homogeneous nature of the build plate. This, combined with the previous results suggesting a single delta-T training dataset can be used throughout a plates lifecycle, show that delta-T could be effectively implemented within the AM500.

The final component of this project was an investigation into whether it would be feasible to classify in-process defects based upon their AE signature. The characterisation chapter consisted of studying how the nature of a signal changes through the build plate and waveguides, and how in-process signals can be separated. Separation of signals was performed by carrying out principal component analysis for each of the three groups of signals; signals from different types of waveguides, signals from different thicknesses of build plates and signals taken from various builds. The waveguides were excited with various different signals (sinusoidal, triangular, sawtooth) to look into whether initially different signals would still be distinct after travelling down the waveguides. Though this showed that certain frequencies are amplified by the propagation down the waveguide, signals are difficult to separate once they have traversed the waveguide using the selected features. This suggests that signals converge as they traverse the waveguide, which would have consequences when attempting to classify in-process signals. When using PCA to separate artificial AE signals generated within plates of different thicknesses, it was also found that there was little separation between them. However, in this case this is a positive result, as it means that the feature content of similar events is not affected by plate thickness. This would mean that the changing thickness of a build plate through its lifecycle should not affect efforts

to classify defects. The final section of the characterisation chapter involved attempting to separate in-process signals, both separating signals within a signal build and an investigation into the separation between different builds. The principal component analysis carried out on AE data from within a single build demonstrated significant separation, which combined with further work to link AE data with physical defects may prove useful. Further work was done using PCA to examine the separation between AE signals recorded from separate but similar builds. When using machine learning techniques such as artificial neural networks, a large, consistent dataset is needed to properly train the algorithm. Therefore, it was important to ascertain whether a suitable training dataset could be generated from a series of builds from the AM500. By conducting a principal components analysis, it was shown that there was significant separation between AM500 builds conducted under similar conditions. This suggests that it will be difficult to collect a large enough dataset to properly use machine learning algorithms to classify in-process signals as there is too much variation between individual builds.

Overall, this project successfully proved that an AE system can be effectively implemented within a commercially-available additive manufacturing machine, the AM500. Studies investigating how signals propagate through the build plate assembly led to significant design changes to the heater plate and waveguide to make accurate location of defects possible, which will be carried through future machines. The chapter focused on locating AE events established that it is possible to locate cracks as they occur within the AM500. It was also established that the delta-T method could accurately locate AE events, and be refined to make the method more feasible for use in production by reducing the training data needed

and requiring a single delta-T dataset for the lifecycle of the build plate. Finally, the characterisation chapter established that due to the complex geometry of the waveguides and variation between different builds, it is likely not possible to classify defects based solely upon their AE signatures, or to build large, consistent datasets for use with machine learning algorithms.

7.2. Future Work

There are many aspects of this projects that can be advanced going forward. Previous work showed how a single set of delta-T grids could be used across a range of thicknesses with little loss of accuracy. To develop this finding to be feasible commercially, studies should be undertaken using a wide range of different plates for each material. This will help to establish whether a single set of delta-T grids could be collected for every plate or whether a standard set of grids could be developed for each material and supplied to the customer. This would remove the burden of generating delta-T maps from the customer.

Over the course of this project, experiments were carried out on aluminium, stainless steel and titanium plates. However, the Renishaw AM500 is also available with other materials such as nickel alloys and cobalt chromium. Therefore, further experiments should be conducted to ensure that the AE methods developed in this project are suitable for all materials available to customers.

Results presented in Section 6.2 indicated that signals are significantly altered by traversing along the waveguide. Ono & Cho (2016) found that longitudinal resonant frequencies were dominant in waveguides below 177mm in length, and further studies found that higher longitudinal and flexural modes arise beyond a diameter

of 6mm. Thus work could be done to further refine the waveguide design, which is currently 100mm long with a 10mm diameter, to improve the fidelity of signals traversing the waveguide. This would involve comparing how signals travel along different length and diameter waveguides, as well as diameter changes. Additional work could be performed to optimise the fixing between the waveguide and build plate, as though this has been improved, fixing them together with a bolt means that the base of the waveguide will act as a tube before transitioning to rod behaviour. Optimising a waveguide design that better preserves the fidelity of the signal would significantly improve the chances of accurately classifying defects.

The largest body of work that could be undertaken would be further studies into characterising AE signals. Firstly, this should involve a study of physical defects and how these defects match to AE signatures. To do this, parts will need to be produced with AE active, and post-processing techniques such as X-ray or CT scans to identify defects. Due to the nature of AE, signals could originate at any layer of the part which would make matching defects to AE a very complex process so this should be repeated multiple times to attain the best possible results. Shevchik et al (2017) combined AE with an infrared thermal system in order to collect further features with which to classify defects, with significantly better results than using only AE. This method could be repeated within the AM500 to further aid with classification.

Finally, a further understanding of how AE develops and propagates through the build material and build plate could be developed by modelling the build plate in COMSOL or in Matlab using the Local Interaction Simulation Technique (LISA). Hamstad (2007) used COMSOL to generate artificial AE sources within a finite

element (FE) model using a database of AE signals collected during previous studies and found that simulated results matched well with experimental results. Marks (2016) instead used LISA, a package of Matlab packages that use the Rayleigh-Lamb wave equations to approximate propagation through a solid, which was verified using 3D vibrometry. Either of these options could be used to model the build plate, though COMSOL would be better suited to more complex studies including waveguides and an AM build attached to the plate.

References

- ADLINK Technology Inc, 2014. *USB-1210 DAQ Module*, Taipei: ADLINK Technology Inc.
- Akaike, H., 1998. *Information Theory and an Extension of the Maximum Likelihood Principle*. Selected Papers of Hirotogu Akaike, pp. 199-213.
- Al-jumaili, S., 2016. *Damage Assessment in Complex Structures using Acoustic Emission*, Cardiff: Cardiff University.
- Al-Jumaili, S. K., Holford, K. M., Eaton, M. J. & Pullin, R., 2015. *Parameter Correction Technique (PCT): A novel method for acoustic emission characterisation in large-scale composites*. Composites Part B, Volume 75, pp. 336-344.
- Al-Jumaili, S., Pearson, M., Holford, K, Eaton, M., Pullin, R., 2016. *Acoustic emission source location in complex structures using full automatic delta-T mapping technique*. Mechanical Systems and Signal Processing, Volume 72, pp. 513-524.
- Bar, H., Bhat, M. & Murthy, C., 2004. *Identification of Failure Modes in GFRP using PVDF Sensors: ANN approach*. Composite Structures, 65(2), pp. 231-237.
- Baxter, M., Pullin, R., Pullin, R., Holford, K., Evans, S., 2007. *Delta T source location for acoustic emission*. Mechanical Systems and Signal Processing, 21(3), pp. 1512-1520.
- Bidare, P.; Maier, R., Beck, R., Shephard, J.D., Moore, A.J., 2017. *An open-architecture metal powder bed fusion system for in-situ process measurement*. Additive Manufacturing, Volume 16, pp. 177-185.
- Boving, K. G., 1989. *NDE handbook: non-destructive examination methods for condition monitoring*. London: Butterworths.
- Buchbinder, D., Schleifenbaum, H. Heidrich, S. Meiners, W. Bultmann, J., 2011. *High Power Selective Laser Melting (HP SLM) of Aluminum Parts*. Physics Procedia, pp. 271-278.
- Clark, D., Sharples, S. & Wright, D., 2011. *Development of online inspection for additive manufacturing products*. Insight: Non-Destructive Testing and Condition Monitoring, 53(11), pp. 61-73.
- Craeghs, T., Clijsters, S., Kruth, J., Bechmann, F., Ebert, M.C., 2012. *Detection of Process Failures in Layerwise Melting with Optical Process Monitoring*. Physics Procedia, Volume 39, pp. 753-759.
- Crivelli, D., Guagliano, M. & Monici, A., 2014. *Development of an artificial neural network processing technique for the analysis of damage evolution in pultruded composites with acoustic emission*. Composites: Part B, Volume 56, pp. 948-959.
- D'Angelo, G., Hansen, H., Nielsen, J.S., Rasmussen, J., Pedersen, D.B., 2014. *A comparative performance analysis of FDM machines based on a calibration artefact*. Boston, American Society for Precision Engineering.

- de Oliveira, R. & Marques, A., 2008. *Health monitoring of FRP using acoustic emission and artificial neural networks*. *Computers and Structures*, Volume 86, pp. 367-373.
- Downs, K., Hamstad, M. & O'Gallagher, A., 2003. *Wavelet Transform Signal Processing to Distinguish Different Acoustic Emission Sources*. *Acoustic Emission*, Volume 21, pp. 52-69.
- Eaton, M., Pullin, R., Hensman, J.J., Holford, K.M., Worden, K., Evans, S.L., 2010. *Principal Component Analysis of Acoustic Emission Signals from Landing Gear Components: An Aid to Fatigue Fracture Detection*. *Strain*, Volume 47, pp. 588-594.
- Eaton, M., Pullin, R. & Holford, K., 2012. *Acoustic emission source location using Delta T Mapping*. *Composites: Part A*, 43(6), pp. 856-863.
- Engineering Toolbox, 2004. *Speed of Sound in Solids and Metals*. [Online]. Available at: https://www.engineeringtoolbox.com/sound-speed-solids-d_713.html. [Accessed 30 September 2021].
- Everton, S., Hirsch, M., Stavroulakis, P., Leach, R., Clare, A., 2016. *Review of in-situ process monitoring and in-situ metrology for metal additive manufacturing*. *Materials and Design*, pp. 431-445.
- Gaja, H. & Liou, F., 2017. *Defects monitoring of laser metal deposition using acoustic emission sensor*. *The International Journal of Advanced Manufacturing Technology*, 90(1-4), pp. 561-574.
- Gibson, I., 2021. *Additive Manufacturing Technologies*. 3rd ed. Cham: Springer.
- Gibson, I., Rosen, D. & Stucker, B., 2015. *Additive Manufacturing Technologies 3D Printing, Rapid Prototyping, and Direct Digital Manufacturing*. 2nd ed. New York: Springer.
- Graff, K. F., 1991. *Wave Motion in Elastic Solids*. 1st ed. Oxford: Clarendon Press.
- Guan, G., Hirsch, M., Lu, Z.H., Childs, T.D., Matcher, S., Goodridge, R., Groom, K., Clare, A., 2015. *Materials and Design. Evaluation of selective laser sintering processes by optical coherence tomography*, Volume 88, pp. 837-846.
- Hamstad, M., 2006. *Small Diameter Waveguide for Wideband Acoustic Emission*. *Journal of Acoustic Emission*, 24(853), pp. 234-247.
- Hanzl, P., Zetek, M., Baksa, T. & Kroupa, T., 2015. *The Influence of Processing Parameters on the Mechanical Properties of SLM Parts*. *Procedia Engineering*, Volume 100, pp. 1405-1413.
- Hensman, J., Mills, R., Pierce, S.G., Worden, K., Eaton, M., 2010. *Locating acoustic emission sources in complex structures using Gaussian processes*. *Mechanical Systems and Signal Processing*, Volume 24, pp. 211-223.
- Holford, K., Eaton, M.J., Hensman, J.J., Pullin, R., Evans, S.L., Dervilis, N., Worden, K., 2017. *A new methodology for automating acoustic emission detection of metallic fatigue fractures in highly demanding aerospace environments: An overview*. *Progress in Aerospace Sciences*, Volume 90, pp. 1-11.

- Holroyd, T. J., 2000. *The acoustic emission and ultrasonic monitoring handbook*. Oxford: Coxmoor.
- Jolliffe, I., 2002. *Principal Component Analysis*. 2nd ed. New York: Springer.
- Koester, L., Taheri, H., Bigelow, T., Bond, L., Faierson, E.J., 2018. *In-situ acoustic signature monitoring in additive manufacturing processes*. Maharashtra, AIP Conference Proceedings.
- Kouprinoff, E. & Luwes, N., 2017. *On-Line Monitoring of Laser Powder Bed Fusion by Acoustic Emission*. IEEE, Issue 203-207.
- Li, X., 2002. *A brief review: Acoustic emission method for tool wear monitoring during turning*. International Journal of Machine Tools and Manufacture, 42(2), pp. 157-165.
- Lowe, M., 2021. *Guided Wave Dispersion Curve Calculation*. [Online]. Available at: <http://www.disperse.software/>
- Mani, M., Lane, B., Donmez, M., Feng, S.C., Moylan, S.P., 2017. *A review on measurement science needs for real-time control of additive manufacturing metal powder bed fusion processes*. International Journal of Production Research, 55(5), pp. 1400-1418.
- Marks, R., 2016. *Methodology platform for prediction of damage events for self-sensing aerospace panels subjected to real loading*. Cardiff: Cardiff University
- Mathworks, 2021. *Analyze Quality of Life in US Cities using PCA*. [Online]. Available at: <https://uk.mathworks.com/help/stats/quality-of-life-in-u-s-cities.html>. [Accessed 29 September 2021].
- Mercelis, P. & Kruth, J., 2006. *Residual stresses in selective laser sintering and selective laser melting*. Rapid Prototyping Journal, 12(5), pp. 254-265.
- Metal AM, 2021. *Applications for metal Additive Manufacturing technology*. [Online]. Available at: <https://www.metal-am.com/introduction-to-metal-additive-manufacturing-and-3d-printing/applications-for-additive-manufacturing-technology/>. [Accessed 26 September 2021].
- Miller, R. K., Hill, E. v. & Moore, P. O., 2005. *Acoustic Emission Testing*. Columbus: American Society for Nondestructive Testing.
- Mistras, 2011. *R15a Product Data Sheet*. [Online]. Available at: http://www.physicalacoustics.com/content/literature/sensors/Model_R15a.pdf
- Mistras, 2011. *WD Sensor Product Data Sheet*. [Online]. Available at: http://www.physicalacoustics.com/content/literature/sensors/Model_WD.pdf
- Mistras, 2013. *F15a Product Data Sheet*. [Online]. Available at: http://www.physicalacoustics.com/content/literature/sensors/Model_F15A.pdf
- Ono, K. & Cho, H., 2016. *Rods and Tubes as AE Waveguides*. Journal of Acoustic Emission, Volume 34, pp. 234-252.

Parry, L., Ashcroft, I. & Wildman, R., 2016. *Understanding the effect of laser scan strategy on residual stress in selective laser melting through thermo-mechanical simulation*. Additive Manufacturing, pp. 1-15.

Pearson, M. R., Eaton, M., Featherston, C., Pullin, R., Holford, K., 2017. *Improved acoustic emission source location during fatigue and impact events in metallic and composite structures*. Structural Health Monitoring, 16(4), pp. 382-399.

Physical Acoustics Corporation, 2007. *PCI-2 Based AE System User's Manual*. Princeton Junction: Physical Acoustics Corporation.

Plotnikov, Y., Henkel, D., Burdick, J., French, A., Sions, J., Bourne, K., 2019. *Infrared-assisted acoustic emission process monitoring for additive manufacturing*. Dubra, AIP Conference Proceedings.

Pollock, A., 1986. *Classical Plate Theory in Practical AE Testing*. Eighth International Acoustic Emission Symposium, The Japanese Society for Nondestructive Testing, pp. 708-721.

Polytec, 2021. *PSV-500 Scanning Vibrometer*. [Online]. Available at: <https://www.polytec.com/uk/vibrometry/products/full-field-vibrometers/psv-500-scanning-vibrometer>

Red Pitaya, 2021. *STEMlab 125-10 Starter Kit*. [Online]. Available at: <https://redpitaya.com/product/stemlab-125-10-starter-kit/>

Renishaw plc, 2021. *Industrial applications of Renishaw metal additive manufacturing technology*. [Online]. Available at: <https://www.renishaw.com/en/industrial-applications-of-renishaw-metal-additive-manufacturing-technology--15256>. [Accessed 26 September 2021].

Renishaw plc, 2021. *Our Technology*. [Online]. Available at: <https://www.renishaw.com/en/our-technology--27362>. [Accessed 26 September 2021].

Rindorf, H., 1981. *Acoustic Emission Source Location in Theory and Practice*. Bruel and Kjaer Technical Review

Rodriguez, E., Mireles, J., Terrazas, C., Espalin, D., Perez, M., Wicker, R., 2015. *Approximation of absolute surface temperature measurements of powder bed fusion additive manufacturing technology using in-situ infrared thermography*. Additive Manufacturing, Volume 5, pp. 31-39.

Samanta, B., 2003. *Gear Fault detection using artificial neural networks and support vector machines with genetic algorithms*. Mechanical Systems and Signal Processing, Volume 18, pp. 625-644.

Sause, M., 2011. *Investigation of Pencil-Lead breaks as acoustic emission sources*. *Journal of Acoustic Emission*, pp. 184-196.

Schwerdtfeger, J., Singer, R. & Korner, C., 2012. *In situ flaw detection by IR-imaging during electron beam melting*. Rapid Prototyping Journal, 18(4), pp. 259-263.

Shevchik, S., Kenel, C., Leinenbach, C. & Wasmer, K., 2018. *Acoustic emission for in situ quality monitoring in additive manufacturing using spectral convolutional networks*. Additive Manufacturing, Volume 21, pp. 598-604.

Srivatsen, T., 2016. *Additive Manufacturing: Innovations, Advances and Applications*. Boca Raton: CRC Press.

Technavio, 2018. *Global Commercial Aircraft Seat Belts Market 2018-2022*. [Online]. Available at: <https://www.businesswire.com/news/home/20180903005118/en/Global-Commercial-Aircraft-Seat-Belts-Market-2018-2022-Use-of-Additive-Manufacturing-Technologies-to-Produce-Belt-Buckles-to-Boost-Growth-Technavio>. [Accessed 26 September 2021].

Teledyne Lecroy, 2021. *Arbitrary Waveform Generators*. [Online]. Available at: <https://teledynelecroy.com/wavestation/detail.aspx?modelid=6863&capid=131&mid=1043>

Thor Labs, 2021. *Optical Table and Active Isolator Leg Bundles*. [Online]. Available at: https://www.thorlabs.com/newgrouppage9.cfm?objectgroup_id=5930

Vishal, R., 2018. *Feature Selection - Correlation and the P-Value*. [Online]. Available at: <https://towardsdatascience.com/feature-selection-correlation-and-p-value-da8921bfb3cf>. [Accessed 29 September 2021].

Wasmer, K., Le-Quang, T., Meylan, B. & Shevchik, S., 2019. *In Situ Quality Monitoring in AM Using Acoustic Emission: A Reinforcement Learning Approach*. Journal of Materials Engineering and Performance, 28(2), pp. 666-672.

Yadroitsev, I., Bertrand, P. & Smurov, I., 2007. *Parametric analysis of the selective laser melting process*. Applied Surface Science, 253(19), pp. 8064-8069.

Yu, W., Sing, S.L., Chua, C.K., Kuo, C.N., Tian, X.L., 2019. *Particle-reinforced metal matrix nanocomposites fabricated by selective laser melting: A state of the art review*. Progress in Materials Science, Volume 104, pp. 330-379.